

University of Arkansas, Fayetteville

ScholarWorks@UARK

Graduate Theses and Dissertations

5-2022

Validation of CFD Tornado Pressure on Building and Wind Field with TTU Vortex Chamber Measurements

Sumit Verma

University of Arkansas, Fayetteville

Follow this and additional works at: <https://scholarworks.uark.edu/etd>



Part of the [Civil Engineering Commons](#), and the [Structural Engineering Commons](#)

Citation

Verma, S. (2022). Validation of CFD Tornado Pressure on Building and Wind Field with TTU Vortex Chamber Measurements. *Graduate Theses and Dissertations* Retrieved from <https://scholarworks.uark.edu/etd/4516>

This Dissertation is brought to you for free and open access by ScholarWorks@UARK. It has been accepted for inclusion in Graduate Theses and Dissertations by an authorized administrator of ScholarWorks@UARK. For more information, please contact scholar@uark.edu, uarepos@uark.edu.

Validation of CFD Tornado Pressure on Building and Wind Field with TTU Vortex Chamber
Measurements

A dissertation submitted in partial fulfillment
of the requirements for the degree of
Doctor of Philosophy in Engineering

by

Sumit Verma
Tribhuvan University
Bachelor of Engineering (Civil), 2015

May 2022
University of Arkansas

This dissertation is approved for recommendation to the Graduate Council.

R. Panneer Selvam, Ph.D.
Dissertation Director

Micah Hale, Ph.D.
Committee Member

Mark E. Arnold, Ph.D.
Committee Member

Ernie Heymsfield, Ph.D.
Committee Member

Abstract

Structural failure of low-rise buildings is the root cause of higher number of casualties, death tolls and economic losses at the place of occurrence of tornadoes. Proper design of low-rise buildings in tornado-prone areas require accurate estimation of tornado-induced wind loads; however, exhaustive research to estimate the wind loads reliably on buildings during tornadic events is still lacking. Several studies have been carried out to investigate the magnitude of forces induced by tornado winds on buildings from experimental as well as computational side. However, the wind pressures obtained on the building from different experimental studies have shown significant variation from one study to another. Similarly, the wind pressures on the building from CFD simulation of tornado vortex often lacks comparison and/or validation with experimental data. Even the modeling of CFD tornado chamber and CFD flow validation is fraught with several challenges such as requirements of high-performance (or supercomputing) resources and lack of guidelines for validation of wind field of tornado vortex from CFD model.

Thus, in this work, a simple yet an effective CFD tornado simulator model is developed, which provides comparable results with experiment without the necessity of supercomputing resources. This work also identifies and proposes four important features of tornado vortex (i.e., touchdown swirl ratio, core radius, the maximum tangential velocity & the elevation of maximum tangential velocity) including the ground pressure profile for validation of wind field obtained from CFD model. A comparative analysis of the four important vortex features from different tornado chambers and different work of literature is also presented. Lastly, the pressures induced by tornado vortex from CFD model on the building is validated with TTU experimental datasets. Furthermore, a detailed analysis on the effect of size of building, flow structure and Reynolds number of vortex on the induced wind pressures on the building is also presented.

Preface

Following papers are the outcomes of this work. The published works is only reviewed as summary as it is already available in the open literature. For the work in review, a detailed discussion is presented. The published papers are as follows:

- I. Verma, S. and Selvam, R.P. (2020), “CFD to VorTECH pressure field comparison & roughness effect on flow”, *Journal of Structural Engineering*, 146(9), 04020187-1. [https://doi.org/10.1061/\(ASCE\)ST.1943-541X.0002766](https://doi.org/10.1061/(ASCE)ST.1943-541X.0002766)
- II. Verma, S., and Selvam, R. P. (2021). CFD model validation with experimental tornado wind field & comparison of wind field in different tornado chambers. *Wind and Structures*, 33(5), 367–381. <https://doi.org/10.12989/WAS.2021.33.5.367>
- III. Verma, S., and Selvam, R.P. (2021). Effect of Height of the Tornado Chamber on Vortex Touchdown. In: *Rushi Kumar, B., Sivaraj, R., Prakash, J. (eds) Advances in Fluid Dynamics. Lecture Notes in Mechanical Engineering*. Springer, Singapore. https://doi.org/10.1007/978-981-15-4308-1_38
- IV. Verma, S., and Selvam, R.P. (2021). Differences in flow structures of tornado vortex and efficiency of different tornado chambers, *6th AAWE workshop organized by Clemson University*, available at: <https://tigerprints.clemson.edu/cgi/viewcontent.cgi?article=1075&context=aawe>
- V. Verma, S., Mansouri, Z., and Selvam, R. P. (2021, November), Incorporating Two Weeks Open Source Software Lab Module in CFD and Fluids Courses, Paper presented at *2021 ASEE Midwest Section Conference, Virtual*. [10.18260/1-2-1125.1128.1153-38325](https://doi.org/10.18260/1-2-1125.1128.1153-38325)

- VI. Mansouri, Z., Verma, S., and Selvam, R. P. (2021, November), Teaching Modeling Turbulent Flow Around Building Using LES Turbulence Method and Open-source Software OpenFOAM, Paper presented at *2021 ASEE Midwest Section Conference*, Virtual. [10.18260/1-2-1125.1128.1153-38326](https://doi.org/10.18260/1-2-1125.1128.1153-38326)
- VII. Sumit Verma, Selvam, R.P., Zhuo, T., and Zuo, D. (2022), Comparison of Tornado-Induced Pressures on Building from CFD Model with TTU Experimental Measurements, In review with *Journal of Wind Engineering and Industrial Aerodynamics*.

The papers listed in V and VI above were prepared for educating students and practicing engineers to be able to set up their own CFD models for evaluating wind loads on the buildings. For hands-on-learning experience, some Github repositories were created to upload and store the OpenFOAM case files so that the readers of the paper could visit the webpage, download relevant case files, and learn along the way by reading the paper. The webpages are as follows:

1. <https://github.com/rpsuark>
2. <https://github.com/timusv5977>

The chapter wise development of this thesis is presented next. The subject (i.e., structural failure of low-rise buildings and wind loads induced by tornadoes on low-rise buildings) is introduced first in Chapter - 1, followed by literature review in Chapter - 2 and details of computational modeling of CFD tornado simulator in Chapter - 3. In Chapter - 4, the flow features of tornado-like vortex obtained from the CFD model is compared and validated with experimental datasets from Texas Tech University (TTU) tornado simulator datasets. In Chapter - 5, the flow features of tornado-like vortex obtained from different experimental and CFD tornado simulators are compared while in Chapter - 6, the pressures induced by tornado-like vortex on the building from

CFD model is validated with experimental datasets from TTU simulator. In addition, the effect of size of the building on the pressures induced by tornado-like vortex is also documented. In Chapter - 7, the effect of different flow-structures and Reynolds number of tornado-like vortex on induced pressures on the building is presented. Lastly, in Chapter - 8, the conclusions from different studies are summarized, the limitation of the present study is pointed out and the directions for future research are delineated.

The content of Chapter-4 is primarily based on Paper - I while the contents of Chapter - 5 is based mostly on Paper - II and some part is taken from Paper - III. Finally, the contents for Chapter - 6 and 7 are derived from Paper-IV. As paper I, II and III are published already, so, the Chapters - 4 and 5 are presented as the summary of published papers highlighting the important outcomes whereas Chapters - 6 and 7 (based on Paper - IV in review) are presented with more details, illustrations, and descriptions.

Acknowledgement

First and foremost, I would like to express my sincerest gratitude to my advisor, Dr. R. Panneer Selvam, for his mentorship over the last four years. His guidance, encouragement and motivation were the key driving force that kept me going with research for the past four years leading to the culmination of this work. I would also like to thank my dissertation committee members, Dr. Micah Hale (Civil Engineering Department Chair), Dr. Ernie Heymsfield, and Dr. Mark Arnold for serving in my dissertation committee and providing me valuable feedback and comments to enhance the quality of this work. I would also like to acknowledge the financial support from the National Science Foundation (NSF) under award No. CMMI-1762999 to pursue this work. In addition, I would also like to take the opportunity to express my gratitude to the University of Arkansas Graduate School and International Education for supporting me financially through Doctoral Academy Fellowship.

I would like to acknowledge Ms. Zahra Mansouri (a member of my research group) for all her help while pursuing research work and course-related matters. I wish her all the best for her PhD program and a bright future ahead after completion of her PhD program.

Lastly, I would also like to acknowledge my family and all my friends in Fayetteville, who have helped me and/or supported me during my PhD journey, and my 4 years long stay in Fayetteville.

Table of Contents

Chapter -1: Introduction and Objectives	1
1.1 Introduction	1
1.2 Different Approach of Exploring the Wind Field and Wind-induced Load by Tornadoes ..	2
1.3 Limitations of Experimental vs Benefits of CFD Tornado Simulation	3
1.4 Challenges with Modeling of CFD Tornado Chamber and CFD Flow Validation	4
1.5 Challenges with Tornado Pressures on Building Using CFD Vortex Chambers.....	5
1.6 Thesis Objectives	6
Chapter-2: Literature Review	8
2.1 Introduction	8
2.2 Post-Storm Damage Investigation.....	8
2.3 Experimental Tornado Simulation	10
2.4 CFD Tornado Simulation	11
2.4.1 Turbulence Models in CFD Tornado Simulation	11
2.5 Validation of CFD Tornado Flow Field.....	14
2.6 Tornado Forces on Building from Experimental Tornado Chambers.....	16
2.7 Tornado Forces on Building from CFD Tornado Chambers	18
Chapter-3: Computational Modeling.....	23
3.1 Introduction	23
3.2 Computational Domain and Meshing of Computational Domain	24
3.2.1 Determination of Depth of Outlet in Simplified CFD Tornado Chamber.....	25
3.2.2 Meshing of Computational Domain	26
3.3 Governing Equations, Solution Schemes and Boundary Conditions.....	28
3.3.1 Non-dimensionalization of NS Equation.....	29
3.3.2 Initial and Boundary Conditions.....	30

3.4 Grid Independence Test	34
3.4.1 Normalized Root Mean Square Error (NRMSE) as Error Estimate.....	34
Chapter-4: Validation of CFD Flow Field with TTU Experiment	37
4.1 Introduction	37
4.1.1 Local Core Radius and Vertical Profile of Core Radius	38
4.1.2 Fluctuation of Maximum Tangential Velocity over Time.....	40
4.1.3 Vortex Wandering and Difficulty in Core Radius Estimation	42
4.1.4 Comparison of Vertical Core Profile from CFD Model with TTU Experiment	42
4.2 Comparison of Near-Surface Pressure Distribution Over a Range of Varying Swirl Ratios from CFD Model with TTU Experiment	43
4.2.1 Fluctuation of Pressure in Time.....	44
4.3 Summary and Conclusion	45
Chapter-5: Comparison of Touchdown Swirl Ratio and Important Vortex Parameters from Different Tornado Chambers	47
5.1 Introduction	47
5.2 Different Definitions of Swirl Ratio.....	48
5.3 Conversion Relations for Swirl Ratio from One Definition to Another	50
5.3.1 Derivation of Conversion Relations for Different Definitions of Swirl Ratio	51
5.4 Different Classification Categories of Tornado Chambers	53
5.5 Effect of Variation in Geometry of Tornado Chambers on Touchdown	57
5.5.1 Effect of Variation of Total Height on Important Vortex Parameters.....	58
5.5.2 Effect of Variation of Outlet Diameter on Touchdown.....	61
5.6 Summary and Conclusion	63
Chapter-6: Validation of Tornado-induced Pressures on Building and Effect of Size of the Building Model on Induced Pressures	65
6.1 Introduction	65

6.2.1 Effect of High Aspect Ratio of Cells in Mesh.....	68
6.3 Validation of Induced Pressures on Building from CFD Model with TTU Simulator	76
6.3.1 Comparison of Mean C_p on Building for Different Radial Location of Building.....	77
6.3.2 Comparison of Minimum C_p on Building for Different Radial Location of Building .	79
6.4 Comparison of Induced Pressure on Building due to Different Sizes of Building	80
6.4.1 Selection of Core Radius of Tornado-like Vortex with Respect to the Size of Building	81
6.4.2 Comparison of Pressure Coefficients Due to Different Sizes of Building	82
6.5 Conclusion.....	87
Chapter-7: Comparison of Pressures on a Building due to Different Flow Structures of Vortex and Different Reynolds Number	88
7.1 Introduction	88
7.2 Previous Work on Various Flow Structure & Reynolds Number of Tornado-like Vortex.	88
7.3 Pressure Coefficient on the Faces of Building due to Different Flow Structure of Vortex	90
7.3.1 Tornado Flow Field at Roof Level around the Building Due to Different Swirl Ratios when Building is located at the Center of Simulator.....	92
7.3.2 Tornado Flow Field at Roof Level around the Building Due to Different Swirl ratios when Building is located at the Core Radius of Vortex	96
7.4 Pressure Coefficient on the Faces of Building due to Different Reynolds Number	102
7.5 Conclusion.....	106
Chapter-8: Conclusion.....	108
8.1 Summary	108
8.2 Conclusion.....	110
8.3 Primary Contributions to the Scientific Community.....	116
8.4 Limitations of Current Study.....	116
8.5 Suggested Future Work.....	118

References	120
Appendices	126
Appendix A: User Manual for CFD Program - “ward79.out”	126
Appendix B: A Simple CFD Tornado Simulator Implementation in OpenFOAM.....	130
Appendix C: Mapping of Experimental Data onto a Contour Plot	152
Appendix D: Computation of Tornado Pressures on Building Using OpenFOAM	164
Appendix E: Parallel Simulation in OpenFOAM	167
CURRICULUM VITAE.....	169

List of Figures

Fig. 1. (a) Major structural failure (roofs uplifted and blown off) of a low-rise building (From Yang et al., 2018) (b) destroyed low-rise building by tornadoes (From Schlueter (2016)).....	1
Fig. 2. CAD model for computational domain (a) VorTECH tornado chamber (Taken from Gairola and Bitsuamlak, 2019) (b) ISU tornado chamber (Taken from Yuan et al., 2019).....	23
Fig. 3. Simplified Computational domain for VorTECH tornado chamber.....	24
Fig. 4. Cross-section of (a) experimental tornado chamber VorTECH at TTU (b) simplified CFD tornado chamber for VorTECH.....	25
Fig. 5. Meshing of computational domain (a) XY-plane (b) 3D domain (c) YZ-plane.....	27
Fig. 6. Different views of computational domain showing different boundary faces (a) Isometric view (b) Perspective view.....	31
Fig. 7. (a) Sectional view through plane ABCD showing the boundaries of computational domain (b) Top view for transverse section at X-X' showing velocity boundary condition at inlet height.....	31
Fig. 8. (a) Tangential velocity profile for $S = 0.15$ at elevation $(z) = 0.075h_o$ (b) Radial ground pressure profile for $S = 0.15$	35
Fig. 9. Local core radius at different elevations (z_1 and z_2) (Modified from Hu et al., 2011).....	39
Fig. 10. Tangential velocity of tornado vortex along line AB (Fig. 9).....	40
Fig. 11. Variation of maximum tangential velocity at the center of CFD tornado chamber at base plane.....	41
Fig. 12. (a) Demonstration of notations used in different definitions of swirl ratio in a tornado chamber (b) different radial locations chosen for defining different swirl ratios.....	48
Fig. 13. Graphical representation of definition of circulation (From Anderson, 2014).....	50
Fig. 14. Major classification category of tornado simulators (a) SOS (b) TFOS (c) TPOS (d) ISU tornado chamber (e) WinDEE dome.....	54
Fig. 15. Demonstration of inlet height (h_o), total height (H), updraft diameter (D_{up}) and outlet diameter (D_{out}) of a tornado chamber considered in parametric variation study.....	58
Fig. 16. CFD Tornado chambers with different total heights to study the effect of variation of total height on touchdown (a) $H = 15h_o$ (b) $H = 18h_o$ (c) $H = 21h_o$	59
Fig. 17. Velocity vector plot with pressure contour in the background for total height of tornado chamber $15h_o$ (a) $S = 0.29$ (before touchdown) (b) $S = 0.45$ (during touchdown) (c) $S = 0.60$ (after touchdown).....	59

Fig. 18. Velocity vector plot with pressure contour in the background for total height of tornado chamber $18h_o$ (a) $S = 0.35$ (before touchdown) (b) $S = 0.43$ (during touchdown) (c) $S = 0.45$ (after touchdown).....	60
Fig. 19. Velocity vector plot with pressure contour in the background for total height of tornado chamber $21h_o$ (a) $S = 0.35$ (before touchdown) (b) $S = 0.41$ (during touchdown) (c) $S = 0.42$ (after touchdown).....	60
Fig. 20. CFD Tornado chambers with different diameter of outlet to study the effect of variation of outlet diameter on touchdown (a) $D_{out} = D_{up}$ (b) $D_{out} = 0.75D_{up}$ (c) $D_{out} = 0.50 D_{up}$	62
Fig. 21. (a) Experimental tornado simulator VorTECH at Texas Tech University (b) Simplified CFD tornado simulator.....	66
Fig. 22. (a) 3D sketch of building model (b) 2D sketch of building – Plan (c) 2D sketch of building model – Elevation.....	66
Fig. 23. (a) Pressure contour plot of tornado flow field with mesh in the background when building is located at core radius ($r_c/h_o = 0.46$) for $S = 0.83$ (b) Zoom in region from Fig. 36 (a) near the core region of tornado vortex.....	68
Fig. 24. Visualization of 3 different meshes in XY-plane (a) Mesh - A (b) Mesh - B (c) Mesh – C.....	70
Fig. 25. Variation in time (a) pressure (b) tangential velocity at the center of tornado chamber in the ground plane.....	71
Fig. 26. (a) Pressure contour plots with mesh and velocity vectors in the background for $S = 0.83$ at $z/h_o = 0.01$ units in XY-plane (tornado flow field only without building) (b) zoom in for Fig. 39 (a) with contour and velocity vectors in the background using Mesh – A.....	72
Fig. 27. (a) Pressure contour plot with mesh and velocity vectors in the background for $S = 0.83$ at $z/h_o = 0.01$ units in XY-plane (tornado flow field only without building) (b) zoom in for Fig. 40 (a) with contour and velocity vectors in the background using Mesh – B.....	73
Fig. 28. (a) Pressure contour plot with mesh and velocity vectors in the background for $S = 0.83$ at $z/h_o = 0.01$ units in XY-plane (tornado flow field only without building) (b) zoom in for Fig. 41 (a) with contour and velocity vectors in the background using Mesh – C.....	73
Fig. 29. Comparison of (a) ground pressure profile (b) tangential velocity profile between 3 grids (from XY-plane at $KM = 1$).....	74
Fig. 30. (a) Schematic diagram of interaction of tornado wind field with the building when it is placed at different radial locations (r) along the X-axis (b) Exploded view of the faces of building.....	76
Fig. 31. Pressure contour plot around the building in XY-plane at $z = 0.01h_o$ when building is placed at (a) center of tornado chamber ($r/r_c = 0$) (b) core radius location ($r/r_c = 0.46$).....	77

Fig. 32. Comparison of Mean C_p contour for swirl ratio (S) = 0.83 when building is placed at the center of tornado chamber (a) CFD (b) TTU Experiment.....	78
Fig. 33. Comparison of Mean C_p contour for swirl ratio (S) = 0.83 when building is placed at the location of core radius ($r_c/h_o = 0.46$) of tornado vortex for $S = 0.83$ (a) CFD (b) TTU Experiment.....	79
Fig. 34. Comparison of Minimum C_p on the faces of building for $S = 0.83$ when the building is placed at (a) the center of CFD tornado simulator (b) the core radius of CFD tornado simulator.....	80
Fig. 35. Comparison of Mean C_p on the faces of building for $S = 0.83$ when the building is placed at the center of CFD tornado simulator (a) of size $0.10h_o \times 0.05h_o \times 0.05h_o$ (b) of size $0.10h_o \times 0.10h_o \times 0.10h_o$	83
Fig. 36. Comparison of Mean C_p on the faces of building when the building is placed at core radius ($r_c/h_o = 0.46$) for $S = 0.83$ in CFD tornado simulator (a) of size $0.10h_o \times 0.05h_o \times 0.05h_o$ (b) of size $0.10h_o \times 0.10h_o \times 0.10h_o$	83
Fig. 37. Comparison of Minimum C_p on the faces of building for $S = 0.83$ when the building is placed at the center of CFD tornado simulator (a) of size $0.10h_o \times 0.05h_o \times 0.05h_o$ (b) of size $0.10h_o \times 0.10h_o \times 0.10h_o$	84
Fig. 38. Comparison of Minimum C_p on the faces of building when the building is placed at core radius ($r_c/h_o = 0.46$) for $S = 0.83$ in CFD tornado simulator (a) of size $0.10h_o \times 0.05h_o \times 0.05h_o$ (b) of size $0.10h_o \times 0.10h_o \times 0.10h_o$	84
Fig. 39. Comparison of Mean C_p profile along the centerline frame of building of two different sizes (i.e. $0.10h_o \times 0.05h_o \times 0.05h_o$ and $0.10h_o \times 0.10h_o \times 0.10h_o$).....	85
Fig. 40. Pressure contour plot on the faces of the building due to a tornado-like vortex with swirl ratio (S) = 0.15 (before touchdown) when building is located at the center of CFD tornado simulator (a) Mean C_p plot (b) Minimum C_p plot.....	90
Fig. 41. Pressure contour plot on the faces of the building due to a tornado-like vortex with swirl ratio (S) = 0.36 (during touchdown) when building is located at the center of CFD tornado simulator (a) Mean C_p plot (b) Minimum C_p plot.....	91
Fig. 42. Pressure contour plot on the faces of the building due to a tornado-like vortex with swirl ratio (S) = 0.83 (post-touched vortex) when building is located at the center of CFD tornado simulator (a) Mean C_p plot (b) Minimum C_p plot.....	92
Fig. 43. Suction vortex attached on the eastward face of the building for swirl ratio (S) = 0.15 and building located at the center of CFD tornado simulator at 4 different time steps (a) $t^* = 19.61$ (b) $t^* = 23.47$ (c) $t^* = 25.15$ and (d) $t^* = 29.00$	94

Fig. 44. Detached suction vortices in the periphery of building for swirl ratio (S) = 0.36 and building located at the center of CFD tornado simulator at 4 different time steps (a) $t^* = 17.96$ (b) $t^* = 22.95$ (c) $t^* = 25.82$ and (d) $t^* = 28.12$	96
Fig. 45. Detached suction vortices in the periphery of building for swirl ratio (S) = 0.83 and building located at the center of CFD tornado simulator at 4 different time steps (a) $t^* = 17.96$ (b) $t^* = 22.95$ (c) $t^* = 25.82$ and (d) $t^* = 28.12$	97
Fig. 46. Pressure contour plot on the faces of the building due to a tornado-like vortex with swirl ratio (S) = 0.15 (before touchdown) when building is located at core radius of tornado-like vortex (a) Mean C_p plot (b) Minimum C_p plot.....	99
Fig. 47. Pressure contour plot on the faces of the building due to a tornado-like vortex with swirl ratio (S) = 0.36 (during touchdown) when building is located at core radius of tornado-like vortex (a) Mean C_p plot (b) Minimum C_p plot.....	99
Fig. 48. Pressure contour plot on the faces of the building due to a tornado-like vortex with swirl ratio (S) = 0.83 (post-touchdown vortex) when building is located at core radius of tornado-like vortex (a) Mean C_p plot (b) Minimum C_p plot.....	99
Fig. 49. Suction vortex attached on the periphery of building when the building is placed at core radius for swirl ratio (S) = 0.15 at 4 different time steps (a) $t^* = 20.17$ (b) $t^* = 24.13$ (c) $t^* = 26.90$ and (d) $t^* = 29.92$	100
Fig. 50. Detached suction vortices around the building when the building is placed at core radius for swirl ratio (S) = 0.36 at 4 different time steps (a) $t^* = 24.93$ (b) $t^* = 25.14$ (c) $t^* = 25.63$ and (d) $t^* = 25.73$	101
Fig. 51. Detached suction vortices around the building when the building is placed at core radius for swirl ratio (S) = 0.83 at 4 different time steps (a) $t^* = 20.27$ (b) $t^* = 20.80$ (c) $t^* = 20.97$ and (d) $t^* = 21.16$	102
Fig. 52. Mean and Minimum C_p on the faces of building for $S = 0.83$ when the building is placed at the center of CFD tornado simulator for $Re = 2.755 \times 10^5$	105
Fig. 53. Mean and Minimum C_p on the faces of building for $S = 0.83$ when the building is placed at the center of CFD tornado simulator for $Re = 1.0 \times 10^6$	105
Fig. 54. Mean and Minimum C_p on the faces of building for $S = 0.83$ when the building is placed at the center of CFD tornado simulator for $Re = 1.0 \times 10^7$	105
Fig. 55. Mean and Minimum C_p on the faces of building for $S = 0.83$ when the building is placed at core radius of vortex for $Re = 2.755 \times 10^5$	106
Fig. 56. Mean and Minimum C_p on the faces of building for $S = 0.83$ when the building is placed at core radius of vortex for $Re = 1.0 \times 10^6$	107

Fig. 57. Mean and Minimum C_p on the faces of building for $S = 0.83$ when the building is placed at core radius of vortex for $Re = 1.0 \times 10^7$	107
Fig. A-1. Sample data for Input Data File.....	130
Fig. B-1. (a) Experimental tornado simulator VorTECH at Texas Tech University (b) Simplified CFD tornado simulator.....	134
Fig. B-2. (a) 3D view of cylindrical computational domain showing different boundary faces (b) Sectional view through plane ABCD showing different boundaries for the computational domain.....	139
Fig. B-3. Top view for transverse section at X-X' showing velocity boundary condition at inlet height.....	139
Fig. B-4. Mesh for the cylindrical computational domain (a) vertical section through the diametric axis of the cylinder showing elevation (b) horizontal section showing plan of the computational domain.....	141
Fig. B-5. Time series plot of (a) non-dimensional pressure and (b) non-dimensional velocity magnitude with respect to non-dimensional time.....	142
Fig. B-6. Instantaneous profile at the bottom of tornado simulator (a) tangential velocity profile at $z/r_{up} = 0.05$ (b) pressure profile at $z/r_{up} = 0.05$	142
Fig. B-7. Mean profiles at the bottom of tornado simulator (a) tangential velocity profile at $z/r_{up} = 0.05$ (b) pressure profile at $z/r_{up} = 0.05$	143
Fig. B-8. Comparison of pressure profile at the base of tornado simulator (i.e., $z/r_{up} = 0$) between the TTU simulator dataset and CFD datasets.....	144
Fig. B-9. Contour plot of Velocity magnitude with velocity vectors in the background through the diametric XZ-plane of CFD tornado simulator.....	144
Fig. B-10. Velocity magnitude contour plot with velocity vectors in the background through the XY-plane of CFD tornado simulator at $z/r_{up} = 0.01$	144
Fig. B-11. Sketch showing different stations for computing NRMSE in pressure profiles.....	145
Fig. C-1. Demo for mapping the pressures recorded on building from csv file to a contour plot.....	153
Fig. D-1. A cubical building model placed at the center of CFD tornado simulator.....	165
Fig. D-2. (a) Background mesh for the computational domain (b) 3D CAD model for CFD tornado simulator with building model inside (c) Background mesh and 3D CAD model (d) Final mesh obtained from “snappyHexMesh”.....	166

Fig. D-3. (a) Exploded view of pressure contour plot on the faces of building model (b) Pressure coefficient along the centerline of the building.....	167
Fig. E-1. Flowchart demonstrating control flow for parallel simulation in OpenFOAM.....	169

List of Tables

Table 1. Wind Speeds in different categories of Fujita (F) and Enhanced Fujita (EF) scale.....	9
Table 2. Tornado forces, moments, and pressures on building from different references.....	19
Table 3. Different features of tornado vortex and scale of building model used for estimating tornado forces on building.....	20
Table 4. Different Grids considered for Grid Independence test with their node count and mesh.....	34
Table 5. Comparison of touchdown swirl ratio and other tornado vortex parameters from different tornado chambers.....	55
Table 6. Effect of variation of Total Height of tornado chamber on S_T	61
Table 7. Effect of variation of outlet diameter of tornado chamber on S_T	62
Table 8. Details of grids to study effect of grid resolution on Tornado flow field without building.....	71
Table 9. Details of 3 different grids used to study grid resolution effect on tornado flow field without building.....	74
Table 10. Comparison of NRMSE between different grids.....	75
Table 11. Comparison of range of mean and the minimum C_p on the building of different sizes.....	82
Table 12. Range of mean and min. C_p on the faces of building due to different swirl ratios of tornado-like vortices.....	103
Table 13. Comparison of Mean and the Minimum C_p for different Reynolds Number.....	107
Table B1. Velocity boundary condition for the inlet patch of CFD tornado simulator.....	140
Table B2. Description of boundary faces, types, and boundary conditions for different faces in computational domain.....	140
Table B3. Calculation of NRMSE between TTU Experimental and CFD Pressure Profile.....	145

Nomenclature

English

a: Aspect ratio of tornado chamber

B: Width of the building

C_{fx} : Force coefficient on a building due to tornado vortex in X-direction

C_{fy} : Force coefficient on a building due to tornado vortex in Y-direction

C_{fxy} : Force coefficient on a building due to tornado vortex in XY-plane

C_{fz} : Force coefficient on a building due to tornado vortex in Z-direction

C_{mxy} : Resultant Moment coefficient on a building due to tornado in XY-plane

C_{mz} : Force coefficient on a building due to tornado in X-direction

C_p : Pressure coefficient on a building due to tornado

C_{sgs} : Smagorinsky constant

D_{con} : Diameter of convergence region

D_{out} : Diameter of outlet

D_{up} : Diameter of updraft hole

EF scale: Enhanced Fujita Scale

F scale: Fujita scale

H: Total height of the tornado chamber

h_o : inlet height of tornado chamber.

h_{out} : depth of outlet of CFD tornado chamber

Max. V_H : Maximum horizontal velocity at building height

OA: Orientation angle of building with respect to tornado vortex

$P_{s,g}$: Reference static pressure at the ground surface

$P_{a,o}$: Ambient pressure outside the tornado chamber considered as reference pressure

$P_{s,f}$: Reference static pressure measured far from tornado vortex

$P_{max,g}$: Maximum pressure at ground surface as reference pressure

P_{atm} : Atmospheric pressure at mean sea level (101 KPa) (as reference pressure)

Q_{out} : Volumetric outflow rate from tornado chamber

Q'_{out} : Volumetric outflow rate per unit axial height (given by $Q'_{out} = Q_{out}/h_o$)

r_c : Core radius

r_{up} : radius of updraft hole

S : Swirl ratio of tornado vortex

S_T : Touchdown Swirl ratio

\overline{S}_{ij} : Filtered Shear rate tensor

V_{out} : Total outlet velocity in the CFD tornado chamber

V_{ro} : Radial velocity at inlet height

V_{to} : Tangential velocity

V_{to} : Tangential velocity at inlet height

V_{tmax} : Maximum tangential velocity

V_{trans} : Translational velocity of tornado-like vortex

z_c : Elevation of the maximum tangential velocity from base of tornado simulator

Greek

Γ_{max} : Maximum circulation in the flow field

Γ_{∞} : Circulation at edge of convergence region

Φ : Diameter of fans in the VorTECH simulator at Texas Tech University

ν_{sgs} : Sub-grid scale viscosity

Δ : Cube root of volume of a Finite Volume Cell

ρ : Density of fluid

μ : Dynamic viscosity of fluid

Acronym

ASCE 7-05: American Society of Civil Engineers code for minimum design load calculations

BCs: Boundary Conditions

CAARC: Commonwealth Advisory Aeronautical Research Council

CAD: Computer Aided Design

CFD: Computational Fluid Dynamics

CSA: Curved Surface Areas

DNS: Direct Numerical Simulation

EXP: Experimental simulation

FVM: Finite Volume Method

ISU: Iowa State University

LES: Large Eddy Simulation

NS: Navier-Stokes

NRMSE: Normalized Root Mean Squared Error

NWS: National Weather Services

QUICK: Quadratic Upstream Interpolation for Convection Kinematics

RANS: Reynolds Averaged Navier Stokes

RCVM: Rankine Combined Vortex Model

RSM: Reynolds Stress Model

Ref. P: Reference pressure considered while calculating pressure coefficient

Ref. Vel.: Reference velocity for calculating pressure coefficient

SL: Straight-line winds

SGS: Sub-grid Stress

SOS: Side Opening Systems

TFOS: Top Full Opening System

TPOS: Top Partial Opening System

TTU: Texas Tech University

VorTECH: Experimental tornado chamber at Texas Tech University

$V_{@RH}$: Reference velocity at roof height

V_{tmax} @ MEH: Maximum tangential velocity at mean eave height

WU: Western University

Chapter -1: Introduction and Objectives

1.1 Introduction

Tornadoes pose a threat to nearly all structures of varying sizes and configuration, whether a high-rise or low-rise building, enclosed, partially enclosed or an open building. Buildings designed to withstand wind loads due to straight-line (SL) winds may sustain major structural failures or may even be destroyed when impacted by tornado-like winds (Refer Fig. 1). This is due to larger forces and pressure loads produced by tornadoes as compared to SL winds (Selvam and Millet, 2005). Among the several categories of buildings, low-rise buildings have been found to be most susceptible to major structural failures often with complete destruction. Higher number of casualties, death tolls and economic losses at the places of occurrence of tornado is often attributed to structural failures of low-rise buildings, which represents the majority of residential houses.



(a)

(b)

Fig. 1. (a) Major structural failure (roofs uplifted and blown off) of a low-rise building (From Yang et al., 2018) (b) destroyed low-rise building by tornadoes (From Schlueter, 2016)

Accurate estimation of tornado-induced wind loads is necessary for proper design of low-rise buildings in tornado-prone areas. However, there are no guidelines in existing building codes and load standards till date regulating the minimum wind loads to be considered for design of buildings in tornado-prone areas. Before quantifying tornado-induced wind loads and proposing a procedure

of design of buildings in tornado-prone areas, the details of tornado flow field (i.e., wind velocity and pressure distribution in tornado vortex) must be well understood first.

1.2 Different Approach of Exploring the Wind Field and Wind-induced Load by Tornadoes

Exploration of tornado wind field and the wind loads induced by them on buildings has been carried out by four different approaches in the existing literature, viz. (a) Field Measurements (b) Post-Storm Damage Investigation (c) Experimental tornado simulation and (d) Computational Fluid Dynamics (CFD) tornado simulation.

Field Measurements involve acquisition of wind velocities and pressure data of real-world tornadoes by chasing a live tornado in real time using radar instruments (Bluestein and Pazmany, 2000, Alexander and Wurman, 2005). However, data collection from field measurements is risky and life threatening at times. Besides, it is hard to predict formation of tornadoes and be equipped with necessary instrument setup to take data measurements of a live tornado. As a result, field data of real-world tornadoes is scarce in the literature. Even the available field data can barely be used for engineering design purposes as the collected data pertains to velocity and pressure measurements of real tornadoes at significant elevations from the ground surface. For engineering design purposes, velocity, and pressure distribution close to the ground surface (within 10m from ground level) is necessary as most of the low-rise residential houses are built within that range of elevation.

Post-storm damage investigation involves correlating a tornado by an equivalent SL wind speed that would result in similar level of damage as the tornado (McDonald, 2001; McDonald et al., 2009). This approach only provides a very coarse estimation of tornado-induced wind loads, which cannot be relied upon for designing buildings as both the nature and magnitude of forces exerted by tornado winds show stark differences from SL winds. In the earliest attempts to quantify tornado

wind loads on building, Selvam and Millet (2003) developed a CFD model of tornado vortex, which was described by the distribution of tangential velocity only. Lack of validation of CFD model with experimental data as well as lacking radial and axial velocity components in CFD tornado model were the two limiting aspects of the work. However, the model could consider vortex of varying sizes relative to the size of building and could account for different ratios of translational to tangential velocity as observed in full-scale tornadoes. Using the model, the pressures could also be compared for straight-line winds to the rotating vortex winds directly. However, in the contemporary CFD tornado chamber models, such comparison cannot be made. Due to limitations of field measurements and post-storm damage surveys, the trend gradually shifted to simulating tornado-like vortices (hereafter referred to as tornado) in a lab setting using experimental tornado chambers. Experimental tornado chambers were used to study the flow characteristics of tornado winds as well as tornado-induced wind loads on buildings (Tang et al., 2018a; Haan et al., 2008; Refan and Hangan, 2018; Haan et al., 2010). However, experimental simulation of tornadoes is also fraught with challenges as explained below.

1.3 Limitations of Experimental vs Benefits of CFD Tornado Simulation

Experimental simulation of tornado vortices in experimental tornado chambers have contributed significantly to the understanding of flow dynamics of tornado vortices over the years but there are still several challenges with experimental tornado chambers. The construction, operation and maintenance of experimental tornado chambers is prohibitively costly on one hand whereas on the other hand, it is challenging to obtain near-surface velocities and pressures which are important from an engineering perspective.

Meanwhile, due to advancements in computing speed and storage technology, CFD is evolving as a tool for numerical simulation of tornado vortices to study the detailed characteristics of tornado

wind field. An experimentally validated CFD model is not only an economical alternative to experimental tornado simulation but is also a faster tool to advance the knowledge in this area. Furthermore, validated models can assist in future design of efficient tornado chambers; the design of an experimental facility known as WindEEE dome was optimized using validated CFD models (Natarajan, 2011). In addition, near-surface velocities and pressures can be acquired easily in CFD tornado chambers as compared to experimental tornado chambers. Thus, numerical simulation using CFD is an alternative cost-effective approach for studying tornadoes and hence this approach is taken for the current work.

1.4 Challenges with Modeling of CFD Tornado Chamber and CFD Flow Validation

Modern day CFD tornado simulation involves modeling geometry of CFD tornado chambers to resemble the shape of experimental simulator facilities (Yuan et al., 2019; Huo et al., 2020); such modeling attempts require CFD tornado chamber to be placed inside a larger computational domain in which the air discharged from outlet is recirculated back into the tornado chamber via the inlet. Consequently, a larger computational domain is required and turning vanes must be modelled physically at the inlet for setting up inflow at required orientation angles. So, this approach becomes very demanding computationally as enormous number of grid points are required for meshing of computational domain due to which grid resolution becomes challenging and consequently the accuracy of model gets compromised. In addition, the sophisticated geometry of CFD tornado simulators with physically modeled mechanical components such as turning vanes and fans often requires supercomputing resources (which in general is not accessible to many people) to obtain a reliable solution. Besides, some guideline as to how the wind field of tornado vortex obtained from the CFD model should be validated against the experimental datasets is also lacking in the existing literature. As a result, some computational studies are validated by

comparing the tangential velocity profile (Ishihara et al., 2011) while a few others are based on ground pressure profiles (Liu and Ishihara, 2015a). While the tangential velocity profile or pressure profile must compare well with experimental measurements for a good CFD model, but validation based on comparison of tangential velocity profile or ground pressure profile alone may not be the sufficient criteria for CFD flow validation. This is because the tornado-induced pressures on the building depend on several other important features of tornado vortex such as touchdown swirl ratios (S_T), core radii (r_c), elevation of core radius (z_c), maximum tangential velocity (V_{tmax}) and pressure distribution. Variation of these important flow features in different tornado chambers changes the flow field of tornado and its interaction with buildings resulting in different pressures on buildings. So, in this work, four important features of tornado vortex including the ground pressure profile are identified and considered for the validation of wind field obtained from CFD model. Additionally, an attempt is made to compare the four important features of tornado vortex from different tornado chambers (both experimental and CFD) available in the existing literature. This is done with the motivation to learn about the similarities and/or differences of the wind field in different tornado chambers.

1.5 Challenges with Tornado Pressures on Building Using CFD Vortex Chambers

Several studies have been undertaken from both the experimental and computational side to estimate wind loads on building subjected to tornadic winds (Mishra et al., 2008; Haan et al. 2010, Sabareesh et al., 2013, Selvam and Millet, 2005). However, the pressure coefficients on the building show significant variation from one experimental study to another. Similarly, the wind pressures on the building obtained from CFD models often lack comparison and/or validation with experimental data (Nasir et al., 2014).

Different works of literature have considered different flow structures (single-celled vortex in Mishra et al., 2008 whereas a double-celled vortex in Li et al., 2019) of tornado vortex while evaluating tornado forces on building. In addition, there seems to be a lot of variability in the scale of building models considered in different work of literature (such as 1:3500 in Mishra et al., 2008, 1:100 in Haan et al., 2010 and 1:1900 in Liu et al., 2015b). Besides, the Reynolds number of flow also varies in different studies of the literature. However, a systematic investigation of tornado pressures on the building due to different flow structures of vortex, different sizes of building and different Reynolds number is lacking in the literature. Consequently, there is lack of understanding on how different sizes of building, different flow structures of vortex and different Reynolds number of flow would affect the pressures induced by tornadoes on building.

Thus, there are several challenges in various steps of CFD tornado simulation starting from the challenges in modelling of an efficient CFD tornado chamber to the challenges in validation of CFD flow field and the validation of tornado pressures on building. Thus, this thesis seeks to resolve the challenges stated above, beginning with the challenges in validation of CFD flow field by developing a simple, efficient CFD tornado chamber that delivers a reliable solution within a reasonable timeframe without the requirements of supercomputing resources. Further details about the objectives of current work are discussed in detail in section 1.6 below.

1.6 Thesis Objectives

The objectives of the current work are enumerated below. Each objective has been split into several tasks for clarity and are listed below.

Obj.-1: To develop a simple and efficient CFD tornado simulator model to reliably simulate the tornado wind field and obtain reliable wind load estimates without supercomputing resources (Details of the model is included in Chapter-3).

Obj.-2: To validate the wind field of tornado vortex from CFD model with experiment. The wind field and pressure measurement on the floor from Texas Tech University (TTU) tornado chamber – VorTECH, are used for comparison.

O-2.1: To compare touchdown swirl ratio from CFD model with TTU experiment.

O-2.2: To compare core radius at different elevations obtained from CFD model with TTU measurements.

O-2.3: To compare pressure distribution at the base of CFD model with pressure measurement on the floor of TTU tornado chamber.

Obj.-3: To compare the four important features of tornado vortex (i.e., touchdown swirl ratio (S_T), core radius (r_c), maximum tangential velocity (V_{tmax}) and elevation of core radius (z_c)) from different tornado chambers.

O-3.1: To review the existing literature and compare touchdown swirl ratio (S_T), core radius (r_c), maximum tangential velocity (V_{tmax}) and elevation of core radius (z_c) from different tornado chambers.

O-3.2: To perform supplementary CFD simulations to understand the effect of geometric variation (total height and outlet diameter) of tornado chamber on the four important vortex features.

Obj.-4: To compare and validate the pressure coefficients on a building due to tornado vortex from CFD model with TTU measurements.

O-4.1: To report and compare the mean and the minimum pressure coefficients on the building obtained from CFD model with TTU experiment when the building is placed at the center and at the core radius of vortex.

O-4.2: To compare the effect of different sizes of the building on the induced pressure coefficients from CFD model.

Obj.-5: To compare wind pressures on a building model due to different flow structures of tornado (prior to, during and after vortex touchdown) as well as different Reynolds number.

O-5.1: To compare the pressure coefficients due to different flow structures of tornado vortex on building from CFD model.

O-5.2: To compare the pressure coefficients on building due to different Reynolds number of flow from CFD model.

Chapter-2: Literature Review

2.1 Introduction

Different approaches to estimate tornado-induced wind loads are reviewed in this chapter. Tornado-induced wind loads, on an engineering scale, are estimated mainly using three approaches, i.e., (a) Post-storm damage investigation (b) Experimental tornado simulation (c) CFD tornado simulation. Several studies carried out using the three approaches are summarized in the following text and are organized into three subsections. In the latter two sections (i.e., experimental tornado simulation and CFD tornado simulation), different work from literature that are based on simulation and description of tornado flow field are described first followed by the studies involving evaluation of tornado-induced forces on buildings.

2.2 Post-Storm Damage Investigation

Post-Storm damage rating is based on the idea of correlating a tornado by an equivalent straight line (SL) wind speed that would result in the same damage levels as the tornado. Fujita (1971) proposed an intensity scale for tornadoes based on wind speeds and categorized different damage levels by distinct range of wind speeds (McDonald, 2001). With advancements in construction technologies and improvements in building materials over time, it was felt that the original Fujita scale under-estimated the wind speeds in different damage categories (McDonald et al., 2009). Thus, a revised scale, also known as Enhanced Fujita Scale (EF-scale) was implemented by National Weather Services (NWS) in 2007 (Huang et al., 2016; Doswell et al., 2009; Potter, 2007). The range of wind speeds in original Fujita scale (F-scale) and Enhanced Fujita scale (EF-scale) obtained from McDonald et al. (2009) is presented in Table 1.

Table 1. Wind Speeds in different categories of Fujita (F) and Enhanced Fujita (EF) scale

Original Fujita Scale		Enhanced Fujita Scale	
Category	Wind Speed¹ Range (mph)	Category	Wind Speed¹ Range (mph)
F0	45-78	EF0	65-85
F1	79-117	EF1	86-109
F2	118-161	EF2	110-137
F3	162-209	EF3	138-167
F4	210-261	EF4	168-199
F5	262-317	EF5	200-234

Note: Wind Speed¹: 3-sec gust wind speed at 10 m height considering open-country terrain

Although post-storm damage investigation provides some outline to estimate wind loads due to tornado winds by correlating with an equivalent SL wind speed, there are still several drawbacks with this approach, which are discussed in the following paragraph.

Tornadoes have very different wind profiles comprising rotational as well as vertical velocity components whereas the rotational and vertical components are nearly absent in SL winds (Selvam and Millet, 2005). Since, the characteristics of tornado winds and SL winds show stark differences, estimated wind loads by correlating winds (i.e. tornadoes and SL winds) with completely different wind profiles also brings the estimated wind loads into question. The extent of structural damage or damage levels caused by tornadoes also depend on the relative size of tornado vortex impacting the structure, the duration of impact of tornado vortex with structures, the size of tornado-borne missiles formed during a tornadic event, etc. but there is no way to account for these factors while estimating equivalent SL wind speeds based on tornado damage assessment surveys. Furthermore, this approach is somewhat subjective in the sense that different damage assessment teams may

assign different damage rating to the same damaged structure, which would result in different wind speeds and thus, different wind loads.

Due to several drawbacks stated above, the trend gradually shifted to simulating tornado-like vortices using experimental tornado chambers. Tornado-like vortices were produced in a lab setting and then the interaction of tornado-like vortices with various structural models were studied. Further detailed review on experimental simulation of tornadoes is provided in section 2.3.

2.3 Experimental Tornado Simulation

The earliest laboratory simulation of tornado-like vortices can be traced back to 1970. Ying and Chang (1970) developed a laboratory model of tornado-like vortex and concluded that strong tangential velocity components were necessary for air converging at the base of the tornado chamber via inlet for the formation of tornado vortex. With some improvements to Ying and Chang model such as introduction of honeycomb section at the top of tornado chamber, Ward (1972) and Church et al. (1977) obtained several configurations of tornado vortices ranging from a single-celled vortex to a double-celled vortex and multi-vortex tornado by varying the inflow angles. Ward (1972) concluded that aspect ratio of tornado chamber should be small (usually less than 1) for the formation of tornado vortices, which are accompanied by a sharp drop in pressure at the center of vortices. On the other hand, Church et al. (1979) reached a conclusion that swirl imparted at the inlet of tornado chamber influences the formation of different configuration of tornado vortices, i.e., either a single-celled vortex or double-celled vortex as previously concluded by Davies-Jones (1973). All these works stated above were driven with the motivation to obtain relevant vortex features and flow structures of tornadoes as observed in real world tornadoes inside a lab environment.

2.4 CFD Tornado Simulation

Early numerical simulation work on tornado vortex modeling were based on axisymmetric models (Harlow and Stein, 1974; Rotunno, 1979; Nolan and Farrell, 1999). Harlow and Stein (1974) proposed an axisymmetric model for tornado vortex and obtained single-celled as well as double-celled flow structures of tornado vortex without imposing any special boundary conditions. Rotunno (1979) also used an axisymmetric model based on Ward tornado chamber for modeling of tornado vortex and reported different features of tornado vortex such as vortex breakdown bubble and vortex touchdown by varying swirl ratios. These early numerical works on tornado vortex simulation were mostly based on idealization of tornado winds by an axisymmetric flow model without any inclusion of turbulence models in them. However, complex tornadic flows are comprised of highly turbulent flow structures in the flow field consisting of turbulent eddies of different shapes and sizes. It is imperative to consider the turbulent eddies either by modeling its effect or by resolving them in the flow field to obtain the true characteristics of tornadic wind field.

2.4.1 Turbulence Models in CFD Tornado Simulation

The effect of turbulent eddies in a flow field are considered with the help of turbulence models in CFD. In a turbulent flow field, eddies of different sizes are present. For the true representation of flow field, eddies formed in a turbulent flow field must be either resolved by the mesh or its effect must be modeled. Depending on whether the turbulent eddies are completely or partially resolved by mesh or completely modeled, there are three methods of turbulence modeling in CFD.

(i) Direct Numerical Simulation (DNS): In DNS, the mesh is very finely resolved such that the mesh captures all the turbulent eddies of varying length and time scales in the flow field. DNS is very accurate, and superior compared to other turbulence modeling methods; however, due to the finely resolved mesh, enormous number of grid points are required to discretize the

computational domain, which makes the computation prohibitively costly. Thus, numerical simulation works using DNS are limited mostly for simple flows with low Reynolds number.

(ii) Large Eddy Simulation (LES): In LES, certain fraction of the turbulent eddies is resolved by mesh itself whereas the effect of turbulent eddies smaller than the smallest grid are modeled by increasing the effective viscosity of flow. The computational cost of LES is lower than DNS as the turbulent eddies beyond a certain cut off size (dictated by the smallest grid size) are not resolved; instead, their effect is modeled. As the turbulent eddies smaller than the smallest grid size are not resolved by mesh, the accuracy is a little compromised in LES. Even with a slightly compromised accuracy level, LES is appropriate for most engineering computations and applications.

(iii) Reynolds Averaged Navier Stokes Equation (RANS): In RANS, none of the turbulent eddies in the flow field is resolved by mesh. Instead, the effect of turbulent eddies is modeled, thus, resulting in the mean flow field. In RANS, the flow field is decomposed into 2 components, i.e. (a) Mean flow component and (b) time varying flow component. Time averaging is applied for the mean component of flow field. Thus, the result of RANS model is a time-averaged flow field without any resolved eddies in the flow domain. Consequently, the accuracy of RANS is low compared to LES but still for some specific engineering applications, RANS may be applicable.

As tornadoes are comprised of highly turbulent flows and Direct Numerical simulation (DNS) is prohibitively expensive, so, it was necessary to include proper turbulence models in tornado vortex modeling for accurate CFD computations. In that regard, Lewellen et al. (1997) introduced large eddy simulation (LES) for modeling of translating tornado-like vortices and observed that translating tornado vortices are more turbulent (due to larger fluctuation of velocity components)

than stationary tornadoes. Nolan and Farrell (1999) studied about flow structures of tornado vortices using an axisymmetric numerical model and proposed a non-dimensional parameter called as vortex Reynolds number (based on eddy viscosity) rather than swirl ratio for studying evolution of different structures of tornado vortices. However, the use of vortex Reynolds number is scarce in the literature since eddy viscosity varies from one location to another location in the flow domain and it is not easily quantifiable. Lewellen and Lewellen (2007), using previously developed LES model, studied intensification of tornado-like vortices near the ground and concluded that the cumulative effect of pressure drop at the center and large tangential velocity near to core of tornado-like vortex was responsible to produce a vertical gradient of pressure. They also concluded that vertical pressure gradients facilitated formation of downdraft and thus were limiting factor for intensification of tornado-like vortices near to the ground. All the CFD studies stated above involved using different numerical techniques to obtain tornado-like flows and comparing vortex features with experimental and full-scale tornadoes. The comparison, however, was only done on a qualitative basis. Hangan and Kim (2008) tried to correlate CFD tornado vortices with full scale tornadoes by proposing a matching technique based on two length scales (core radius and elevation of core radius) at the location of maximum tangential velocity. Although Lewellen et al. (1997) had done some preliminary work on translating tornadoes, the differences between a stationary and a translating tornado vortex was not very well understood. Natarajan and Hangan (2012) tried to explore the effect of translation and surface roughness on tornado vortices using Large Eddy simulation (LES) and concluded that translation causes a reduction of maximum tangential velocity for low swirl ratio vortices whereas the maximum tangential velocity slightly increases for high swirl ratio vortex. They also concluded that increasing roughness produces a similar effect as reducing swirl ratio of tornado-like vortex.

2.5 Validation of CFD Tornado Flow Field

Simulation of tornado vortices using CFD can be traced back to early 2000s (Selvam and Millet, 2003) but validation of CFD flow field with experimental data was limited due to scarce experimental and field data at that time. In a decade long period from 2005 to 2015, some important contributions were made towards experimental simulation of tornado vortices with the construction of large experimental tornado chambers in different parts of the world (Mayer, 2009; Haan et al. 2008; Hangan, 2014; Wang et al., 2016). As more experimental data became available, more studies were done on validation of CFD work with experimental measurements (Ishihara et al. 2011, Liu et al., 2015a). In the following paragraph, a succinct review of comparison and validation attempts of CFD flow field with experimental measurements is provided, limitations in existing CFD validation efforts are pointed out and the important features of tornado vortex that should be compared while validating CFD flow field are listed.

Ishihara et al. (2011) modeled a CFD tornado chamber based on dimensions of experimental tornado chamber used by Matsui and Tamura (2009). The CFD flow field was validated by comparing the tangential velocity profile from CFD model with experimental measurements. However, the study was limited to two test cases of swirl ratio (i.e., $S = 0.31$ and $S = 0.65$) only and it is unclear whether vortex had touched down or not in either of the two swirl ratios. Liu et al. (2015a) developed a CFD model and validated it by comparing time-averaged ground pressure profile from CFD model with experimental measurements of Kikitsu et al. (2012). The pressure profile obtained from CFD model showed good match with experimental pressure profile, but the comparison was limited only to a single test case of swirl ratio, i.e., $S = 2.44$. In addition, neither information about vortex touchdown nor the kind of flow structure represented by $S = 2.44$ was provided. Kuai et al. (2008) and Fangpin et al. (2016) modeled CFD tornado chamber based on

the experimental Iowa State University (ISU) tornado simulator and computed the tornado wind field; however, a direct comparison of vortex features from the CFD model was lacking with ISU experimental measurements. Gairola and Bitsuamlak (2019) modeled all the three major tornado chambers in the world, i.e., VorTECH tornado chamber, ISU tornado chamber and WindEEE dome using Large Eddy Simulation. However, validation of flow field was limited to ground pressure profile and tangential velocity profiles at certain specific elevations. Later, a simplified CFD model was proposed to represent the flow field of all the major experimental tornado chambers. Due to very high computational costs, majority of the work was done using a simplified CFD model based on Reynolds Stress Model (RSM) under RANS framework. The selection of RANS turbulence model instead of LES was a major factor in limiting the scope of the work. In the CFD community, it is very well agreed that LES turbulence models are better and more accurate than RANS models as the mesh employed in LES simulation resolves the turbulent eddies in flow field rather than modeling the effect of those eddies. For a complicated flow phenomenon such as that of tornadoes, it would have been a better choice to compare the results from simplified CFD model based on LES rather than RANS.

From the review, it can be said that validation of flow field is mostly based on comparison of tangential velocity profile from the CFD model with experimental measurements and a few studies are also based on comparison of pressure profile. However, validation of CFD flow field is lacking with respect to important tornado vortex features such as touchdown swirl ratio (S_T), core radius (r_c) and pressure distribution over a range of varying swirl ratios, which are of engineering significance and strongly influence the tornado loading on buildings. The end goal of CFD flow validation is to obtain a reliable model for accurate estimation of tornado-induced forces on a building, so, it is important to validate CFD flow field by identifying the important tornado vortex

features, which influence tornado forces on building. However, the existing literature is lacking validation of CFD flow field based on important tornado vortex features listed above. Further detailed discussion about the important tornado vortex features, and how they influence tornado-induced forces on building is discussed in section 1.1 of Verma and Selvam (2021b).

2.6 Tornado Forces on Building from Experimental Tornado Chambers

Mishra et al. (2008) investigated pressure and force coefficients on the faces of a cubical building model using an experimental tornado chamber called TTU-VSII at Texas Tech University (TTU). Due to small size of TTU-VSII tornado chamber, the size of building model used for wind load estimation was also very small (1:3500). Such small scale posed a great problem in proper resolution and interpretation of tornado forces on the structural model. This was the motivating factor for construction of a large-scale Ward type tornado chamber at TTU called the VorTECH (Mayer, 2009). However, the major limitation with Ward type tornado chambers is that translating tornado vortices cannot be produced in those chambers. Instead, the building must be moved relative to tornado vortex to mimic the relative motion of tornado vortex with respect to building for evaluating tornado forces on building. The limitation of considering a stationary tornado vortex for quantifying tornado forces on buildings was finally eliminated when the tornado chamber at Iowa State University (ISU) came into operation in 2004. Sengupta et al. (2008), Haan et al. (2010) and Hu et al. (2011), using the ISU tornado chamber, computed force, and moment coefficients on a building model due to tornado winds and compared with ASCE 7-05 provisions. They concluded that the forces on building due to tornado winds were significantly higher (by up to 200%) than SL winds, thus, buildings designed for SL wind loads were under-designed for loads induced by tornado winds and were likely to fail during tornadic events. Although ISU tornado chamber with its vortex translation mechanism is somewhat able to mimic the translating nature of real-world

tornadoes but it is still not fully representative of real-world tornadoes. This is because the generated tornado vortices are moved in a pre-defined path in ISU tornado chamber whereas the path traced by real-world tornadoes changes over time and is often unpredictable and random. To investigate flow characteristics and forces exerted by different kinds of winds such as tornadoes and microbursts, another large-scale experimental facility called as WindEEE dome (Hangan, 2014) was constructed at Western University (WU). Refan et al. (2014, 2016) investigated different flow structures of tornado-like vortices in scaled WindEEE dome and proposed a scaling technique for matching the simulated tornado vortex with full-scale tornadoes. Hence, the trend of developing tornado-like winds inside a laboratory setting that started in 1970s has seen several changes over the period of 4 decades with incorporation of several improvements in design and construction of tornado chambers as described above. In that regard, from an engineering perspective, three major experimental tornado chambers, i.e., (a) VorTECH at TTU (b) ISU tornado chamber at ISU and (c) WindEEE dome at WU represent the state-of-the-art in experimental modeling and simulation of tornado winds and for evaluation of tornado-induced wind loads on buildings. Further details about the tornado chambers can be obtained from Tang et al. (2018a), Haan et al. (2008) and Hangan (2014) respectively. All the experimental tornado chambers stated above have their own distinct geometric configuration and flow generation mechanism (Gairola and Bitsuamlak, 2019).

Despite being a valuable tool for studying about tornado vortices and tornado-induced forces on building, there are several limitations with experimental tornado chambers. Many tornado chambers can only produce a stationary tornado vortex such as VorTECH at TTU, Purdue University tornado chamber (Church et al., 1977), University of Birmingham tornado chamber (Gillmeier, 2019) while only a few tornado chambers can produce a translating tornado vortex

such as ISU tornado chamber and WindEEE dome. Even in ISU tornado chamber and WindEEE dome, neither the translation speed nor the mechanism of tornado translation bears resemblance to real-world tornadoes. In addition, tornado vortices generated in experimental tornado chambers have only been able to achieve a match in terms of geometric similarity while failing to match the kinematic and dynamic similarities of real-world tornadoes (Baker and Sterling, 2019). On top of that, the construction, operation, and maintenance of experimental tornado chambers as well as data acquisition is very costly. Thus, there are several challenges with experimental tornado chambers that needs to be resolved before a tornado vortex fully representative of full-scale tornadoes is produced and wind loads are assessed.

2.7 Tornado Forces on Building from CFD Tornado Chambers

With advancements in computing speed and storage technology, CFD has evolved over the years as a tool for numerically simulating tornado vortices and estimating tornado-induced wind loads on building. Selvam and Millet (2003) numerically simulated tornado-like vortex based on Rankine Combined Vortex Model (RCVM) using Large Eddy Simulation (LES). As there was ample information about the nature and magnitude of wind loads produced by straight line winds from wind tunnel tests, the wind loads induced by tornado winds were often compared with SL winds and ASCE 7 provisions (for wind load estimation due to SL winds). Selvam and Millet (2005) compared force coefficients on a cubical building with SL winds and concluded that forces due to tornado could rise by up to 50 % for walls while even higher for roof by up to 100%. Nasir et al. (2014) computed wind load due to a single-celled tornado vortex on a tall building (Commonwealth Advisory Aeronautical Research Council (CAARC) building) using RANS model and concluded that the largest suction forces is encountered by building when it is at the center of tornado vortex. They also concluded that the suction forces are due to large pressure

drops that occur at the center of tornado vortex and such pressure drops dominate the overall loading of structures due to tornado. The tornado vortex considered in the study was geometrically scaled with the Happy Texas tornado (Bluestein et al., 2004) using the technique proposed by Refan et al. (2014). However, there were certain shortcomings in the computed pressures on building from Nasir et al. (2014) such as (a) comparison and validation with experimental measurements was lacking; instead, pressure obtained from a tall building was compared with a short building and (b) a less accurate RANS model instead of LES was chosen in the CFD model. Hence, on the computational modeling side, there is a need for validation of tornado pressures on building from CFD model with experimental measurements.

After reviewing the existing literature, the forces, moments, and pressures induced by tornado-winds on building are documented in Table 2. It can be readily noticed in Table 2 that there is significant variation in reported forces and pressures on building due to tornado winds. Several factors may be responsible for the variation of tornado forces such as different scale of building model, different flow structures of tornado vortex (different swirl ratios) and differences in reference quantities (reference velocity and pressure) considered while evaluating force and pressure coefficients.

Table 2. Tornado forces, moment, and pressures on building from different references

SN	Reference	C_{fx}	C_{fy}	C_{fxy}	C_{fz}	C_{mxy}	C_{mz}	C_p	Ref. P
1	Selvam and Millet (2005)	1.33	1.36	-	1.81	-	-	-2.82	0
2	Sengupta et al. (2008)	-	-	1.97 ^C 2.17 ^{TB}	1.44 ^C 1.78 ^{TB}	1.14 ^C 1.15 ^{TB}	0.34 ^C 0.53 ^{TB}	-	-
3	Mishra et al. (2008)	2.4	2.45	-	2	-	-	-1	P _{s,g}

Table 2. Tornado forces, moment, and pressures on building from different references (Cont.)

SN	Reference	C_{fx}	C_{fy}	C_{fxy}	C_{fz}	C_{mxy}	C_{mz}	C_p	Ref. P
4	Haan et al. (2010)	2.7	2	-	4	-	-	-5	$P_{a,o}$
5	Hu et al. (2011)	0.8	0.6	-	2.75	-	-1	-4.2	$P_{a,o}$
6	Sabareesh et al., (2012, 2013)	-	-	-	-5.5 ST -9.0 ^{RT}	-	-	-19	$P_{s,f}$
7	Liu et al. (2015a)	2.3	0.9	-	-1.2	-	-	-1.1	0
8	Nasir and Bitsuamlak (2014)	-	-	-	-	-	-	-2.5	$P_{max,g}$
9	Li et al. (2019)	0.1 ^D 1.5 ^S	-0.2 ^D -1 ^S	-	-2.4 ^D -8.4 ^S	-	-	-0.6 ^D -2.0 ^S	P_{atm} (101 KPa)

***Note: - C: Cube building; TB: Tall building; S: single-celled tornado; D: double-celled tornado; r: roof; ST: smooth terrain; RT: rough terrain

Of the several possibilities, it can be clearly observed from Table 3 that a diverse range of flow structure of tornado vortices have been considered in the existing literature for evaluating tornado forces on building. Different flow structures of tornado have different wind velocity profiles and pressure distribution; different velocity and pressure distribution results in different loading conditions on building. The difference in flow structure is one of the most important factors leading to a wide variation of tornado forces on building. However, the kind of tornado flow structure that would result in most severe loading conditions on a building is not yet known in the existing literature.

Table 3. Different features of tornado vortex and scale of building model used for estimating tornado forces on building

SN	Reference	Model Scale	S	r_c	V_{tmax}	OA	Ref. Vel.
1	Selvam and Millet (2005)	-	-	60 m = 3 units	90 m/s = 4.5 units/s	0°, 45°	$V_t + V_{trans}$

Table 3. Different features of tornado vortex and scale of building model used for estimating tornado forces on building (Cont.)

SN	Reference	Model Scale	S	r_c	V_{tmax}	OA	Ref. Vel.
2	Mishra et al. (2008)	1:3500	0.19	-	-	-	-
3	Sengupta et al. (2008)	1:100	0.24, 1.14	0.3m, 0.53m	9.7 m/s	0°, 45°	V_{tmax}
4	Haan et al. (2010)	1:100	0.08-1.14	0.23-0.53 m	8.3 - 11.9 m/s	0° - 90° @ 15°	Max. V_H
5	Hu et al. (2011)	1:200	0.1	0.16m	10 m/s	0°	V_{tmax}
6	Sabareesh et al. (2012)	-	1.3	37.3 mm	-	-	$V@RH$
7	Sabareesh et al. (2013)	-	0.43, 0.87	Fully engulfed	-	-	$V@RH$
8	Liu et al. (2015b)	1:1900	2.44	0.112m	18.6 m/s	10° - 50° @ 10°	$V_{tmax}@MEH$

***Note: - Fully Engulfed implies that the building model considered was fully engulfed inside the core of tornado vortex. Also, 0° - 90° @ 15° implies that the orientation angles in the study was varied from 0° to 90° in increments of 15°

Li et al. (2020) investigated the effect of different flow structures of tornado vortex on a dome-shaped building and concluded that single-celled vortex produces more critical loading conditions on a building than double-celled vortex; however, they also speculated that the double-celled vortex have greater potential of producing dynamic loading effects on a building. Most of the residential houses are comprised of cubical or prismatic buildings while dome-shaped buildings comprise only a small subset of residential housing. Thus, there is a need for systematic investigation of tornado-induced forces on building due to different flow structures of tornado vortices to determine a reference tornado model (or reference flow structure of tornado) that produces the worst-case loading scenario on a building. Selection of a reference tornado model (or a reference flow structure) would help to reduce if not eliminate the variability in tornado-induced forces on building. Extensive case studies carried out considering a reference flow structure of

tornado on buildings of different shapes, sizes and configuration would help to establish and codify design procedures for buildings in tornado-prone areas.

Chapter-3: Computational Modeling

3.1 Introduction

The geometry of computational domain must be created first before tornado-like vortices can be simulated using a CFD model. The geometry of computational domain is modeled in such a way that the modeled geometry bears resemblance to experimental tornado chambers to the greatest extent possible. In that regard, it is a common practice to use Computer Aided Design (CAD) packages to create a solid model for the computational domain as shown in Fig. 2.

However, the problem with sophisticated 3D CAD models is that the simulation process becomes too demanding computationally and often high-performance (supercomputing) resources become necessary to obtain the solution. Due to very high requirements of computational resources, a simplified model is considered for the current work and is described in the following section 3.2.

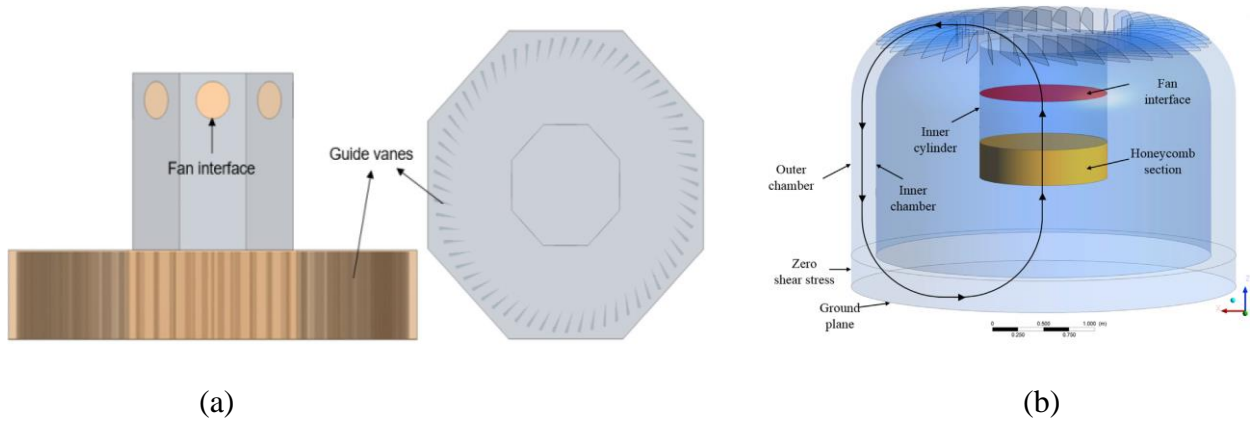


Fig. 2. CAD model for computational domain (a) VorTECH tornado chamber (Taken from Gairola and Bitsuamlak, 2019) (b) ISU tornado chamber (Taken from Yuan et al., 2019)

Even in sophisticated 3D CAD models shown in Fig. 2, there are certain simplifications made such as in VorTECH tornado chamber (Gairola and Bitsuamlak, 2019), the effect of fan is created by providing a definite mass outflow rate at the location of fans instead of modeling the fans. Similarly, in ISU tornado chamber, the effect of fan is created by providing a pressure jump at the location of fans (Yuan et al., 2019) instead of modeling and rotating the fan blades.

3.2 Computational Domain and Meshing of Computational Domain

Even in the sophisticated 3D CAD models as described in section 3.1, there were certain simplifications made and even with certain simplifications as described above, the computational cost of CFD simulations was very high. Thus, a relatively simple geometry for computational domain is considered in the current work as shown in Fig. 3. As shown in Fig. 3, air enters through an inlet at the base of CFD tornado chamber and is transported up through the chamber before exiting via outlet at the top of tornado chamber.

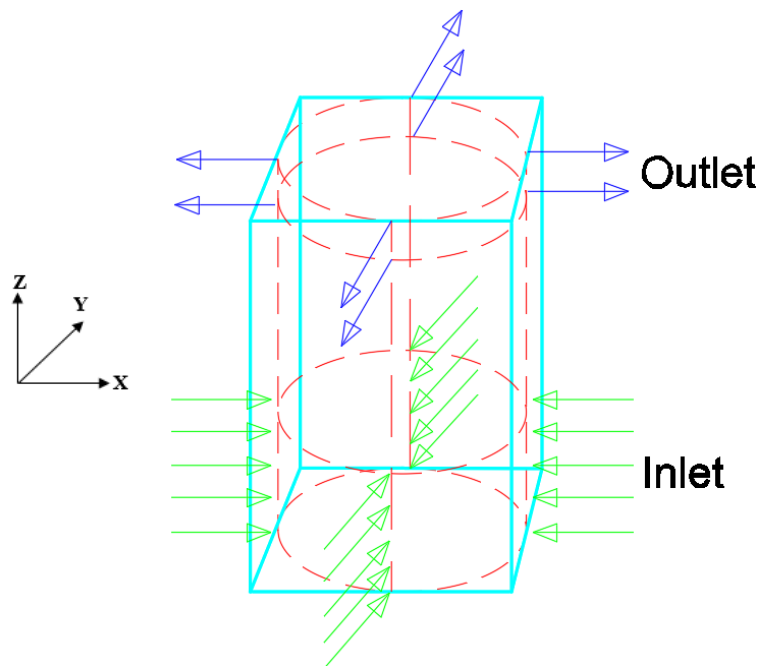


Fig. 3. Simplified Computational domain for VorTECH tornado chamber

The cross-section of experimental tornado chamber called VorTECH at Texas Tech University (TTU) and the simplified CFD tornado chamber for VorTECH are shown in Fig. 4. As shown in Fig. 4 (a), the inlet height of experimental tornado chamber (VorTECH) is kept the same in CFD tornado chamber but there were some simplifications made to the outlet of CFD tornado chamber. The fans from VorTECH tornado chamber were not explicitly modeled in the simplified CFD tornado chamber.

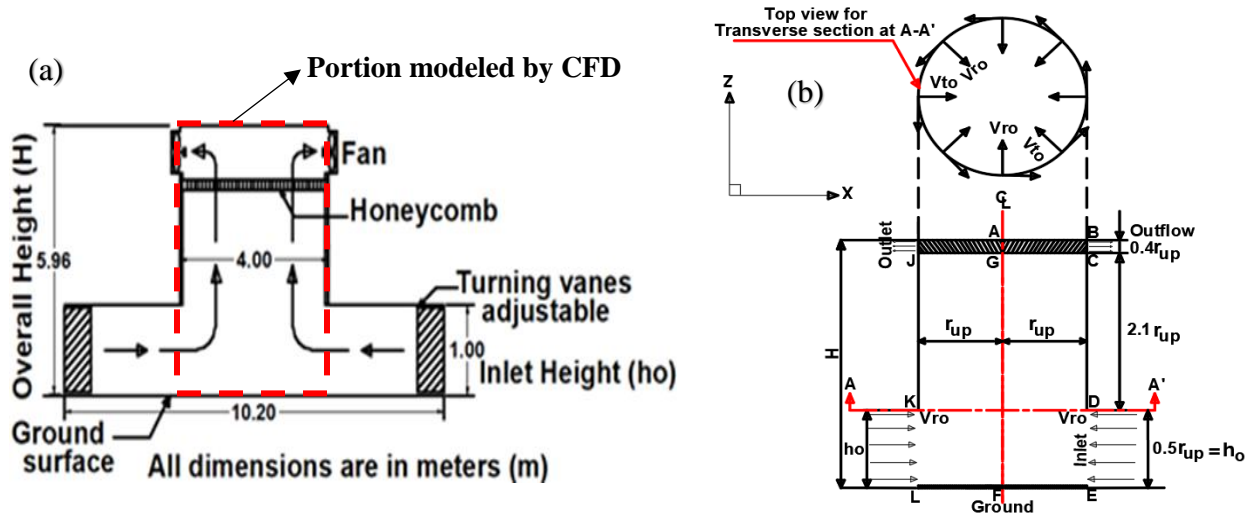


Fig. 4. Cross-section of (a) experimental tornado chamber VorTECH at TTU (b) simplified CFD tornado chamber for VorTECH

3.2.1 Determination of Depth of Outlet in Simplified CFD Tornado Chamber

The experimental tornado chamber (VorTECH) at TTU consists of 8 fans altogether, each with a diameter of 4ft. The total area of 8 fans was determined next using the diameter of fans. Later, an effective side hole along the periphery (or circumference) of CFD tornado chamber was provided with a depth that would result in the same area as the 8 fans taken together. The calculation to determine the depth of outlet in CFD tornado chamber is as follows:

$$\text{Diameter of each fan in VorTECH } (\phi) = 4 \text{ ft} = 1.2192 \text{ m} \quad (1)$$

$$\text{Total area of 8 fans} = 8 \times \left(\frac{\pi \phi^2}{4} \right) = 9.34 \text{ m}^2 \quad (2)$$

$$\text{Curved Surface Area (CSA) of outlet at the top of CFD tornado chamber} = 2 \pi r_{up} h_{out} \quad (3)$$

Equating (2) and (3), we have,

$$\Rightarrow 2 \pi r_{up} h_{out} = 9.34 \text{ m}^2$$

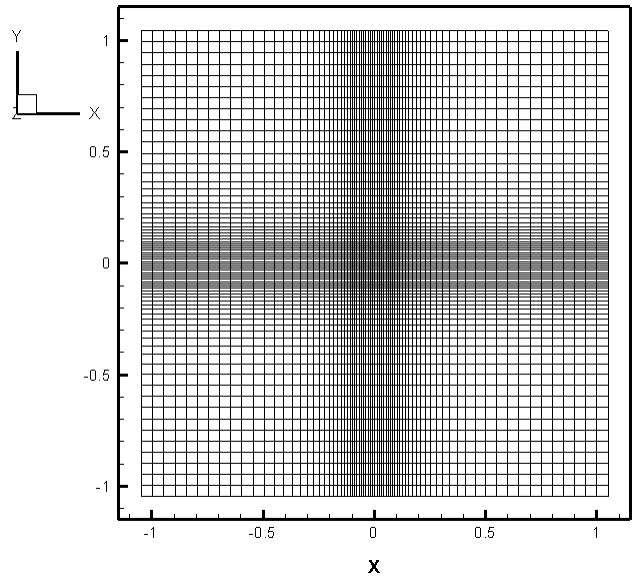
$$\Rightarrow h_{out} = \frac{9.34 \text{ m}^2}{2 \pi r_{up}} = \frac{9.34 \text{ m}^2}{2 \pi (2 \text{ m})} = 0.743 \text{ m}$$

Thus, the depth of outlet at the top of CFD tornado chamber (h_{out}) was found to be 0.743 m. Except for the size of outlet, remaining dimensions are kept same in CFD tornado chamber as they are in the experimental TTU tornado chamber.

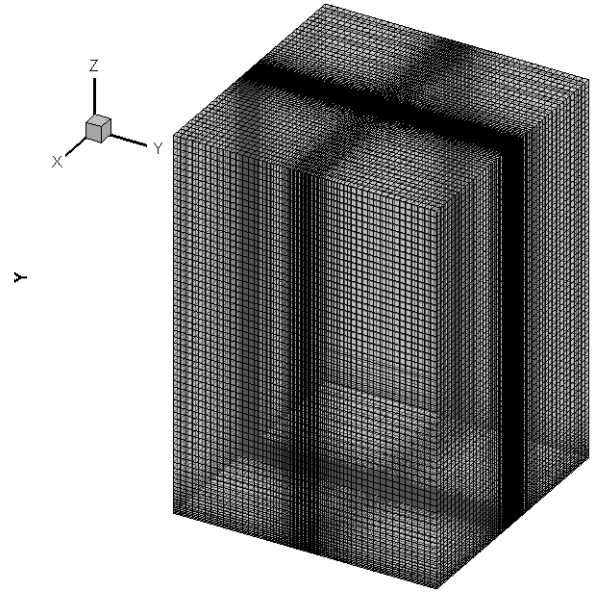
3.2.2 Meshing of Computational Domain

The computational domain is discretized by a structured 3D grid in Cartesian coordinate system. Origin is chosen at the base center of computational domain as shown in Fig. 5 (a). The smallest grid size is provided as $0.01h_o$ and it is stretched in all the 3 directions (i.e. X, Y and Z direction) by a grid expansion factor of 1.1 until the size of grid becomes $0.05h_o$. Once, the largest grid size of $0.05h_o$ is reached in all the 3 directions, the grid size thereafter is kept constant at $0.05h_o$. Thus, the maximum aspect ratio (ratio of max. grid size to min. grid size) of cells in the mesh is kept at 5. Initially, a semi-staggered node-centered grid system was chosen to discretize the computational domain. However, a physically unrealistic pressure field (checkerboard pressure oscillation) was obtained as the final solution using the semi-staggered grid system. Thus, a staggered grid system was introduced later and is used in the current work.

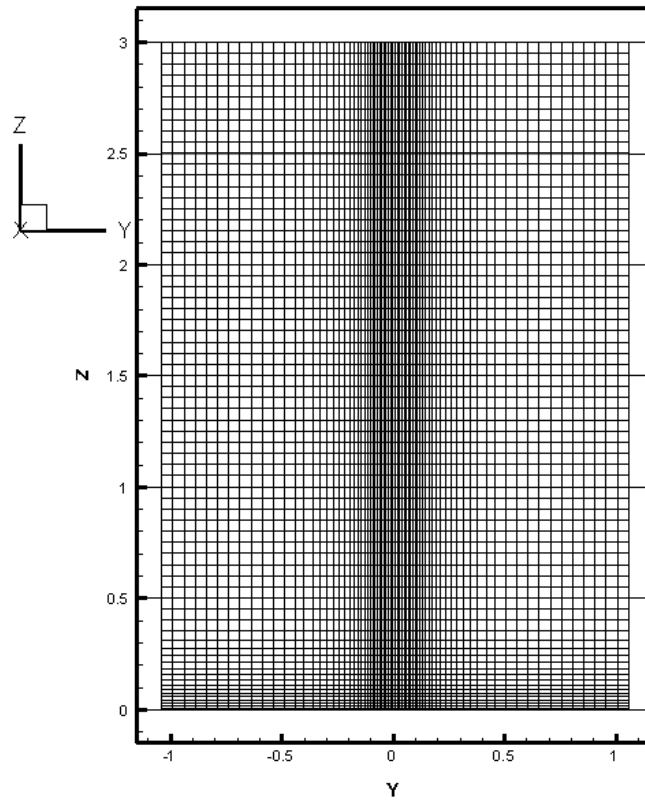
Figure 5 (b) shows the mesh composition for the entire 3D computational domain. If the mesh of 3D computational domain is viewed in XY-plane, mesh composition as shown in Fig. 5 (a) is obtained whereas if viewed in YZ-plane, mesh composition as shown in Fig. 5 (c) is obtained.



(a)



(b)



(c)

Fig. 5. Meshing of computational domain (a) XY-plane (b) 3D domain (c) YZ-plane

3.3 Governing Equations, Solution Schemes and Boundary Conditions

Flow in a CFD tornado chamber is considered incompressible as the density of air inside the tornado chamber is constant over time. As the computational domain is discretized in 3D Cartesian coordinate system, so, the 3D Navier-Stokes (NS) equation in Cartesian coordinate system is used to solve for the velocity and pressure field as unknowns in the computational domain. The flow inside a tornado chamber takes place at a very high Reynolds number (Re) such as $Re = 4 \times 10^5$. Thus, the flow is turbulent inside a tornado chamber. The turbulent flow inside a tornado chamber is comprised of eddies of various sizes or length scales. Not all the turbulence length scales can be captured by the grid used to discretize the computational domain. To resolve the eddies of all the turbulent length scales, Direct Numerical Simulation (DNS) must be employed but it is prohibitively costly whereas Reynolds Averaged Navier-Stokes (RANS) model resolves none of the turbulent eddies in the flow field. Thus, Large Eddy Simulation (LES) based on Smagorinsky model that resolves certain fraction of turbulent eddies formed in flow field by the grid itself and models the effect of smaller eddies by sub-grid stress (SGS) modeling (i.e., increasing effective viscosity by adding turbulent or sub-grid scale viscosity - ν_{sgs}) is used for the current work.

The governing 3D incompressible NS equations used in the current work are as follows:

Continuity equation:

$$\frac{\partial \bar{U}_i}{\partial x_i} = 0 \quad (4)$$

Momentum Equation:

$$\frac{\partial \bar{U}_i}{\partial t} + \bar{U}_j \frac{\partial \bar{U}_i}{\partial x_j} = - \frac{\partial \bar{P}}{\partial x_i} + 2 \frac{\partial}{\partial x_j} (\nu + \nu_{sgs}) \bar{S}_{ij} \quad (5)$$

$$\nu_{sgs} = (C_{sgs} \Delta)^2 \sqrt{2 \bar{S}_{ij} \bar{S}_{ij}} \quad (6)$$

In Eq. (6), $C_{sgs} = 0.1$ is the Smagorinsky constant and $\Delta = \sqrt[3]{(\Delta x \Delta y \Delta z)}$ is the length scale of sub-grid scale (SGS) turbulence and \overline{S}_{ij} is the LES filtered strain rate tensor given by (7).

$$\overline{S}_{ij} = \frac{1}{2} \left(\frac{\partial \overline{u}_i}{\partial x_j} + \frac{\partial \overline{u}_j}{\partial x_i} \right) \quad (7)$$

Further details on flow modeling used for the current work can be obtained from Selvam (1997). Finite Volume Method (FVM) with a node-centered scheme is used to obtain the linear system of equations for solving the unknowns (i.e., velocities and pressures) in the computational domain. The convection terms in NS equation are approximated by QUICK scheme (Leonard, 1979) while the diffusion terms are approximated using central difference scheme. Momentum equations are solved using line iteration method while continuity is satisfied by SOLA procedure as reported in Hirt and Cook (1972).

3.3.1 Non-dimensionalization of NS Equation

In CFD modeling, it is a common practice to non-dimensionalize the governing equations by using some reference values. The non-dimensional equations are numerically stable as the magnitude of variables remain low during computations. Non-dimensionalization becomes more important when dealing with non-linear partial differential equations such as NS equation because non-dimensionalization tries to prevent computation from diverging. During the process of non-dimensionalization, dimensionless numbers appear in the governing equation. For instance, a dimensionless number called Reynolds number (Re) appears during the non-dimensionalization of NS equation. The Reynolds number is defined by (8).

$$Re = \frac{\rho V l}{\mu} \quad (8)$$

Thus, non-dimensionalization has another advantage that the dimensionless number (such as Re) can be varied to understand its effect on flow field rather than varying the individual terms that appears in the definition of Re given by (8) above.

For non-dimensionalization of NS equation, two reference variables are considered in the current work. Either the inlet height (h_o) or the radius of tornado chamber (r_{up}) is chosen as the reference length for the current work. Similarly, the radial velocity at the inlet height (V_{ro}) is chosen as the reference velocity for non-dimensionalization of NS equations.

If x , y , and z denote the coordinates along x -axis, y -axis, and z -axis of the discretized computational domain in dimensional form then, the corresponding non-dimensional coordinates are given by x^* , y^* and z^* respectively. Similarly, if U , V , and W denote the velocity components along x -axis, y -axis, and z -axis in the discretized computational domain in dimensional form then, the corresponding non-dimensional velocities are given by U^* , V^* and W^* respectively. In the similar manner, the solved non-dimensional pressure field in the computational domain is represented by P^* for the actual physical pressure field (P). The relationship between the dimensional and the corresponding non-dimensional variables is as follows:

$$U^* = \frac{U}{V_{ro}}; \quad V^* = \frac{V}{V_{ro}}; \quad W^* = \frac{W}{V_{ro}}; \quad x^* = \frac{x}{h_o}; \quad y^* = \frac{y}{h_o}; \quad z^* = \frac{z}{h_o}; \quad t^* = \frac{V_{ro} t}{h_o}; \quad P^* = \frac{P}{\rho V_{ro}^2}; \quad Re^* = \frac{V_{ro} h_o}{\nu}$$

Further details about non-dimensionalization of NS equations can be obtained from Cengel and Cimbala (2014).

3.3.2 Initial and Boundary Conditions

Different boundary faces of the computational domain indicated by different colors are shown in Fig. 6 (a) and (b). The inlet boundary face, side wall boundary face and the outlet boundary face are represented by red, blue and yellow color respectively (Fig. 6 (a)). Similarly, the top wall is represented by cyan color (in Fig. 6 (a)) whereas the bottom wall is represented by green color

(Fig. 6 (b)). A section plane ABCD dissects the computational domain into 2 halves and passes through the diametric axis (AB or CD) of cylindrical computational domain. The sectional view through plane ABCD formed by the intersection of cylindrical computational domain and plane ABCD is shown in Fig. 7 (a) whereas in Fig. 7 (b), the top view when a transverse section is taken at X-X' (in Fig. 7 (a)) is shown. The names of each of the boundary faces are stated at the location of respective boundaries (such as Inlet, Outlet, etc.) in Fig. 7 (a).

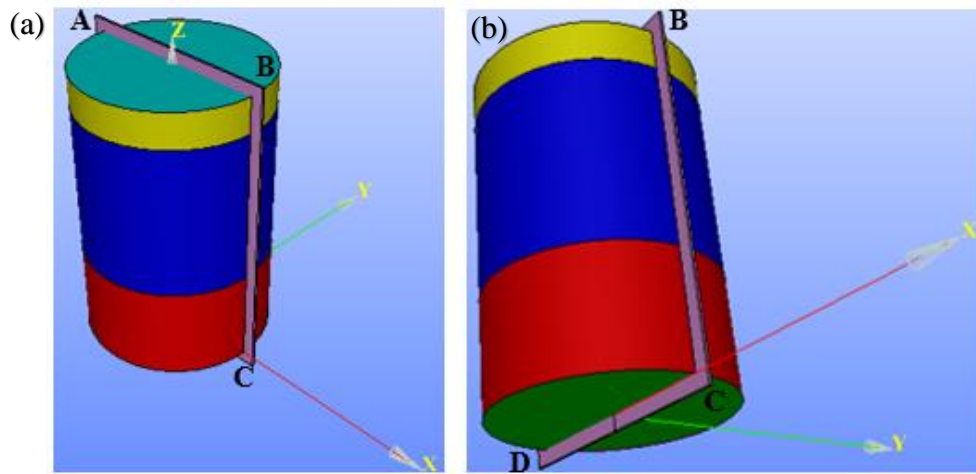


Fig. 6. Different views of computational domain showing different boundary faces (a) Isometric view (b) Perspective view

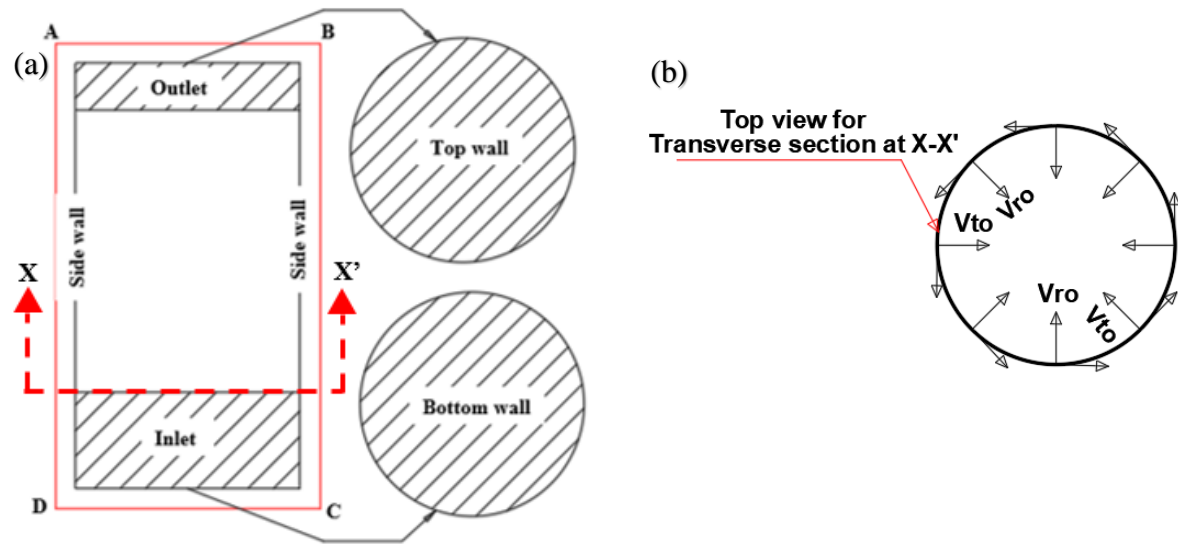


Fig. 7. (a) Sectional view through plane ABCD showing the boundaries of computational domain (b) Top view for transverse section at X-X' showing velocity boundary condition at inlet height

The velocity and pressure boundary conditions (BCs) in each of the boundary faces as shown in Fig. 7 (a) are stated below:

(a) Inlet:

Velocity BC: A logarithmic velocity profile is provided at the inlet given by (9) and (10), which is also shown in Fig. 7 (b). The radial component of velocity is given by (9) whereas the tangential velocity component is given by (10). The vertical velocity component is taken as 0, i.e. $V_z^* = 0$.

$$V_r^* = C_1^* \ln \left(\frac{z^* + z_o^*}{z_o^*} \right) \quad (9)$$

In Eq. (9), $V_r^* (z^* = 1) = 1$ and z_o^* is non-dimensional roughness length considered as per the terrain conditions. Knowing $V_r^* (z^*)$ and z_o^* in Eq. (9), C_1^* is calculated for the problem.

$$V_t^* (z^*) = 2 a S V_r^* (z^*), \quad (10)$$

where a = aspect ratio of CFD tornado chamber given by $a = h_o/r_{up}$ and S = swirl ratio of flow.

Pressure BC: Neumann boundary condition is provided at the inlet by specifying a zero gradient condition for pressure in the normal direction.

$$\frac{\partial P^*}{\partial n} = 0 \quad (11)$$

(b) Side wall:

Velocity BC: No-slip boundary condition is provided for the side wall and is given by (12).

$$U^* = V^* = W^* = 0 \quad (12)$$

Pressure BC: Neumann boundary condition is provided at the side wall by specifying a zero gradient condition for pressure in the normal direction.

$$\frac{\partial P^*}{\partial n} = 0 \quad (13)$$

(c) Outlet:

Velocity BC: Total inlet velocity is provided as the outlet velocity (V_{out}) boundary condition and is given by

$$V_{\text{out}} = \sqrt{V_{\text{ro}}^{*2} + V_{\text{to}}^{*2}} \quad (14)$$

Pressure BC: Neumann boundary condition is provided at the side wall by specifying a zero gradient condition for pressure in the normal direction.

$$\frac{\partial P^*}{\partial n} = 0 \quad (15)$$

(d) Bottom wall:

Velocity BC: No-slip boundary condition is provided for the bottom wall and is given by (16).

$$U^* = V^* = W^* = 0 \quad (16)$$

Pressure BC: Neumann boundary condition is provided at the bottom wall by specifying a zero gradient condition for pressure.

$$\frac{\partial P^*}{\partial n} = 0 \quad (17)$$

(e) Top wall:

Velocity BC: No-slip boundary condition is provided for the top wall and is given by (18).

$$U^* = V^* = W^* = 0 \quad (18)$$

Pressure BC: Neumann boundary condition is provided at the top wall by specifying a zero gradient condition for pressure.

$$\frac{\partial P^*}{\partial n} = 0 \quad (19)$$

In addition to the boundary conditions stated above, law of the wall boundary condition is also implemented at the walls. The velocities and pressure in the computational domain is initialized to

zero. All the simulation test cases are run for a total non-dimensional time (t^*) of 25 units unless stated otherwise.

3.4 Grid Independence Test

In CFD work, it is a common practice to obtain solution for the same problem using different grids. If the solution obtained from different grids such as a coarse grid, a moderately refined grid and a fine grid show only a marginal change in the finally obtained solution then, the obtained solution is said to be grid independent.

In the similar line, for the current work, three different grids (G1: coarse grid, G2: moderately refined grid and G3: fine grid) are considered for grid independence test. Details of the grids such as the smallest and the largest grid spacing, total number of grid points used for discretizing the computational domain, etc. is reported in Table 4.

Table 4. Different Grids considered for Grid Independence test with their mesh sizes

Grid resolution	G1	G2	G3
Grid points in X-direction	61	75	85
Grid points in Y-direction	61	75	85
Grid points in Z-direction	50	70	85
Total no. of grid points	186050	393750	614125
Smallest size of grid	0.006 h_o	0.005 h_o	0.004 h_o
Largest size of grid	0.030 h_o	0.025 h_o	0.020 h_o

3.4.1 Normalized Root Mean Square Error (NRMSE) as Error Estimate

When the pressure profiles or tangential velocity profiles obtained from different grids are superimposed on one another, the profiles do not overlay perfectly over each other. Thus, there are some deviations in the obtained solution from one grid to another. Such deviations are quantified by an error estimate known as Normalized Root Mean Square Error (NRMSE) and is given by Eq. (20).

$$\text{NRMSE} = \frac{\sqrt{\frac{\sum_i^N (P_{i,\text{Grid X}} - P_{i,\text{Grid Y}})^2}{N}}}{|P_{\max} - P_{\min}|} \quad (20)$$

In Eq. (20), the variable ' $P_{i,\text{Grid X}}$ ' represents the property of flow field (such as pressure or tangential velocity) at i^{th} coordinate in the profile from a grid (here named as Grid X) and ' $P_{i,\text{Grid Y}}$ ' represents the same property of flow field (pressure or tangential velocity) at the same i^{th} coordinate in the profile from another grid (here named as Grid Y). Finally, the NRMSE is normalized by the range of dataset and is given by $|P_{\max} - P_{\min}|$, where P_{\max} is the maximum value of flow property under consideration (pressure or tangential velocity) and P_{\min} is the minimum value of flow property under consideration (pressure or tangential velocity).

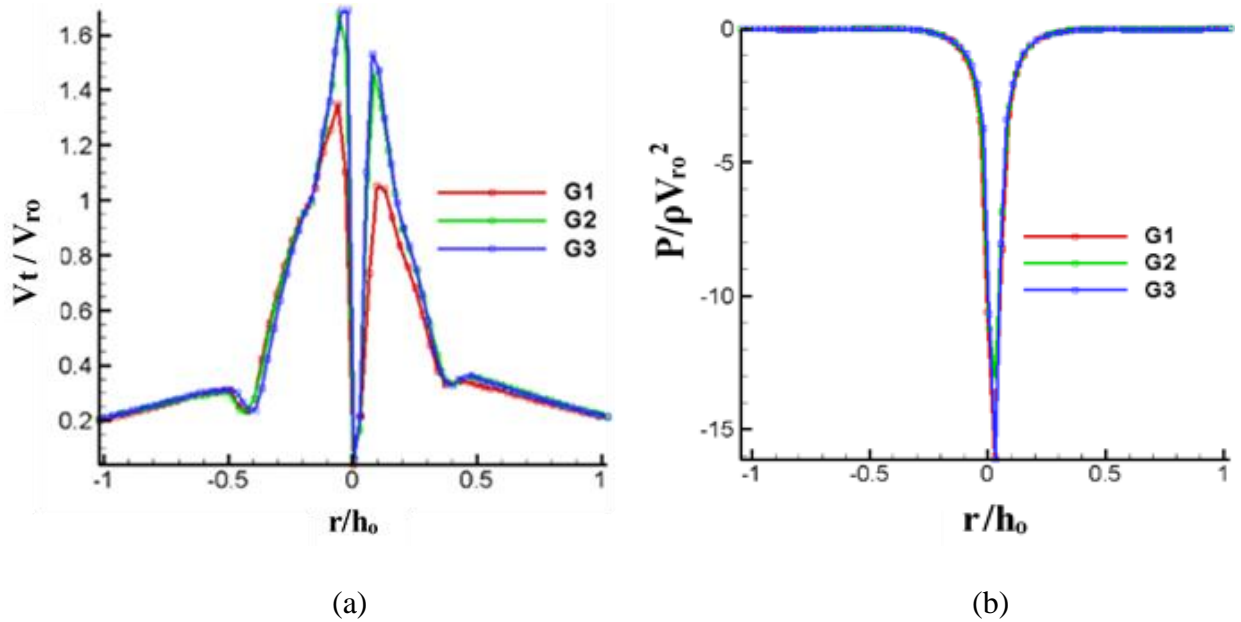


Fig. 8. (a) Tangential velocity profile for $S = 0.15$ at elevation $(z) = 0.075h_0$ (b) Radial ground pressure profile for $S = 0.15$

Finally, the profiles of pressure at ground surface as well as the profiles of tangential velocity at elevation of $z = 0.075h_0$ obtained from 3 grids (G1, G2 and G3) are shown in Fig. 8. The pressure and tangential velocity profiles are both taken along the diametric axis of tornado chamber. The

pressure profile is taken on the ground plane with the pressure values calculated relative to the inlet of tornado chamber, whereas the tangential velocity profile is taken at an elevation of $z = 0.075h_0$ above the ground plane. The radial ground pressure profile from the grids (G2 and G3) collapses well with the normalized root mean square error (NRMSE) of about 3.97%. Similarly, the NRMSE for a tangential velocity profile was obtained at 2%. As the NRMSE values for both ground pressure profile and tangential velocity profile are less than 5%, it is concluded that the obtained solution is grid independent. For further studies and analyses, the grid (G2) is used unless otherwise stated.

Chapter-4: Validation of CFD Flow Field with TTU Experiment

4.1 Introduction

The tornado flow field obtained from CFD model needs to be validated with experimental data first before validating tornado forces on building. Since it is not very practical to compare every single aspect or feature of tornado vortex from a CFD model with experimental data, it is necessary first to identify the most important features of tornado vortex for comparison and validation that strongly influences the tornado forces on building.

While identifying the important tornado vortex features, attention has been provided to those select features of tornado vortex that are expected to play the most important role during validation of tornado pressures on building. A validated CFD model with respect to the important vortex features provides greater confidence in computed loads during validation of tornado pressures on building. It also ensures that the interaction of tornado vortex with building models in a numerical simulation environment exhibits greater resemblance to real world tornadic events. The important features of tornado vortex that are considered in CFD flow validation with experimental measurements are as follows: (a) Swirl ratio at vortex touchdown or alternatively called touchdown swirl ratio (S_T), (b) Core radius of tornado vortex, and (c) the near-surface pressure distribution with varying swirl ratios. Further details about the important tornado vortex features and the reason for considering those features important in CFD flow validation are described in section 1.1 of Verma and Selvam (2021b).

(a) Touchdown Swirl ratio (S_T): While comparing the value of touchdown swirl ratio for both the aspect ratios ($a = 0.5$ and 1.0 of tornado simulator), a good match was obtained between the results from CFD model and the TTU experimental results; touchdown was observed for the swirl ratio (S) value of 0.22 , when the aspect ratio of simulator was unity and for the swirl ratio (S) of

0.36 when the aspect ratio of the simulator was 0.5 for both the CFD model and TTU experimental tornado simulator. Further details about the flow field with flow visualizations such as pressure contour plots and velocity vector plots are available in Verma and Selvam (2020) for the case of tornado simulator with aspect ratio of unity and from Verma and Selvam (2021b) for the case of tornado simulator with aspect ratio of 0.5. The aspect ratio of experimental TTU tornado simulator can have only two values, i.e., $a = 0.5$ and 1.0 . As the CFD model predicted touchdown swirl ratios of TTU tornado simulator reasonably well at both the aspect ratios, i.e., $S_T = 0.22$ for aspect ratio of unity and $S_T = 0.36$ for aspect ratio of 0.5, it is concluded that the CFD model can predict the evolution of tornado vortex in TTU tornado simulator facility reasonably well.

(b) Core radius (r_c) of tornado vortex: Core radius of tornado vortex is the distance between the center of tornado vortex and the point where the maximum tangential velocity is located. The core radius of tornado vortex depends on the location of center of tornado vortex as well as the location of maximum tangential velocity in flow domain. So, the maximum value of tangential velocity including its location must be ascertained first before core radius of tornado vortex can be estimated.

Some of the key technical terms used in comparison of core radius are introduced first in the following text before discussing the results of comparison of core radius from the CFD model with TTU experimental results.

4.1.1 Local Core Radius and Vertical Profile of Core Radius

In Fig. 9 below, a typical tornado vortex indicated by red dotted line is shown. In the same figure, different XY-planes dissecting the tornado vortex at different elevations are also shown such as $z_0 = 0$, $z_1 = 65$ & $z_2 = 150$ (Refer Fig. 9). Considering the XY-plane at $z_0 = 0$, different flow properties of tornado vortex such as velocity (tangential and radial), and pressure can be measured along line

AB (in Fig. 9). When tangential velocity is measured along the line AB in experimental tornado chamber (or extracted in a CFD tornado chamber), and the distribution of tangential velocity is plotted along the line AB, then a typical tangential velocity profile as shown in Fig. 10 is obtained.

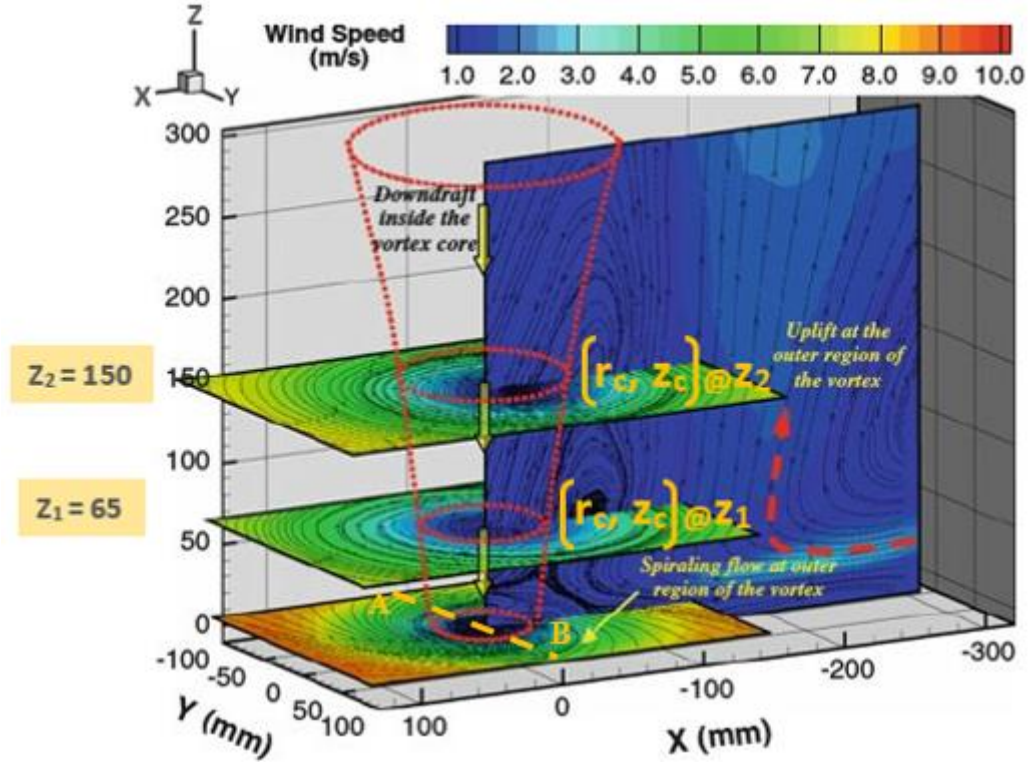


Fig. 9. Local core radius at different elevations (z_1 and z_2) (Modified from Hu et al., 2011)

As shown in Fig. 10, the core radius (r_c) of tornado vortex is the distance between location of the maximum and the minimum tangential velocity. However, tangential velocity also varies with elevation from the ground level. For instance, if tangential velocities are measured at different points along line AB at elevations such as $z_0 = 0$, $z_1 = 65$ and $z_2 = 150$, then different tangential velocity profiles (although with similar shape of profile but with varying magnitude of tangential velocity) are obtained at different elevations.

So, at each elevation, the points of the maximum and the minimum tangential velocity can be located and the distance between those two points gives the local core radius at that elevation.

When the local core radii (r_c) are plotted against the corresponding elevations at which they occur, the plot so obtained is called the vertical profile of core radius (such as Fig. 3 from Verma and Selvam, 2021b). From the different elevations, the elevation at which the maximum of the maximum tangential velocity is obtained is the final core radius of the tornado vortex ($r_{c, \max}$) and the corresponding elevation is called the elevation of core radius of tornado vortex ($z_{c, \max}$).

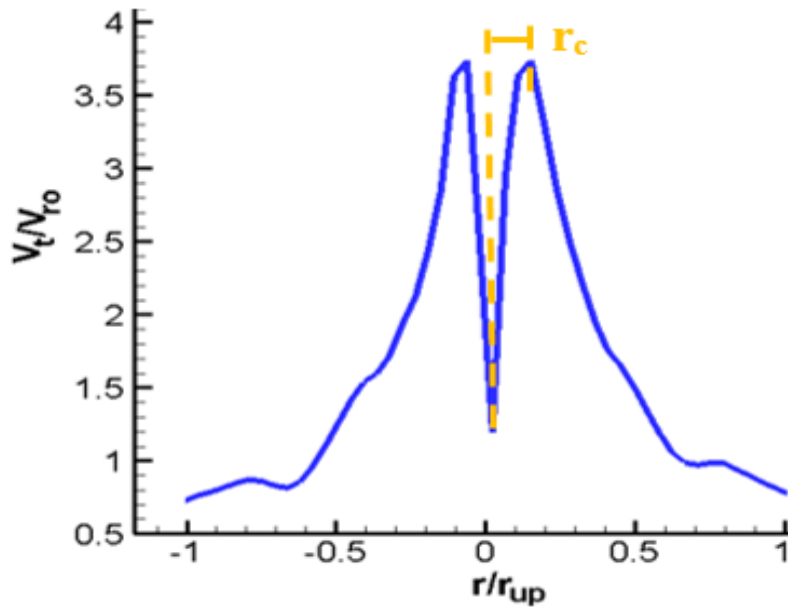


Fig. 10. Tangential velocity of tornado vortex along line AB (Fig. 9)

4.1.2 Fluctuation of Maximum Tangential Velocity over Time

The core radius of tornado vortex is defined with reference to the maximum tangential velocity in the flow domain. However, the maximum tangential velocity (or tangential velocity in general) changes with respect to time as shown in Fig. 11. As the maximum tangential velocity changes over time as shown in Fig. 11, the value of core radius of tornado vortex also changes over time. For complicated flows, which comprise of fluctuating velocities and pressures in time, it is a common practice to consider a suitable length of time and then calculate time-averaged velocities and pressures for comparison.

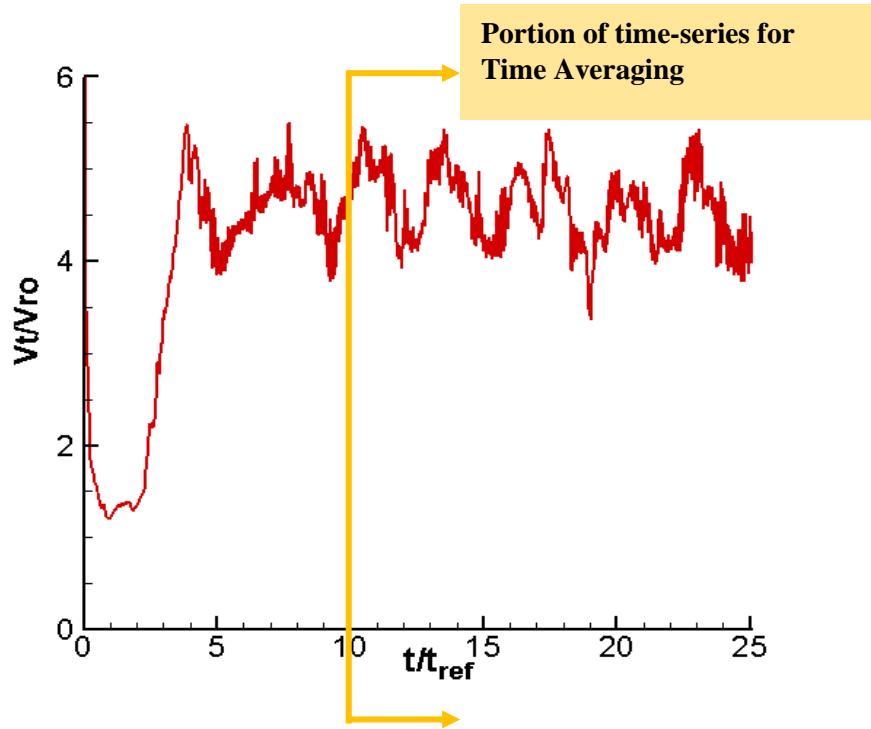


Fig. 11. Variation of maximum tangential velocity at the center of CFD tornado chamber at base plane

For the current work, time series of tangential velocity after non-dimensional time of 10 units (i.e., from $t/t_{ref} = 10$ units to $t/t_{ref} = 25$ units as shown in Fig. 11) is considered to calculate the time-averaged core radius and elevation of core radius. The period before $t/t_{ref} = 10$ non-dimensional time units is not considered for time-averaging of core radius as the flow in CFD tornado chamber is not fully developed. For time-varying flows, it is a common practice to start time-averaging of flow properties only after the initial transients have been eliminated. In Fig. 11, the tangential velocity before non-dimensional time of 5 units has more abrupt variation as during that time, the tornadic flow is trying to reach a fully developed state. Thus, after monitoring the tangential velocity up to 10 non-dimensional time units, the averaging of tangential velocity, core radius and elevation of core radius was done.

However, there is an added complexity in tornadic flow phenomena besides the variation of flow properties over time. The center of tornado vortex itself does not remain fixed in space at the center of tornado chamber. Rather, during the evolution of tornado vortex over time, the center of tornado

vortex keeps shifting from the center of tornado chamber. This phenomenon is described in the literature by the term called vortex wandering (Refan et al. 2018, Gairola, 2017). Further details about vortex wandering observed in this work can be obtained from the section on “Phenomena of Vortex Wandering” in Verma and Selvam (2020) and from section 3.1.5 in Verma and Selvam (2021b).

4.1.3 Vortex Wandering and Difficulty in Core Radius Estimation

The phenomena of vortex wandering, thus, creates a problem in estimation of core radius of tornado vortex as the center of tornado vortex and the location of the maximum tangential velocity must be located simultaneously to calculate the core radius. As the tornado vortex continues to evolve over time, the process of determining the center (represented by location of the minimum tangential velocity) and the location of the maximum tangential velocity must be performed at each time-step. Finally, a time-averaged core radius must be calculated from the time series of core radius. The step-by-step procedure of determining the minimum and the maximum tangential velocity over different time steps and finally the time-averaged core radius can be obtained from section 3.1.2.1 in Verma and Selvam (2021b). Using the procedure, the vertical core profiles for a vortex with two swirl ratios, i.e., $S = 0.24$ and $S = 0.78$ were extracted from CFD simulation as well as digitized from Tang et al. (2018 b). Further details about the comparison of vertical core profile between the CFD model and the TTU experiment can be obtained from section 3.1.2 in Verma and Selvam (2021b).

4.1.4 Comparison of Vertical Core Profile from CFD Model with TTU Experiment

The profile obtained from CFD simulation for a vortex with swirl ratio, $S = 0.24$ showed an overall good agreement with experimental result of $S = 0.24$ (both of which are representative of single-celled vortices in the respective simulation) with an average deviation (AD) of 0.016 times the

updraft radius (r_{up}). However, for the double-celled vortex (corresponding to $S = 0.78$), larger deviation as compared to $S = 0.24$ was observed. The average deviation is about 0.066 times the updraft radius ($0.066r_{up}$). The observed discrepancy for $S = 0.78$ may be attributed to flow measurement challenges in a post-touched down tornado vortex. On the CFD side, the grid becomes coarser as the distance from the center of CFD simulator increases, thus, it may also have contributed to the observed discrepancy. Due to greater turbulence in the vortex core in a post touchdown condition and due to vortex wandering effects, it is suspected that taking flow measurement becomes very challenging at proper location as stated in Tang et al. (2018 a), and thus may be the probable cause for observed deviation. Since the average deviation of vertical core profile for both the vortices, i.e., at swirl ratio (S) = 0.24 and $S = 0.78$ are low and the vertical profile of core radii from the CFD model shows an overall good agreement with TTU experimental core profile, thus, it is concluded that the CFD model can produce similar tornado vortices as the TTU tornado chamber.

4.2 Comparison of Near-Surface Pressure Distribution Over a Range of Varying Swirl Ratios from CFD Model with TTU Experiment

Tornado winds comprise of a sharp drop in pressure at the core of tornado vortex. The sharp drop in pressure causes large suction forces on the roofs, facades, and walls of the building, thus, causing uplifting of roofs and collapse of walls of the building. As most of the residential buildings are located within an elevation of 10 meters (Kashefzadeh et al., 2019) from the ground level, the pressure distribution due to tornado winds close to the ground surface is of great importance from an engineering standpoint. As tornadoes of different flow structures are obtained by varying swirl ratio and each of the different flow structures possess different pressure distribution close to the

ground surface, thus, the near surface pressure distribution due to tornado over a range of varying swirl ratios was considered important for CFD flow validation.

4.2.1 Fluctuation of Pressure in Time

Pressure at the ground surface due to tornado vortex was found to be varying in time (refer Fig. 4 (b) in Verma and Selvam, 2020). When flow properties are varying with respect to time, it is a common practice to consider a suitable length of time to calculate time-averaged velocity and pressure to describe the flow field. The experimental pressure profiles from TTU were calculated as an ensemble average of 10 different pressure measurements. To calculate the time-averaged flow properties, it is necessary first to understand the nature of variation of flow properties over time. The time-series plot of the minimum pressure (Fig. 4 (b) in Verma and Selvam, 2020) shows an approximate sinusoid-like variation of waveform. The nature of variation of waveform is an important clue as to what length of time should be considered for computing the time-averaged flow properties. Thus, a procedure was adopted for time-averaging of pressure which is described in detail in the section “Time-Dependent Flow Phenomena” from Verma and Selvam (2020).

Finally, using the same procedure, the time-averaged pressure profiles obtained from the CFD model are compared with TTU experimental pressure profiles. A good qualitative agreement was readily noticed between the CFD pressure profiles and TTU experimental pressure profiles at aspect ratio of unity (refer the section on “Touchdown S and Effect of Varying S on Radial Ground Pressure Distribution” and Fig. 10 from Verma and Selvam, 2020). Similarly, the time-averaged pressure profiles obtained from the CFD model at aspect ratio of 0.5 are compared with TTU experimental pressure profiles (refer section 3.1.4 from Verma and Selvam, 2021b). The pressure profiles again show a good qualitative agreement as the peak negative pressures are observed for the tornado vortex corresponding to $S = 0.36$. Finally, the pressure profile (in dimensional form

where pressure is expressed in Pascals) from the CFD model for $S = 0.44$ at $a = 1$ is compared with pressure profile from TTU experiment for same swirl ratio and aspect ratio (refer Fig. 4(b) from Verma and Selvam, 2021b). The pressure profile from the CFD model matches well with TTU experimental profile except for some differences in pressure gradient close to the center of tornado vortex. Considering TTU pressure measurement as the reference, the deviation in negative peak pressure predicted by the CFD model is about 4.42 %.

As the pressure profiles obtained from the CFD model show good qualitative agreement with TTU experimental pressure profiles over a range of varying swirl ratios and the comparison of dimensional negative peak pressure from CFD model to TTU experiment shows deviation less than 5%, thus, it is concluded that the CFD model predicts the pressure field of TTU tornado simulator reasonably well.

4.3 Summary and Conclusion

The features of tornado vortex, which are important from an engineering perspective and can strongly influence the tornado forces on building are identified for comparison and validation of CFD flow field. The important tornado vortex features are (a) touchdown swirl ratio (S_T) (b) core radius (r_c) of tornado vortex and (c) near-surface pressure distribution over a range of varying swirl ratios. When these vortex features from CFD model are compared with TTU experimental measurements, a reasonable agreement is observed in the flow field. The conclusions drawn from the comparison of CFD flow field with TTU experiment are summarized below:

1. The value of touchdown swirl ratio (S_T) = 0.22 at aspect ratio (a) = 1, obtained from the CFD model matches with TTU experimental results at aspect ratio of unity. Similarly, the value of touchdown swirl ratio (S_T) = 0.36 obtained from the CFD model matches with TTU experimental results at aspect ratio of 0.5. The aspect ratio of TTU tornado chamber

can only vary between 0.5 and 1.0. As the CFD model predicts touchdown swirl ratio very well for both the aspect ratios (i.e., $a = 0.5$ and $a = 1$), it is concluded that the CFD model reasonably predicts the evolution of flow field of TTU tornado chamber.

2. The average deviation in vertical core profile from the CFD model with TTU experiment for $S = 0.24$ is $0.016r_{up}$ whereas for $S = 0.78$, the average deviation is about $0.066r_{up}$. As the average deviation for both the core profiles are low and the vertical profile of core radii from CFD model shows an overall good agreement with TTU experimental core profile, it is concluded that the CFD model can produce similar tornado vortices as the TTU tornado chamber.
3. As the pressure profiles from the CFD model show good qualitative agreement with TTU experimental pressure profiles over a range of varying swirl ratios and the comparison of dimensional negative peak pressure from the CFD model to TTU experiment shows deviation less than 5%, thus, it is concluded that the CFD model predicts the pressure field of TTU tornado chamber reasonably well. As the important features of tornado vortex from CFD model agrees well with TTU flow field, it is, thus, concluded that an experimentally validated CFD model is obtained.

Chapter-5: Comparison of Touchdown Swirl Ratio and Important Vortex Parameters from Different Tornado Chambers

5.1 Introduction

The swirl ratio of a vortex and the rationale for considering it important in CFD flow validation was discussed in Chapter-4 as well. Swirl ratio strongly influences the drop in pressure at the center of tornado vortex. The maximum drop in pressure that has been observed during tornado touchdown (Tang et al., 2018 a) is one of the most important factors to influence wind loading on buildings (Nasir and Bitsuamlak, 2016). From literature review, it has been found that different tornado chambers have different touchdown swirl ratios. This implies that tornado forces on building from different tornado chambers would also differ from one chamber to another due to differences in flow structure of tornado vortices. In the following text, the touchdown swirl ratio (S_T) of different tornado chambers and other important vortex parameters (such as core radius, elevation of core radius, maximum tangential velocity, etc.) from different tornado chambers are reviewed. Although there exist differences from one tornado chamber to another, the similarities in flow pattern of different tornado chambers are identified. Based on the similarities in flow pattern of tornado chambers, the reviewed tornado chambers are grouped into five major categories. However, the value of touchdown swirl ratio is found to differ from one tornado chamber to another even within a given category. Finally, some supplementary CFD simulations are carried out to understand the effect of geometric variations (such as differences in total height and size of outlet) in different tornado chambers on the important vortex parameters. Reviewing the literature, however, it was found that there exists different definition of swirl ratio (Gillmeier, 2019). For comparison of touchdown swirl ratio of different tornado chambers, it would be logical to compare the value of touchdown swirl ratio when they are all expressed according to a common

definition. Hence, conversion relations are worked out between the different definitions of swirl ratio and the details of conversion relations follow in the upcoming text.

Firstly, the most popular variants of definition of swirl ratio from the existing literature are reviewed and then conversion relations are worked out for comparison of touchdown swirl ratio from different tornado chambers based on a single consistent definition.

5.2 Different Definitions of Swirl Ratio

The key terms used in different definitions of swirl ratio (S) are defined below and are illustrated in Figure 12 (a). Similarly, Figure 12 (b) shows the radial locations of flow domain (tornado chamber) where different swirl ratios are defined on a typical tangential velocity profile plot.

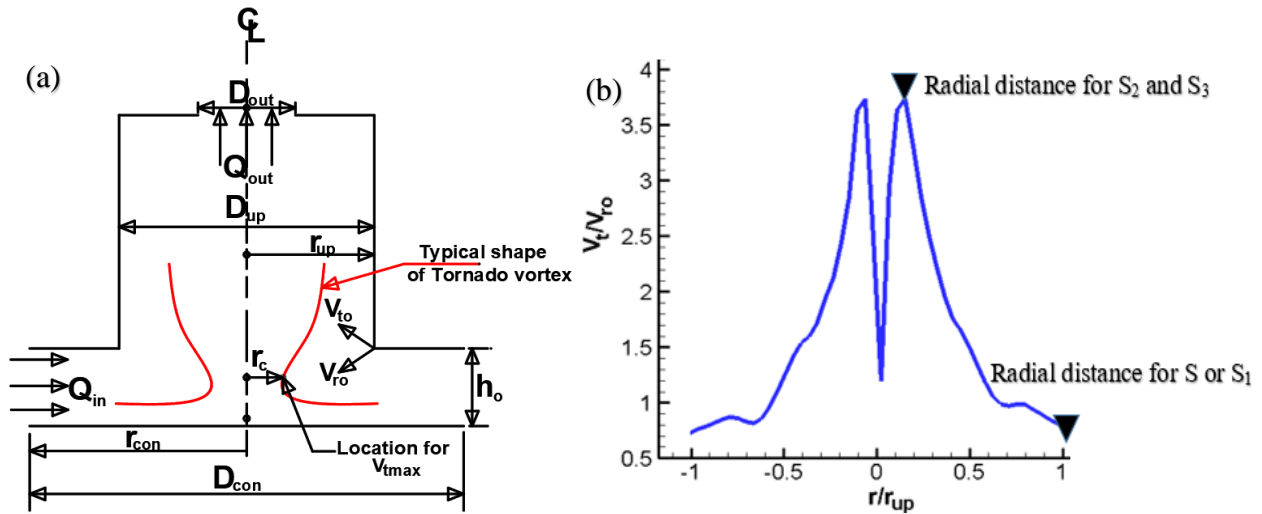


Fig. 12. (a) Demonstration of notations used in different definitions of swirl ratio in a tornado chamber (b) different radial location chosen for defining different swirl ratios

One of the most popular definitions of swirl ratio that is also used throughout the current work is given by

$$S = \frac{V_{to}}{2 a V_{ro}}, \quad (22)$$

where 'a' is the aspect ratio of tornado chamber in Eq. (22) and is given by

$$a = \frac{h_o}{r_{up}} \quad (23)$$

The definition of swirl ratio described by Eq. (22) is used by Natarajan and Hangan (2012), Refan and Hangan (2016), Kashefzadeh (2018), Gairola and Bitsuamlak (2019), Gillmeier (2019) and Verma and Selvam (2020). Besides, there exists another definition of swirl ratio (S_1) given by Eq. (24), which uses circulation at the edge of convergence region (Γ_∞) and volumetric outflow rate (Q_{out}) from the tornado chamber to evaluate the value of swirl ratio.

$$S_1 = \frac{r_{up} \Gamma_\infty}{2 Q'_{out} h_o} \quad (24)$$

The definition of swirl ratio described by (24) is considered by Church et al. (1977). Besides (22) & (24), some other common definitions of swirl ratio found in literature which uses the updraft radius (r_{up}), maximum circulation in the flow field (Γ_{max}), volumetric flow rate per unit axial height (Q'_{out}), inlet height (h_o), the maximum tangential velocity (V_{tmax}), radial velocity at inlet height (V_{ro}), core radius (r_c), etc. in their definition are listed in Eq. (25) and Eq. (26).

$$S_2 = \frac{r_{up} \Gamma_{max}}{2 Q'_{out} h_o} \quad (25)$$

The definition of swirl ratio given by Eq. (25), is used by Refan and Hangan (2018) while Haan et al. (2008), Liu et al. (2015b) and Yuan et al. (2019) have used the definition given by Eq. (26).

$$S_3 = \frac{\pi r_c^2 V_{tmax}}{Q_{out}} \quad (26)$$

It can be readily noticed in equations from Eq. (22) to Eq. (26) that different terms (or variables) are used in the definition of swirl ratio. Therefore, it is hard to compare touchdown swirl ratio from different works of literature unless the values of touchdown swirl ratio are calculated according to a common definition. Hence, it is necessary first to derive conversion relations to convert the value of swirl ratio from one definition to another. The procedure followed to obtain the conversion relations is described in detail in section 5.3 below.

5.3 Conversion Relations for Swirl Ratio from One Definition to Another

Two terms, i.e. (a) circulation and (b) mass outflow rate are used frequently in several definitions of swirl ratio above. Thus, it is necessary to understand and simplify those terms first before conversion relations are derived.

(a) Circulation: Circulation (Γ) in the flow field is defined by closed path integral of dot product of velocity vector (\vec{V}) and a directed line segment (\vec{ds}) and is given by Eq. (27). As circulation is defined by a closed path integral, so, the magnitude of circulation depends on the chosen path.

$$\Gamma = - \oint \vec{V} \cdot \vec{ds} \quad (27)$$

If the chosen path is located at the edge of convergence region and is formed by the circumference of tornado chamber, then the computed value of circulation is called far field circulation and is denoted by Γ_{∞} . In a similar manner, if the chosen path is located at the location of maximum tangential velocity in the flow domain, then the computed value of circulation is called maximum circulation and is denoted by Γ_{\max} .

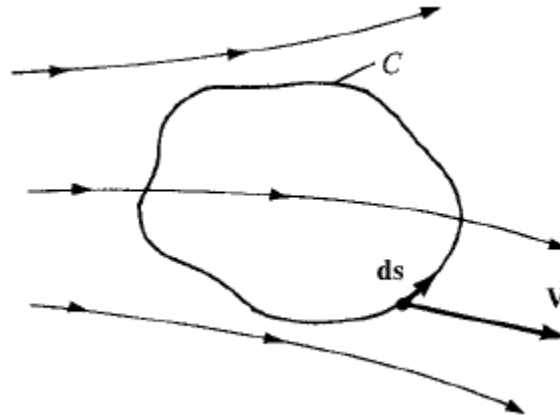


Fig. 13. Graphical representation of definition of circulation (From Anderson, 2014)

When the expression of closed path integral given in Eq. (27) is simplified, the far field circulation and the maximum circulation in a tornado chamber are respectively given by

$$\Gamma_{\infty} = 2\pi r_{up} V_{to} \quad (28)$$

$$\Gamma_{max} = 2\pi r_c V_{tmax} \quad (29)$$

(b) Mass flow rate: The mass flow rate (inflow and outflow) in a tornado chamber is defined by the dot product of velocity vector (\vec{V}) and the normal to the surface vector (\vec{A}) and is given by

$$Q = \vec{V} \cdot \vec{A} \quad (30)$$

The magnitude of the \vec{A} is the surface area. When the area $|\vec{A}|$ in Eq. (30) is considered at the inlet of tornado chamber, the obtained mass flow rate is called inflow rate and when it corresponds to the outlet of tornado chamber, the calculated mass flow rate is called the outflow rate. The mass inflow rate and mass outflow rate in a tornado chamber are given by Eq. (31) and Eq. (32) respectively.

$$Q_{in} = 2 \pi r_{up} h_o V_{ro} \quad (31)$$

$$Q_{out} = \pi r_{up}^2 V_{ro} \quad (32)$$

Using mass conservation principle, the mass inflow rate and outflow rate can be equated in a tornado chamber as the flow under consideration is incompressible flow. Thus, the volumetric outflow rate (Q_{out}) can be substituted by inflow rate (Q_{in}), i.e.

$$Q_{out} = 2 \pi r_{up} h_o V_{ro} \quad (33)$$

5.3.1 Derivation of Conversion Relations for Different Definitions of Swirl Ratio

As stated earlier, the swirl ratio definition given by Eq. (22) is taken as the reference and all other definitions are converted into a form like that given by Eq. (22).

(a) Conversion relation between S and S₁: Simplifying Eq. (24) by substituting Eq. (28) and Eq. (33) in Eq. (24), the following relation is obtained.

$$S_1 = \frac{V_{to}}{2 \left(\frac{h_0}{r_0} \right) V_{ro}} \quad (34)$$

Thus, it can be readily observed that the definition of swirl ratio defined by Eq. (22) and Eq. (24) leads to same expression (given by Eq. (22)) even though different combination of variables are used in the definition.

(b) Conversion relation between S and S₂: Simplifying Eq. (25) by substituting Eq. (29) and Eq. (33) in Eq. (25), the following relation is obtained.

$$S_2 = \frac{V_{tmax}}{2 \left(\frac{h_0}{r_c} \right) V_{ro}} \quad (35)$$

If we assume that the maximum tangential velocity (V_{tmax}) and core radius (r_c) can be expressed into tangential velocity component at inlet height (V_{to}) and the updraft radius (r_{up}) using multipliers α_v & α_r such that

$$\alpha_v = V_{tmax}/V_{to} \quad (36)$$

$$\alpha_r = r_c/r_{up} \quad (37)$$

and simplify Eq. (35) by substituting Eq. (36) and Eq. (37), the following expression is obtained.

$$S_2 = \frac{V_{to}}{2 \left(\frac{h_0}{r_0} \right) V_{ro}} \alpha_r \alpha_v = S \alpha_r \alpha_v \quad (38)$$

Thus, it can be readily observed that the value of swirl ratio calculated using Eq. (22) and Eq. (25) for the same flow condition would differ by a factor of ' $\alpha_r \alpha_v$ '.

(c) Conversion relation between S and S₃: Simplifying Eq. (26) by substituting Eq. (33) in Eq. (26), the following relation is obtained.

$$S_3 = \frac{\pi V_{tmax}}{2\pi \left(\frac{h_0}{r_c} \right) \left(\frac{r_{up}}{r_c} \right) V_{ro}} \quad (39)$$

Using similar assumption as made in (b) above and substituting Eq. (36) and Eq. (37) in Eq. (38), the following expression is obtained.

$$S_3 = \frac{V_{to}}{2 \left(\frac{h_0}{r_0} \right) V_{ro}} \alpha_r^2 \alpha_v = S \alpha_r^2 \alpha_v \quad (40)$$

Thus, it can be readily observed that the value of swirl ratio calculated using Eq. (22) and Eq. (26) for the same flow condition would differ by a factor of ' $\alpha_r^2 \alpha_v$ '.

The conversion relations worked out above implies that the value of touchdown swirl ratio evaluated using Eq. (25) and Eq. (26) would also differ by the same factors ' $\alpha_r \alpha_v$ ' and ' $\alpha_r^2 \alpha_v$ ' than that calculated from Eq. (22). So, in the following section, the value of touchdown swirl ratio of different tornado chambers is converted into a single consistent form given by Eq. (22) for comparison.

Tornado chambers with different geometrical configuration and flow generation mechanism exists in the literature. However, there still exists some similarities in the flow pattern of several tornado chambers. Accordingly, the reviewed tornado chambers were grouped into five major categories by identifying macroscale flow similarities such as the mechanism of flow entry into a tornado chamber, progression of flow inside the tornado chamber and exit of flow out of the tornado chamber.

5.4 Different Classification Categories of Tornado Chambers

Although there exists different configurations of tornado chambers in literature, each of them can be broadly classsified into five major types as shown in Fig. 14. The classification is based on flow generation mechanism of tornado vortex and outlet condition. The tornado chambers can be broadly categorized into (a) Side Opening System (SOS) (b) Top Full Opening System (TFOS)

and (c) Top Partial Opening System (TPOS) (d) ISU (Iowa State University type tornado chamber), and (e) WinDEEE dome.

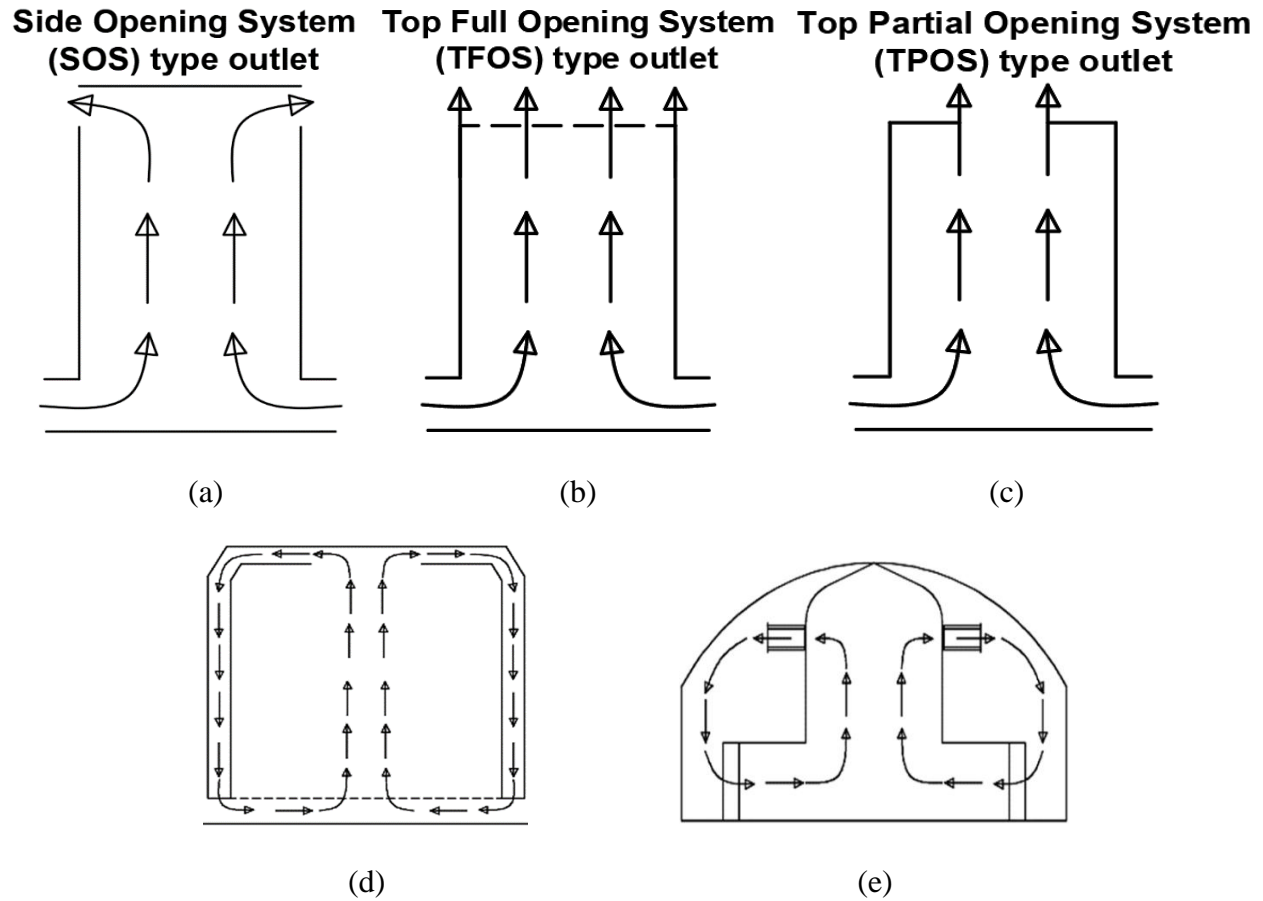
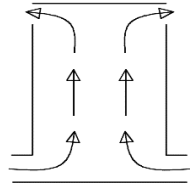
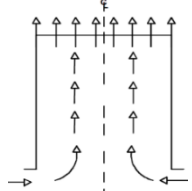
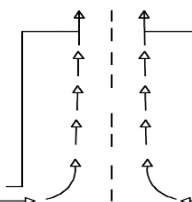
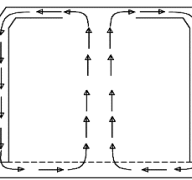
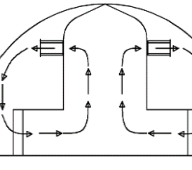


Fig. 14. Major classification category of tornado simulators (a) SOS (b) TFOS (c) TPOS (d) ISU tornado chamber (e) WinDEEE dome

In Table 5 below, the values of touchdown swirl ratio, the maximum tangential velocity, core radius, and elevation of core radius are reported from different tornado chambers, which are classified into 5 major categories. The value of touchdown swirl ratio is calculated according to a single consistent definition given by Eq. (22).

Table 5. Comparison of touchdown swirl ratio and other important vortex parameters from different tornado chambers

S. N.	Tornado Chambers	References	S_T	V_{tmax}/V_{ro}	r_c/r_{up}	z_c/r_{up}
1		a) Tang et al. (2018 a, b) – EXP b) Verma et al. (2020, 2021a) – CFD c) Harlow et al. (1974) - CFD	a) 0.22/0.36 b) 0.22/0.36 c) 0.30	a) - / - b) 3.7/3.5 c) -	a) 0.05/ - b) 0.04/ 0.11 c) 0.10	a)0.025/ - b)0.021/ 0.021 c) -
2		a) Verma et al. (2021c) - CFD b) Rotunno (1977) - CFD c) Verma et al. (2021a) - CFD d) Ward (1972) - EXP e) Kashefzadeh et al. (2019) –CFD	a) 0.40 b) ≈ 0.40 c) 0.45 d) 0.48 e) 0.50	a) 4.9 b) - c) 3.8 d) - e) 5.0	a) 0.07 b) 0.22 c) 0.12 d) 0.21 e) 0.12	a) 0.034 b) - c) 0.048 d) - e) 0.028
3		a) Church et al. (1977) – EXP b) Verma et al. (2021c)-CFD c) Verma et al. (2021c)-CFD d) Gillmeier (2019) - EXP e) Liu et al. (2015b) - CFD	a) 0.34 b) 0.45 c) 0.60 d) 0.69 e) 4.42	a) 3.8 b) 6.7 c) 9.6 d) 4.7 e) 6.0	a) 0.24 b) 0.07 c) 0.06 d) 0.15 e) 0.16	a) 0.177 b) 0.048 c) 0.078 d) 0.075 e) 0.095
4		a) Yuan et al. (2019) - CFD b) Haan et al. (2008) - EXP	a) 1.46 b) 2.23	a) 6.3 b) 6.0	a) 0.19 b) 0.12	a) 0.024 b) -
5		a) Karami et al. (2019) & Refan et al. (2018) - EXP	a) 1.96	a) 1.9	a) 0.19	a) 0.089

The major observations and conclusions drawn from Table 5 are summarized below:

1. Different categories of tornado chambers have different range for values of touchdown swirl ratio. This implies that different categories of tornado chambers produce different kind of tornado vortices (or different flow structures) of tornado vortices at similar value of swirl ratio unless the values are expressed according to a common definition.
2. The SOS category of tornado chambers have the lowest value of touchdown swirl ratio.

Following the trend of SOS category of tornado chambers, the next in the list comes the

TFOS category of tornado chambers with S_T values clustered around 0.45-0.48. The TPOS category of tornado chambers have higher values of touchdown swirl ratio than TFOS category.

3. In the TPOS category of tornado chamber, the value of touchdown swirl ratio for Liu and Ishihara (2015a) is extraordinarily high. In the tornado chamber model used by Liu and Ishihara (2015a), the circulation provided to inflow at the inlet gets diffused in a large region of space due to expansion of air as it progresses above the updraft hole in course of its upward motion. Due to diffusion of circulation provided at the inlet, it is suspected that the value of touchdown swirl ratio may have become very high.
4. Lastly, the ISU tornado chamber and WindEEE dome take the bottommost places in Table 5 with significantly higher value of touchdown swirl ratios compared to the previous categories.
5. For ISU tornado chamber, it may seem at a brief glance that touchdown swirl ratio from CFD model to experimental chamber vary significantly. Further attempts were made to understand the cause of deviation and it is suspected that (a) different vane angles at touchdown (30° for Yuan et al., 2019 and 35° for Haan et al., 2008) and (b) streamlining of vanes and ducts in Yuan et al. (2019), may have been the major causes of variation in value of touchdown swirl ratio. Swirl ratio is directly proportional to tangent of vanes angles, thus, if we scale the magnitude of touchdown swirl ratio from Yuan et al. (2019) by the ratio $\tan 35^\circ / \tan 30^\circ$, the new S_T value for Yuan et al. (2019) is obtained as $S_T = 1.8$. Thus, previously observed deviation is reduced significantly. The process of streamlining tends to have a smoothing effect on flow transport phenomena. So, streamlining of vanes and ducts may have been another reason to lower the value of touchdown swirl ratio in

Yuan et al. (2019), thus some discrepancies have been noticed between the CFD model and experimental touchdown swirl ratio of ISU tornado chamber.

6. Finally, touchdown swirl ratio for WindEEE dome is also significantly higher than other categories. In WindEEE dome, fans are located very far from the updraft section which tends to diffuse the circulation supplied at the inlet of tornado chamber and the size of outlet to the size of updraft is also very low ($\approx 0.064 - 0.18$). It is suspected that due to those reasons the value of touchdown swirl ratio in WindEEE dome is significantly higher than other tornado chambers.

It can also be noticed from Table 5 that the value of touchdown swirl ratio shows variation within a given classification category of tornado chamber. For instance, in TPOS category, the value of touchdown swirl ratio varies in a wide range from 0.34 to 4.42. Thus, attention was now fixed to geometrical details (total height and size of outlet) of tornado chamber and the effect of total height and outlet size (outlet diameter) on important vortex parameters was investigated next.

5.5 Effect of Variation in Geometry of Tornado Chambers on Touchdown

Tornado chambers differ from one to another with regards to geometrical features and dimensions such as the total height (H), inlet height (h_o), size of updraft radius (r_{up}), ceiling height, size (diameter) of outlet, mass outflow rate via exhaust, etc. It is not practical to study the effect of variation of each of those geometrical details as it would demand an enormous number of parametric case studies by varying one geometric aspect (such as total height) while keeping other geometrical dimensions same. Thus, two major geometrical dimension of tornado chamber, i.e. (a) total height of tornado chamber (H) and (b) diameter of outlet (D_{out}) are identified and chosen for parametric study.

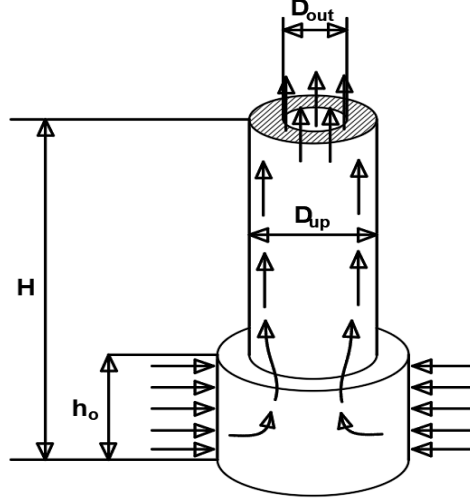


Fig. 15. Demonstration of inlet height (h_o), total height (H), updraft diameter (D_{up}) and outlet diameter (D_{out}) of a tornado chamber considered in parametric variation study

As the effect of variation of total height and diameter of outlet can be readily observed in TFOS and TPOS category of tornado chambers, thus, TFOS and TPOS category of tornado chambers are chosen for the parametric case studies. The variation of total height of tornado chamber on the important vortex parameters is studied using TFOS type chamber and later the opening at the top of TFOS type tornado chamber will be gradually reduced (resulting in TPOS type tornado chamber) to study the effect of variation of outlet diameter on touchdown.

5.5.1 Effect of Variation of Total Height on Important Vortex Parameters

Gairola and Bitsuamlak (2019) have proposed a simplified tornado chamber with a height of $15h_o$ to represent tornado flow field of the major experimental tornado chambers, i.e. VorTECH, ISU tornado chamber and WinDEEE dome. Hence, in this work, the total height of tornado chamber with $15h_o$ was chosen as a base case and then the total height was gradually increased to $18h_o$ and $21h_o$ to understand the effect on important vortex parameters.

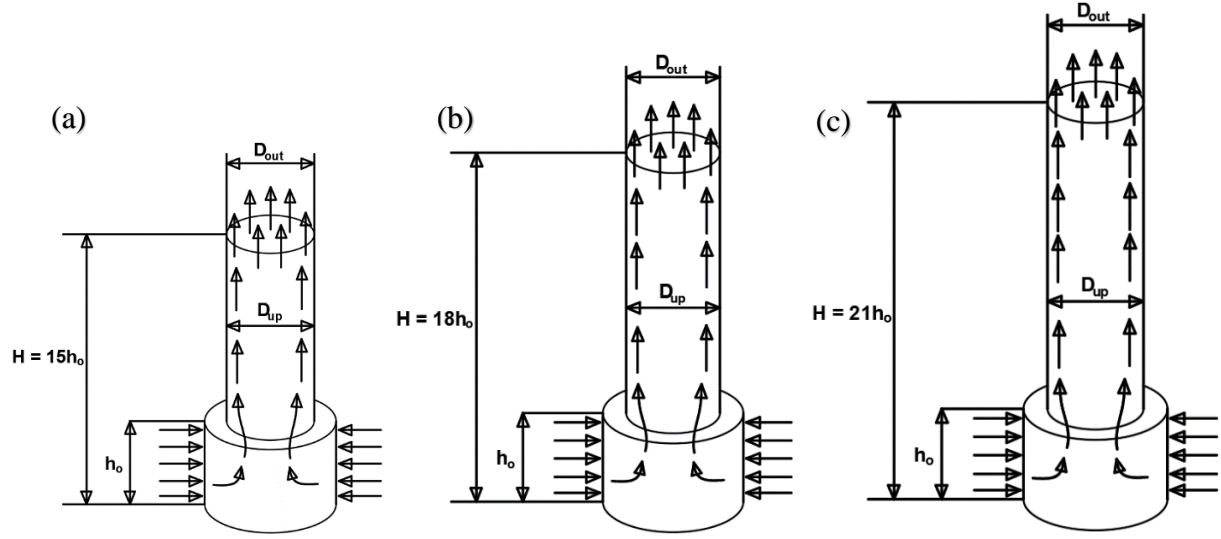


Fig. 16. CFD Tornado chambers with different total heights to study the effect of variation of total height on touchdown (a) $H = 15h_o$ (b) $H = 18h_o$ (c) $H = 21h_o$

The velocity vector plot along with pressure contour in the background for flows before, during and after touchdown are shown in Fig. 17 when the total height for tornado chamber is kept at $H = 15h_o$. Similar plots follow in Fig. 18 and Fig. 19 for the total height of tornado chamber maintained at $H = 18h_o$ and $H = 21h_o$ respectively.

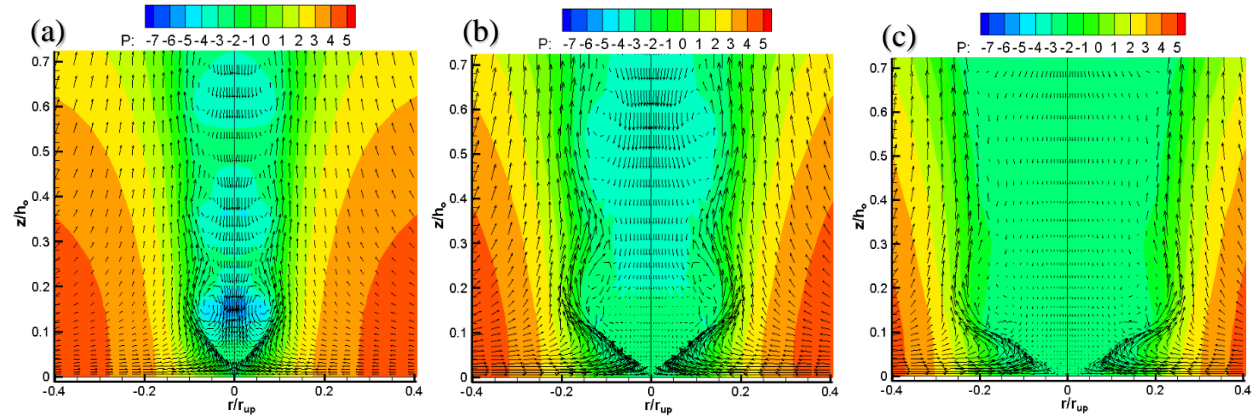


Fig. 17. Velocity vector plot with pressure contour in the background for total height of tornado chamber $15h_o$ (a) $S = 0.29$ (before touchdown) (b) $S = 0.45$ (during touchdown) (c) $S = 0.60$ (after touchdown)

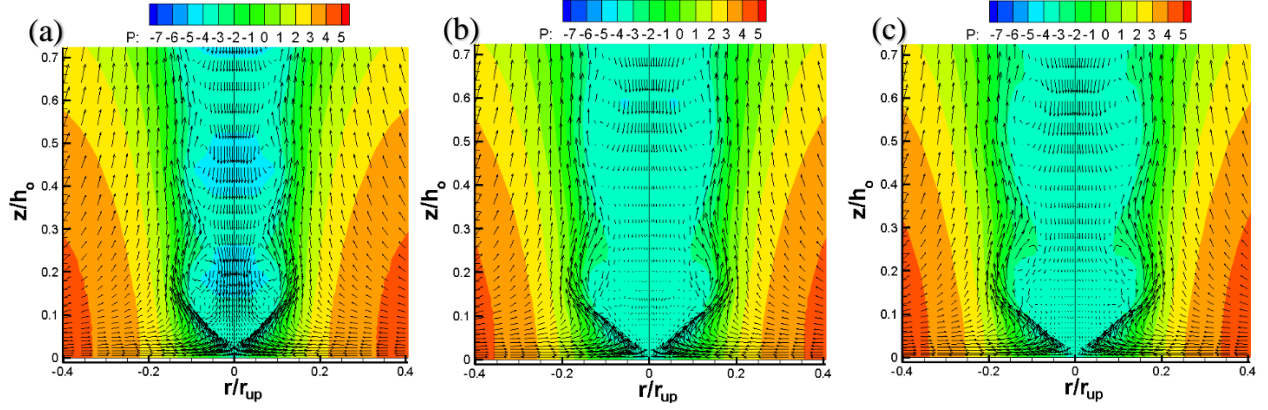


Fig. 18. Velocity vector plot with pressure contour in the background for total height of tornado chamber $18h_o$ (a) $S = 0.35$ (before touchdown) (b) $S = 0.43$ (during touchdown) (c) $S = 0.45$ (after touchdown)

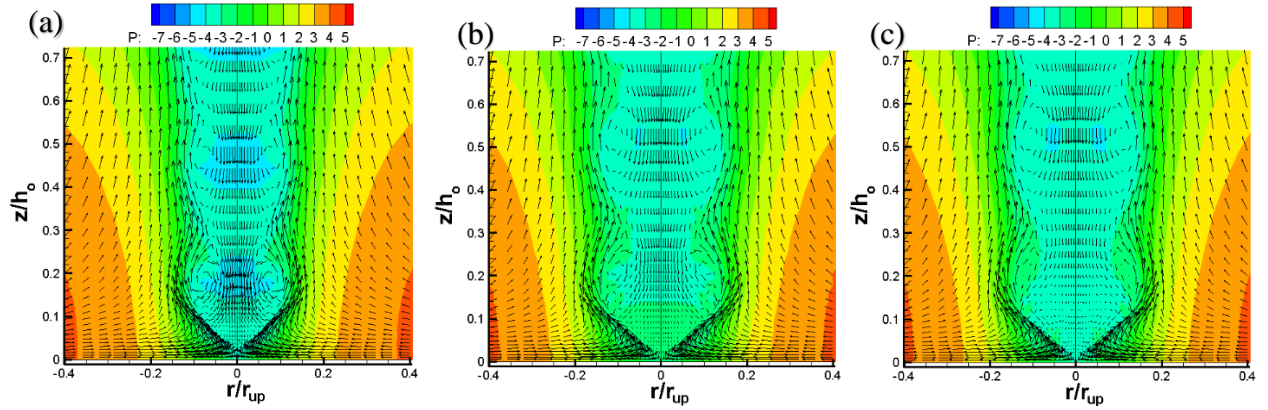


Fig. 19. Velocity vector plot with pressure contour in the background for total height of tornado chamber $21h_o$ (a) $S = 0.35$ (before touchdown) (b) $S = 0.41$ (during touchdown) (c) $S = 0.42$ (after touchdown)

The values of touchdown swirl ratio for the tornado chamber with total height $15h_o$, $18h_o$ and $21h_o$ were obtained at 0.45, 0.43 and 0.41 respectively and are shown in Fig. 17, 18 and 19 respectively. Further details about the effect of variation of height of tornado chamber on vortex touchdown can be obtained from section 3.2.2 of Verma and Selvam (2021b) and section 3.1.2 of Verma and Selvam (2021a). The values of touchdown swirl ratio and other important vortex parameters including the percentage change in touchdown swirl ratio with increase in total height of tornado simulator is shown in Table 6.

Table 6. Effect of variation of Total Height of tornado chamber on important Vortex Parameters

S.N.	H	S _T	% (ΔH)	% (ΔS_{TD})	V_{tmax}/V_{ro}	r_c/r_{up}	z_c/r_{up}
1	15h _o	0.45	-	-	3.8	0.119	0.048
2	18h _o	0.43	20	4.44	3.7	0.113	0.052
3	21h _o	0.41	40	8.89	3.6	0.107	0.049

From Table 6, two conclusions can be drawn, i.e. (a) the value of touchdown swirl ratio decreases with increase in total height of tornado simulator and (b) large changes in total height of tornado simulator can only produce a small change in value of touchdown swirl ratio (For instance, in either of the cases with total height as 18h_o and 21h_o in Table 6, the change in value of touchdown swirl ratio is only about 20% of change in total height of the tornado chamber). Similarly, the maximum tangential velocity as well as the core radius of tornado vortex are found to be decreasing with increase in total height of tornado chamber. However, any specific trend is not observed for the elevation of maximum tangential velocity as it increases first when height of tornado chamber is increased from 15h_o to 18h_o and then decreases when total height is increased further from 18h_o to 21h_o.

5.5.2 Effect of Variation of Outlet Diameter on Touchdown

The TFOS category of tornado chamber was considered as a base case with fully open outlet at the top of tornado chamber, i.e. with outlet diameter as $D_{out} = D_{up}$. Later, the diameter of outlet was gradually decreased to $D_{out} = 0.75D_{up}$ and $D_{out} = 0.50D_{up}$ (resulting in TPOS type tornado chamber) to understand the effect of reduction in outlet size of tornado chamber on touchdown. Further details with velocity vector plot along with pressure contour in the background for flows before, during and after touchdown for different outlet sizes of the tornado simulator can be obtained from section 3.2.1 of Verma and Selvam (2021b).

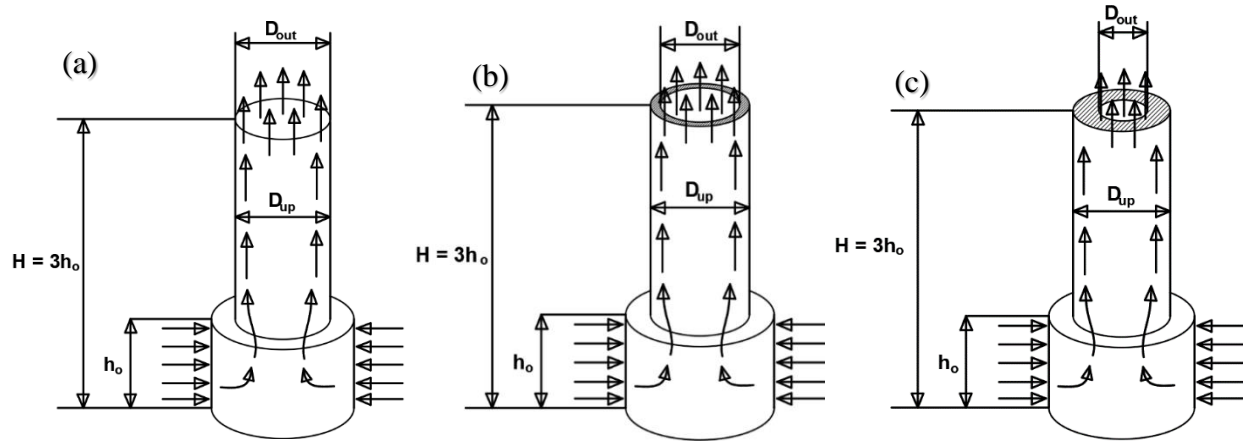


Fig. 20. CFD Tornado chambers with different diameter of outlet to study the effect of variation of outlet diameter on touchdown (a) $D_{out} = D_{up}$ (b) $D_{out} = 0.75D_{up}$ (c) $D_{out} = 0.50 D_{up}$

The values of touchdown swirl ratio for tornado chambers with outlet diameter of D_{up} , $0.75D_{up}$ and $0.50D_{up}$ were obtained at 0.40, 0.45 and 0.60 respectively. The values of touchdown swirl ratio and other important vortex parameters including the percentage change in touchdown swirl ratio with decrease in outlet diameter of tornado chamber is shown in Table 7.

Table 7. Effect of variation of outlet diameter of vortex chamber on important vortex parameters

S.N.	D_{up}	D_{out}	D_{out}/D_{up}	S_T	% (ΔD_{out})	% (ΔS_T)	V_{tmax}/V_{ro}	r_c/r_{up}	z_c/r_{up}
1	$2h_o$	$2h_o$	1.00	0.40	-	-	4.9	0.073	0.034
2	$2h_o$	$1.5h_o$	0.75	0.45	25	12.5	6.7	0.067	0.048
3	$2h_o$	$1.0h_o$	0.50	0.60	50	50	9.6	0.063	0.078

From Table 7, two conclusions can be drawn, i.e. (a) the value of touchdown swirl ratio increases with decrease in outlet diameter of tornado chamber and (b) the change in touchdown swirl ratio with decrease in outlet diameter of tornado chamber is more pronounced than the former case (i.e. change of touchdown swirl ratio with increase in height of tornado chamber). Decreasing the size of outlet diameter increases the touchdown swirl ratio, the maximum tangential velocity, and the elevation of occurrence of maximum tangential velocity while decreases the core radius.

5.6 Summary and Conclusion

Different definitions of swirl ratio are reviewed and conversion relations are worked out to connect different definitions of swirl ratio. When the value of swirl ratio is expressed according to a single consistent definition, it is observed that different tornado chambers have different values of touchdown swirl ratio. Identifying the macroscale similarities in flow pattern of different tornado chambers, the reviewed tornado chambers are classified into 5 major categories. However, it is found that there exists variation in value of touchdown swirl ratio within a category of tornado chambers (for instance, in TPOS category from Table 5, S_T varies from 0.34 to 4.42). So, attention is provided to study the effect of variation of geometric features (total height and outlet diameter) of tornado chamber on touchdown and other important vortex parameters. The conclusions drawn from literature review and parametric variation study are summarized below.

1. Different tornado chambers have different values of touchdown swirl ratio when touchdown swirl ratio is evaluated based on a single consistent definition of swirl ratio.
2. Among the different classification categories of tornado chamber, the SOS category of tornado chambers have the lowest value of touchdown swirl ratio followed by TFOS and TPOS categories. As compared to other tornado chambers, ISU tornado chamber and WindEEE dome have higher value of touchdown swirl ratio. Thus, the SOS category of tornado chamber seems to be the most efficient tornado chamber configuration for producing a touched-down tornado vortex.
3. TFOS and TPOS categories of tornado chambers have similar flow generation mechanism. However, some variation in the values of touchdown swirl ratio was observed in TFOS and TPOS categories of tornado chamber. So, attention was then fixed to understand the effect

of geometric variations (such as variation of total height and size of outlet of tornado chamber) on touchdown and other important vortex parameters.

4. It was observed that the value of touchdown swirl ratio decreases with increase in total height of tornado chamber and large changes in total height of tornado chamber can only produce a small change in value of touchdown swirl ratio.
5. Similarly, the value of touchdown swirl ratio increases with decrease in outlet diameter of tornado chamber and the change in touchdown swirl ratio with decrease in outlet diameter of simulator is more pronounced than that with the increase in height of tornado chamber.
6. Overall, it is observed that decreasing the outlet diameter of tornado chamber has a stronger effect on the wind field of tornado vortex than increasing the total height of chamber.

Chapter-6: Validation of Tornado-induced Pressures on Building and Effect of Size of the Building Model on Induced Pressures

6.1 Introduction

Numerous studies have been carried out both on the experimental as well as on the CFD side, yet there seems to be quite a lot of variation in pressure and force coefficients induced by tornado-like vortex on buildings from different work of literature. Consequently, it is hard for an engineer/designer to make a reasonable estimate of wind loads due to tornado-like winds for designing buildings in tornado-prone areas. In addition, there is no well-established procedure for estimating tornado-induced wind loads on buildings (like that of straight-line winds) in ASCE 7-16 or other relevant building codes and load standards. The pressure and force coefficients differ from one study to another on the experimental side (Refer Table 2 & Table 3 in Chapter - 2) whereas on the computational side, tornado-induced pressures lack comparison and/or validation with experiments. Thus, in this work, the wind field and the induced pressures on buildings obtained from the CFD model are compared/validated with TTU experimental measurements. This would provide greater confidence in the estimated pressure coefficients evaluated from the CFD model. However, in this work, the interaction of wind field of a stationary tornado-like vortex with building model is considered instead of a translating one. Even though the full-scale tornadoes are translating in nature, the interaction of wind field of a stationary tornado-like vortex with building placed at different locations can still provide valuable insights on the flow physics and forces induced by tornado-like vortex on a building. This is because the interaction of a stationary tornado-like vortex with building can still be viewed as the interaction with a translating tornado-like vortex at some particular time instant. Thus, in this section, the pressures induced by tornado-

like vortex on the building from CFD model are compared/validated with TTU experimental measurements.

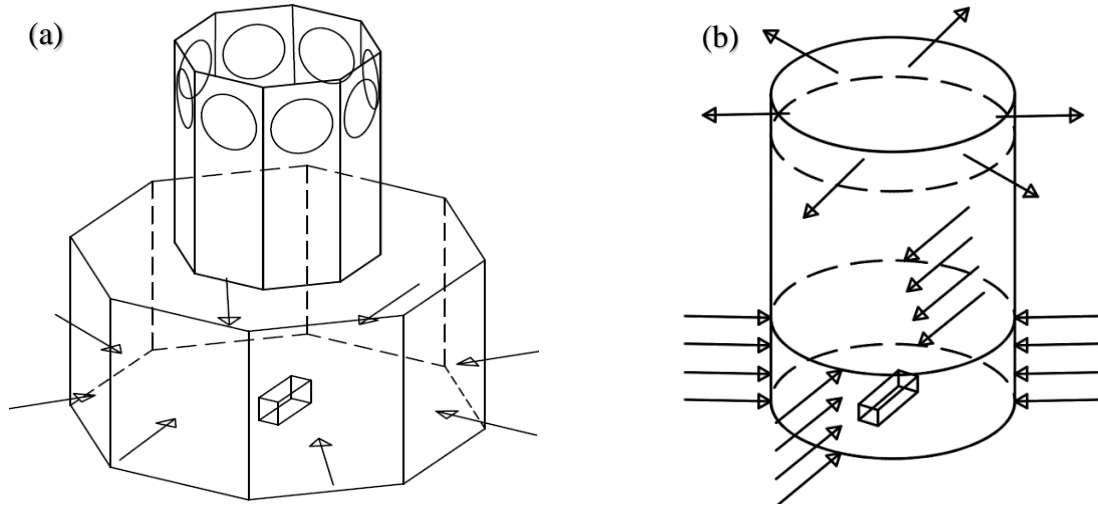


Fig. 21. (a) Experimental tornado simulator VorTECH at Texas Tech University (b) Simplified CFD tornado simulator Model

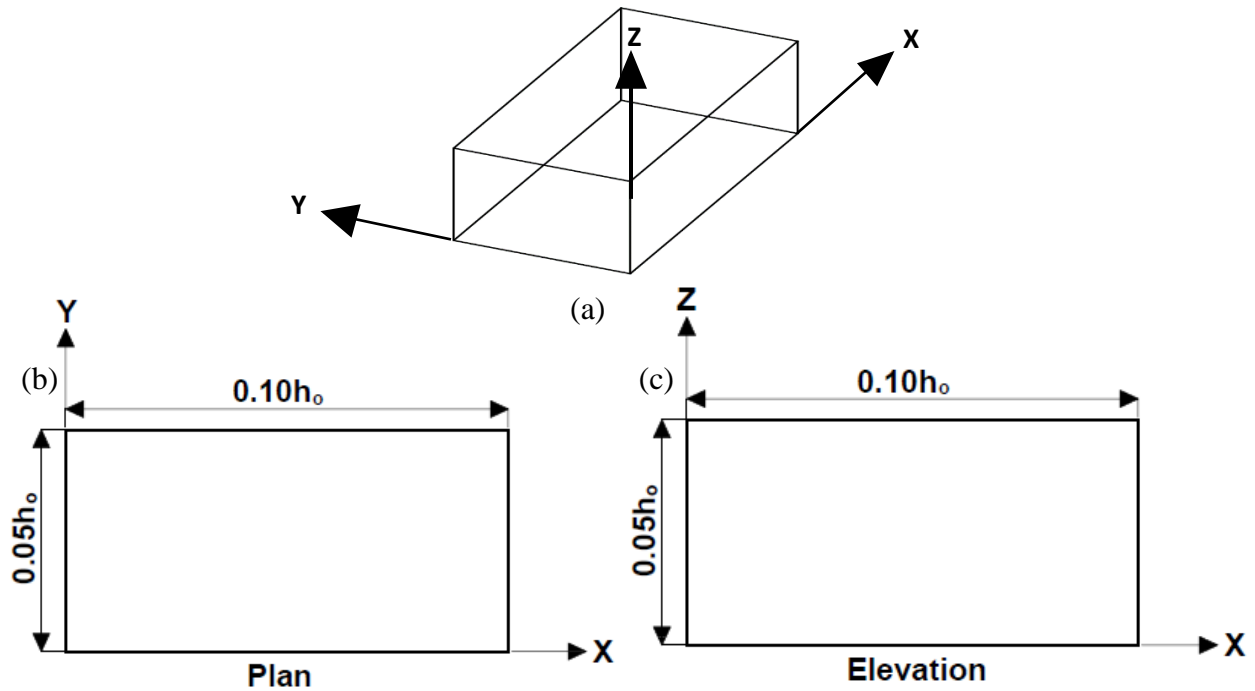


Fig. 22. (a) 3D sketch of building model (b) 2D sketch of building – Plan (c) 2D sketch of building model – Elevation

On the other hand, different sizes/scales of building models are considered in different work of literature while evaluating the pressures on the building due to tornado-like vortex (Refer Table-3 in section 2.7). Different sizes or scale of buildings used to quantify wind loads on the building can affect the magnitude of induced pressures and forces on building. Alrasheedi and Selvam (2011) studied the influence of plan area of building on the forces induced by tornado-like vortex and observed that the vertical uplift forces on the roof of building decreases with increase in plan area of the building. Gorecki and Selvam (2012) drew similar conclusion after studying the forces produced on a 2D cylinder using different sizes of tornado. Although it is evident from these studies that the size of building relative to tornado-like vortex can influence the interpretation of induced pressures and forces on the building but any guidelines for selecting the size or scale for a building model was not provided in those studies. Thus, in this chapter (specifically in section 6.4), the criterion for selecting the size of building relative to the core of tornado-like vortex proposed by Kikitsu and Okuda (2016) is discussed in detail and the comparison of pressures induced by tornado-like vortex on two different sizes of the building model is also presented.

Before discussing the results on validation of wind-induced pressures on building from CFD model with TTU experimental results, the effect of grid resolution on the wind field of tornado-like vortex is presented. Some interesting results were observed (such as numerous suction vortices in the region of stretching cells in the mesh, different number of suction vortices as well as different location of suction vortices) while studying the wind field of a stationary tornado-like vortex interacting with the building model. Thus, different grids were used to check the influence of grid resolution and cell aspect ratio on the formation of suction vortices and other relevant flow parameters (such as the near-surface tangential velocity and the ground pressure profile). The results from the study are documented next in section 6.2.

6.2 Effect of Grid Resolution on the Wind Field of Tornado-like Vortex without Building

The grid used for CFD computations can greatly influence the accuracy of solution obtained from numerical model. When the interaction of wind field of tornado-like vortex and the building model was studied at core radius location, multiple suction spots or vortices were observed as shown in Fig. 23. It was also noted that the vortices were formed in the regions comprising of stretched hexahedral cells. So, it was felt necessary to investigate whether if the formed multiple vortices are due to a complex interaction of tornado wind field with building or if the grid consisting of high aspect ratio cells introduce any artificial flow features or vortices in the flow field.

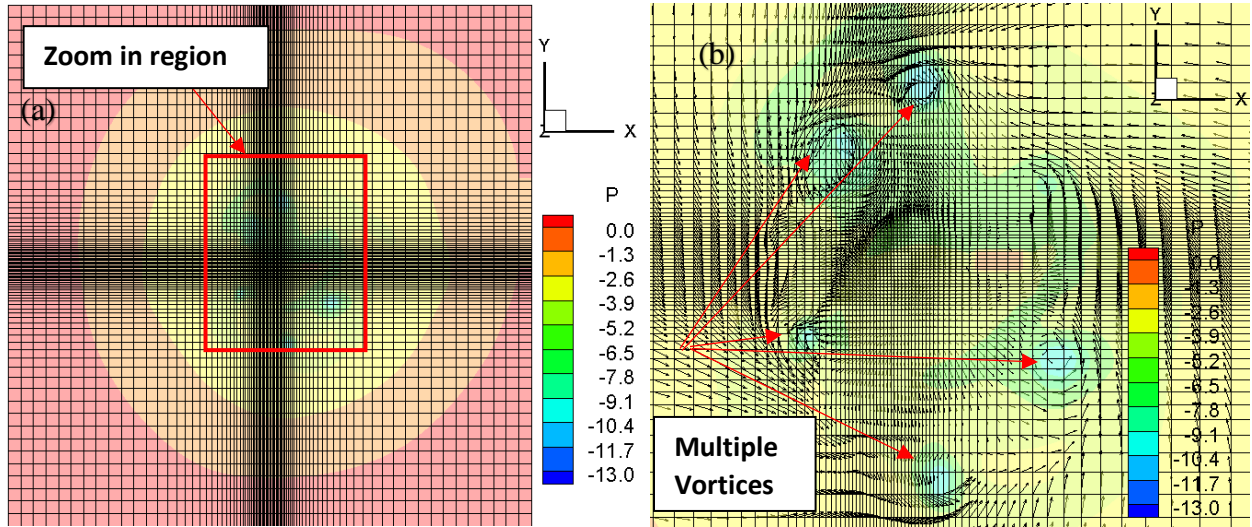


Fig. 23. (a) Pressure contour plot of tornado flow field with mesh in the background when building is located at core radius ($r_c/h_0 = 0.46$) for $S = 0.83$ (b) Zoom in region from Fig. 23 (a) near the core region of tornado vortex

6.2.1 Effect of High Aspect Ratio of Cells in Mesh

During the discretization of governing equations using Control Volume Method (CVM), the governing NS equations are integrated over a control volume, which are then simplified further to form a linear system of equations. The linear system of equations consists of terms with coefficients containing area of faces. So, the shape or the geometry of cells has an influence on the linear system of equations. Thus, if the cells have high aspect ratio, the linear system formed

becomes ill-conditioned and ill-conditioned systems are hard to solve/converge and are likely to diverge as well. Thus, high aspect ratio cells in the grid can be a potential problem leading to convergence issues as well as multiple vortices observed in Fig. 23.

In Fig. 23 (a), the pressure contour plot of the flow field around a building is shown when the building is placed at core radius location including the mesh in the background and in Fig. 23 (b), a close-up view of the core region (marked in Fig. 23 (a)) is shown including the mesh and velocity vectors in the background. It can be observed that multiple vortices are formed in the vicinity of center of CFD tornado simulator in Fig. 23 (b) instead of a central tornado core. Also, it should be noted that the vortices are formed in the region where the cells start stretching leading to higher aspect ratio hexahedral cells. Cell aspect ratio is an important mesh quality metric, and it is generally recommended to have a cell aspect ratio equal to or close to unity for stable and accurate numerical simulations. Thus, in the following text, three different grids are used to compare the wind field of tornado-like vortex and to assess if multiple vortices observed in Fig. 23 (b) are due to the influence of high aspect ratio cells in the grid.

The three grids used to assess the tornado wind field consists of the following:

- (a) A uniform grid with constant grid spacing in the X, Y and Z-direction with a cell size of $0.04h_0$ units. For simplicity and convenience in naming, the grid is designated as “Mesh-A”. The uniform grid spacing gives second order approximation as compared to close to linear approximation for variable grid spacing. However, the downside of this kind of grid is that it would result in a large grid with very high number of grid points, which increases computational cost and time by many folds.
- (b) A non-uniform grid with stretching cells from the center and with the maximum cell aspect ratio of 10, designated as “Mesh-B”. Using a grid of this type consisting of stretching cells

from the center, the computational cost and time can be reduced but high aspect ratio cells could lead to formation of ill-conditioned system of equations and furthermore lead to convergence issues as well as formation of artificial vortices as explained above.

- (c) A hybrid grid with uniform cells at the center (up to $0.78r_c$ units on either side of center of computational domain) followed by stretching cells with maximum cell aspect ratio of 5, designated as “Mesh-C”. Combining the arguments from (a) and (b) above, a third type of grid was made consisting of finely resolved uniform mesh in the center containing the core of tornado vortex and with stretching cells with maximum cell aspect ratio of 5 in the regions away from the center of tornado simulator. This grid combines the positive aspects of both the meshes, i.e., Mesh-A and Mesh-B as it consists of finely resolved uniform mesh at the center to capture important flow-critical phenomena and also eliminates the formation of ill-conditioned system of linear equations that can cause convergence issues. Furthermore, the computational cost and time is also optimized by coarser grid away from the center of tornado simulator.

The visualization of mesh in XY-plane for the 3 grids mentioned above is shown in Fig. 24 and the details of 3 different grids used to study the effect of grid resolution on tornado flow field is reported in Table 8.

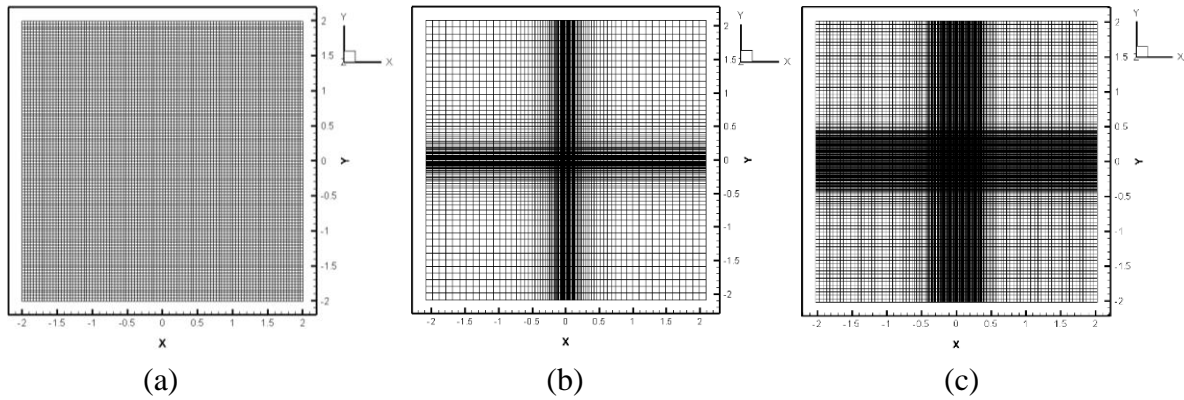


Fig. 24. Visualization of 3 different meshes in XY-plane (a) Mesh - A (b) Mesh - B (c) Mesh – C

Table 8. Details of grids to study effect of grid resolution on Tornado flow field without building

Grids	Mesh – A	Mesh – B	Mesh - C
Min. Grid Size	$0.04h_o$	$0.01h_o$	$0.01h_o$
Max. Grid Size	$0.04h_o$	$0.10h_o$	$0.05h_o$
Max. Cell aspect ratio	1	10	5
Cells in X-direction	101	91	157
Cells in Y-direction	101	91	157
Cells in Z-direction	151	81	134
Total Cell Count	1540351	670761	3302966

Using the three grids, the solution of flow field for swirl ratio case of $S = 0.83$ is obtained; the time series plot of pressure and the maximum tangential velocity at the bottom of CFD simulator is shown in Fig. 25. After non-dimensional time of $t^* = tV_{ro}/h_o = 20$ units, the pressure time-series plot seems to have developed a periodic waveform (particularly for Grid-B (green color) and Grid-C (blue color)). Similarly, the time-series plot of tangential velocity indicates a statistically steady state condition as the time-series is fluctuating around the value of $V_t/V_{ro} = 4.5$.

Thus, it is concluded that the flow field has attained a statistically steady state condition and there is no effect of initial transient phenomena in the solved tornado wind field after $t^* = 20$ units. Now, a qualitative inspection of tornado flow field is carried out by plotting the contour plots in XY-plane at the bottom plane of tornado simulator.

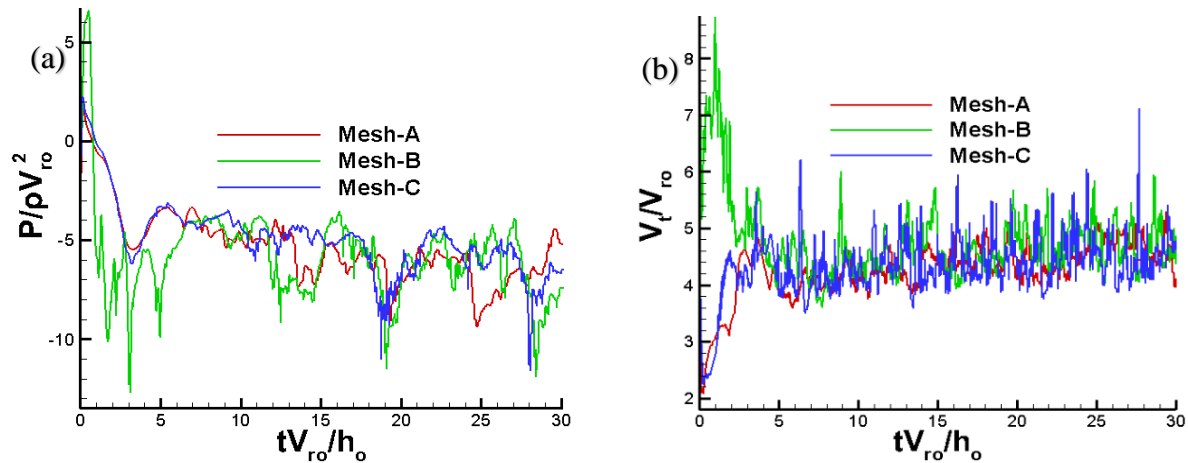


Fig. 25. Variation in time (a) pressure (b) tangential velocity at the center of tornado chamber in the ground plane

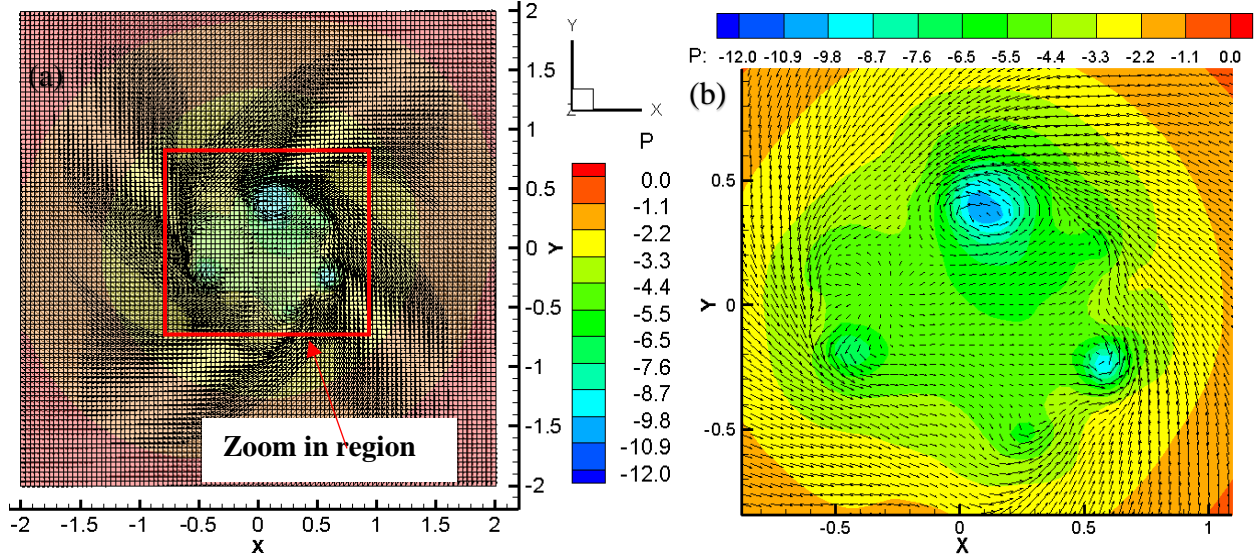


Fig. 26. (a) Pressure contour plots with mesh and velocity vectors in the background for $S = 0.83$ at $z/h_0 = 0.01$ units in XY-plane (tornado flow field only without building) (b) zoom in for Fig. 26 (a) with contour and velocity vectors in the background using Mesh – A

From Figs. 26 (b), 27 (b) and 28 (b), it can be concluded that the number of suction spots (or vortices) as well as their location varies from one mesh to another. For instance, using Mesh-A, tentatively 5 vortices are obtained whereas using Mesh-B, only 3 vortices are obtained. Similarly, using Mesh-C also, 3 vortices are formed; however, the location of vortices are different in Mesh-B and Mesh-C even when all the flow parameters and total simulation time are kept constant for all the 3 grids. Thus, it is concluded that different grids affects the flow field of tornado-like vortex to some extent even when all the simulations are carried out for the same final time ($t^* = 30$ units) with all the input parameters same except for the grid.

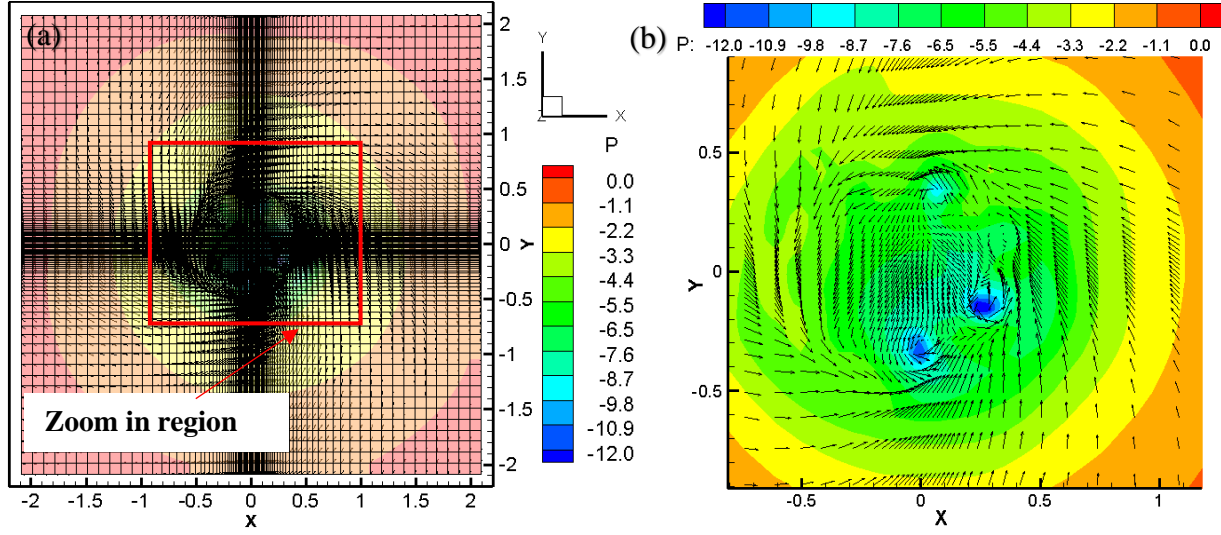


Fig. 27. (a) Pressure contour plot with mesh and velocity vectors in the background for $S = 0.83$ at $z/h_0 = 0.01$ units in XY-plane (tornado flow field only without building) (b) zoom in for Fig. 27 (a) with contour and velocity vectors in the background using Mesh - B

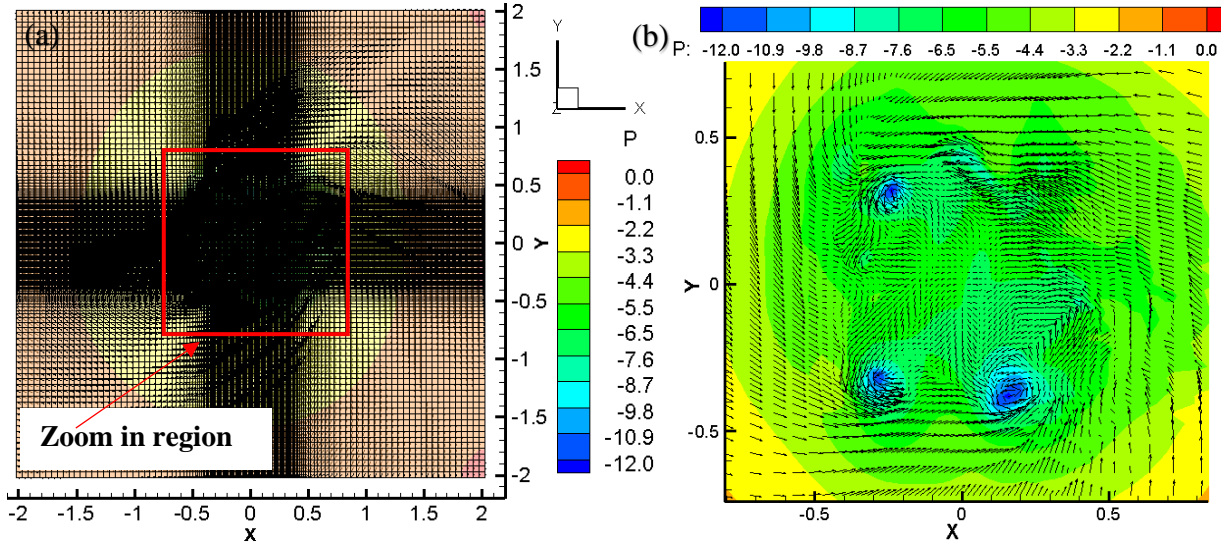


Fig. 28. (a) Pressure contour plot with mesh and velocity vectors in the background for $S = 0.83$ at $z/h_0 = 0.01$ units in XY-plane (tornado flow field only without building) (b) zoom in for Fig. 28 (a) with contour and velocity vectors in the background using Mesh - C

Now, some of the important features of tornado-like vortex such as the maximum tangential velocity (V_{tmax}), core radius (r_c), elevation of core radius (z_c) and minimum pressure (P_{min}) obtained from three different grids are reported in Table 9. It can be observed that the value of maximum tangential velocity from all the 3 grids tend to coincide around a value of $V_{\text{tmax}}/V_{\text{ro}} = 3.4$ units and similarly for the elevation of core radius at a value of $z_c/h_0 = 0.1$ units roughly. On the other hand,

some deviation in core radius is obtained from different grids as the value roughly differs by a margin of about 0.1 units from different grids. Similarly for the minimum pressure values, which differs by roughly 2 units in different grids. While on a minuscule level, the flow field differs from one grid to another; it can be concluded that the important vortex features generally point towards a similar value.

Table 9. Details of three different grids used to study grid resolution effect on tornado flow field

Grids	Total number of grid points	$V_{\text{tmax}}/V_{\text{ro}}$	r_c/h_o	z_c/h_o	$P_{\text{min}}/\rho V_{\text{ro}}^2$
Mesh-A	1540351	3.494095	0.739208	0.101512	-10.8160
Mesh-B	670761	3.581230	0.495324	0.077522	-14.5748
Mesh-C	3302966	3.325525	0.593047	0.113028	-12.7066

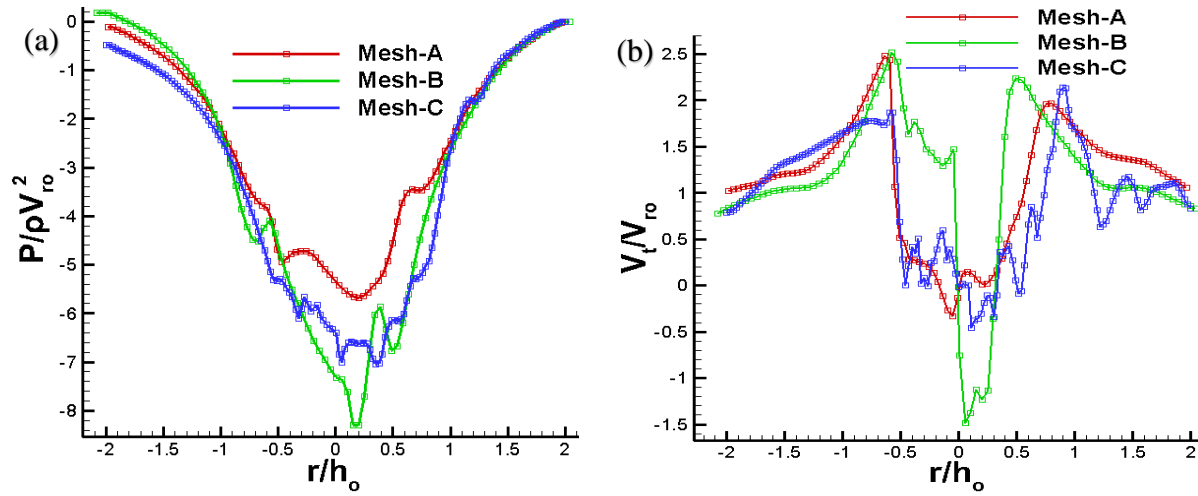


Fig. 29. Comparison of (a) ground pressure profile (b) tangential velocity profile between 3 grids (from XY-plane at $KM = 1$)

A grid independence study was also carried out by considering the 3 grids and the ground pressure profile as well as the tangential velocity profile in XY-plane at $z/h_o = 0.01$ units is compared between the grids as shown in Fig. 29. From the plots in Fig. 29, it can be again concluded that the pressure distribution and tangential velocity profile generally follows similar trend with some local variation of respective quantities (pressure and tangential velocity) at different locations. As Mesh-

C is the most-refined grid, thus, the deviation in profile from Mesh-A and B are compared with reference to Mesh-C in Table 10. The normalized root mean squared error (NRMSE) calculated using Eq. (20) for Mesh-A is 13.51% for pressure whereas 7.23% for tangential velocity whereas the corresponding values are 15.48% and 41.46% for Mesh-B.

Table 10. Comparison of NRMSE between different grids

Grids	NRMSE (Pressure profile)	NRMSE (Tangential velocity profile)
Mesh-A	13.51%	7.23%
Mesh-B	15.48%	41.46%
Mesh-C	-	-

Based on the qualitative analysis of flow field from different grids as well as the quantitative analysis of NRMSE from different grids, it is concluded that the grid does influence wind field of tornado-like vortex on a minuscule scale (different number of suction vortices at different locations). However, the important tornado vortex parameters from different grids generally agree with each other. Nonetheless, numerous suction vortices observed in Fig. 23 seem to be artificially created because of the grid with large aspect ratio cells. Thus, from different grids considered above, it is concluded that Mesh-C would be appropriate for further CFD computations (interaction of tornado flow field with building) as the core of tornado is contained within the uniform region extending up to $0.78r_c$ from the center of tornado simulator, where the important flow-critical phenomena are happening. A finely resolved uniform mesh at the center inhibits formation of ill-conditioned linear system of equations as well as inhibits any possible issues with convergence or formation of multiple vortices as observed in Fig. 23. Hence, Mesh-C is used for further analyses and calculations unless stated otherwise.

6.3 Validation of Induced Pressures on Building from CFD Model with TTU Simulator

The relative position of a building with respect to the center of tornado-like vortex greatly influences the magnitude of pressures induced by a tornado-like vortex on the building. Thus, in this section, the mean pressures induced by tornado-like vortex on a building placed at two radial locations, i.e., $r/r_c = 0$ and $r/r_c = 1.0$ are computed using the CFD model and compared with corresponding TTU experimental measurements.

As shown in Fig. 30 (a), the radial distances ($r = 0$ and $r = r_c$) are measured along the X-axis and the stationary tornado-like vortex is fixed at the center of tornado simulator (if vortex wandering phenomena is neglected). Similarly, in Fig. 30 (b), an exploded view of the building is shown. To estimate the wind loads due to a stationary tornado wind field interacting with the building model placed at different radial locations with respect to the center of the tornado simulator, the values of pressure coefficient (C_p) is computed as per Eqn. (41) below.

$$C_p = \frac{(P - P_{ref})}{0.5 \rho V_{t,max}^2} = \frac{(P^* - P_{ref}^*) \rho V_{ro}^2}{0.5 \rho V_{t,max}^2 V_{ro}^2} = \frac{(P^* - P_{ref}^*)}{0.5 V_{t,max}^2} \quad (41)$$

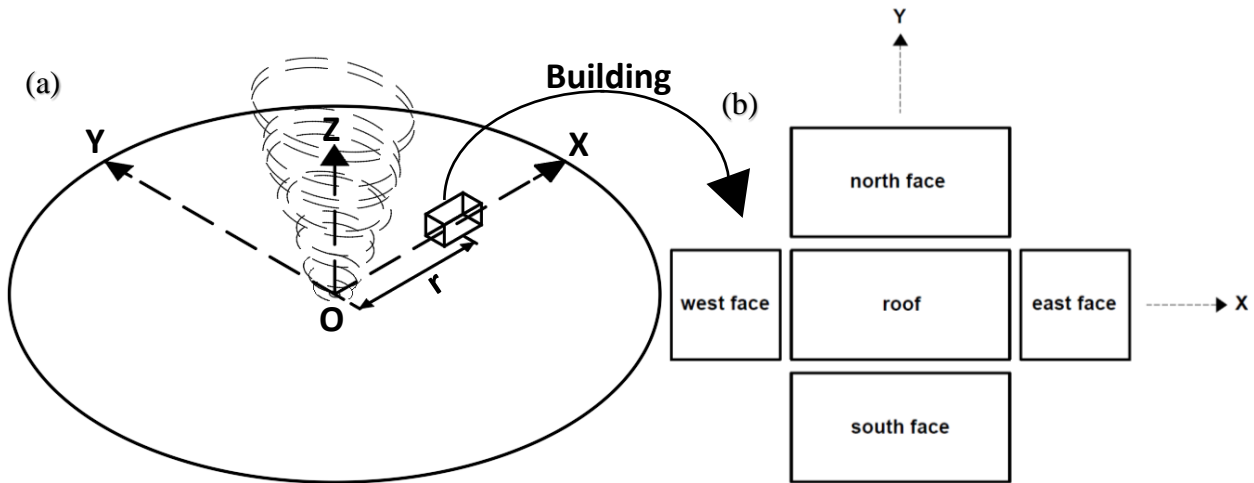


Fig. 30. (a) Schematic diagram of interaction of tornado wind field with the building when it is placed at different radial locations (r) along the X-axis (b) Exploded view of the faces of building

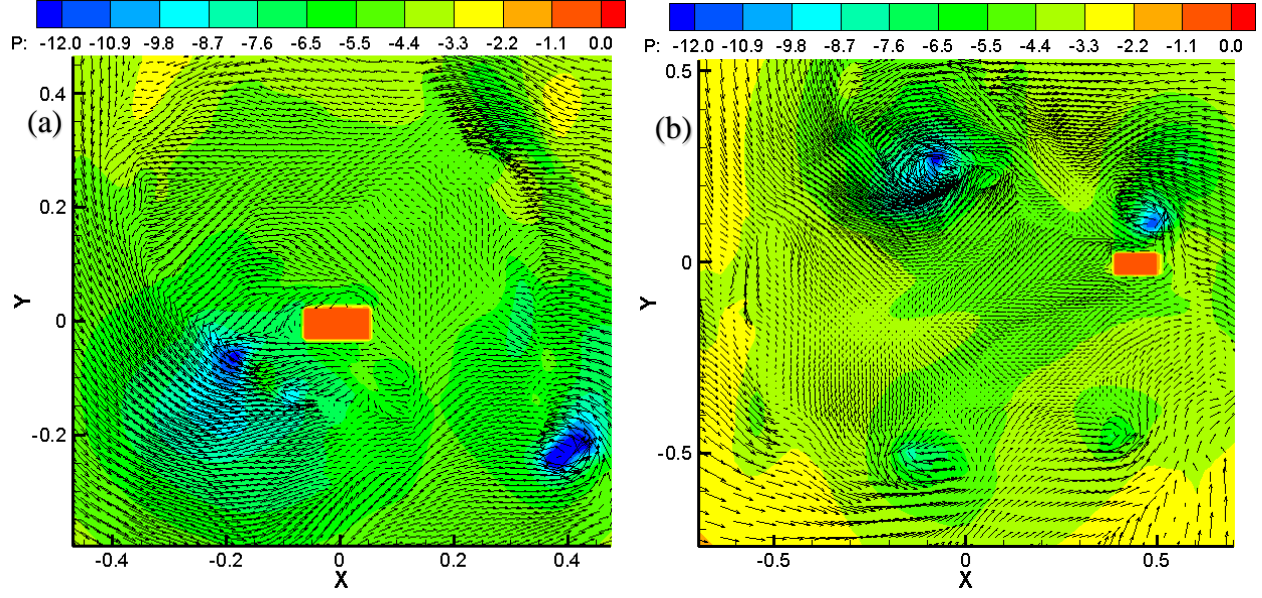


Fig. 31. Pressure contour plot around the building in XY-plane at $z = 0.01h_o$ when building is placed at (a) center of tornado chamber ($r/r_c = 0$) (b) core radius location ($r/r_c = 0.46$)

During CFD computations, the pressure in the domain is already deducted from the reference pressure value ($P_{ref}^* = 0$). So, to obtain the values of pressure coefficient, the resulting values from CFD computations are divided by $0.5V_{t,max}^2$. The reference velocity is taken as the maximum tangential velocity in the flow domain without the presence of building, which is the same as in TTU experiment. The value of maximum tangential velocity is obtained as $V_{t,max} = 3.33V_{ro}$.

6.3.1 Comparison of Mean C_p on Building for Different Radial Location of Building

In Fig. 32 below, the pressure coefficient (C_p) contour plots from CFD model is compared with TTU experiment. The comparisons are made for the swirl ratio (S) case of $S = 0.83$, which in both the experimental and CFD simulator represents a double-celled tornado-like vortex beyond touchdown. The value of pressure coefficient is calculated using Eq. (41) in which the relative pressure ($P^* - P_{ref}^*$) is already computed from CFD, which is then divided by $\frac{1}{2} V_{t,max}^{*2}$ (where $V_{t,max}^* = V_{t,max}/V_{ro} = 3.33$ is the maximum tangential velocity in the flow domain without the building) to

yield the value of pressure coefficient. Using maximum tangential velocity value of $V_{tmax}^* = 3.33$, the mean C_p contour plot as shown in Fig. 32 (a) is obtained.

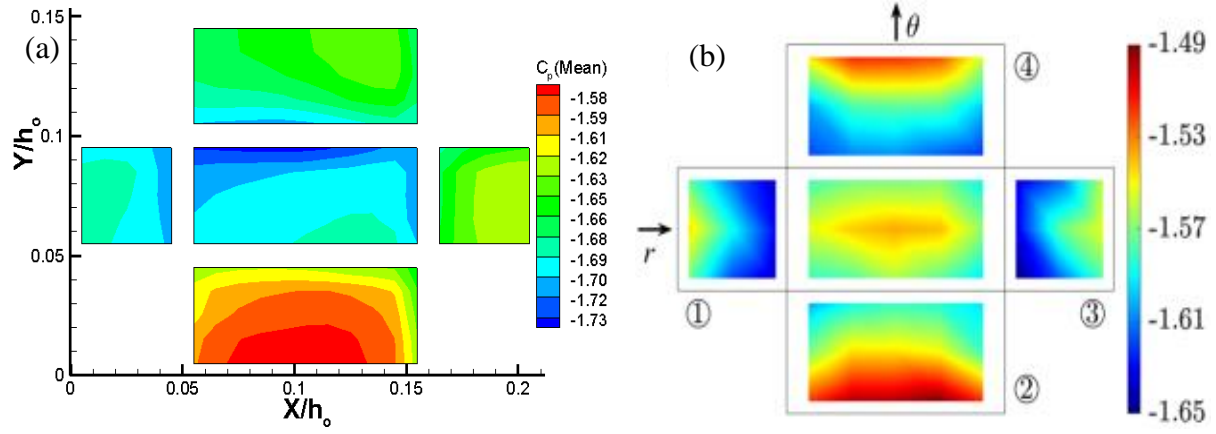


Fig. 32. Comparison of Mean C_p contour for swirl ratio (S) = 0.83 when building is placed at the center of tornado chamber (a) CFD (b) TTU Experiment

The values of mean pressure coefficient on the faces of the building shows reasonable agreement between the CFD model and the TTU experimental datasets. When the building is placed at the center of CFD tornado simulator, the mean C_p values range from -1.58 to -1.73, whereas that for TTU experiment, the corresponding C_p values range from -1.49 to -1.65. The values obtained from CFD agrees reasonably with the TTU experimental datasets except for some discrepancy, which may be due to slight variation in the magnitude of maximum tangential velocity, which is used for computing the pressure coefficient (C_p). As C_p depends on the square of maximum tangential velocity (V_{tmax}), so even a slight variation in V_{tmax} can strongly affect the values of C_p . Applying the same reasoning, it is suspected that the slight variation between the CFD results and TTU datasets may have occurred.

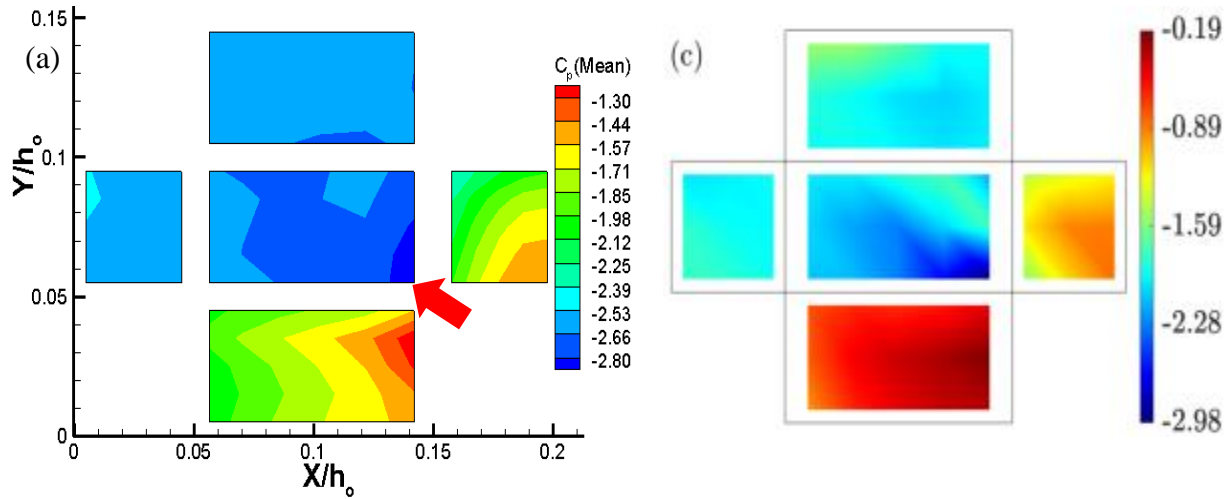


Fig. 33. Comparison of Mean C_p contour for swirl ratio (S) = 0.83 when building is placed at the location of core radius ($r_c/h_o = 0.46$) of tornado vortex for $S = 0.83$ (a) CFD (b) TTU Experiment

For the case when the building is placed at the location of core radius (Fig. 33), a good qualitative agreement in the C_p contour values can be noticed readily again. The minimum C_p occurs on the south-east corner of the roof (pointed by arrow pointers) with a magnitude of about -2.8 for CFD model whereas for TTU experiment, the magnitude of minimum C_p is about -2.98 at tentatively the same location as the CFD model. However, the range of pressure variation is different between the CFD model and TTU experiment; the range of mean C_p varies between -1.3 to -2.8 for the CFD model whereas for TTU experiment, the range varies between -0.19 to -2.98. The reason for such deviation is not very well understood at this time; however, a comparatively coarser grid at the location of core radius may have caused the deviation. In addition, the sparse distribution of measurement points on the faces of building as shown in Fig - C1 (b) (in Appendix C) may also have attributed to challenges in obtaining a high resolution of pressure measurements in the experimental work.

6.3.2 Comparison of Minimum C_p on Building for Different Radial Location of Building

During tornadic events, usually, roofs are blown off due to static pressure drop caused by tornadoes, so, it would be of engineering significance to determine the minimum values of C_p

when the building model is placed at different radial locations with respect to the center of tornado simulator. In Fig. 34, the C_p contour plots of minimum pressure obtained from CFD model are plotted when building is placed at two different radial locations, i.e., at $r/h_0 = 0$ in Fig. 34 (a) and $r/h_0 = 0.46$ in Fig. 34 (b). From the contour plots, it is deduced that the roof region and wall to roof connection are indeed the most critical parts of a building/structure which encounters enormous magnitude of suction forces on them (-2.9 in Fig. 34 (a) and -5.0 in Fig. 34 (b)) resulting in uplifting of roof and breach of the building envelope.

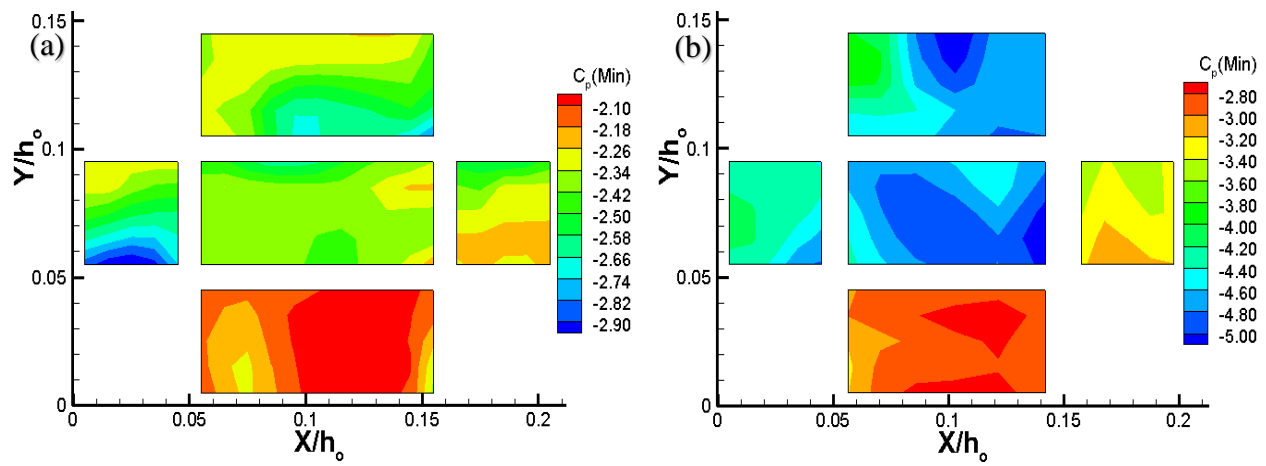


Fig. 34. Comparison of Minimum C_p on the faces of building for $S = 0.83$ when the building is placed at (a) the center of CFD tornado simulator (b) the core radius of CFD tornado simulator

Since the pressure coefficients on the faces of building show reasonable agreement between the CFD model and TTU experiment, it is concluded that a validated CFD model is obtained for studying the interaction of tornado-like vortex with building model. Furthermore, the study also shows that the roof region and parts of the building comprising of roof to wall connections are the most vulnerable parts of the building and susceptible to damage.

6.4 Comparison of Induced Pressure on Building due to Different Sizes of Building

As discussed in section 6.1, the size of building models used for vortex-building interaction studies in different work of literature can influence the magnitude and interpretation of pressures induced

by tornado-like vortices. In that regard, Kikitsu and Okuda (2016) proposed some guidelines on selecting the size of building as compared to the size of tornado-like vortex, which is discussed next in section 6.4.1.

6.4.1 Selection of Core Radius of Tornado-like Vortex with Respect to the Size of Building

Kikitsu and Okuda (2016) used different sizes, and scale of building model in experimental tornado-like wind simulator at Building Research Institute (BRI), Japan and concluded that different sizes/scale of building results in different pressures and force coefficients. They also proposed the idea of equivalent radius ($r_{eq} = \sqrt{BD}/\sqrt{\pi}$), which is the radius for a circle whose area is equivalent to the plan area (BD, where ‘B’ and ‘D’ are planar dimensions) of the structure. The scale ratio (R_r), which is the ratio of size of building relative to the core radius of tornado-like vortex is computed using (42).

$$R_r = \frac{1}{r_c} \sqrt{\frac{BD}{\pi}} \quad (42)$$

Based on Eq. (42), Razavi and Sarkar (2018) and Alipour et al. (2020) have selected the scale of building model in their work. Kikitsu and Okuda (2016) proposed to use the scaling ratio R_r less than 0.45 based on the comparison of load characteristics obtained from tornado simulator with Rankine vortex. However, it is pointed out that Rankine vortex model represents a tornado-like vortex primarily by the distribution of tangential velocity profile, but it is also well-understood now that wind field of tornado-like vortex comprises of all the 3 components, i.e., radial, tangential, and axial velocity components. The contribution of radial and axial velocity component is missed out in the Rankine vortex model, so, it might affect the proposition to use an effective building scaling ratio (R_r) of 0.45 or less while evaluating the loads exerted by tornado-like vortex on the buildings, thus, limiting the scope of the proposition.

6.4.2 Comparison of Pressure Coefficients Due to Different Sizes of Building

In this work, the effect of all the 3 velocity components on the wind field and on the induced pressures on building is accounted for by solving the 3D Navier-Stokes (NS) Equation. Two different sizes of building ($0.10h_o \times 0.05h_o \times 0.05h_o$ & $0.10h_o \times 0.10h_o \times 0.10h_o$) are considered to learn about the differences in magnitude of induced pressures on the building when the same tornado-like vortex interacts with building of different sizes. In addition, the range of C_p (max. C_p – min. C_p) for both the mean and the minimum pressure coefficient is computed for two cases, i.e., (a) when the building is located at the center of tornado simulator ($r/h_o = 0$) and (b) when the building is located at the core radius of tornado simulator ($r/h_o = 0.46$).

Table 11. Comparison of range of mean and the minimum C_p on the building of different sizes

Building Size	$r/h_o = 0$				$r/h_o = 0.46$			
	Mean C_p		Min. C_p		Mean C_p		Min. C_p	
	Min.	Max.	Min.	Max.	Min.	Max.	Min.	Max.
$0.10h_o \times 0.05h_o \times 0.05h_o$	-1.25	-0.96	-3.00	-2.03	-2.89	-1.20	-5.22	-2.65
$0.10h_o \times 0.10h_o \times 0.10h_o$	-2.30	-2.05	-7.33	-3.57	-2.58	-1.45	-6.79	-2.56

The pressure coefficients for all the different cases are included in Table 11. For the first building (with size $0.10h_o \times 0.05h_o \times 0.05h_o$), the scale ratio computed using Eq. (42) is 0.087 and for the second building (with size $0.10h_o \times 0.10h_o \times 0.10h_o$), the scale ratio is 0.123, which are both less than the critical value (0.45) suggested by Kikitsu and Okuda (2016). From Table 11, it can be observed that the range of mean pressure coefficient is almost the same for both the sizes of building when building is located at the center of CFD tornado simulator. However, the absolute value of mean C_p is roughly about 2 times for the building of size $0.10h_o \times 0.10h_o \times 0.10h_o$ as compared to the building of size $0.10h_o \times 0.05h_o \times 0.05h_o$. A similar trend is observed for the

minimum pressure coefficient when the building is placed at the center of CFD tornado simulator. This observation indicates that the induced pressures on the building can differ by about 100% when the building of different sizes or scales are used in a tornado simulator with all the relevant flow conditions remaining constant even when the scaling ratio (R_c) is significantly lower than the critical value of 0.45. Thus, it seems that maintaining a scale ratio (R_r) of less than 0.45 (or significantly lower than 0.45) may not be a sufficient criterion to eliminate the effect of the size or scale of a building model on induced pressure or load characteristics.

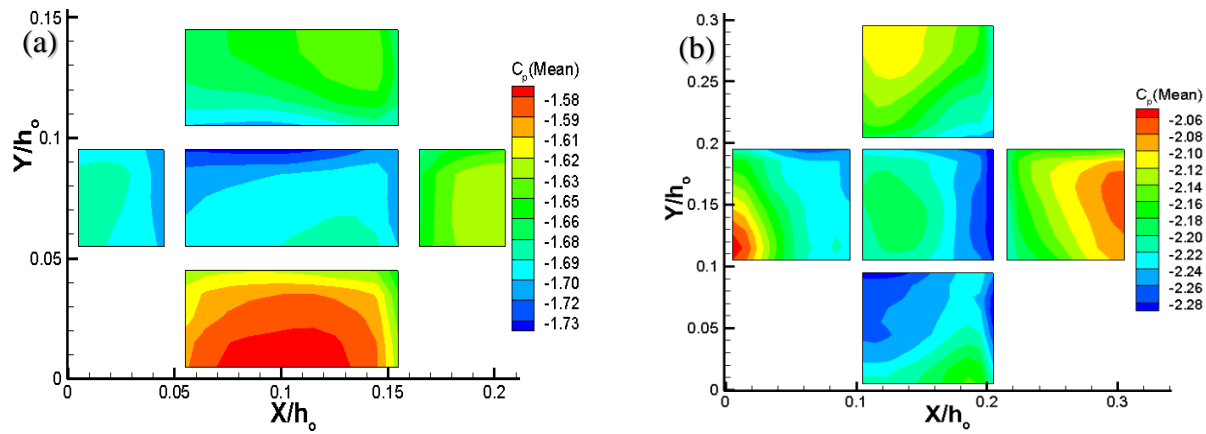


Fig. 35. Comparison of Mean C_p on the faces of building for $S = 0.83$ when the building is placed at the center of CFD tornado simulator (a) of size $0.10h_0 \times 0.05h_0 \times 0.05h_0$ (b) of size $0.10h_0 \times 0.10h_0 \times 0.10h_0$

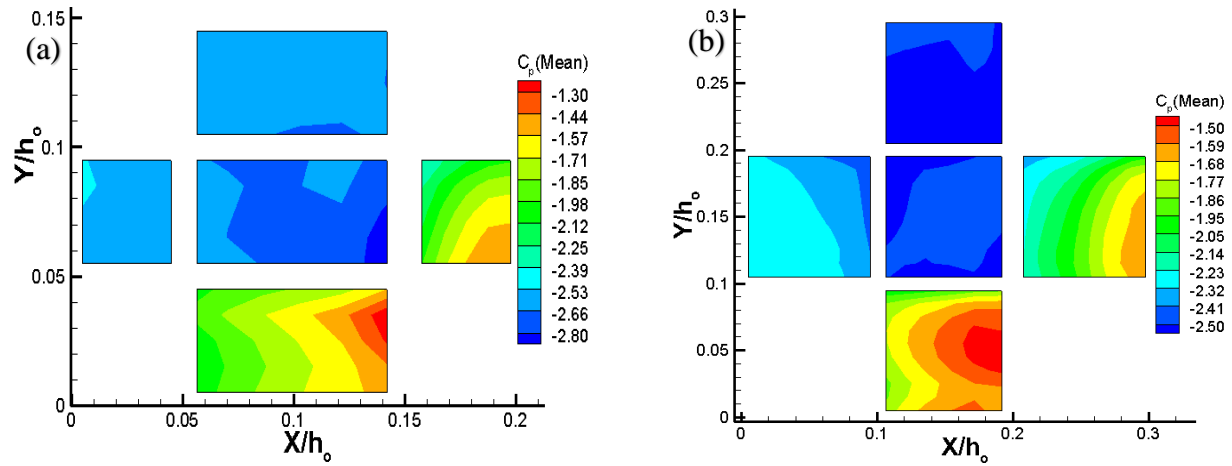


Fig. 36. Comparison of Mean C_p on the faces of building when the building is placed at core radius ($r_c/h_0 = 0.46$) for $S = 0.83$ in CFD tornado simulator (a) of size $0.10h_0 \times 0.05h_0 \times 0.05h_0$ (b) of size $0.10h_0 \times 0.10h_0 \times 0.10h_0$

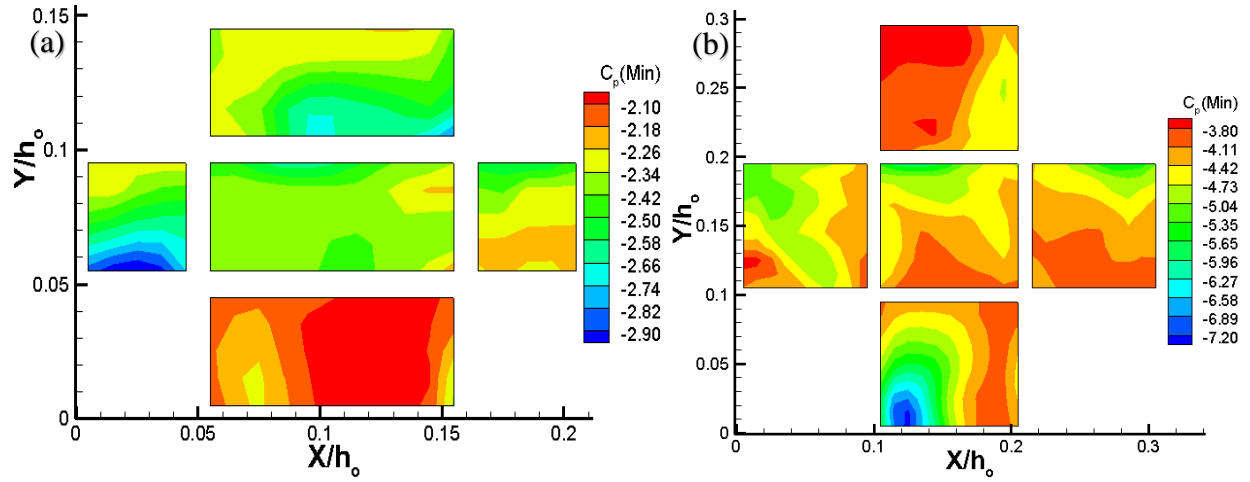


Fig. 37. Comparison of Min. C_p on the faces of building for $S = 0.83$ when the building is placed at the center of CFD tornado simulator (a) of size $0.10h_0 \times 0.05h_0 \times 0.05h_0$ (b) of size $0.10h_0 \times 0.10h_0 \times 0.10h_0$

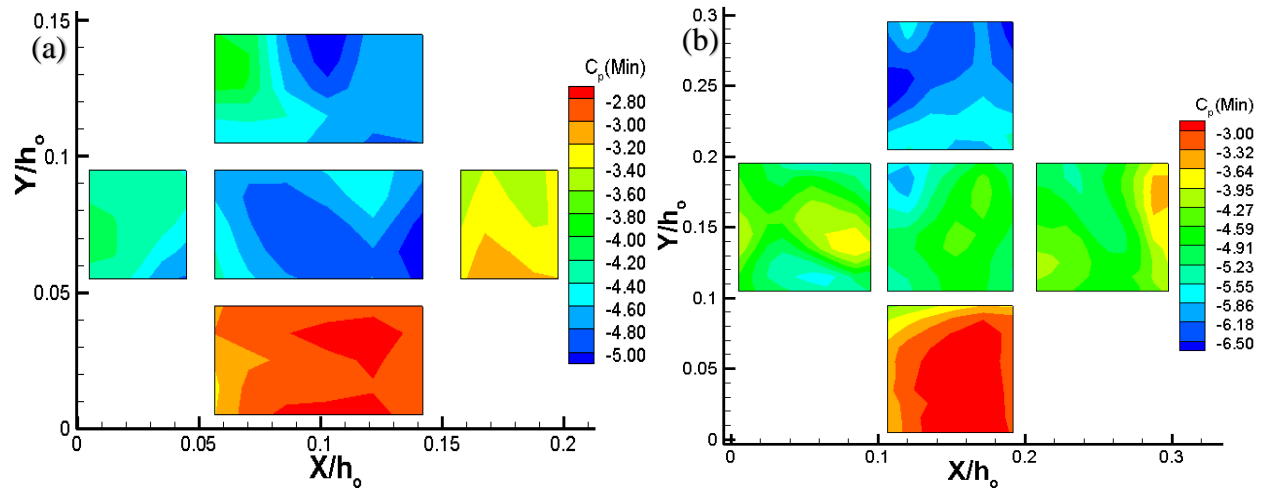


Fig. 38. Comparison of Min. C_p on the faces of building when the building is placed at core radius ($r_c/h_0 = 0.46$) for $S = 0.83$ in CFD tornado simulator (a) of size $0.10h_0 \times 0.05h_0 \times 0.05h_0$ (b) of size $0.10h_0 \times 0.10h_0 \times 0.10h_0$

For the case when the building is placed at core radius, the range of mean and the minimum C_p shows some variation; however, the absolute value of mean and the minimum C_p generally do not differ by a large margin. The absolute value of mean and the minimum C_p varies roughly about 3% to 30% in Table 11. So, it seems like the influence of size of the building on induced pressures is more pronounced when the building is fully engulfed inside the core of tornado-like vortex rather than when it is located at the outer core (core radius) of tornado-like vortex. The distribution

of mean C_p on the faces of building of both the sizes when it is located at the center and the core radius of CFD tornado simulator are included in Figs. 35-36 whereas that of the minimum pressure distribution on the building faces are included in Figs. 37-38.

Finally, the values of mean pressure coefficient (C_p) along the centerline of the frame of the building is plotted along the Y-axis whereas the corresponding distances (d) is plotted along the X-axis in Fig. 39. The centerline C_p profile for both the buildings (i.e. building of size $0.10h_o \times 0.05h_o \times 0.05h_o$ and of size $0.10h_o \times 0.10h_o \times 0.10h_o$) is included in Fig. 39 and it can be clearly noticed that the the size of building can influence the tornado-induced loads on the building. For building of size $0.10h_o \times 0.05h_o \times 0.05h_o$, the pressure coefficient on the westward face is about -1.7 whereas the corresponding C_p value for building of size $0.10h_o \times 0.10h_o \times 0.10h_o$ is roughly around -2.2. Considering these two values of C_p , the tornado-induced wind load on the west face of the building varies roughly about 25% and similar trend can be observed for roof as well as the eastward wall. Hence, it seems critically important to consider an appropriate benchmark for size and scale of the building while determining tornado-induced wind pressures on building.

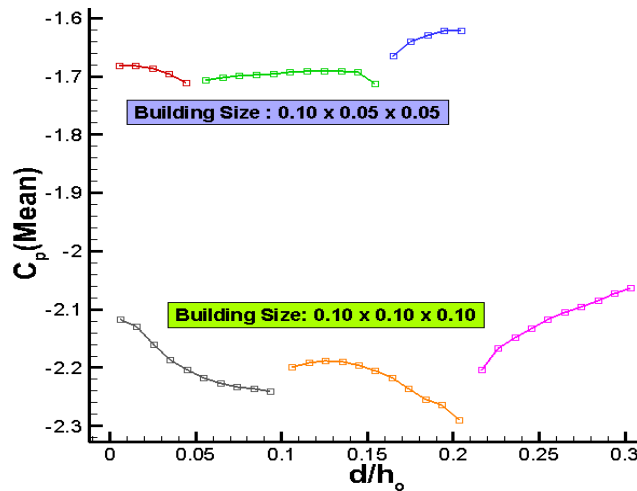


Fig. 39. Comparison of Mean C_p profile along the centerline frame of building of two different sizes (i.e., $0.10h_o \times 0.05h_o \times 0.05h_o$ and $0.10h_o \times 0.10h_o \times 0.10h_o$)

For the first building (with size $0.10h_o \times 0.05h_o \times 0.05h_o$), the ratio (R_r) is 0.087 and for the second building (with size $0.10h_o \times 0.10h_o \times 0.10h_o$), the scale ratio is 0.123, which are both less than the critical value (0.45) suggested by Kikitsu and Okuda (2016). It is observed that the range of mean pressure coefficient is almost the same for both the sizes of building when building is located at the center of CFD tornado simulator. However, the absolute value of mean C_p is roughly about 2 times for the building of size $0.10h_o \times 0.10h_o \times 0.10h_o$ as compared to the building of size $0.10h_o \times 0.05h_o \times 0.05h_o$. Similar trend is observed for the minimum pressure coefficient when the building is placed at the center of CFD tornado simulator. This observation indicates that the induced pressures on the building can differ by about 100% when the building of different sizes or scales are used in a tornado simulator with all the relevant flow conditions remaining constant even when the ratio (R_r) is significantly lower than the critical value of 0.45. Thus, it seems that maintaining a ratio (R_r) of less than 0.45 (or significantly lower than 0.45) may not be a sufficient criterion to eliminate the effect of size or scale of a building model on induced pressure or load characteristics.

For the case when the building (of different sizes) is placed at core radius, the range of mean and the minimum C_p shows some variation; however, the absolute value of mean and the minimum C_p generally do not differ by a large margin. The absolute value of mean and the minimum C_p varies roughly about 3% to 30%. So, it seems like the influence of size of the building on induced pressures is more pronounced when the building is fully engulfed inside the core of tornado-like vortex rather than when it is located at the outer core (core radius) of tornado-like vortex. It can be clearly noticed that the size of building can influence the tornado-induced loads on the building. For building of size $0.10h_o \times 0.05h_o \times 0.05h_o$, the pressure coefficient on the west face is about -1.7 whereas the corresponding C_p value for building of size $0.10h_o \times 0.10h_o \times 0.10h_o$ is roughly

around -2.2. Considering these two values of C_p , the tornado-induced wind load on the west face of the building varies roughly about 25% and similar trend can be observed for roof as well as the east wall.

6.5 Conclusion

The mean pressure coefficients on the faces of building show good agreement between the CFD model and TTU experiment as discussed in detail in section 6.3. Thus, the CFD model is validated using TTU experimental datasets for conducting further studies on the interaction of tornado-like vortex with building model. Besides, it is also concluded that the size of building model can influence the magnitude of pressure induced by a tornado-like vortex on the building model. Hence, it seems critically important to consider an appropriate benchmark for size and scale of the building while determining the pressure induced by tornado-like vortex on building models.

Chapter-7: Comparison of Pressures on a Building due to Different Flow Structures of Vortex and Different Reynolds Number

7.1 Introduction

A diverse range of flow structures (with different swirl ratios) of tornado-like vortex have been considered in the existing literature for evaluating tornado forces on building (Refer Table 3 in section 2.7). Different flow structures of tornado-like vortex have different wind velocity profile and pressure distribution, which may result in different loading conditions on building. The difference in flow structure is likely to be one of the most important factors leading to a wide variation of tornado forces on building. However, the kind of tornado flow structure that would be suitable to develop wind load provisions for buildings in tornado-prone areas is not very well explained in the existing literature. Besides, the details of flow field and/or the coherent structures in the wind field including the cause of variation in induced pressures on the building are also not available. Furthermore, the definition of swirl ratio also varies from one work of literature to another as pointed out by Gillmeier (2019), so, the value of swirl ratio calculated using different definitions/expressions can lead to further disparity in flow structure of tornado-like vortices from different work. Verma and Selvam (2021c) tried to connect different definitions/expressions of swirl ratio and then compare the flow structure of tornado vortices in different tornado simulators using a consistent definition/expression of swirl ratio. They observed that different flow structures of tornado vortices may exist in different tornado simulators at similar values of swirl ratio if a consistent definition is not used, which may further lead to disparity in induced pressures during the interaction of tornado-like vortex with buildings.

7.2 Previous Work on Various Flow Structure & Reynolds Number of Tornado-like Vortex

The experimental study carried out by Razavi and Sarkar (2018) examined the forces induced by

tornado-like vortex on a building due to a single-celled tornado-like vortex ($S = 0.16$) as well as a two-celled tornado-like vortex ($S = 0.86$). They concluded that the former produced larger peak loads on a building compared to two-celled tornado-like vortex. They also observed that the horizontal drag and vertical lift forces occurred on the building concurrently, and thus could be a significant contributing factor for the loads induced by tornado-like vortex on building. Similarly, Li et al. (2020) used CFD simulation to investigate tornado-induced loads on a dome due to a single-celled and double-celled tornado-like vortex. They concluded that a single-celled vortex can produce peak load on a building than a double-celled vortex; however, they also speculated that a double-celled vortex could cause dynamic loading effect on the dome due to rapidly fluctuating forces over a short interval of time. Even though different flow structures of tornado-like vortex can lead to different magnitude of vortex induced pressures and forces on building, there are no such guidelines in the existing literature and/or building codes that provides recommendation for selecting a particular flow structure (or swirl ratio) of vortex for load estimation and building design purposes. Besides, the studies mentioned above are mostly based on comparison of vortex-induced forces on building between a single-celled and double-celled tornado-like vortex; however, the kind of vortex (or the flow structure) that would be suitable for developing wind load provisions for load calculation and design of buildings in tornado-prone areas is not generally identified and/or suggested. Thus, in this work, a systematic investigation is carried out to quantify the pressures induced on a building model due to different flow structures of tornado-like vortex by gradually varying the flow structure (swirl ratio (S) = 0.15, 0.36 and 0.83, which are representative of vortex before, during and after touchdown respectively) and the observations/results are discussed.

7.3 Pressure Coefficient on the Faces of Building due to Different Flow Structure of Vortex

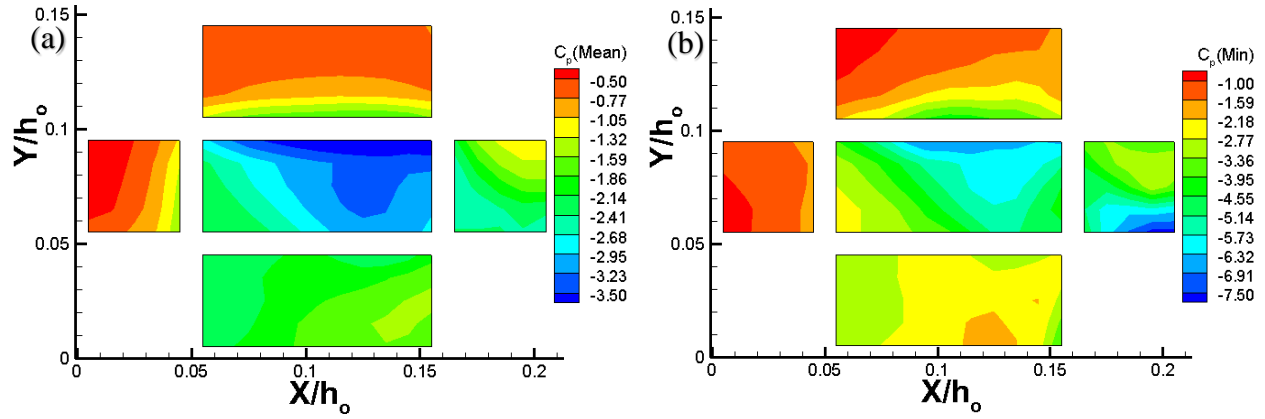


Fig. 40. Pressure contour plot on the faces of the building due to a tornado-like vortex with swirl ratio (S) = 0.15 (before touchdown) when building is located at the center of CFD tornado simulator (a) Mean C_p plot (b) Minimum C_p plot

In Fig. 40, the mean and the minimum pressure coefficient (C_p) contour plot due to the interaction of a single-celled tornado-like vortex ($S = 0.15$) with building is included. From the collected datasets, it is observed that a stationary tornado-like vortex with low swirl ratio can produce drastic loading conditions on a building with a minimum pressure coefficient value as low as -7.5.

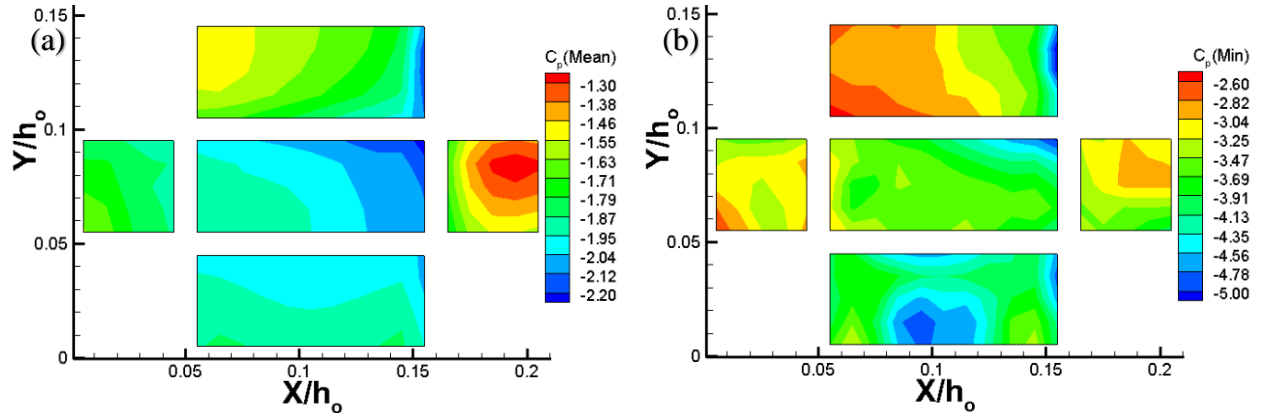


Fig. 41. Pressure contour plot on the faces of the building due to a tornado-like vortex with swirl ratio (S) = 0.36 (during touchdown) when building is located at the center of CFD tornado simulator (a) Mean C_p plot (b) Minimum C_p plot

Similarly, the mean and the minimum pressure coefficient (C_p) contour plot due to the interaction of a touched-down tornado-like vortex ($S = 0.36$) with building is included in Fig. 41. From Fig.

40 and 41, it can be observed that the minimum pressure coefficient on the faces of building goes on decreasing with increasing swirl ratios, i.e. $C_p = -7.5$ for $S = 0.15$ and $C_p = -5.0$ for $S = 0.36$. Similar trend is observed in case of mean pressure coefficient as well in that the minimum mean pressure coefficient drops from $C_p = -3.5$ for $S = 0.15$ to $C_p = -2.2$ for $S = 0.36$. Also, the range of both the mean and the minimum pressure coefficient is observed to be decreasing when the swirl ratio of tornado-like vortex is increased from $S = 0.15$ to $S = 0.36$.

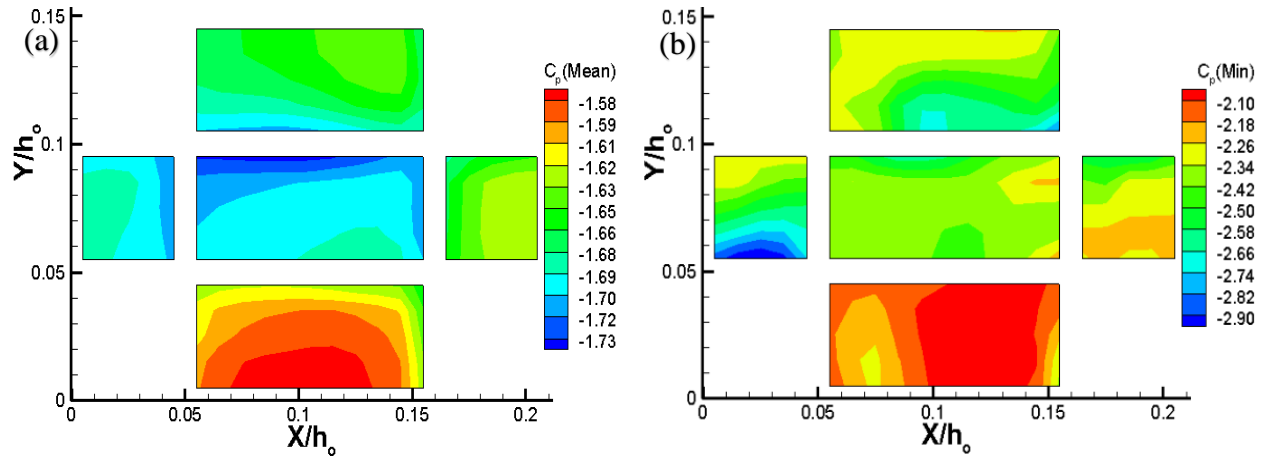


Fig. 42. Pressure contour plot on the faces of the building due to a tornado-like vortex with swirl ratio (S) = 0.83 (post touchdown vortex) when building is located at the center of CFD tornado simulator (a) Mean C_p plot (b) Minimum C_p plot

Similarly, the mean and the minimum pressure coefficient (C_p) contour plot due to the interaction of a post touched-down vortex ($S = 0.83$) with building is included in Fig. 42. From Fig. 41 and 42, it can be again observed that the minimum pressure coefficient on the building decreases further to $C_p = -2.90$ when the swirl ratio of vortex increases from $S = 0.36$ to $S = 0.83$ and similar trend follows for the mean pressure coefficient as well. Also, the range of both the mean and the minimum pressure coefficient decreases further for $S = 0.83$ as compared to $S = 0.36$.

This observation indicates that when the swirl ratio of a stationary tornado-like vortex increases or when the tornado-like vortex gradually transitions from a single-celled vortex to a touched-down or a post-touched down vortex, the effect of drop in static pressure influencing the loading

conditions on a building is also gradually reduced. As the swirl ratio of tornado-like vortex increases, the tangential velocity component becomes stronger thus, it seems probable that the interaction of tornado-like vortices at high swirl ratio is more dominated by aerodynamic forces that involves separation of detached suction vortices, which then exhibit circular motion around the building rather than the static pressure deficit (Refer Fig. 44 and Fig. 45). Furthermore, the range of pressure coefficient (C_p) is also found to be decreasing when the swirl ratio of tornado-like vortex goes on increasing and this holds true for both the mean and the minimum pressure coefficients. It has been commonly observed that a tornado-like vortex before touchdown bears a slender filament like structure (Rotunno, 2013) with large pressure drops at the center of vortex whereas the core of tornado-like vortex becomes larger with increasing value of swirl ratio and the static pressure deficit in the core of tornado-like vortex also becomes lower compared to a single-celled tornado-like vortex (Tang et al., 2018a, 2018b; Verma and Selvam, 2020). Based on this observation, it can be inferred that a tornado-like vortex interacting with building at higher swirl ratios engulfs a building completely with a larger core radius; however, due to lower drop in static pressure deficit compared to a single-celled vortex as well as lower pressure gradient at the core of vortex, the range of pressure coefficient (C_p) goes on decreasing for larger swirl ratio cases.

7.3.1 Tornado Flow Field at Roof Level around the Building Due to Different Swirl Ratios when Building is located at the Center of Simulator

In addition, it is observed that the low pressure suction vortex remains attached to the east face of the building consistently over different time steps for the lower swirl ratio case ($S = 0.15$) as shown in Fig. 43. The low pressure suction vortex which remains attached to the building might be the probable cause for a very low value of the minimum pressure coefficient ($C_p = -7.5$) in Fig. 40 for $S = 0.15$. However, in case of a touched-down tornado vortex (with $S = 0.36$), it has been observed

that the low pressure suction vortex gets detached from the face of building and then exhibits a circular motion around the building. As the suction vortices detach from the faces of building and exhibit a circular motion, the vortex dynamics changes and thus the aerodynamic forces dominate over the forces resulting from static pressure drop. Consequently, the pressure coefficient as well as the range of pressure coefficient on the faces of building decreases.

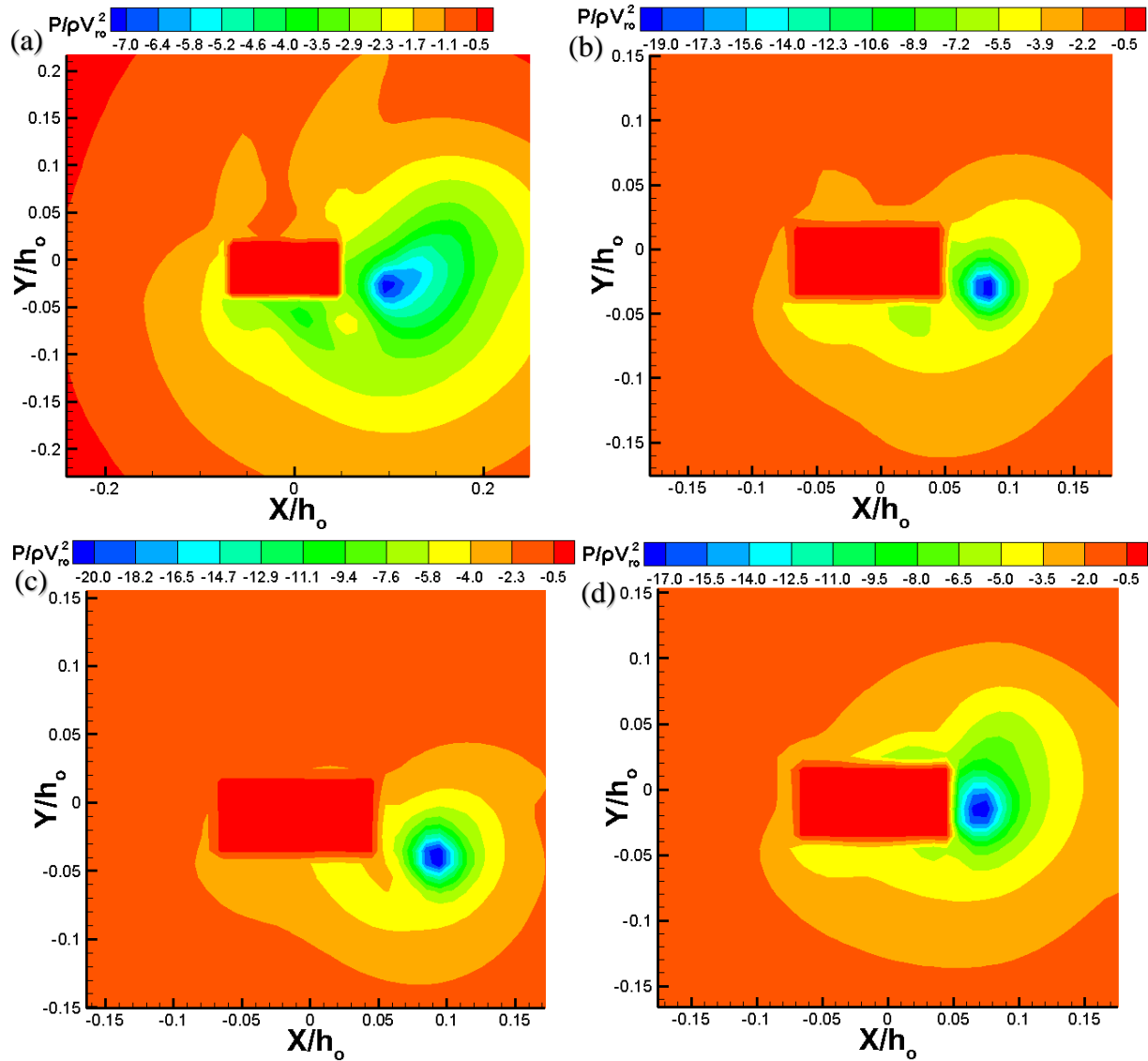


Fig. 43. Suction vortex attached on the eastward face of the building for swirl ratio (S) = 0.15 and building located at the center of CFD tornado simulator at 4 different time steps (a) $t^* = 19.61$ (b) $t^* = 23.47$ (c) $t^* = 25.15$ and (d) $t^* = 29.00$

The flow field of tornado-like vortex around the building for $S = 0.15$ starting from non-dimensional time of $t^* = 19.61$ units to $t^* = 29.00$ units is shown in Fig. 43, which clearly demonstrates that the low pressure suction vortex remains attached to the east face of building in each of the time steps. Whereas for a tornado-like vortex during touchdown ($S = 0.36$) and after touchdown ($S = 0.83$), the low pressure suction vortex detaches from the faces of building and exhibits a circular motion around the building as shown in Figs. 44-45. The unsteady detached suction vortices in the periphery of building seems somewhat comparable to Von Karman vortex street observed in straight line wind flows. In a straight line wind flow around a solid obstacle object, the vortices detach from the solid object and are carried away in streamwise direction of flow beyond certain critical Reynolds number. However, in tornado-like wind flow, the detached vortices begin to exhibit circular motion around the solid object (building in this case) under the influence of tangential and radial velocity components. The detached suction vortices in the periphery of building are unsteady in nature and could be another contributing factor for wind load on buildings during tornadic events as these vortices possess momentum due to their circular motion. When these vortices transfer their momentum to stationary buildings during the impact then, it can produce impact loading on the buildings. However, in this relatively simplistic model, such dynamic effects have not been considered, so, the mean as well as the minimum pressure coefficients may be much higher for the single-celled tornado-like vortex ($S = 0.15$) than the touched-down ($S = 0.36$) or double-celled vortex ($S = 0.83$). Hence, considering the induced wind loads on building due to static pressure drop, tornado-like vortex before touchdown seems to be more devastating than a vortex during and beyond touchdown. Nevertheless, the impact loading due to exchange of momentum between the detached suction vortices around the building and the

stationary building could be another important factor contributing to tornado-induced loads on building leading to disintegration of building envelope.

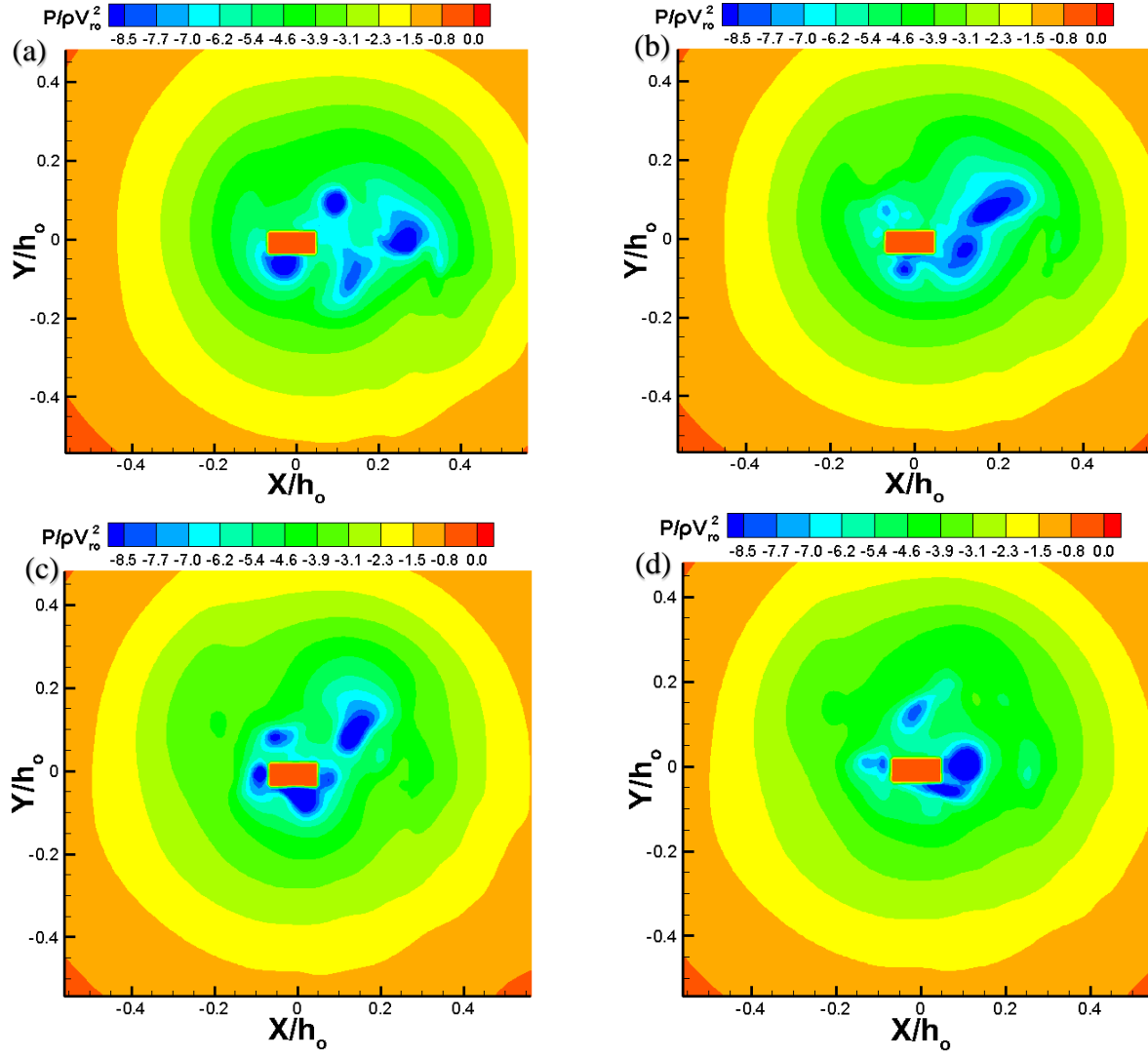


Fig. 44. Detached suction vortices in the periphery of building for swirl ratio (S) = 0.36 and building located at the center of CFD tornado simulator at 4 different time steps (a) $t^* = 17.96$ (b) $t^* = 22.95$ (c) $t^* = 25.82$ and (d) $t^* = 28.12$

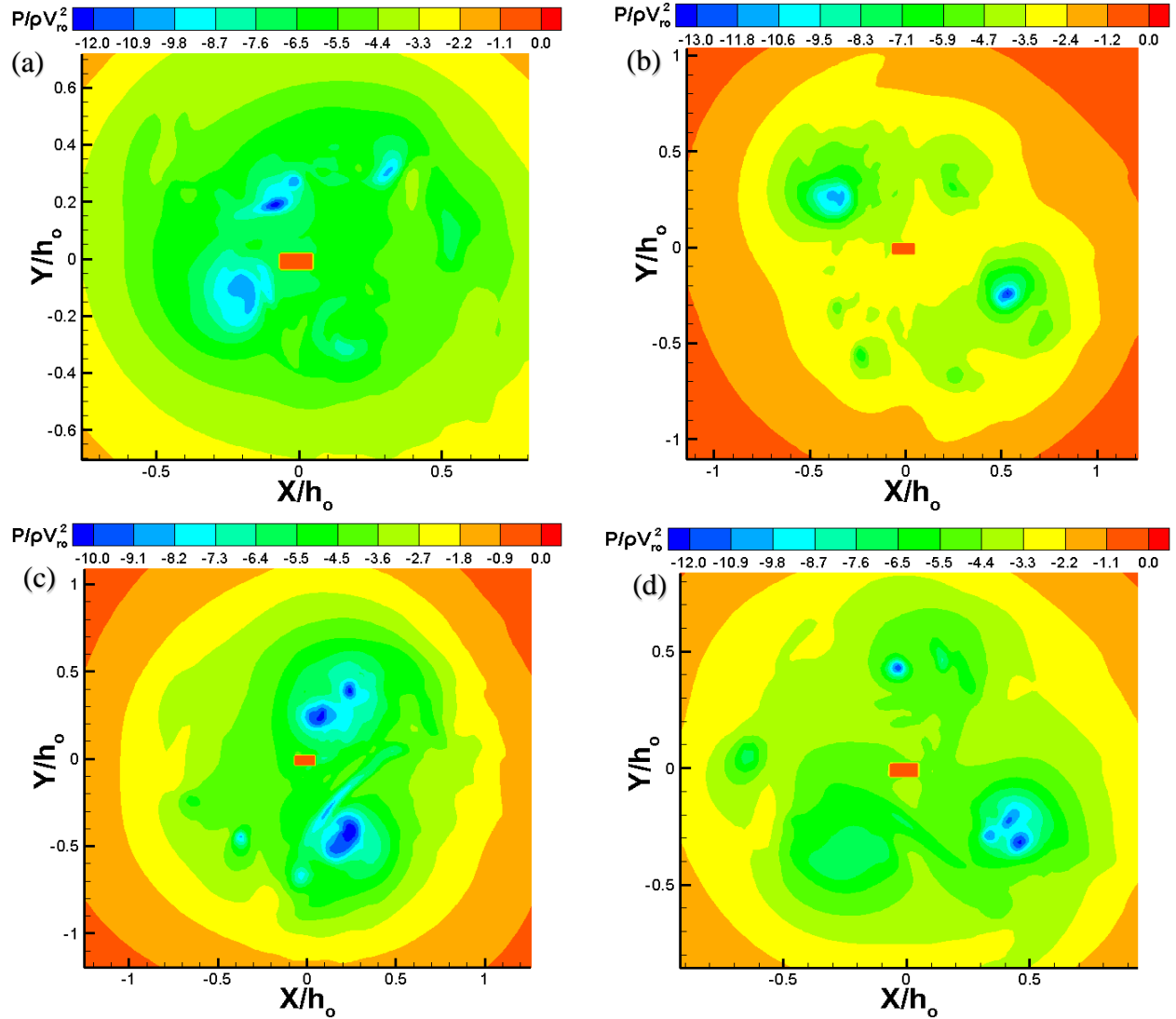


Fig. 45. Detached suction vortices in the periphery of building for swirl ratio (S) = 0.83 and building located at the center of CFD tornado simulator at 4 different time steps (a) $t^* = 17.96$ (b) $t^* = 22.95$ (c) $t^* = 25.82$ and (d) $t^* = 28.12$

7.3.2 Tornado Flow Field at Roof Level around the Building Due to Different Swirl ratios when Building is located at the Core Radius of Vortex

In general, the induced negative pressures on the building is reduced for the case when the building is placed at the location of core radius compared to the center of tornado-like vortex since the building experiences positive pressures due to the direct impact of tangential velocity component. Thus, the magnitude of negative pressures is most likely to decrease for the case when building is

placed at core radius rather than at the center of tornado-like vortex. However, it is observed from the collected datasets in this study that suction vortices formed in the periphery of building remains attached to the building for a low swirl ratio case ($S = 0.15$) as shown in Fig. 49. The attached suction vortices on the building is most likely the reason for low mean and minimum pressure coefficient ($C_p = -3.8$ for mean and $C_p = -5.0$ for minimum respectively) on the building in Fig. 46 below. However, in case of a touched-down ($S = 0.36$) and post-touched-down vortex, the low pressure suction vortices is observed to detach from the faces of building and then exhibit circular motion around the building. The detached suction vortices revolve around the building with different radii; the radius for higher swirl ratio ($S = 0.83$) is greater than that for $S = 0.36$. Despite the anticipated direct impact of tangential velocity component reducing the negative pressures on the building, it is observed that the suction vortices that detach from the building during the circular motion around the building could impact the building as well as get attached to the building momentarily. The pressure drop in these suction vortices is a lot higher than that of the surrounding core region of vortex. Thus, it seems to be the reason for higher magnitude of negative pressures on the building even when the building is placed at core radius location. The mean and the minimum pressure coefficient contour plots when the building is placed at core radius of tornado-like vortex for different swirl ratios ($S = 0.15, 0.36$ and 0.83) are included in Figs. 46-48. Similarly, the attached suction vortices around the building for $S = 0.15$ and the detached suction vortices revolving around the building for $S = 0.36$ and $S = 0.83$ are included in Figs. 49-51.

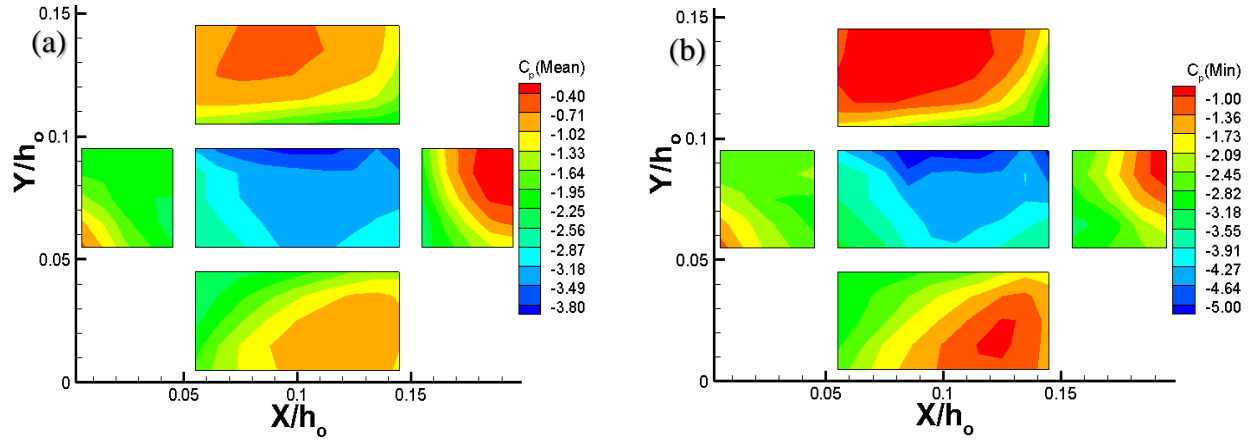


Fig. 46. Pressure contour plot on the faces of the building due to a tornado-like vortex with swirl ratio (S) = 0.15 (before touchdown) when building is located at core radius of tornado-like vortex (a) Mean C_p plot (b) Minimum C_p plot

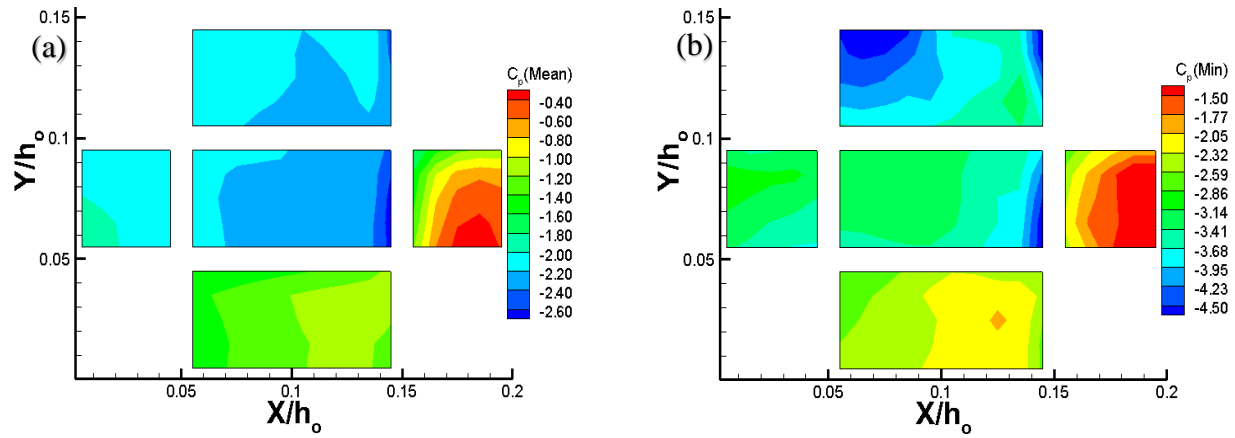


Fig. 47. Pressure contour plot on the faces of the building due to a tornado-like vortex with swirl ratio (S) = 0.36 (during touchdown) when building is located at core radius of tornado-like vortex (a) Mean C_p plot (b) Minimum C_p plot

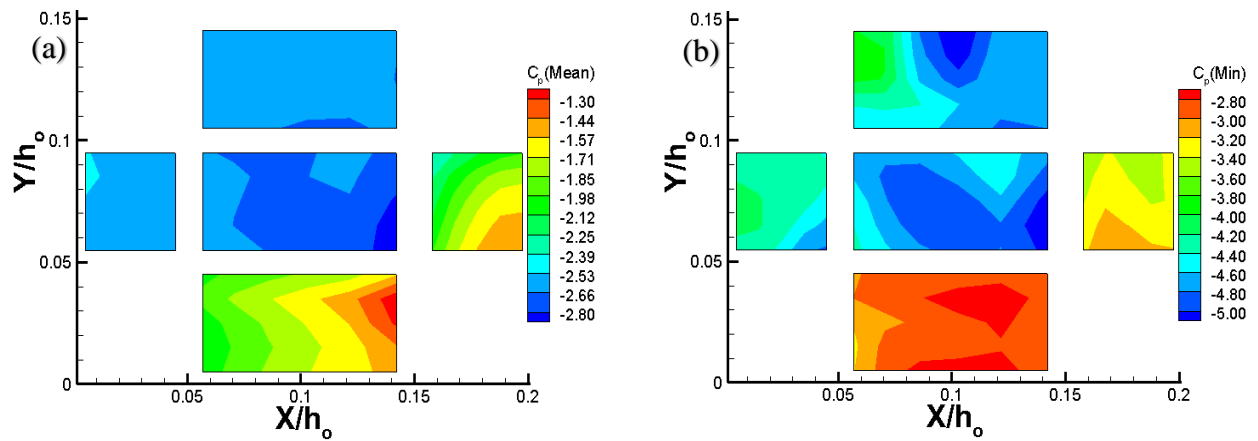


Fig. 48. Pressure contour plot on the faces of the building due to a tornado-like vortex with swirl ratio (S) = 0.83 (post-touchdown vortex) when building is located at core radius of tornado-like vortex (a) Mean C_p plot (b) Minimum C_p plot

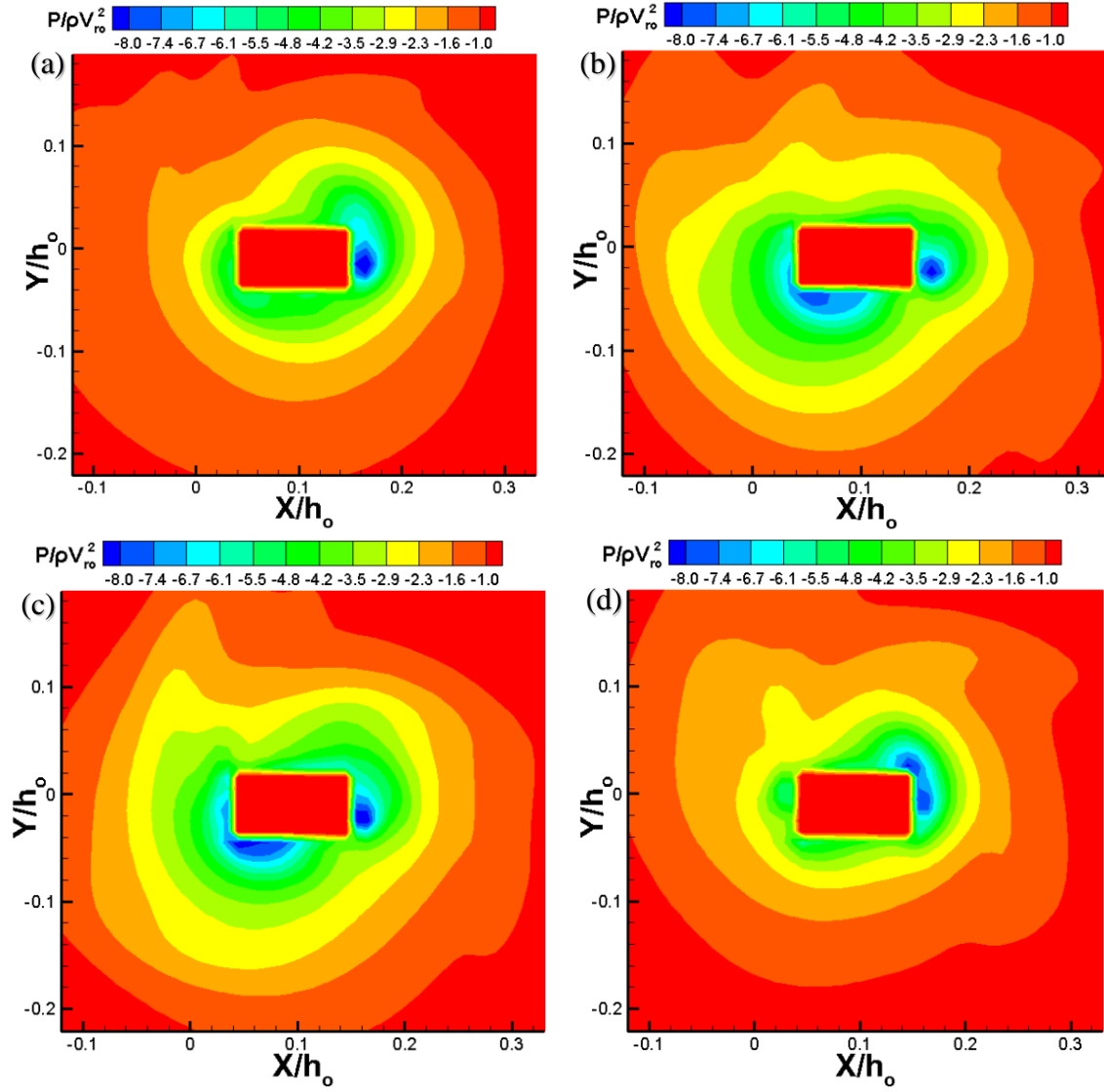


Fig. 49. Suction vortex attached on the periphery of building when the building is placed at core radius for swirl ratio (S) = 0.15 at 4 different time steps (a) $t^* = 20.17$ (b) $t^* = 24.13$ (c) $t^* = 26.90$ and (d) $t^* = 29.92$

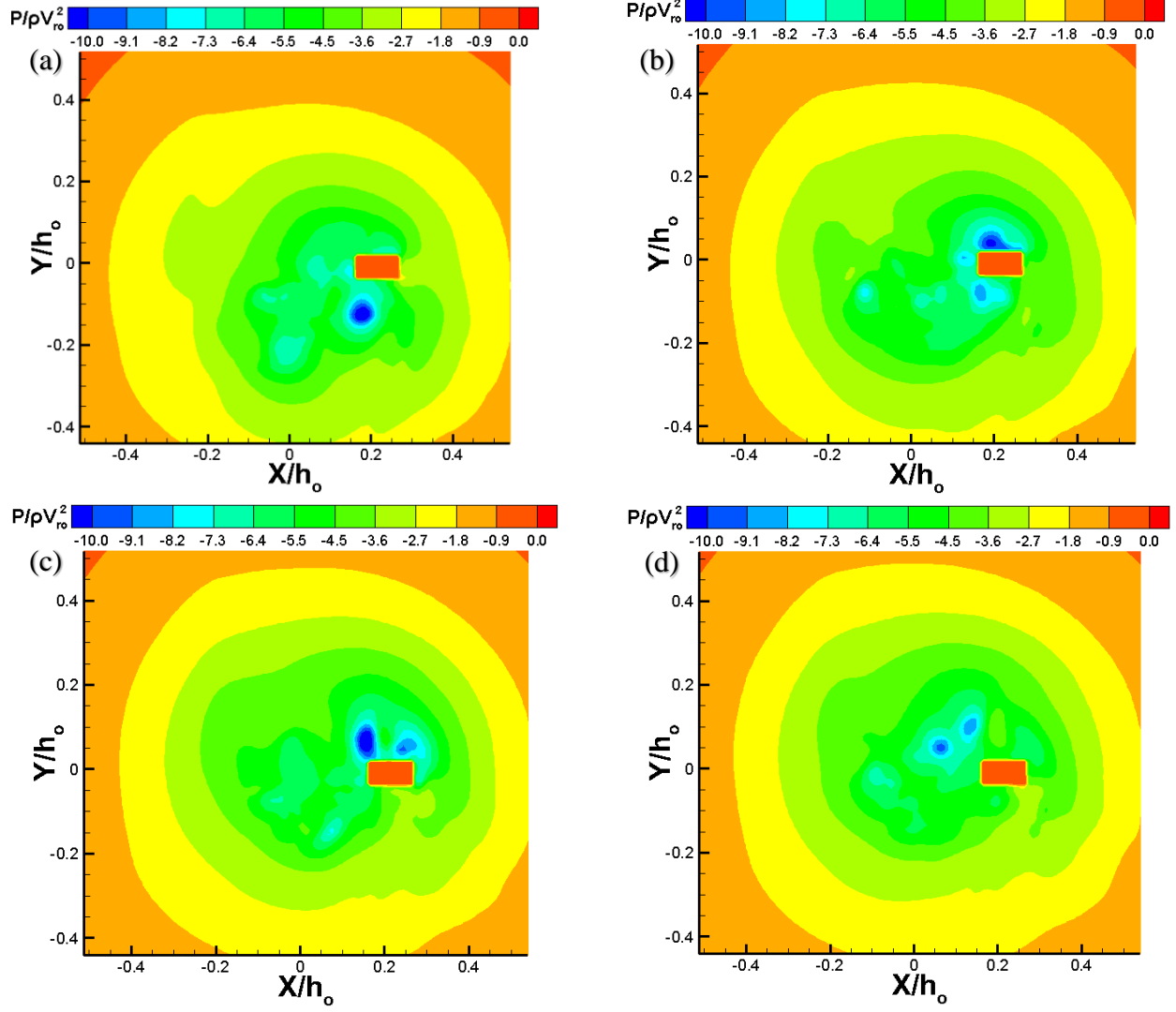


Fig. 50. Detached suction vortices around the building when the building is placed at core radius for swirl ratio (S) = 0.36 at 4 different time steps (a) $t^* = 24.93$ (b) $t^* = 25.14$ (c) $t^* = 25.63$ and (d) $t^* = 25.73$

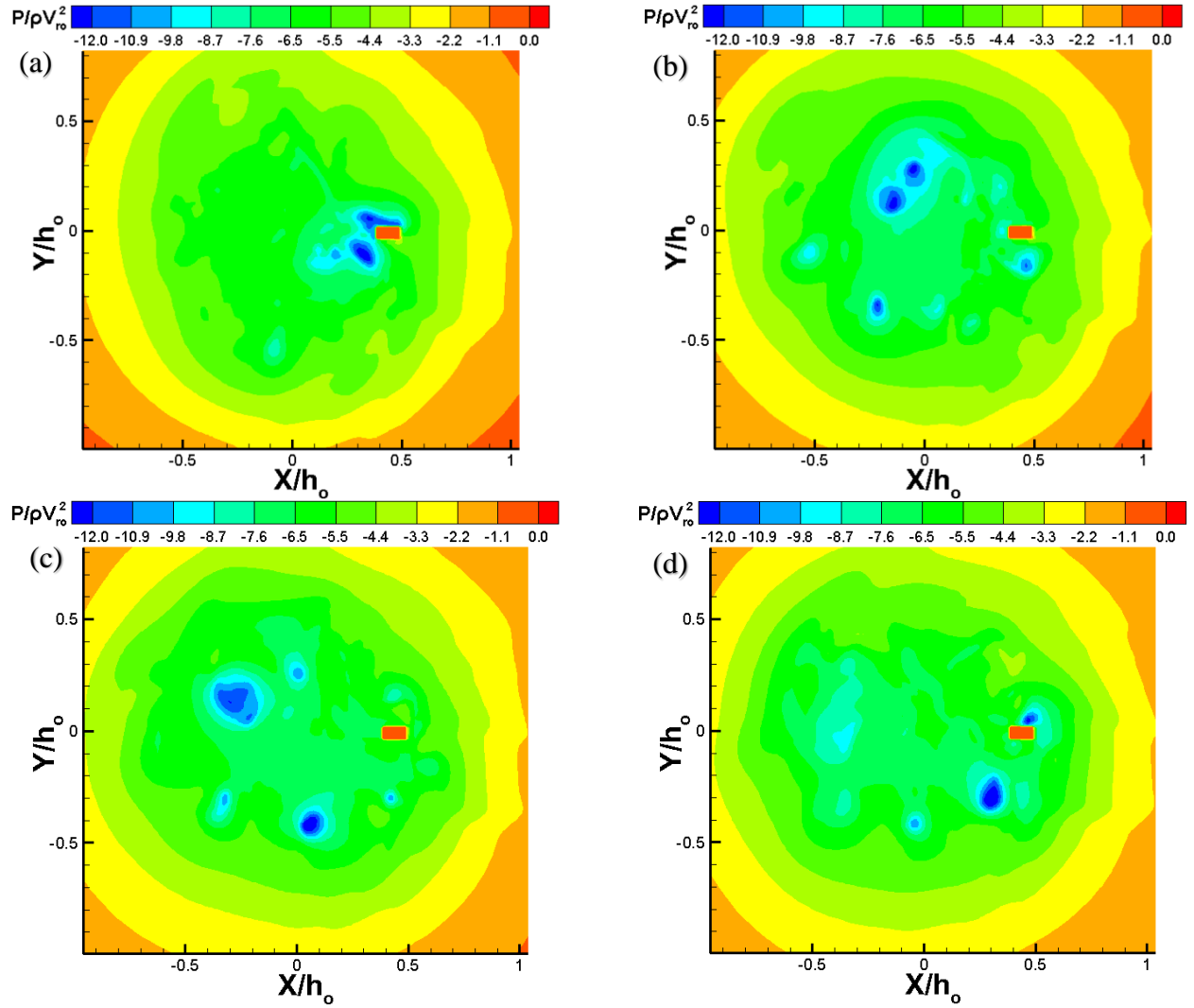


Fig. 51. Detached suction vortices around the building when the building is placed at core radius for swirl ratio (S) = 0.83 at 4 different time steps (a) $t^* = 20.27$ (b) $t^* = 20.80$ (c) $t^* = 20.97$ and (d) $t^* = 21.16$

Finally, a summary of the minimum and the maximum of the mean and the minimum pressure coefficient for the case when the building is located at the center of simulator and at the location of core radius of tornado-like vortex is documented in Table 12 below. From the collected datasets in Table 12, it can be observed that the minimum of mean pressure coefficient for each of the flow structure of tornado-like vortex is recorded at the location of core radius than at the center of tornado simulator. Thus, a building placed at the location of core radius experiences a comparatively higher negative mean pressure and could be more vulnerable to failure. However,

considering the magnitude of the minimum pressure coefficient, the suction experienced by the building at the center of vortex is slightly higher than that at the core radius of vortex for $S = 0.15$ and $S = 0.36$.

Table 12. Range of mean and min. C_p on the faces of building due to different swirl ratios of tornado-like vortices

S.N.	Swirl ratio	$r/r_c = 0$				$r/r_c = 1$			
		Mean C_p		Minimum C_p		Mean C_p		Minimum C_p	
		Min.	Max.	Min.	Max.	Min.	Max.	Min.	Max.
1	0.15	-3.885	-0.363	-7.709	-0.623	-5.422	-0.204	-7.214	-0.876
2	0.36	-2.247	-1.246	-5.162	-2.509	-2.426	-0.266	-4.247	-0.98
3	0.83	-1.736	-1.571	-3.000	-2.301	-2.889	-1.201	-5.223	-2.652

Hence, it is concluded that the interaction of wind field of a tornado-like vortex at low swirl ratio (or a single-celled tornado vortex) produces the severest suction pressure and thus the most adverse loading conditions on a structure. This observation also complies well with the results obtained by Razavi and Sarkar (2018) and Li et al. (2020). However, from real-life experience, the double-celled tornadoes, and the multi-vortex tornadoes such as El Reno tornado (Seimon et al., 2016) are the most violent tornadoes, which have even killed storm chasers. This could be because the current CFD model cannot account for the debris and wind-borne debris impact on the building model. Thus, in the future, a more sophisticated CFD model may be necessary that can account for the motion of debris particles and their impact on the structures to infer realistic results from the model.

7.4 Pressure Coefficient on the Faces of Building due to Different Reynolds Number

Refan and Hangan (2016, 2018) analyzed the effect of Reynolds number ($Re = 1.6 \times 10^4 - 2.0 \times 10^6$) on the flow field of tornado-like vortex. They concluded that the surface pressure due to

tornado-like vortex is quasi-independent of the Reynolds number beyond a critical Reynolds number (of $Re = 4.5 \times 10^4$). Even though some studies have been carried out on the effect of variation of Reynolds number on the flow field of tornado-like vortex, its effect on the pressures induced on buildings is relatively unexplored. Liu et al. (2018) compared the pressure coefficients on a cooling tower from the CFD model with the experimental results from Cao et al. (2015). They observed that there was significant variation in the values of pressure coefficient between the CFD model and the experimental results and speculated that the difference in Reynolds number may have been a probable cause. As the effect of variation of Reynolds number on the pressures induced by tornado-like vortex on a building is not readily available in the existing literature, so, in the following section, the Reynolds number of flow is varied systematically to study its effect on the building pressures.

Three different Reynolds number (i.e., $Re = 2.755 \times 10^5$, 1.0×10^6 and 1.0×10^7) are considered to study the effect of variation of Reynolds number on the pressures induced by a double-celled tornado-like vortex with Swirl ratio (S) = 0.83. In addition, two different cases are considered for the relative position of building with respect to the tornado-like vortex (i.e., building placed at the center and at the core radius of tornado-like vortex). The pressure contours on the building when it is placed at the center of CFD tornado simulator for the three different Reynolds number are included in Figs. 52-54. From Figs. 52-54, it is observed that the value of maximum negative pressure coefficient on the building model goes on increasing with increase in the value of Reynolds number.

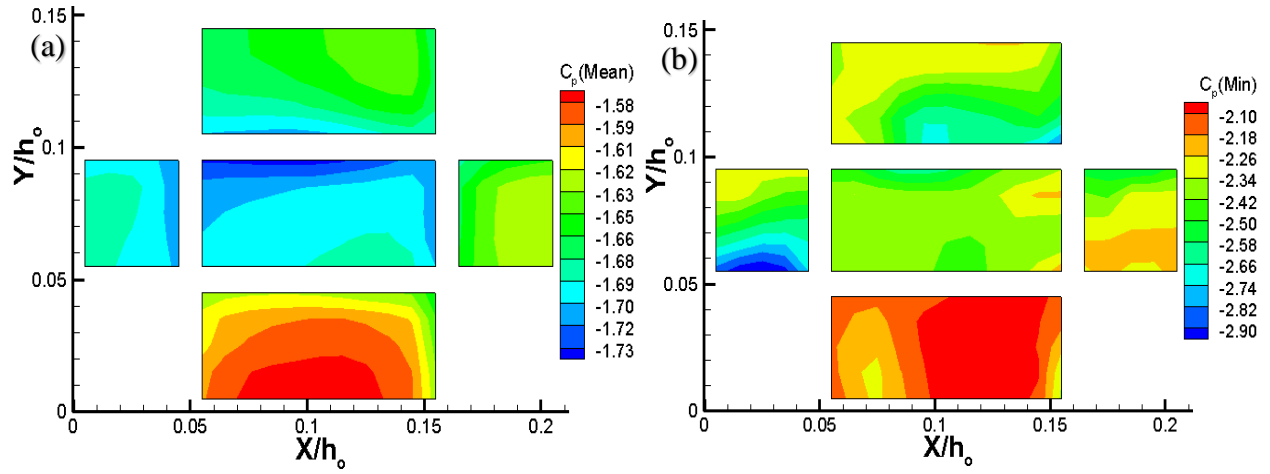


Fig. 52. Mean and Minimum C_p on the faces of building for $S = 0.83$ when the building is placed at the center of CFD tornado simulator for $Re = 2.755 \times 10^5$

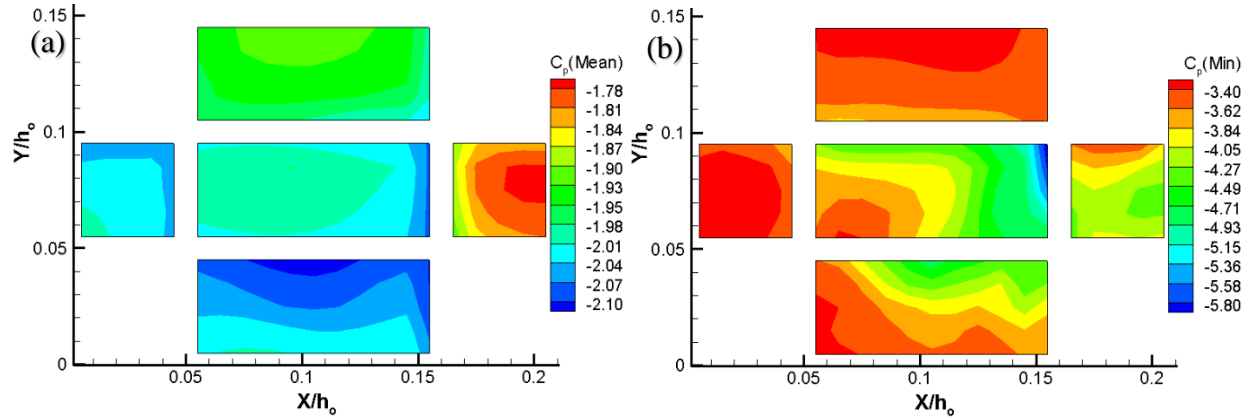


Fig. 53. Mean and Minimum C_p on the faces of building for $S = 0.83$ when the building is placed at the center of CFD tornado simulator for $Re = 1.0 \times 10^6$

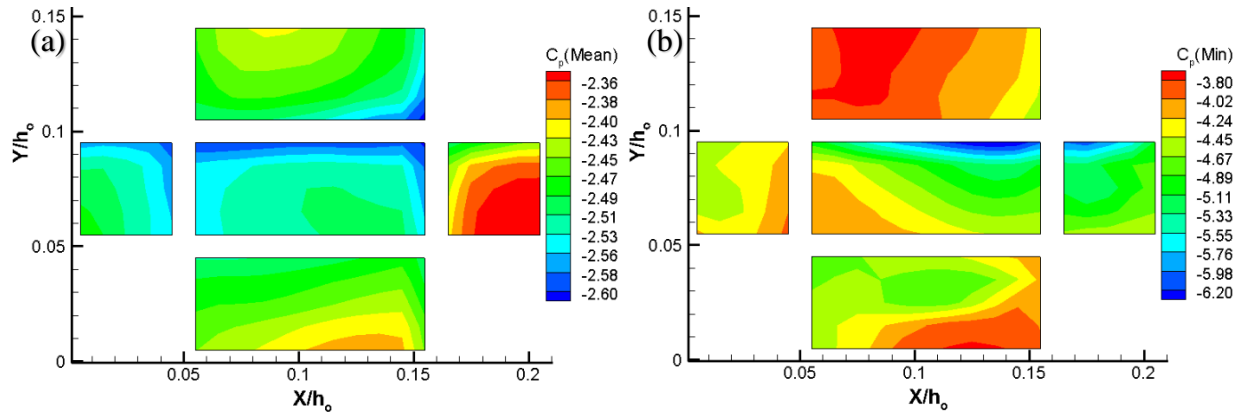


Fig. 54. Mean and Minimum C_p on the faces of building for $S = 0.83$ when the building is placed at the center of CFD tornado simulator for $Re = 1.0 \times 10^7$

As shown in Figs. 52-53, the maximum negative pressure coefficient increases from -1.73 to -2.10 as the Reynolds number increases from $Re = 2.755 \times 10^5$ to $Re = 1.0 \times 10^6$. Similarly, from Fig. 53-54, it can be observed that the maximum negative pressure coefficient increases from -2.10 to -2.60 as the Reynolds number increases further from $Re = 1.0 \times 10^6$ to $Re = 1.0 \times 10^7$. Similar trend is observed for the minimum pressure coefficients on the building. Thus, it can be said that the pressure coefficients on the building goes on increasing with increasing value of Reynolds number in CFD simulation.

When the building is placed at the location of core radius, the mean and the minimum pressure coefficients are found to be increasing with the increase in value of Reynolds number. The peak negative mean pressure coefficient, however, shows a slight decrease in the value (i.e., from $C_p = -2.80$ to $C_p = -2.70$) for $Re = 2.755 \times 10^5$ as compared to $Re = 1.0 \times 10^6$. The pressure contour plots on the building for three different Reynolds number when the building is placed at core radius location are shown in Figs. 55-57. Finally, the range of pressure coefficients for both the mean and the minimum pressure on the building is summarized in Table 13.

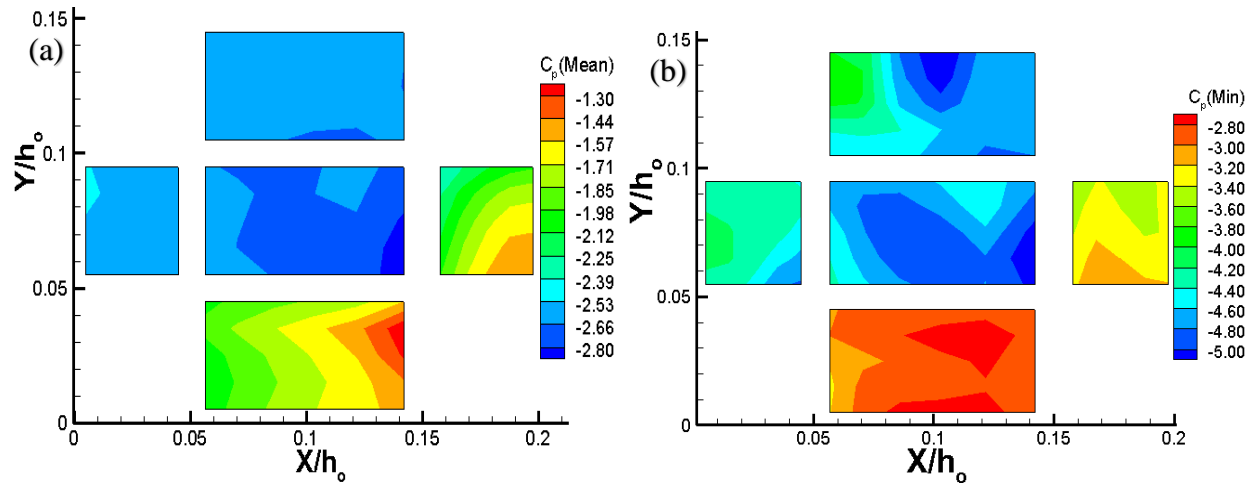


Fig. 55. Mean and Minimum C_p on the faces of building for $S = 0.83$ when the building is placed at core radius of vortex for $Re = 2.755 \times 10^5$

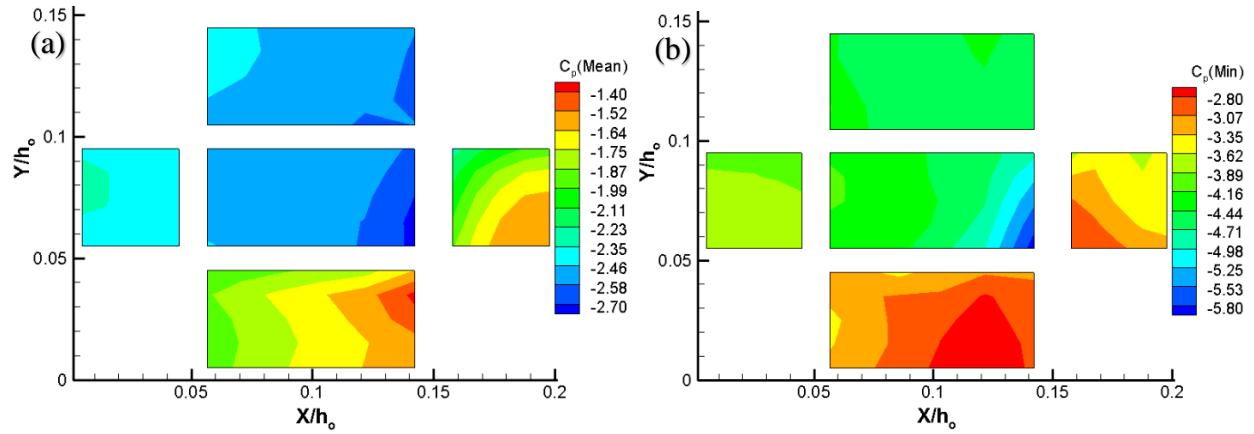


Fig. 56. Mean and Minimum C_p on the faces of building for $S = 0.83$ when the building is placed at core radius of vortex for $Re = 1.0 \times 10^6$

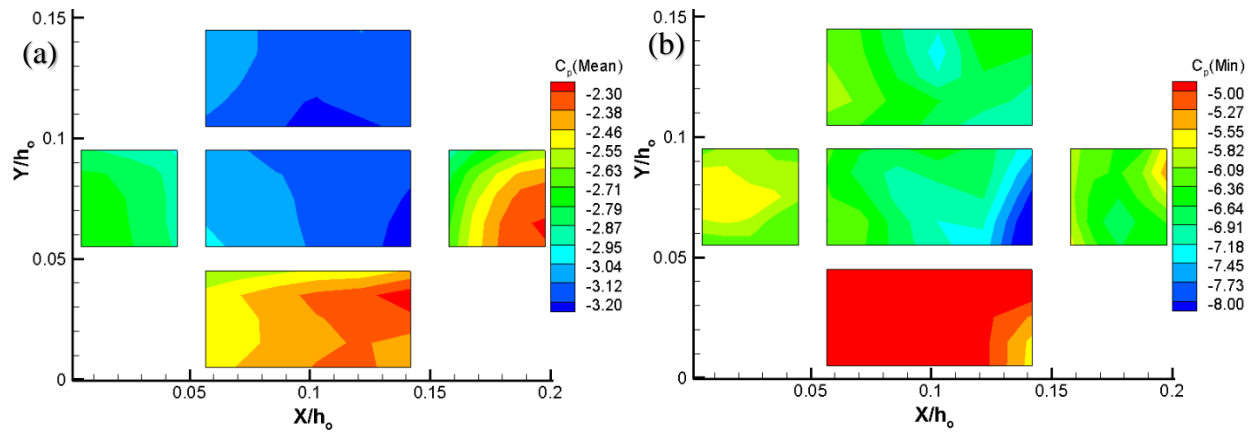


Fig. 57. Mean and Minimum C_p on the faces of building for $S = 0.83$ when the building is placed at core radius of vortex for $Re = 1.0 \times 10^7$

Table 13. Comparison of Mean and the Minimum C_p for different Reynolds Number

C_p	$Re = 2.755 \times 10^5$				$Re = 1.0 \times 10^6$				$Re = 1.0 \times 10^7$			
	$r/r_c = 0$		$r/r_c = 1$		$r/r_c = 0$		$r/r_c = 1$		$r/r_c = 0$		$r/r_c = 1$	
	Max	Min	Max	Min	Max	Min	Max	Min	Max	Min	Max	Min
Mean	-1.6	-1.7	-1.2	-2.9	-1.8	-2.1	-1.4	-2.7	-2.3	-2.6	-2.3	-3.3
Min.	-2.0	-3.0	-2.7	-5.2	-3.2	-6.0	-2.7	-5.9	-3.6	-6.5	-4.7	-8.6

7.5 Conclusion

Hence, it is concluded that the interaction of wind field of a tornado-like vortex at low swirl ratio (or a single-celled tornado vortex) produces the severest suction pressure and thus the most adverse

loading conditions on a building. When the swirl ratio of stationary tornado-like vortex increases or when the tornado-like vortex gradually transitions from a single-celled vortex to a touched-down or to a post-touched down vortex, the effect of drop in static pressure influencing the loading conditions on a building is also gradually reduced. As the swirl ratio of tornado-like vortex increases, the tangential velocity component becomes stronger thus, it seems probable that the interaction of tornado-like vortices at high swirl ratio is more dominated by aerodynamic forces that involves separation of detached suction vortices, which then exhibit circular motion around the building rather than the static pressure deficit. A tornado-like vortex interacting with building at higher swirl ratios engulfs a building completely within a larger core radius; however, due to a comparatively lower drop in static pressure deficit compared to a single-celled vortex as well as lower pressure gradient at the core of vortex, the range of pressure coefficient (C_p) goes on decreasing for larger swirl ratio cases.

On the other hand, it is observed that the pressures induced on a building due to a double-celled tornado-like vortex goes on increasing with the increasing value of Reynolds number. The trend holds for both the mean and the minimum pressure coefficients. Also, the maximum negative pressure coefficient ($C_p = -8.60$) is obtained on the building for the case of $Re = 1.0 \times 10^7$. As the Reynolds number of real –world tornadoes are very high (in the range of $10^7 - 10^8$), so, it seems necessary to maintain a high Reynolds number flow while studying the interaction of tornado-like vortex with building models to obtain more precise values of induced pressures on the building.

Chapter-8: Conclusion

8.1 Summary

There are several challenges in experimental simulation of tornado-like vortices in experimental simulators such as scaling of simulated vortices with the real-world tornadoes, differences in the kinematic and dynamic characteristics of flow field of simulated vortices as compared to full-scale tornadoes, challenges in data acquisition near to the ground-surface as well as high construction and operational costs of the experimental facilities. Many challenges encountered in the experimental simulation of tornado-like vortices can be eliminated using validated CFD models. However, modeling of an efficient CFD tornado simulator to obtain data with reasonable accuracy and within a reasonable timeframe is a challenge in itself. CFD tornado simulators that are based on the idea of replicating the geometry of experimental simulators often require modeling of mechanical parts such as the turning vanes and the fans. To resolve the flow domain along with the mechanical parts of experimental tornado simulators requires an enormous number of grid points in the CFD model. So, it is often necessary to run the simulation using high performance computing system for several days to weeks to obtain the simulation results. Hence, in this work, a simple CFD model of a tornado simulator (resembling the experimental tornado simulator at Texas Tech University) is implemented and the details of the implementation are discussed. Although some challenges faced in experimental tornado simulators can be overcome by CFD tornado simulators, there are still some challenges with CFD models that it must be validated against the experimentally simulated results to ensure that the model follows the trend of real-world physical simulation. Thus, in this work, the important features of tornado-like vortex (such as the touchdown swirl ratio, core radius, the maximum tangential velocity and elevation of the maximum tangential velocity) are validated with the experimental results from experimental TTU

tornado simulator. In addition, the profiles of core radius and the pressure profiles close to the ground surface are also compared with experimental results. Results from the comparison indicate that the CFD model agrees reasonably well with experimental results for the majority of the compared flow features. Thus, it is concluded that the CFD model can produce similar flow features as the experimental TTU tornado simulator.

After validation of CFD flow field, the flow features of tornado-like vortex such as the touchdown swirl ratio, the maximum tangential velocity, core radius and the elevation of maximum tangential velocity in different experimental and CFD simulators are compared. In the process, it is observed that different flow structures of tornado-like vortex can exist in different tornado simulators at similar value of swirl ratio unless a consistent definition of swirl ratio is used. In addition, it is also found that different tornado simulators have different touchdown swirl ratios, different maximum tangential velocity, core radius of tornado-like vortex, etc. Each of these vortex features such as the size of core radius, the maximum tangential velocity, etc. can significantly influence the pressures induced by a tornado-like vortex during its interaction with building models. Similarly, the effect of geometric variation in tornado simulators such as the total height and the outlet diameter is also investigated, and it is found that these features also influence the features of tornado-like vortex. Hence, it is concluded that the differences in geometry of tornado simulators as well as the flow features of tornado-like vortex may lead to different interpretation of pressures and forces induced by a tornado-like vortex.

From literature review, it is found that the peak pressures on building from experiment differs from one study to another on the experimental side whereas on the computation side, the pressures induced by tornado-like vortex on the building models lack validation with experimental results. Therefore, in this work, the pressures on the building model induced by a double-celled vortex (S

$= 0.83$) are computed from the CFD model. The results are then, compared with the experimental results from TTU simulator. Results of the comparison exhibit a good agreement between the CFD results and the TTU experiment. Also, different sizes (or scale) of building models and different flow structure of tornado-like vortices are used in different work of literature while evaluating the pressures and forces on building. However, the effect of differences in the size of building as well as the flow structure and Reynolds number on the pressures induced by tornado-like vortex on the building is not understood very well. Hence, in this work, a systematic investigation is carried out on the effect of variation of the size of building on the pressures induced by a tornado-like vortex. Similarly, the effect of the flow structure and the Reynolds number on the pressures induced by tornado-like vortex is also investigated and the details are discussed. The major conclusions drawn from different studies is summarized in section 8.2 below.

8.2 Conclusion

Firstly, the features of tornado vortex important from an engineering perspective and that can strongly influence the tornado pressures on building are identified for validation of CFD flow field. The important tornado vortex features considered in this work are (a) touchdown swirl ratio (S_T) (b) core radius (r_c) of vortex and (c) the maximum tangential velocity (V_{tmax}) (d) elevation of maximum tangential velocity (z_c). The reason for considering these features important in CFD flow validation is discussed in detail in section 1.1 of Verma and Selvam (2021b). In addition, the pressure distribution close to the ground surface is also considered for validation of CFD flow field. Results of the comparison indicate that the vortex features from CFD model compare reasonably well with the experimental measurements from Texas Tech University tornado simulator. The major conclusions drawn from the comparison of CFD flow field with TTU experiment are summarized below:

- The value of touchdown swirl ratio (S_T) = 0.22 at aspect ratio (a) = 1, obtained from CFD model matches with TTU experimental results at aspect ratio of unity. Similarly, the value of touchdown swirl ratio (S_T) = 0.36 obtained from CFD model matches with TTU experimental results at aspect ratio of 0.5. The aspect ratio of TTU tornado chamber can only vary between 0.5 and 1.0. As the CFD model predicted touchdown swirl ratio very well for both the aspect ratios (i.e., $a = 0.5$ and $a = 1$), it is concluded that the CFD model reasonably predicts the evolution of vortex in TTU tornado simulator.
- The average deviation in vertical core profile from CFD model with TTU experiment for a vortex with swirl ratio (S) = 0.24 is $0.016r_{up}$ whereas for the vortex with swirl ratio (S) = 0.78, the average deviation is about $0.066r_{up}$. As the average deviation for both the core profiles are low and the vertical profile of core radii from CFD model shows an overall good agreement with TTU experimental core profile, so, it is concluded that the CFD model can produce similar vortices as the TTU tornado simulator.
- As the pressure profiles from CFD model show good qualitative agreement with TTU experimental pressure profiles over a range of varying swirl ratios and the comparison of dimensional negative peak pressure from CFD model to TTU experiment shows deviation less than 5%, thus, it is concluded that the CFD model predicts the pressure field of TTU tornado chamber reasonably well. As the important features of tornado vortex from CFD model agrees well with TTU flow field, thus, it is concluded that an experimentally validated CFD model is obtained.

Different definitions of swirl ratio are reviewed and conversion relations are worked out to connect different definitions of swirl ratio. When the value of touchdown swirl ratio is expressed according to a single consistent definition, it is observed that different tornado simulators have different

values of touchdown swirl ratio. Identifying the macroscale similarities in flow pattern of different tornado simulators, the reviewed tornado simulators are classified into 5 major categories. However, it is found that there exists variation in value of touchdown swirl within a category of tornado chambers (for instance, in TPOS category from Table 5, S_T varies from 0.34 to 4.42). So, attention is provided to study the effect of variation of geometric features (total height and outlet diameter) of tornado chamber on touchdown. The conclusions drawn from literature review and parametric variation study are summarized below.

- Different tornado simulators have different values of touchdown swirl ratio when touchdown swirl ratio is evaluated based on a single consistent definition of swirl ratio.
- Among the different classification categories of tornado simulators, the SOS category of tornado simulator have the lowest value of touchdown swirl ratio followed by TFOS and TPOS categories. As compared to other tornado chambers, ISU tornado chamber and WindEEE dome have higher value of touchdown swirl ratio.
- TFOS and TPOS categories of tornado chambers have similar flow generation mechanism. However, some variation in the values of touchdown swirl ratio was observed in TFOS and TPOS categories of tornado chamber. So, attention was then fixed to understand the effect of geometric variations (such as variation of total height and size of outlet of tornado chamber) on touchdown.
- It was observed that the value of touchdown swirl ratio decreases with increase in total height of tornado chamber and large changes in total height of tornado chamber can only produce a small change in value of touchdown swirl ratio.

- Similarly, the value of touchdown swirl ratio increases with decrease in outlet diameter of tornado chamber and the change in touchdown swirl ratio with decrease in outlet diameter of simulator is more pronounced than that with the increase in height of tornado chamber.

Following the comparison of flow features of tornado-like vortex in different tornado simulators and the effect of geometric variation of different simulators on the flow field, the pressures induced on buildings by tornado-like vortex is studied. The mean and the minimum pressures induced on building by tornado-like vortex are computed from the CFD model and the results are compared with corresponding TTU experimental measurements. The major conclusions drawn from the comparison of vortex-induced pressures on building model with TTU experimental results and the effect of building size, the flow structure of vortex and the Reynolds number is summarized below.

- Using a hybrid grid with uniform cells at the center followed by stretching cells beyond $0.78r_c$ on either side of the center of computational domain, the values of mean pressure coefficient on the faces of building shows reasonable agreement between the CFD model and the TTU experimental datasets. When the building is placed at the center of CFD tornado simulator, the mean C_p values range from -1.58 to -1.73, whereas that for TTU experiment, the corresponding C_p values range from -1.49 to -1.65. The values obtained from CFD agrees reasonably with the TTU experimental datasets except for some discrepancy, which may be due to slight variation in the magnitude of maximum mean tangential velocity, which is used for computing the pressure coefficient (C_p).
- For the case when the building is placed at the location of core radius, a good qualitative agreement in the C_p contour values can also be noticed easily. The minimum C_p occurs on the south-east corner of the roof with a magnitude of about -2.8 for CFD model whereas for TTU experiment, the magnitude of minimum C_p is about -2.98 at tentatively the same location as

the CFD model. However, the range of pressure variation is different between the CFD model and TTU experiment; the range of mean C_p varies between -1.3 to -2.8 for the CFD model whereas for TTU experiment, the range varies between -0.19 to -2.98. It is suspected that the deviation could be due to lower grid resolution at the location of core radius, which is not as fine as at the center of tornado simulator in the CFD model. Thus, lower grid resolution could be the cause for the discrepancy.

- For the first building (with size $0.10h_o \times 0.05h_o \times 0.05h_o$), the ratio (R_r) is 0.087 and for the second building (with size $0.10h_o \times 0.10h_o \times 0.10h_o$), the scale ratio is 0.123, which are both less than the critical value suggested by Kikitsu and Okuda (2016). It is observed that the range of mean pressure coefficient is almost the same for both the sizes of building when building is located at the center of CFD tornado simulator; however, the absolute value of mean C_p is roughly about 2 times for the building of size $0.10h_o \times 0.10h_o \times 0.10h_o$ as compared to the building of size $0.10h_o \times 0.05h_o \times 0.05h_o$. Similar trend is observed for the minimum pressure coefficient when the building is placed at the center of CFD tornado simulator. This observation indicates that the induced pressures on the building can differ by about 100% when the building of different sizes or scales are used in a tornado simulator with all the relevant flow conditions remaining constant even when the ratio (R_r) is significantly lower than the critical value of 0.45. Thus, it seems that maintaining a ratio (R_r) of less than 0.45 (or significantly lower than 0.45) may not be a sufficient criterion to eliminate the effect of size or scale of a building model on induced pressures.
- For the case when the building (of different sizes) is placed at core radius, the range of mean and the minimum C_p shows some variation; however, the absolute value of mean and the minimum C_p generally do not differ by a large margin. The absolute value of mean and the

minimum C_p varies roughly about 3% to 30%. So, it seems like the influence of size of the building on induced pressures is more pronounced when the building is fully engulfed inside the core of tornado-like vortex rather than when it is located at the outer core (core radius) of tornado-like vortex. It can be clearly noticed that the size of building can influence the tornado-induced loads on the building. For building of size $0.10h_o \times 0.05h_o \times 0.05h_o$, the pressure coefficient on the westward face is about -1.7 whereas the corresponding C_p value for building of size $0.10h_o \times 0.10h_o \times 0.10h_o$ is roughly around -2.2. Considering these two values of C_p , the tornado-induced wind load on the westward face of the building varies roughly about 25% and similar trend can be observed for roof as well as the eastward wall. Hence, it seems critically important to consider an appropriate benchmark for size and scale of the building while determining tornado-induced wind loads on buildings.

- When the swirl ratio of stationary tornado-like vortex increases or when the tornado-like vortex gradually transitions from a single-celled vortex to a touched-down or a post-touched down vortex, the effect of drop in static pressure influencing the loading conditions on a building is also gradually reduced. As the swirl ratio of tornado-like vortex increases, the tangential velocity component becomes more stronger thus, it seems probable that the interaction of tornado-like vortices at high swirl ratio is more dominated by aerodynamic forces that involves separation of detached suction vortices, which then exhibit a circular motion around the building rather than the static pressure deficit. A tornado-like vortex interacting with building at higher swirl ratios engulfs a building completely within a larger core radius; however, due to a comparatively lower drop in static pressure deficit compared to a single-celled vortex as well as lower pressure gradient at the core of vortex, the range of pressure coefficient (C_p) goes on decreasing for larger swirl ratio cases.

8.3 Primary Contributions to the Scientific Community

The content of this thesis advances the existing body of knowledge by elucidating the details of the interaction of wind field of a tornado-like vortex with buildings of different sizes and different flow structures of tornado-like vortices. The salient research contributions of the current work are as follows:

- Development of a simple CFD model (resembling TTU tornado simulator) without turning vanes, fans, etc. that can run on a regular computer and can deliver a reliable solution within a reasonable time-frame. Because of the simplified CFD tornado simulator model, the computational cost of CFD simulation reduces significantly and a more refined study could be done with higher grid resolution at the core and at the base of the simulator.
- Identification of important tornado vortex features (touchdown swirl ratio (S_T), core radius (r_c), maximum tangential velocity (V_{tmax}), elevation of maximum tangential velocity (z_c) and pressure distribution with varying swirl ratios) for validation of CFD flow field which strongly influences the tornado-induced pressures on building.
- Categorization of different tornado simulators from the existing literature into 5 major types based on the recognition of similarity of flow pattern, which makes the comparison of flow field in different tornado simulators relatively systematic and easy.
- Validation of tornado-induced pressures on building from CFD model with experimental measurements. At present, the computed tornado pressures on building from CFD models lack validation with experimental measurements.

8.4 Limitations of Current Study

The conclusions reached in the current study are based on the datasets obtained by the 3D CFD tornado simulator model used in the current work. The details of the CFD model are provided in

Appendix A. The results and the conclusions drawn in this work pertains directly to the scope of the CFD model and the parameter ranges considered in this work.

In this work, the interaction of a stationary tornado-like vortex with building models is investigated instead of a translating vortex. Since, the real-life tornadoes are always translating in nature, so, the stationary tornado-like vortex considered in this work could be a possible limiting factor in extending the scope of the results in this work to real-life and practical applications. The pressures induced on the building by tornado-like vortex is the maximum for a single-celled vortex; however, it has been observed in real-life situations that a double-celled and multi-vortex tornadoes have caused huge economic losses and higher number of casualties. In real-life situation, debris impact due to wind-borne missiles is an important contributing factor for the wind loads. However, in this relatively simple CFD model, there is no way to account for the debris impact due to wind-borne missiles. Therefore, the analysis of datasets in this work may have led to the conclusion that a single-celled tornado-like vortex produces the most drastic loading conditions on a building as compared to the touched-down and double-celled tornado-like vortex.

Another limitation of the current work is that the building model considered in this work is impermeable. Therefore, the flow cannot enter the building at all; however, in a real-life situation, the wind flows can enter the building via openings such as the doors and the windows and can alter the internal pressures inside the building. This could be another limiting factor confining the scope of the results in this work to practical applications. In addition, the building used in the current work is modeled as a rigid structure; however, the real-world structures possess at least some degree of elasticity. This could be another factor to limit the scope of the work described in this thesis.

8.5 Suggested Future Work

In section 8.4, the limitations of the current work were discussed. Based on the same discussion, several topics have been identified for future research. The topics identified for future research are discussed below in a sequential order.

- First of all, the interaction of a stationary tornado-like vortex with building is considered in this work. In the future, the interaction of a translating tornado-like vortex with building model can be investigated to learn if translation of vortex has any effect on the interpretation of pressures and forces on the building.
- In this work, a preliminary study is carried out on the influence of Reynolds number's effect on the pressures induced by a tornado-like vortex but only a double-celled vortex is considered here. In the future, more exhaustive studies can be carried out using different combinations of Reynolds number and flow structure of tornado-like vortex.
- The building considered in this work is modeled as a rigid structure, which does not deform under the influence of applied wind loads (pressure and shear stress due to the vortex flow). In reality, however, a structure experiences an incremental effect on deformation due to the application of wind loads due to the vortex flow. To capture such effects, a two-way coupled CFD-FEM simulation in which the deformed state of the structure is shared between the CFD and FEM solver can be implemented in the future computer models. This would help in better understanding of the deformation of building models exposed to tornado-like winds and the failure mechanism.
- As pointed out earlier, in this model, there is no way to account for the debris impact on the building due to wind-borne missiles. In the future models, CFD-DEM coupling could be

applied or the debris could be modeled as Lagrangian particles to account for the effect of wind-borne debris on buildings.

- In this work, it is concluded that a single-celled flow structure of tornado-like vortex produces the most drastic loading conditions on a building; however, it may not be practical to develop wind load provisions based on a single flow structure of vortex. For future studies, the historical database pertaining to occurrence of tornadoes of different intensities (EF scale) in different states/regions of mainland United States could be considered for statistical analysis (such as the frequency of occurrence of tornadoes of different intensities, the return period and the probability of exceedence of a tornado of a given intensity). From the analysis, a probabilistic framework of design for buildings subjected to tornadoes of varying intensities could be developed in the future.

References

1. Alipour, A., Sarkar, P., Dikshit, S., Razavi, A. and Jafari, M. (2020), Analytical approach to characterize tornado-induced loads on lattice structures, *J. Struct. Eng.*, 146, Article 04020108.
2. Alrasheedi, N.H. & Selvam, R.P. (2011), Tornado forces on different building sizes using compuser modeling, 2011 ECTC Proceedings, ASME Early Career Technical Conference, March 31-April 02, Hosted by ASME District E and University of Arkansas, Fayetteville, AR.
3. Alexander, C.R. & Wurman, J. (2005), The 30 May 1998 Spencer, South Dakota, Storm. Part I: The Structural Evolution and Environment of the Tornadoes, *Mon. Wea. Rev.*, 133, 72-97.
4. Anderson, J.D. (2014), Fundamentals of Aerodynamics, 5th ed. McGraw Hill Education Private Limited.
5. Baker, C. & Sterling, M. (2019), Are Tornado Vortex Generators fit for purpose? *J. Wind Eng. Ind. Aerodyn.*, 190, 287-292.
6. Bluestein, H.B. & Pazmany, A.L. (2000), Observations of Tornadoes and Other Convective Phenomena with a Mobile, 3-mm Wavelength, Doppler Radar: The Spring 1999 Field Experiment, *Bull. American Meteor. Soc.*, 81, 2939-2952.
7. Bluestein, H.B., Weiss C.C. & Pazmany A.L (2004), The vertical structure of a tornado near Happy, Texas, on 5 May, 2002: high-resolution, mobile, W-band, doppler radar observations, *Monthly Weather Review*, 132, 2325-2337.
8. Cao S., Wang J., Cao J., Zhao L., Chen X. (2015), Experimental study of wind pressures acting on a cooling tower exposed to stationary tornado-like vortices, *J. Wind Eng. Ind. Aerodyn.*, 145, pp. 75-86.
9. Cengel, Y. A. & Cimbala J.M. (2014), Fluid mechanics: Fundamentals and applications. 3rd ed. New York: McGraw Hill.
10. Church, C.R., Snow, J.T. & Agee, E.M. (1977), Tornado Vortex Simulation at Purdue University, *Bull. Amer. Meteor. Soc.*, 58, 900-909.
11. Church, C.R., Snow, J.T., Baker, G.L., & Agee E.M. (1979), Characteristics of tornado-like vortices as a function of swirl ratio: a laboratory investigation, *J. Atmos. Sci.*, 36, 1755–1776.
12. Davies-Jones, R.P. (1973), The dependence of core radius on swirl ratio in a tornado simulator, *J. Atmos. Sci.*, 30, 1427-1430.
13. Doswell, C.A. III, Brooks, H.E., Dotzek, N. (2009), On the implementation of the enhanced fujita scale in the USA, *Atmos Res*, 93, 554–563.
14. Fangping, Y., Guirong, Y., Ryan, H., Isaac, K. M., & Ruoqiang, F. (2016), Effects of chamber shape on simulation of tornado-like flow in a laboratory, Proceedings of Engineering Mechanics Institute Conference, chapter 8.

15. Fujita, T.T. (1971), Proposed characterization of tornadoes and hurricanes by area and intensity, SMRP Research Paper 91, University of Chicago, IL, 42 pp.
16. Gairola, A. (2017), Generic numerical tornado model for common interpretation of existing experimental simulators, Master's thesis, Department of Civil and Environmental Engineering, University of Western Ontario.
17. Gairola, A., Bitsuamlak, G. (2019), Numerical tornado modeling for common interpretation of experimental simulators, *J. Wind Eng. Ind. Aerodyn.*, 186, 32-48.
18. Gillmeier, S. (2019), An investigation concerning the simulation of tornado-like vortices, PhD dissertation, University of Birmingham.
19. Gorecki, P.M. & Selvam, R.P. (2015), "Rankine combined vortex interaction with rectangular prism", *Int. J. Comput. Fluid Dynam.*, 29, 120-132.
20. Haan, F.L., Sarkar, P.P. & Gallus, W.A. (2008), Design, construction and performance of a large tornado simulator for wind engineering applications, *Engineering Structures*, 30, 1146-1159.
21. Haan Jr. F.L, Balaramudu, V.K. & Sarkar, P.P. (2010), Tornado-induced wind loads on a low-rise building, *J. Struct. Eng.*, 136, 106-116.
22. Hangan, H., Kim, J.D., (2008), Swirl ratio effects on tornado vortices in relation to the Fujita scale. *Wind Struct.*, 11, 291–302.
23. Hangan H. (2014), The wind engineering energy and environment (WindEEE) Dome at Western University, Canada, *Wind Engineers*, JAWWE, 39.
24. Harlow, F.H., & Stein L.R. (1974), Structural Analysis of Tornado-like Vortices, *J. Atmos. Sci.*, 31, 2081-2098.
25. Hirt, C. W. & Cook, J. L. (1972), The calculation of three-dimensional flows around structures and over rough terrain, *Journal of Computational Physics*, 10, 324-340.
26. Hu, H., Yang, Z., Sarkar, P. et al. (2011), Characterization of the wind loads and flow fields around a gable-roof building model in tornado-like winds. *Exp Fluids*, 51, 835.
27. Huang, Z., Fan, X., Cai, L. et al. (2016), Tornado hazard for structural engineering, *Natural Hazards*, 83, 1821-1842.
28. Huo, S., Hemida, H. & Sterling, M. (2020), Numerical study of debris flight in a tornado-like vortex, *J. Fluids and Struct.*, 99, 103134.
29. Ishihara, T., Oh, S., & Tokuyama, Y. (2011), Numerical study on flow fields of tornado-like vortices using the LES turbulence model, *J. Wind Eng. Ind. Aerodyn.*, 99, 239-248.

30. Karami, M., Hangan, H., Carassale, L. & Peerhossaini, H. (2019), Coherent structures in tornado-like vortices, *Physics of Fluids*, 31, 085118.
31. Kashifizadeh, M.H, Verma, S., & Selvam, R.P. (2019), Computer modelling of close-to-ground tornado wind-fields for different tornado widths, *J. Wind Eng. Ind. Aerodyn.*, 191, 32-40.
32. Kashefzadeh, M. (2018), Computer Modeling of Close-to-Ground Tornado Wind-Fields for Different Tornado Widths. *Graduate Theses and Dissertations* Retrieved from <https://scholarworks.uark.edu/etd/2881>
33. Kikitsu H., Okuda Y., Kawai H., Kanda J. (2012), Experimental study on characteristics of tornado-induced wind force on a low-rise building, *Proceedings of the 22nd National Symposium on Wind Engineering*, 209-214.
34. Kikitsu, H., and Okuda, Y. (2016), Tornado-induced wind load model on a building considering relative size of building and tornado-like vortex, *In Proc., 6th U.S.-Japan Workshop on Wind Engineering*, 12 –14. Yokohama, Kanagawa: Yokohama National Univ. and Ames, IA: Iowa State Univ.
35. Kuai, L., Haan, F.L., Gallus, W. A. and Sarkar, P. (2008), CFD simulations of the flow field of a laboratory-simulated tornado for parameter sensitivity studies and comparison with field measurements, *Wind and Struct.*, 11, 75-96.
36. Leonard, B.P. (1979), A stable and accurate convective modelling procedure based on quadratic upstream interpolation, *Comput. Methods Appl. Mech. Eng.*, 19, 1, 59-98.
37. Lewellen, W.S., Lewellen, D.C., Sykes, R.I. (1997), Large-eddy simulation of a tornado's interaction with the surface, *J. Atmos. Sci.*, 54, 581-605.
38. Lewellen, D.C., Lewellen, W.S. (2007), Near-surface intensification of tornado vortices. *J. Atmos. Sci.*, 64, 2176-2194.
39. Li, T., Yan, G., Yuan, F., & Chen G. (2019), Dynamic structural responses of long-span dome structures induced by tornadoes, *J. Wind Eng. Ind. Aerodyn.*, 190, 293-308.
40. Li, T, Yan, G., Feng, R., & Mao X., (2020), Investigation of the flow structure of single- and dual-celled tornadoes and their wind effects on a dome structure, *Eng. Struct.*, 209, 109999.
41. Liu, Z., Ishihara, T. (2015a), A study of tornado induced mean aerodynamic forces on a gable-roofed building by the large eddy simulations, *J. Wind Eng. Ind. Aerodyn.*, 146, 39-50.
42. Liu, Z., Ishihara, T. (2015b), Numerical study of turbulent flow fields and the similarity of tornado vortices using large-eddy simulations, *J. Wind Eng. Ind. Aerodyn.*, 145, 42-60.
43. Liu, Z., Zhang, C. and Ishihara, T. (2018), Numerical study of the wind loads on a cooling tower by a stationary tornado-like vortex through LES, *J. Fluids and Struct.*, 81, 656-672.

44. Matsui, M., Tamura, Y. (2009), Influence of swirl ratio and incident flow conditions on generation of tornado-like vortex, *Proceedings of EACWE 5*, Florence, Italy.
45. Mayer, L.J., (2009). Development of a Large-scale Simulator. M.S. thesis. Texas Tech University.
46. McDonald, J.R. (2001). T. Theodore Fujita: His contribution to tornado knowledge through damage documentation and the Fujita scale, *Bull. of American Meteorol. Soc.* 82, 63-72.
47. McDonald, J.R, Mehta, K.C., Smith, D.A. & Womble, J.A. (2009), The Enhanced Fujita Scale: Development and Implementation, *Fifth Forensic Engineering Congress, Washington D.C., American Society of Civil Engineers*, 719-728.
48. Mishra, A.R., James, D.L., Letchford, C.W. (2008), Physical simulation of a single-celled tornado-like vortex, Part B: Wind loading on a cubical model, *J. Wind Eng. Ind. Aerodyn.*, 96, 1258-1273.
49. Nasir, Z., Bitsuamlak, G.T., Hangan, H. (2014), Computational modeling of tornadic load on a building, *6th International Symposium on Computational Wind Engineering*, Hamburg, Germany, June 8-12, 2014.
50. Nasir, Z., & Bitsuamlak, G.T. (2016), NDM-557: Computational Modeling of Hill Effects on Tornado-like Vortex, *In: CSCE Annual Conference*, London Convention Center, London, Ontario, Canada.
51. Natarajan, D., (2011), Numerical simulation of tornado-like vortices, PhD dissertation, University of Western Ontario.
52. Natarajan, D., & Hangan, H. (2012), Large eddy simulations of translation and surface roughness effects on tornado-like vortices, *J. Wind Eng. Ind. Aerodyn.*, 104-106, 577-584.
53. Nolan, D.S., Farrell, B.F. (1999), The structure and dynamics of tornado-like vortices, *J. Atmos. Sci.*, 56, 2908-2936.
54. Potter, S. (2007), Fine-tuning Fujita: after 35 years, a new scale for rating tornadoes takes effect, *Weatherwise*, 60, 64–71.
55. Razavi, A., & Sarkar, P. (2018), Tornado-induced wind loads on a low-rise building: Influence of swirl ratio, translation speed and building parameters, *Eng. Struct.*, 167, 1-12.
56. Refan, M., Hangan, H. & Wurman. J. (2014), Reproducing tornadoes in laboratory using proper scaling, *J. Wind Eng. Ind. Aerodyn.*, 135, 136-148.
57. Refan, M., & Hangan, H. (2016), Characterization of tornado-like flow fields in a new model scale wind testing chamber, *J. Wind Eng. Ind. Aerodyn.*, 151, 107-121.
58. Refan, M., & Hangan, H. (2018), Near surface experimental exploration of tornado vortices, *J. Wind Eng. Ind. Aerodyn.*, 175, 120-135.

59. Rotunno, R. (1977), Numerical simulation of a laboratory Vortex, *J. Atmos. Sci.*, 34, 1942–1956.
60. Rotunno, R. (1979), A study in tornado-like vortex dynamics, *J. Atmos. Sci.*, 36, 140-155.
61. Rotunno, R. (2013), The Fluid Dynamics of Tornadoes, *Annual Review of Fluid Mechanics*, 45, 59-84.
62. Sabareesh, G.R., Matsui, M., Tamura, Y, (2012), Dependence of surface pressures on a cubic building in tornado like flow on building location and ground roughness, *J. Wind Eng. Ind. Aerodyn.*, 103, 50-59.
63. Sabareesh, G.R., Matsui, M., Tamura, Y. (2013), Ground roughness effects on internal pressure characteristics for buildings exposed to tornado-like flow, *J. Wind Eng. Ind. Aerodyn.*, 122, 113-117.
64. Schlueter, M. (2016, May 19), How the definition of “collapse” can affect property insurance coverage, Schlueter, Mahoney & Ross, P.C.
<https://www.smlaw.net/resource/how-the-definition-of-collapse-can-affect-property-insurance-coverage/>
65. Seimon, A., Allen, J. T., Seimon, T. A., Talbot, S. J., & Hoadley, D. K. (2016). Crowdsourcing the El Reno 2013 Tornado: A New Approach for Collation and Display of Storm Chaser Imagery for Scientific Applications, *Bull. of the Amer. Meteorol. Soc.*, 97, 2069-2084.
66. Selvam, R.P. (1997), Finite element modelling of flow around a circular cylinder using LES, *J. Wind Eng. Ind. Aerodyn.*, 67-68, 129-139.
67. Selvam, R.P., Millett, P.C. (2003), Computer modeling of tornado forces on buildings, *Wind and Struct.*, 6, 209-220.
68. Selvam, R.P., Millett, P.C. (2005), Large eddy simulation of the tornado-structure interaction to determine structural loadings, *Wind and Struct.*, 8, 49-60.
69. Sengupta, A., Haan, F.L., Sarkar, P.P., Balaramudu, V. (2008). Transient loads on buildings in microburst and tornado winds, *J. Wind Eng. Ind. Aerodyn.*, 96, 2173-2187.
70. Tang, Z., Feng, C., Wu, L. et al. (2018 a), Characteristics of tornado-like vortices simulated in a large scale wind type simulator, *Boundary-Layer Meteorol.*, 166, 327-350.
71. Tang, Z., Zuo, D., James, D. et al. (2018 b), Effects of aspect ratio on laboratory simulation of tornado-like vortices, *Wind and Struct.*, 27, 111-121.
72. Verma, S., Selvam, R.P. (2020), CFD to VorTECH pressure field comparison & roughness effect on flow, *J. Struct. Eng.*, 146, 04020187-1 to 12.

73. Verma, S., Selvam, R.P. (2021a), Effect of height of the tornado chamber on vortex touchdown. In: Rushi Kumar B., Sivaraj R., Prakash J. (eds) *Advances in Fluid Dynamics. Lecture Notes in Mechanical Engineering*. Springer, Singapore.
74. Verma, S., & Selvam, R. P. (2021b). CFD model validation with experimental tornado wind field & comparison of wind field in different tornado chambers. *Wind and Struct.*, 33, 367–381.
75. Verma, S. and Selvam, R.P., (2021c). Differences in flow structures of tornado vortex and efficiency of different tornado chambers, *6th AAWE workshop organized by Clemson University*. <https://tigerprints.clemson.edu/cgi/viewcontent.cgi?article=1075&context=aawe>
76. Wang, J., Cao, S., Pang, W., Cao, J. and Zhao, L. (2016), Wind-load characteristics of a cooling tower exposed to a translating tornado-like vortex, *J. Wind Eng. Ind. Aerodyn.*, 158, 26-36.
77. Ward N.B. (1972), The exploration of certain features of tornado dynamics using a laboratory model, *J Atmos. Sci.*, 29, 1194-1204.
78. Yang, Q., Gao, R., Bai, F. et al. (2018), Damage to buildings and structures due to recent devastating wind hazards in East Asia, *Nat Hazards*, 92, 1321–1353.
79. Ying, S. J., & Chang, C. C., (1970), Exploratory model study of tornado-like vortex dynamics. *J. Atmos. Sci.*, 27, 3–14.
80. Yuan F., Yan, G., Honerkamp, R. (2019), Numerical simulation of laboratory tornado simulator that can produce translating tornado-like wind flow, *J. Wind Eng. Ind. Aerodyn.*, 190, 200-217.

Appendices

Appendix A: User Manual for CFD Program - “ward79.out”

A.1 Introduction and Overview

The study carried out in this work is undertaken by the 3D incompressible Navier-Stokes Equation solver (based on Finite Volume Method - FVM) developed by Dr. R. Panneer Selvam. Using the Linux executable “**ward79.out**”, the author designed the mesh for computational domain and performed calculations on flow parameters to be used as input for CFD simulation. The Linux executable “**ward76.out**” (obtained by compiling ForTRAN code) computes the tornado wind field around a building which can be placed at different locations within the computational domain. This code has a feature that different K-planes (K-index) can be selected by the user to visualize the tornado wind field around the building at different elevations from the base (or ground level).

A.2 Preparation of Input Data File

The required input data files for code execution are “**ward74-i.txt**”. Another text file named “**char.txt**” should also be contained in the same working folder. During the execution of program, the name of the files (such as mv1.plt, mv2.plt,...,etc.) will be picked from the text file “**char.txt**” for writing the contour plots at different time-steps at the elevation level (or K-index) specified by the user. The series of saved contour plot files are later used to make an animation for the evolution of tornado-like vortex over time in the computational domain.

Users can modify the numerical value for several keywords in the input data file; the variation of numerical values of those keywords leads to different geometrical configuration of the CFD tornado simulator and the tornado-like vortex simulated in it.

Following are the keywords used in the input data file, the variation of which leads to creation of different physical conditions and boundary conditions for the CFD model. Users should adjust the

numerical values based on flow calculations, desired level of mesh resolution, required flow structure (or swirl ratio) of tornado-like vortex and/or the intended geometric configuration of tornado simulator. If the simulation of tornado-like vortex is carried out in the presence of building then, the start and the end index for the building in XY-plane and the number of points up to the height of the building in the Z-direction should be specified. This program (ward79.out) can also be used for vortex simulation without the presence of the building by specifying the same value for start and end index for the building and specifying '0' as the number of points for elevation of the building. In the input data file, users should specify the numerical values for keywords in 3 lines similar to what is demonstrated below.

LINES FROM INPUT DATA FILE:

1. READ (4, *) HVMIN, HVMAX, FAC, XMAX, ZMAX, DTT, REN, S, TTIME

HVMIN	Min spacing in between the grid lines in the vertical direction = 0.01
HVMAX	Max allowed spacing in between the grid lines in the vertical direction = 0.05
FAC	Stretching Factor for grid spacing from minimum grid spacing = 1.1
XMAX	Maximum distance for the grid in X-direction = 2.0
ZMAX	Maximum distance for the grid in Z-direction = 6.0
DTT	Time step size = 0.001
REN	Reynolds Number = 2.755e5
S	Swirl Ratio
TTIME	Total Simulation time = 30.1

2. READ (4, *) HXMIN, HXMAX, ZHOLE, IMOVIE, IFLAG, C11, Z0, ZH

HXMIN	Min grid spacing in the horizontal direction = 0.01
HXMAX	Max allowed grid spacing in the horizontal direction = 0.05

ZHOLE	Height from the base of CFD simulator for locating the effective top hole
IMOVIE	Interval for time step index for writing two successive movie files
IFLAG	Index number of the time-step from which the movie files are written
C11	Roughness parameter (=0.0924) at reference height of 1.0 non-dimensional units (at the radius of the updraft hole) defined by U^*/K , where U^* = Shear velocity and K = Von-Karman Constant = 0.4
Z0	Roughness height = 0.00004
ZH	Height of the inlet =1.0 (1 m height which is equivalent to 1.0 unit in non-dimensional form)

3. READ (4, *) IMK1, IMK2, JMK1, JMK2, KH, IBUILX, IBUILZ, TAVE, KMOVIE

IMK1	Index for starting point of building in X-direction
IMK2	Index for end point of building in X-direction
JMK1	Index for starting point of building in Y-direction
JMK2	Index for end point of building in Y-direction
KH	Number of points from base (or ground level) up to building height
IBUILX	No. of points on either side of center of CFD simulator for which uniform minimum spacing value is considered in X-direction
IBUILZ	No. of points in Z-dir. for which uniform min spacing value is considered
TAVE	Time from which the time-averaging and calculation of pressure statistics on building faces starts
KMOVIE	K-index from base (or ground) where the movie files are written for making animation/movie file

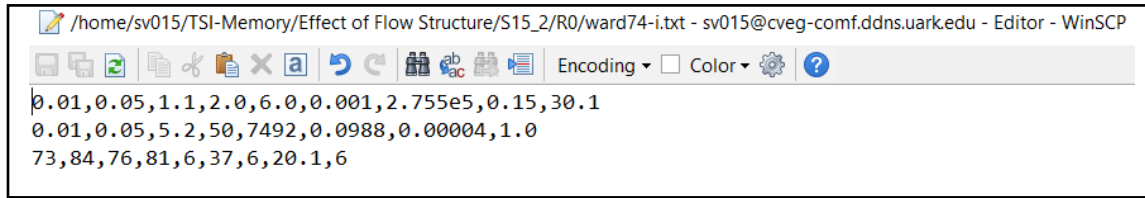


Fig. A-1. Sample data for Input Data File

A.3 Output Files Obtained from the Program

Several output files are created in the directory where the Linux executable resides once the execution of program (**ward79.out**) starts. These output (Tecplot) files contain the necessary data and information for post-processing of CFD simulation results. The output files are: (1) ward74-o.plt (2) ward74-p.plt (3) ward74-gr.plt (4) ward74-m.txt (5) mv1.plt and so on up to the end of simulation time.

CAUTION: The output files listed above are the files generated by Linux executable (**ward79.out**). If the user wants to run the same executable after making some modifications to the input data file, then the output files obtained earlier should be renamed before executing the program. If not renamed, the output data files are overwritten when the program is executed the second time and valuable data may be lost.

To tackle this problem, the program can be executed from different directories such as if we want to obtain data for three different swirl ratios then, we can create three different directories for three different swirl ratio case studies, modify the input file as required in each of the directories and then run the executable through their own respective directories.

Appendix B: A Simple CFD Tornado Simulator Implementation in OpenFOAM

Abstract

Tornadoes have caused the loss of billions worth of properties and hundreds of casualties in the United States. In addition to the US, Canada, China, and Europe too have encountered numerous tornadoes over the past couple of decades and the trend is expected to continue in the coming days as well when the conditions required for tornado-spawning thunderstorms are met. Even though the occurrence and/or the frequency of natural hazards (such as tornadoes) are beyond our control, nevertheless, the engineering community collectively can certainly contribute to better understanding of the wind field (velocity and pressure distribution) of tornado vortices as well as the nature and magnitude of forces that these severe storms produce on buildings and built-up infrastructure. Such understanding can help to design the buildings and the built-up infrastructure adequately, thus, diminishing (or possibly eliminating) the loss of lives and properties in the future. Hence, in this work, the implementation of a simple numerical tornado simulator using OpenFOAM (OF) is discussed. The details of the employed model including the implementation of boundary conditions are discussed in detail. The distribution of tangential velocity and pressure distribution in a tornado vortex is extracted and compared/validated with the experimental measurements. It is demonstrated that OpenFOAM can be employed as a reliable CFD solver for simulating tornado vortices and computing the pressures and forces exerted by tornado vortices on the buildings and the built-up infrastructure.

1. Introduction

Tornadoes have caused the loss of billions worth of properties [1] as well as hundreds of casualties [2]. So, the exploration of tornado wind field and the pressures (or forces) induced by tornadoes on buildings and the built-up infrastructure has received more attention in the research community

in the past couple of decades. The first step in building safer infrastructure against the tornadic hazards is to develop a sound understanding of the wind field of the tornado vortex itself and many field campaigns have been carried out with the same motivation in the past [3], [4], [5], [6]. Field studies involve chasing and tracking a live tornado in real-time using radar instruments mounted on a vehicle to capture its wind field (velocity and pressure distribution). However, such pursuits can be extremely risky and life threatening at times. Besides, the resolution of measurements (which may be in few kilometers to a few hundred meters resolution) provided by field measurements is inadequate for engineering purposes (which may require a resolution in measurement of a few meters to a few centimeters). Due to these challenges, gradually, the research community started studying about the wind field of tornado vortices in experimental tornado simulators [7], [8], [9], [10], [11]. Although some of the challenges encountered in the field studies of tornadoes were circumvented by experimental tornado simulation, there were other challenges with this approach. Firstly, a scaled-down model of building is used in experimental tornado simulators to measure the pressures and forces exerted by tornadic wind flows; however, due to small size of the model, it becomes difficult to acquire the velocity and pressure measurements with required resolution. Secondly, the cost of construction, operation and maintenance of experimental tornado simulators is very high. Due to these drawbacks with experimental simulation of tornado-like vortices, numerical simulation of tornado-like vortices using Computational Fluid Dynamics has been gaining momentum in the research community to explore the wind field of tornado-like vortices and the pressures exerted by tornadic winds on the buildings and the built-up infrastructure. Numerical simulation of tornado vortices can be traced back to as early as 1970s and 1980s. Early CFD simulation of tornado vortices mostly entailed modeling the wind field of tornado vortex by a simple axisymmetric wind field comprising of

rotating winds [12], [13]. However, it was realized later that the wind field of a tornado vortex bears a three-dimensional character where all the 3 velocity components play an important role in defining its velocity profile and pressure distribution. Thus, in the recent times, CFD studies on numerical simulation of tornadoes have been carried out using a replica CAD geometry of the popular experimental tornado simulators [9], [10], [11]. However, in those replica CFD tornado simulators [14], [15], some simplifications have been applied such as modeling the outlet as outflow (zero gradient) boundary condition instead of modeling the physical fans and applying pressure jump [15] to mimic the effect of fans. Despite these sophisticated numerical models, an engineer/designer can barely estimate the value of wind loads reliably for design of buildings from the existing literature. In addition, the access to numerical tornado simulator model is severely restricted to select research groups in select universities pursuing research on numerical simulation of tornadoes and its fluid-structure interaction. Thus, in this work, a simple tornado simulator is modeled and the details of the implementation of the simulator model using OpenFOAM is discussed. In addition, the flow visualizations obtained from the CFD model are qualitatively compared and the pressure profile is quantitatively validated with experimental tornado simulator (called VorTECH) measurements. Further details about the experimental tornado simulator and the wind field obtained in the simulator facility can be obtained from [11], [16].

2. Simplified Geometrical Idealization for CFD Tornado Simulator

In Fig. B-1 (a), a 3D view of experimental tornado simulator at Texas Tech University (also called VorTECH) is shown with a prismatic building model placed at the center of simulator whereas in Fig. B-1 (b), the equivalent CFD model considered for this work is shown. In Fig. B-1 (a), the fans and the turning vanes of the experimental tornado simulator are not drawn. Further details on the geometry of VorTECH simulator can be obtained from [11] and [16]. The experimental tornado

simulator is octagonal in shape with 8 fans of 1.2192 m (4 ft.) diameter each. The inlet height of experimental tornado simulator is $h_o = 1$ m and the updraft radius is $r_{up} = 2$ m. The aspect ratio of the experimental tornado simulator is thus maintained at aspect ratio $(a) = h_o/r_{up} = 0.5$. The total height of the experimental tornado simulator is $H = 5.96$ m.

To create a replica CFD model of tornado simulator, some simplifications are applied to the numerical model implemented in this work. Firstly, the octagonal shape of experimental tornado simulator (with an inscribed circle diameter of 4m) is approximated with a circular section of a cylinder with the same diameter of 4 m. The inlet height (h_o) is kept at 1m (same as the experimental tornado simulator) and the total height (H) is approximated as 6m. Similarly, the updraft radius ($r_{up} = 2$ m) for the CFD tornado simulator is kept the same as the experimental tornado simulator. However, the outlet region provided by 8 fans of 1.2192 m diameter each in the experimental tornado simulator is replaced in the CFD tornado simulator by an effective outlet height of 0.743 m. The effective height for the CFD tornado simulator is simply obtained by equating the combined area of the 8 fans of the experimental tornado simulator with the curved surface area of the cylindrical domain at the outlet region as shown in Fig. B-1 (b).

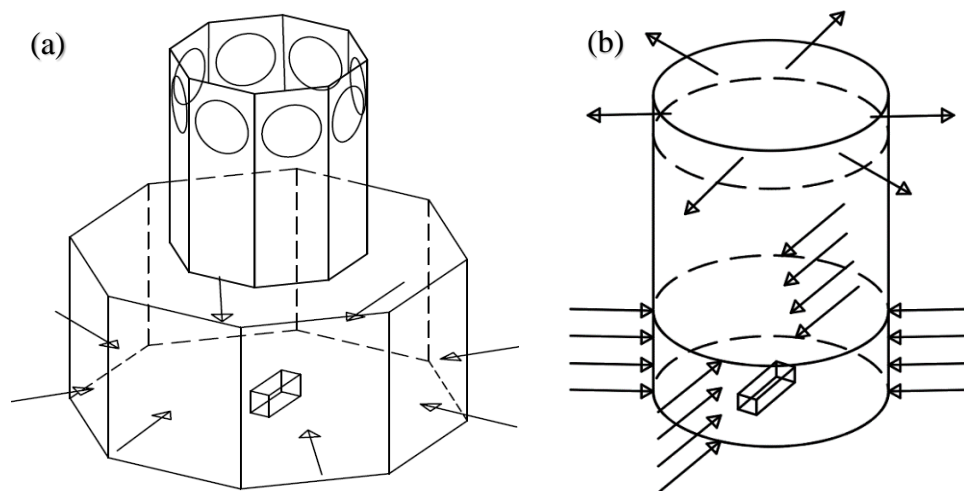


Fig. B-1. (a) Experimental tornado simulator VorTECH at Texas Tech University (b) Simplified CFD tornado simulator

3. Mathematical Formulation

3.1 Governing Equations

The governing equations for incompressible fluid flow of Newtonian fluid are given by

$$\nabla \cdot \mathbf{u} = 0 \quad (1)$$

$$\frac{\partial \mathbf{u}}{\partial t} + \nabla \cdot (\mathbf{u}\mathbf{u}) = -\nabla \mathbf{p} + \nu \nabla^2 \mathbf{u} + \mathbf{F} \quad (2)$$

In Eq. (2), the convection part comprises of multiplication of velocity vector (\mathbf{u}) by itself finally resulting in a tensor. Such multiplication is also known as dyadic multiplication. Also, the pressure (\mathbf{p}) in equation (2) is the kinematic pressure given by (P/ρ), where ‘ P ’ is the dynamic pressure and ‘ ρ ’ is the density of the fluid and ‘ \mathbf{F} ’ is the external force (or source term) in the momentum equation. In Large Eddy Simulation (LES), the governing equations are spatially averaged using a low-pass filter resulting in the following form:

$$\nabla \cdot \tilde{\mathbf{u}} = 0 \quad (3)$$

$$\frac{\partial \tilde{\mathbf{u}}}{\partial t} + \nabla \cdot (\tilde{\mathbf{u}}\tilde{\mathbf{u}}) = -\nabla \tilde{\mathbf{p}} + \nu \nabla^2 \tilde{\mathbf{u}} + \tilde{\mathbf{F}} \quad (4)$$

In Eq. (3) and (4), the symbol tilde ‘ \sim ’ used over the variables represent the spatially averaged terms. Different filtering functions can be applied for the low pass filter; however, the most common filter is the top-hat filter, which physically signifies the volume average of a physical quantity in a cell of finite volume mesh. For homogeneous filters (i.e., the filters for which filtering, and differentiation does not depend on the spatial coordinates), the following is obtained:

$$\nabla \cdot (\tilde{\mathbf{u}}\tilde{\mathbf{u}}) = \nabla \cdot (\tilde{\mathbf{u}} \tilde{\mathbf{u}}) + \nabla \cdot \boldsymbol{\tau}^{sgs} \quad (5)$$

In Eq. (5), ' τ^{sgs} ' or ' τ_{ij}^{sgs} ', in tensor notation is called the residual stress tensor or the subgrid-scale (SGS) stress tensor. Using the principles of tensor mathematics, a stress tensor can be split into two parts: i.e. (a) a hydrostatic (isotropic) part and (b) a deviatoric part.

$$\tau_{ij}^{dev} = \tau_{ij}^{sgs} - \frac{1}{3} \delta_{ij} \tau_{kk} \quad (6)$$

In Eq. (6), the term ' $\frac{1}{3} \delta_{ij} \tau_{kk}$ ' is the hydrostatic part of stress tensor and the negative sign implies a compressive stress due to the action of pressure force. Thus, Eq. (4) finally takes the following form:

$$\frac{\partial \tilde{u}}{\partial t} + \nabla \cdot (\tilde{u} \tilde{u}) = - \nabla \tilde{p} + \nu \nabla^2 \tilde{u} - \nabla \cdot \tau_{ij}^{sgs} + \tilde{F} \quad (7)$$

Considering that there are no external forces on the fluid, the term ' \tilde{F} ' can be dropped from Eq. (7) resulting in

$$\frac{\partial \tilde{u}}{\partial t} + \nabla \cdot (\tilde{u} \tilde{u}) = - \nabla \tilde{p} + \nu \nabla^2 \tilde{u} - \nabla \cdot \tau_{ij}^{sgs} \quad (8)$$

The hydrostatic part of SGS tensor can be incorporated into the pressure term and the effect of deviatoric part of stress tensor is modeled analogously to the viscous stress tensor. Thus, the following form is obtained.

$$\tau_{ij}^{sgs} = -\tau_{ij}^{dev} + \frac{1}{3} \delta_{ij} \tau_{kk} \quad (9)$$

$$\tau_{ij}^{dev} = 2\nu_{sgs} \tilde{S}_{ij} \quad (10)$$

In Eq. (10), the filtered rate of strain tensor is given by

$$\tilde{S}_{ij} = \frac{1}{2} \left(\frac{\partial \tilde{u}_i}{\partial \tilde{x}_j} + \frac{\partial \tilde{u}_j}{\partial \tilde{x}_i} \right) \quad (11)$$

For the current work, Smagorinsky sub-grid stress model is used and the turbulent kinematic viscosity ' ν_{sgs} ' used in the Smagorinsky model is given by

$$\nu_{sgs} = C_k \Delta k^{0.5} \quad (12)$$

In Eq. (12), ‘k’ represents the turbulent kinetic energy, which is obtained by solving the following quadratic equation:

$$ak^2 + bk + c = 0 \quad (13)$$

The coefficients of the quadratic equation are given by

$$\left. \begin{aligned} a &= \frac{C_e}{\Delta} \\ b &= \frac{2}{3} * \text{tr}(\mathbf{D}) \\ c &= 2 C_k \Delta (\text{dev}(\mathbf{D}) : \mathbf{D}) \\ \mathbf{D} &= 1/2 (\nabla \mathbf{u} + \nabla (\mathbf{u}^T)) \end{aligned} \right\} \quad (14)$$

, where $\text{tr}(\mathbf{D})$ represents the trace of tensor ‘D’ and $\text{dev}(\mathbf{D})$ represents the deviatoric of tensor ‘D’ and finally, the default model coefficients used in OpenFOAM for ‘C_e’ and ‘C_k’ are 1.048 and 0.094 respectively.

3.2 Non-dimensional Form of Navier-Stokes Equation

In this work, non-dimensional form of Navier-Stokes (NS) is used. The reference values considered to non-dimensionalize the NS equation are (a) inlet height (h_o) for length scale and (b) radial velocity at inlet height (V_{ro}) for velocity. If x, y, and z denote the coordinates along x-axis, y-axis, and z-axis of the discretized computational domain in dimensional form then, the corresponding non-dimensional coordinates are given by x^{*}, y^{*} and z^{*} respectively. Similarly, if U, V, and W denote the velocity components along x-axis, y-axis, and z-axis in the discretized computational domain in dimensional form then, the corresponding non-dimensional velocities are given by U^{*}, V^{*} and W^{*} respectively. In the similar manner, the solved non-dimensional pressure field in the computational domain is represented by P^{*} for the actual physical pressure field (P). The relationship between the dimensional and the corresponding non-dimensional variables is as follows:

$$U^* = \frac{U}{V_{ro}} \quad V^* = \frac{V}{V_{ro}} \quad W^* = \frac{W}{V_{ro}} \quad x^* = \frac{x}{h_o} \quad y^* = \frac{y}{h_o} \quad z^* = \frac{z}{h_o} \quad t^* = \frac{V_{ro} t}{h_o} \quad P^* = \frac{P}{\rho V_{ro}^2} \quad Re^* = \frac{V_{ro} h_o}{\nu}$$

Further details about the conversion of dimensional form of NS equations to non-dimensional form can be obtained from [17].

3.2 Boundary Conditions

A logarithmic velocity profile is used to model the inlet velocities in X and Y direction for the tornado simulator. The vertical velocity component is considered zero throughout the inlet height. The maximum non-dimensional radial velocity is taken as $V_r(z = h_o) = V_{ro} = 1$, and the corresponding tangential component is designated as V_{to} . The distribution of radial velocity from the base of tornado simulator up to the inlet height is expressed as a function of elevation and is given as

$$V_r(z) = C_1 \ln\left(\frac{z+z_o}{z_o}\right) = C_1 \ln\left(1 + \frac{z}{z_o}\right) \quad (15)$$

The swirl ratio (S) for flow is calculated by

$$S = \frac{V_{to}}{2 \left(\frac{h_o}{r_{up}}\right) V_{ro}} \quad (16)$$

Using the definition of 'S', the tangential component of velocity is computed as

$$V_t(z) = 2 V_r(z) S \left(\frac{h_o}{r_{up}}\right) \quad (17)$$

Now, the velocity components in the radial and tangential direction needs to be resolved in the X and Y-direction to be provided as the boundary condition for the velocity inlet since the computational domain (cylinder) is based on Cartesian grid system. In this work, a tornado vortex rotating in anticlockwise direction is assumed. The radial and tangential velocity components are decomposed into its constituent x-component and y-component locally with respect to the direction (α) as shown in Fig. B-3. Here, the angle is always measured in the anticlockwise

direction from the local X-direction up to the direction of radial velocity component at the point of interest (P) (refer Fig. B-3). For instance, in Fig. B-3, the value of angle ' α ' is $(\pi + \tan^{-1} y/x)$ radians for a generic point in the first quadrant in which 'x' and 'y' are the x-coordinate and y-coordinate of point P respectively. For the 1st quadrant, the limits for the quadrant angle ' θ ' is given by $(0 \leq \theta \leq \pi/2)$ radians. Now, if the radial and tangential velocity components are decomposed in the local X-direction and Y-direction then, the effective velocity component in the X-direction and Y-direction are obtained as:

X-direction: $V_r \cdot \cos(\alpha) + V_t \cdot \cos(\alpha - \pi/2)$

Y-direction: $V_r \cdot \sin(\alpha) + V_t \cdot \sin(\alpha - \pi/2)$

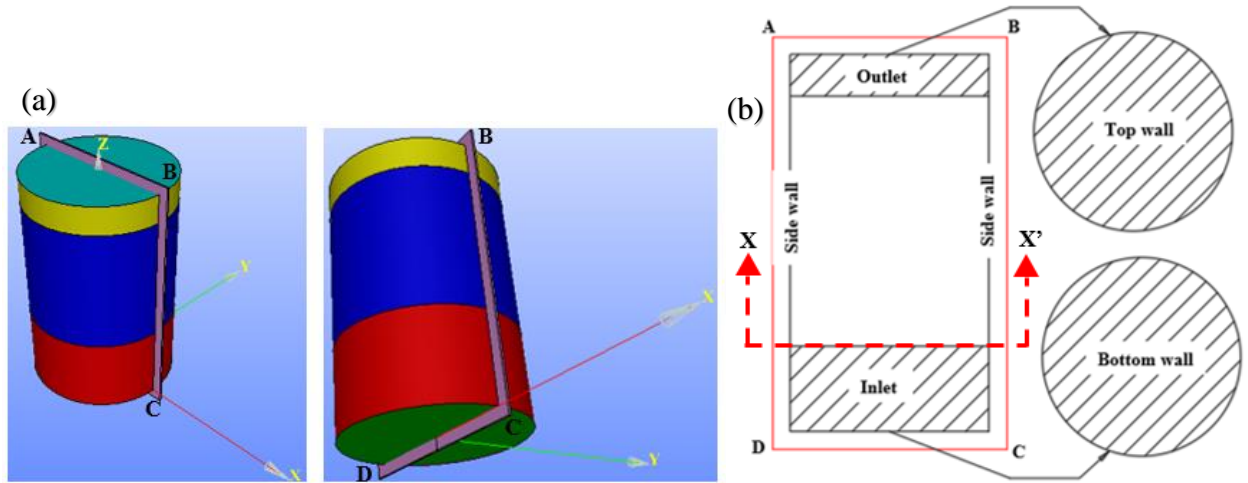


Fig. B-2. (a) 3D view of cylindrical computational domain showing different boundary faces (b) Sectional view through plane ABCD showing different boundaries for the computational domain

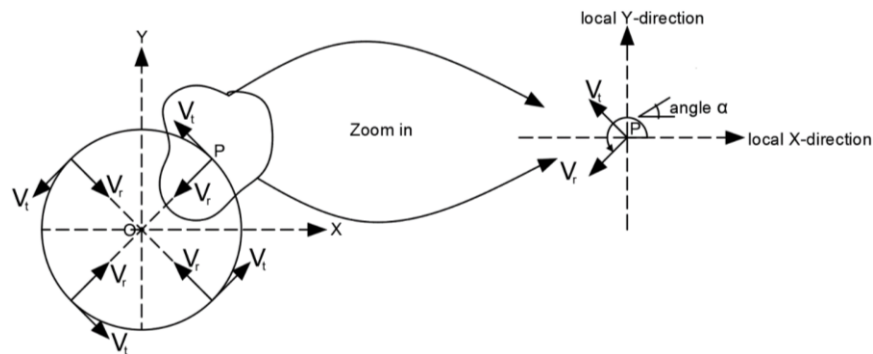


Fig. B-3. Top view for transverse section at X-X' showing velocity boundary condition at inlet height

In the similar manner, for each of the 4 quadrants, the value of angle ‘ α ’ is determined and the radial-tangential velocity components are resolved in the X (U_x) and Y-direction (U_y) and reported in Table B1. In Table B1, the Z-component (U_z) is taken as ‘0’ throughout the inlet height.

Table B1. Velocity boundary condition for the inlet patch of CFD tornado simulator

Quadrant	Angle ‘ α ’	U_x	U_y	U_z
1 st ($0 \leq \theta \leq \pi/2$)	$\pi + \tan^{-1}(y/x)$	$V_r * \cos(\alpha) + V_t * \cos(\alpha - \pi/2)$	$V_r * \sin(\alpha) + V_t * \sin(\alpha - \pi/2)$	0.0
2 nd ($\pi/2 \leq \theta \leq \pi$)	$\tan^{-1}(y/x)$	$V_r * \cos(\alpha) + V_t * \cos(\alpha - \pi/2)$	$V_r * \sin(\alpha) + V_t * \sin(\alpha - \pi/2)$	0.0
3 rd ($\pi \leq \theta \leq 3\pi/2$)	$2\pi + \tan^{-1}(y/x)$	$V_r * \cos(\alpha) + V_t * \cos(3\pi/2 + \alpha)$	$V_r * \sin(\alpha) + V_t * \sin(3\pi/2 + \alpha)$	0.0
4 th ($3\pi/2 \leq \theta \leq 2\pi$)	$\pi + \tan^{-1}(y/x)$	$V_r * \cos(\alpha) + V_t * \cos(\alpha - \pi/2)$	$V_r * \sin(\alpha) + V_t * \sin(\alpha - \pi/2)$	0.0

At the inlet, Neumann boundary condition, i.e., a zero gradient condition for pressure is applied for the pressure field. Similarly, at the walls (bottomWall, sideWall and topWall), no slip boundary condition is applied where the velocities are considered equal to ‘0’ and the gradient of pressure is also equated to ‘0’. For the outlet, an outlet pressure boundary condition is applied with pressure equated to ‘0’ and the gradients of velocity components are also taken as ‘0’. Different boundary conditions applied to different boundary faces of the computational domain are summarized in Table B2.

Table B2. Description of boundary faces, types, and boundary conditions for different faces in computational domain

S.N.	Boundary name	BC type	Color Coding	BC in mathematical form
1	Inlet	Patch	Red	velocity as per Table 1; $\frac{\partial p}{\partial n} = 0$
2	bottomWall	Wall	Green	$u = v = w = 0$; $\frac{\partial p}{\partial n} = 0$
3	sideWall	Wall	Blue	$u = v = w = 0$; $\frac{\partial p}{\partial n} = 0$
4	outlet	Patch	Yellow	$p = 0$; $\frac{\partial u}{\partial n} = \frac{\partial v}{\partial n} = \frac{\partial w}{\partial n} = 0$

Table B2. Description of boundary faces, types, and boundary conditions for different faces in computational domain (Cont.)

S.N.	Boundary name	BC type	Color Coding	BC in mathematical form
5	topWall	Wall	Cyan	$u = v = w = 0; \frac{\partial p}{\partial n} = 0$

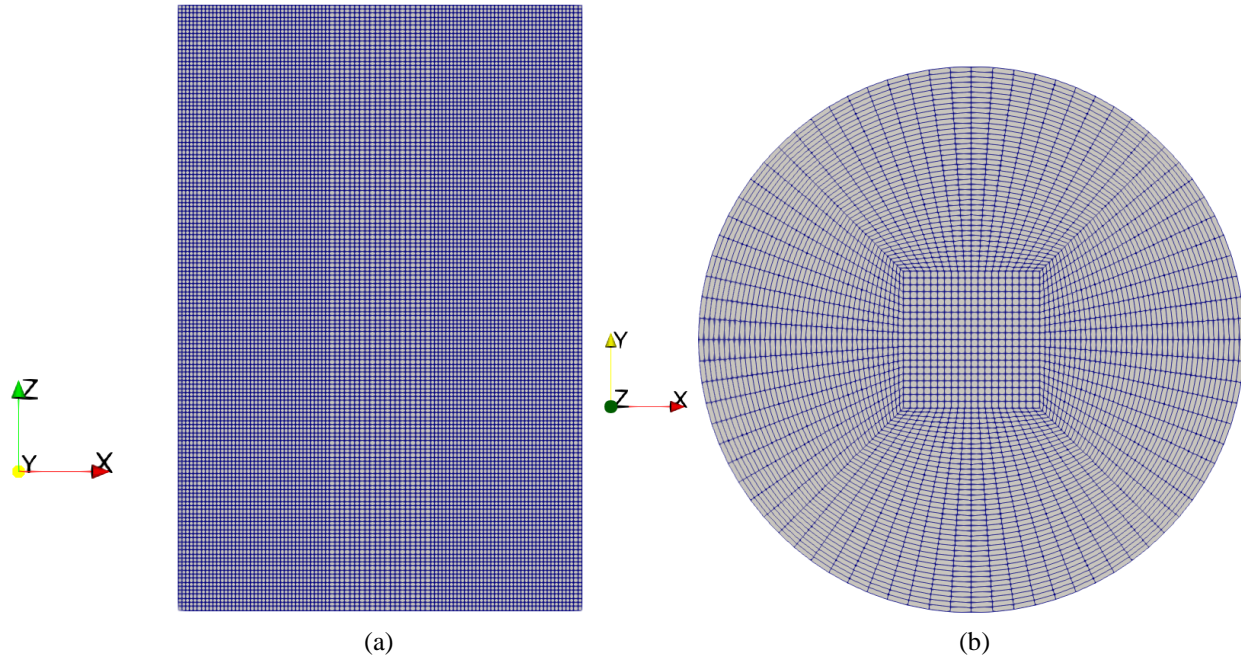


Fig. B-4. Mesh for the cylindrical computational domain (a) vertical section through the diametric axis of the cylinder showing elevation (b) horizontal section showing plan of the computational domain

The roughness parameters considered in the model are $z_o = 0.00004h_o$ and $C_1 = 0.0924V_{to}$ (refer Eq. (15)). The Reynolds number considered for flow computation is 2.755×10^5 , which is calculated at the inlet height (h_o) of tornado simulator. The elevation and plan of the mesh for the cylindrical computational domain is shown in Fig B-4 (a) and (b) respectively and it consists of 540,000 hexahedral cells.

3. Results and Validation

As the Reynolds number of flow is very high at $Re = 5.51 \times 10^5$, thus, the flow is highly turbulent and so the flow properties (velocity and pressure) changes from one time instant to another. Since the turbulent flows are commonly described the flow statistics. So, an attempt is made to track the

pressure and velocity close to the ground surface at 4 different points, viz. probe 1, 2, 3 and 4. The coordinates of each of the probes in shown in Fig. B-5.

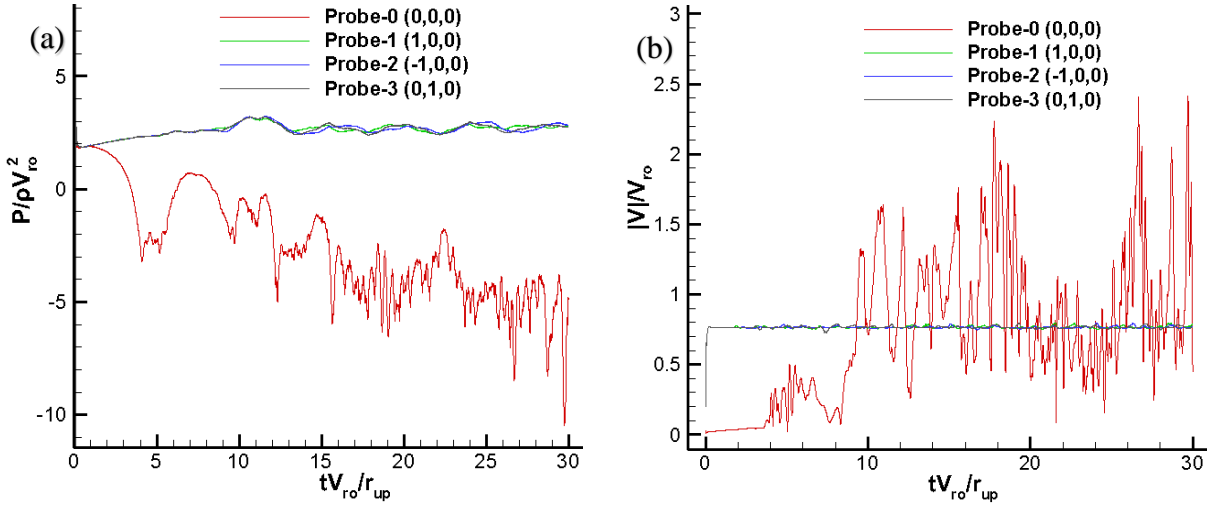


Fig. B-5. Time series plot of (a) non-dimensional pressure and (b) non-dimensional velocity magnitude with respect to non-dimensional time

In Fig. B-5 (a), it can be observed that the pressure at probes 1, 2 and 3 have attained a relatively steady state (although a slightly upward trend can be observed) as the perturbations in the magnitude is very low. The pressure at probe location 1, however, shows a decreasing trend and the simulation may be run a bit longer further so that the flow attains a statistically steady state.

However, for the purpose of this work, the duration of simulation would be kept 30 time units.

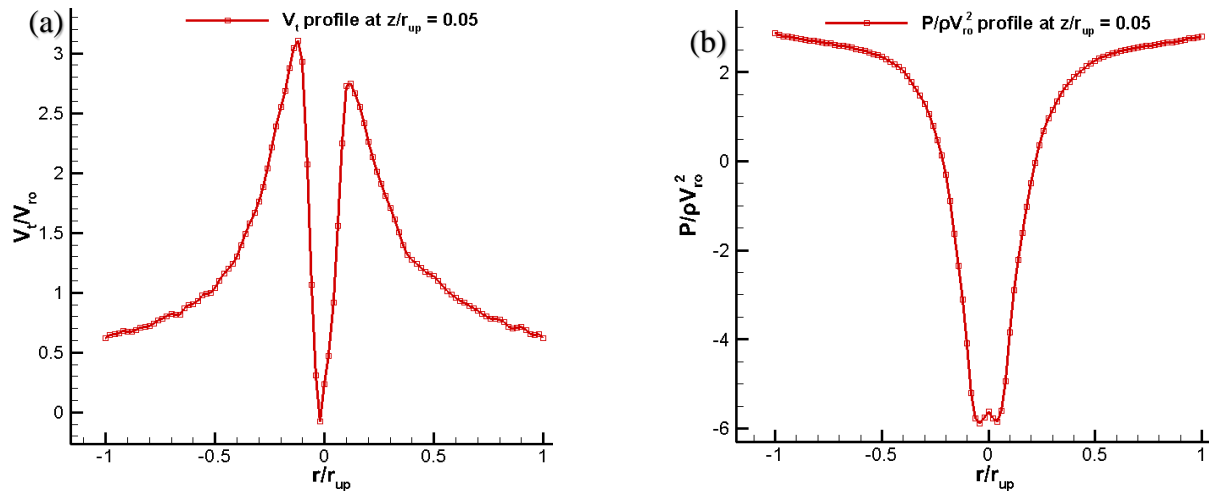


Fig. B-6. Instantaneous profile at the bottom of tornado simulator (a) tangential velocity profile at $z/r_{up} = 0.05$ (b) pressure profile at $z/r_{up} = 0.05$

After monitoring the pressure and velocity statistics over time at 4 different locations in the flow domain, the instantaneous profiles for tangential velocity and pressure are extracted in Fig. B-6 corresponding to the final time step, i.e., $t^* = 30$ units. A slightly flattened pressure profile at the core of tornado vortex in Fig. B-6 (b) indicates a vortex beyond touchdown. Similar observations were made by [16], in which the sharp gradient of pressure at the core of vortex was transformed into a flattened profile in a post-touchdown tornado-like vortex.

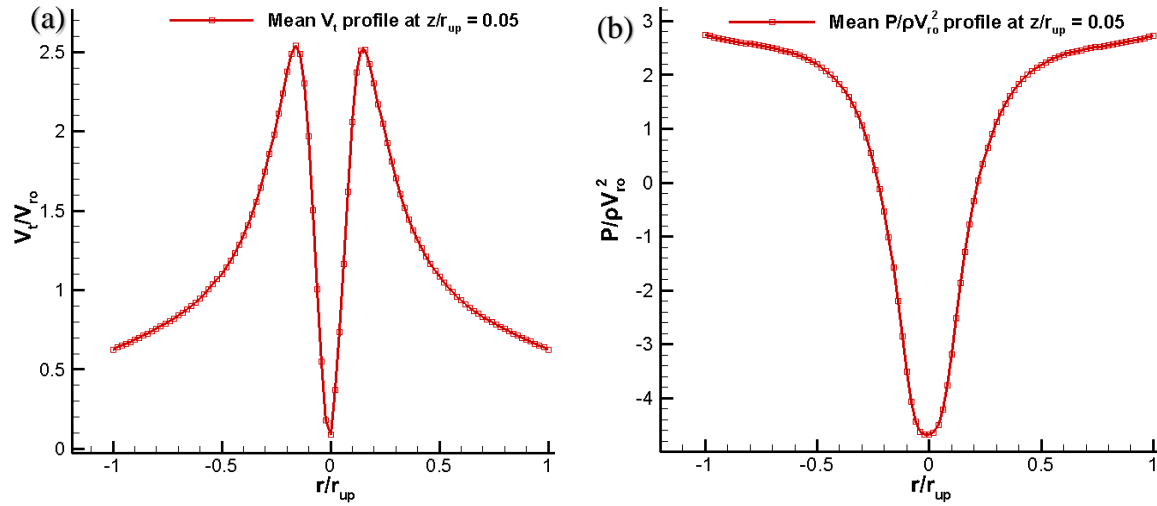


Fig. B-7. Mean profiles at the bottom of tornado simulator (a) tangential velocity profile at $z/r_{up} = 0.05$ (b) pressure profile at $z/r_{up} = 0.05$

The mean profiles are shown in Fig. B-7 in which the profiles exhibit a smoother nature because of time averaging after $t^* = 20$ units until the final time step, i.e., $t^* = 30$ units. Finally, the experimental pressure profile for $S = 0.83$ is compared with the predicted pressure profile from CFD for $S = 0.83$ in Fig. B-8. A good qualitative agreement can be readily noticed between the profiles in Fig. B-8. Furthermore, the contour plot for velocity magnitude including the velocity vectors through a section plane passing through the diametric axis of tornado simulator in XZ-plane and XY-plane are shown in Fig. B-9 and Fig. B-10 respectively.

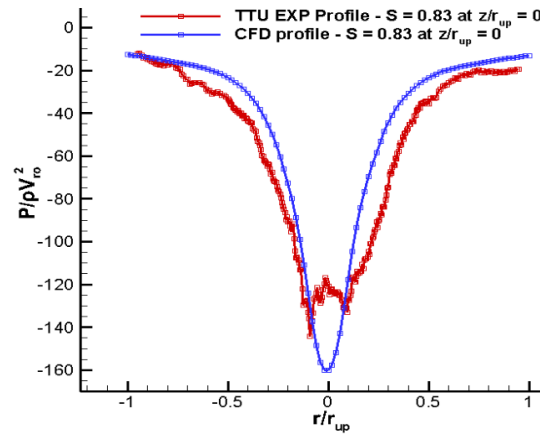


Fig. B-8. Comparison of pressure profile at the base of tornado simulator (i.e., $z/r_{up} = 0$) between the TTU simulator dataset and CFD datasets

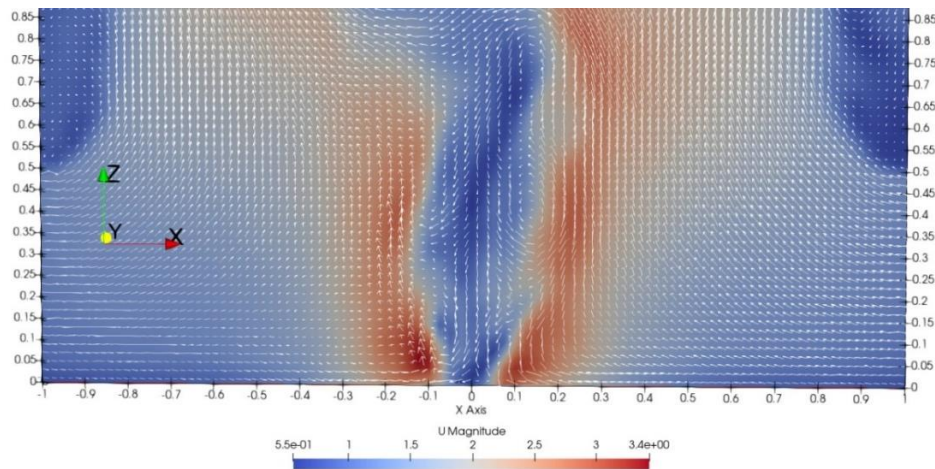


Fig. B-9. Contour plot of Velocity magnitude with velocity vectors in the background through the diametric XZ-plane of CFD tornado simulator

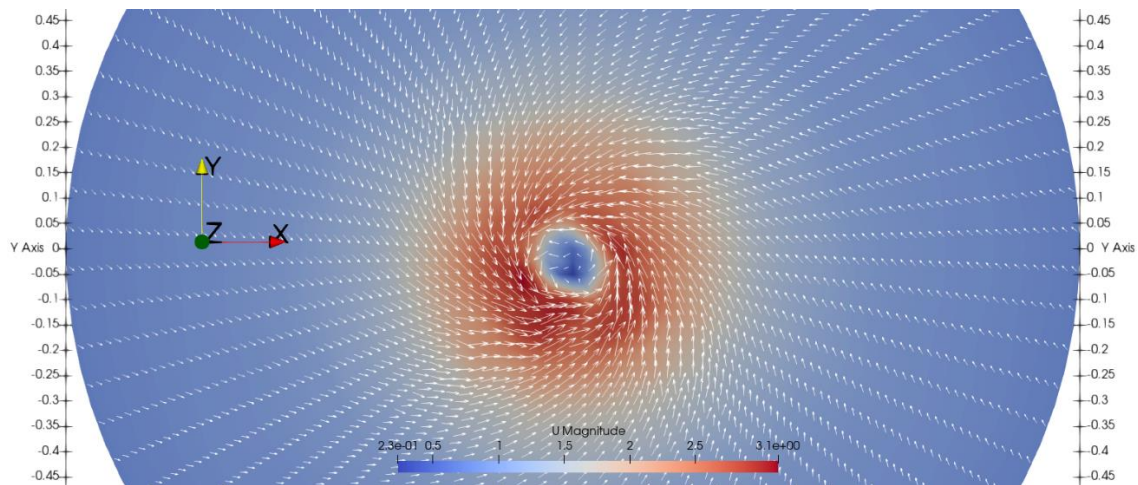


Fig. B-10. Velocity magnitude contour plot with velocity vectors in the background through the XY-plane of CFD tornado simulator at $z/r_{up} = 0.01$

3.1 Computation of Normalized Root Mean Square Error (NRMSE)

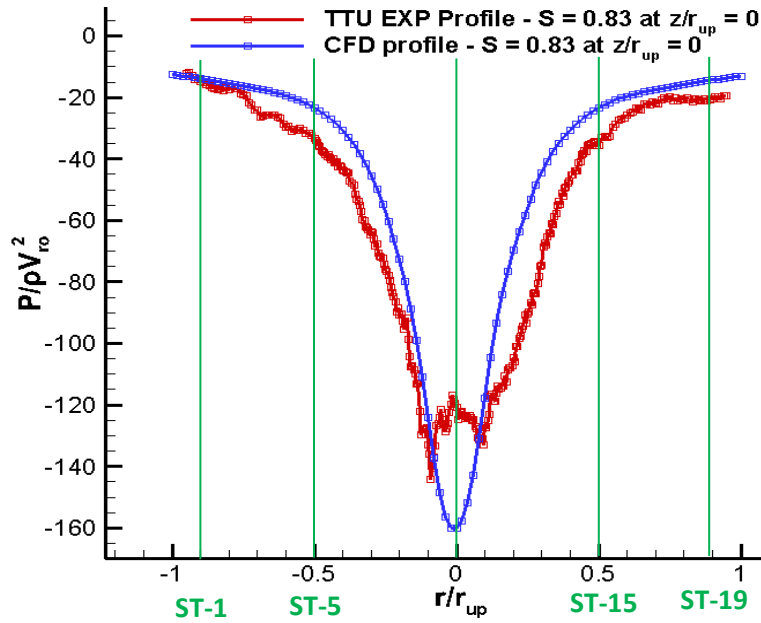


Fig. B-11. Sketch showing different stations for computing NRMSE in pressure profiles

To quantify the error between the TTU experimental pressure profile and the pressure profile predicted by CFD model, normalized root mean squared error (NRMSE) is taken as the error estimate. To calculate NRMSE, 19 stations are considered along the X-axis (represented by green lines) in Fig. B-11 below starting from -0.9 to 0.9 with an interval of 0.1. At each of the stations, the value of pressure from TTU experiment were determined (represented by variable-v1) and the values predicted by CFD model at those stations were also determined (represented by variable-v2). Then, the value of error between the experimental values and that predicted by the CFD model was calculated as $e = (v1-v2)$. Further calculations are shown in Table B3.

Table B3. Calculation of NRMSE between TTU Experimental and CFD Pressure Profile

ST (n)	TTU EXP (v1)	CFD (v2)	$e = (v1-v2)$	e^2
1	-14.7111	-13.919	-0.7921	0.627422

Table B3. Calculation of NRMSE between TTU Experimental and CFD Pressure Profile (Cont.)

ST (n)	TTU EXP (v1)	CFD (v2)	e = (v1-v2)	e ²
2	-17.3703	-15.4102	-1.9601	3.841992
3	-24.1965	-17.0386	-7.1579	51.23553
4	-29.4922	-19.3613	-10.1309	102.6351
5	-33.182	-23.2249	-9.9571	99.14384
6	-43.4235	-30.713	-12.7105	161.5568
7	-63.8347	-45.7704	-18.0643	326.3189
8	-90.2808	-72.183	-18.0978	327.5304
9	-133.148	-124.112	-9.036	81.6493
10	-122.068	-159.899	37.831	1431.185
11	-127.932	-118.478	-9.454	89.37812
12	-106.467	-70.9353	-35.5317	1262.502
13	-72.2159	-44.0176	-28.1983	795.1441
14	-46.3381	-30.6529	-15.6852	246.0255
15	-35.4588	-23.4277	-12.0311	144.7474
16	-25.8303	-19.6924	-6.1379	37.67382
17	-21.6502	-17.4124	-4.2378	17.95895

Table B3. Calculation of NRMSE between TTU Experimental and CFD Pressure Profile (Cont.)

ST (n)	TTU EXP (v1)	CFD (v2)	e = (v1-v2)	e ²
18	-20.6138	-15.8171	-4.7967	23.00833
19	-20.3549	-14.3266	-6.0283	36.3404
				$\sum e^2 = 5238.502$

Once, the sum of squared error ($\sum e^2$) is determined in Table 1, the value of mean squared error (MSE) is computed using Eq. (18).

$$\text{Mean Squared Error (MSE)} = \sum e^2/n \quad (18)$$

, where n represents the number of stations where the deviation between the TTU experimental pressure profile and the CFD pressure profile were taken. The value of MSE is obtained as MSE = 275.7106 using Eq. (18). Then, the value of RMSE is computed using Eq. (19) and obtained as RMSE = 16.60454.

$$\text{Root Mean Squared Deviation (RMSE)} = \sqrt{(\sum e^2)/n} \quad (19)$$

Finally, the value of Normalized Root Mean Squared Error (NRMSE) is computed using Eq. (20) and obtained as NRMSE = 0.113745 (11.3745 %).

$$\text{NRMSE} = \frac{\sqrt{(\sum e^2)/n}}{(\max.(v1,v2) - \min.(v1,v2))} \quad (20)$$

While computing NRMSE, the value of NRMSE is normalized by the range of dataset, which is computed as the difference of maximum of (v1, v2) and the minimum of (v1, v2) from Table B3.

4. Conclusion

A qualitative analysis of the wind field of tornado-like vortex obtained from the CFD model for $S = 0.83$ is done. Results indicate that for $S = 0.83$, a vortex beyond touchdown is obtained as the downdraft winds can be clearly observed at the center of CFD tornado simulator. This observation from CFD simulator model agrees very well with the observations of experimental TTU tornado simulator, in which a double-celled tornado vortex is obtained for $S = 0.83$. Then, the pressure profile close to the ground surface is extracted from CFD model, and compared with experimental TTU profile, which again exhibits a reasonable agreement between the experimental datasets and the CFD results. In this work, NRMSE (Normalized Root Mean Squared Error) is taken as the measure of error estimate and the deviation between the experimental profile and that predicted by CFD model is computed to be 11.37%. Even though an error percentage below 10% would have been much better, the pressure profile predicted by the CFD model still exhibits a good prediction for the experimental pressure profile. Thus, the CFD model is validated against the experimental measurements; based on a good qualitative agreement between the CFD results as well as a good quantitative agreement on the pressure profile, it is concluded that a validated CFD model is obtained. All the relevant case files for CFD tornado simulator model described in this work can be accessed at https://github.com/timusv5977/CFD_Tornado_Simulator.

Acknowledgments

The authors acknowledge the support received from National Science Foundation (NSF) under the award number CMMI-1762999.

References

- [1] Changnon, S. A. (2009). "Tornado losses in the United States." *Natural Hazards Review*, **10**(4), 145–150. [https://doi.org/10.1061/\(asce\)1527-6988\(2009\)10:4\(145\)](https://doi.org/10.1061/(asce)1527-6988(2009)10:4(145))

- [2] Molloy, S. L. and Mihaltcheva, S. (2013), "1.01 - Extreme Weather Events". Editor(s): Roger A. Pielke, *Climate Vulnerability*, Academic Press, 3-16. <https://doi.org/10.1016/B978-0-12-384703-4.00103-9>
- [3] Bluestein, H. B. and Pazmany, A. L. (2000). Observations of Tornadoes and Other Convective Phenomena with a Mobile, 3-mm Wavelength, Doppler Radar: The Spring 1999 Field Experiment, *Bulletin of the American Meteorological Society*, **81**(12), 2939-2952. [https://doi.org/10.1175/1520-0477\(2000\)081<2939:OOTAOC>2.3.CO;2](https://doi.org/10.1175/1520-0477(2000)081<2939:OOTAOC>2.3.CO;2)
- [4] Alexander, C.R. and Wurman, J. (2005), The 30 May 1998 Spencer, South Dakota, Storm. Part I: The Structural Evolution and Environment of the Tornadoes, *Mon. Wea. Rev.*, **133**, 72-97.
- [5] Kosiba, K. and Wurman, J. (2010). The Three-Dimensional Axisymmetric Wind Field Structure of the Spencer, South Dakota, 1998 Tornado, *Journal of the Atmospheric Sciences*, **67**(9), 3074-3083. <https://doi.org/10.1175/2010JAS3416.1>
- [6] Kosiba, K. A. and Wurman, J. (2013). The Three-Dimensional Structure and Evolution of a Tornado Boundary Layer, *Weather and Forecasting*, **28**(6), 1552-1561. <https://doi.org/10.1175/WAF-D-13-00070.1>
- [7] Ward N.B. (1972), "The exploration of certain features of tornado dynamics using a laboratory model", *J Atmos. Sci.*, **29**(6), 1194-1204. [https://doi.org/10.1175/1520-0469\(1972\)029<1194:TEOCFO>2.0.CO;2](https://doi.org/10.1175/1520-0469(1972)029<1194:TEOCFO>2.0.CO;2)
- [8] Church, C.R., Snow, J.T. and Agee, E.M. (1977), "Tornado vortex simulation at Purdue University", *Bull. Amer. Meteor. Soc.*, **58**(9), 900-909. [https://doi.org/10.1175/1520-0477\(1977\)058<0900:TVSAPU>2.0.CO;2](https://doi.org/10.1175/1520-0477(1977)058<0900:TVSAPU>2.0.CO;2)
- [9] Haan Jr. F.L, Balaramudu, V.K. and Sarkar, P.P. (2010), "Tornado-induced wind loads on a low-rise building", *J. Struct. Eng.*, **136**(1), 106-116. [https://doi.org/10.1061/\(ASCE\)ST.1943-541X.0000093](https://doi.org/10.1061/(ASCE)ST.1943-541X.0000093)
- [10] Hangan H. (2014), "The wind engineering energy and environment (WindEEE) dome at Western University, Canada", *Wind Engineers, JAWE*, **39**(4), 350-351. <https://doi.org/10.5359/jawe.39.350>
- [11] Tang, Z., Feng, C., Wu, L., Zuo, D. and James, D.L. (2018a), "Characteristics of tornado-like vortices simulated in a large scale ward type simulator", *Boundary-Layer Meteorol.*, **166**, 327-350. <https://doi.org/10.1007/s10546-017-0305-7>
- [12] Harlow, F.H. and Stein L.R. (1974), "Structural analysis of tornado-like vortices", *J. Atmos. Sci.*, **31**(8), 2081-2098. [https://doi.org/10.1175/1520-0469\(1974\)031<2081:SAOTLV>2.0.CO;2](https://doi.org/10.1175/1520-0469(1974)031<2081:SAOTLV>2.0.CO;2)
- [13] Rotunno, R. (1977), "Numerical simulation of a laboratory vortex", *J. Atmos. Sci.*, **34**(12), 1942-1956. [https://doi.org/10.1175/1520-0469\(1977\)034<1942:NSOALV>2.0.CO;2](https://doi.org/10.1175/1520-0469(1977)034<1942:NSOALV>2.0.CO;2)

- [14] Gairola, A. and Bitsuamlak, G. (2019), “Numerical tornado modeling for common interpretation of experimental simulators”, *J. Wind Eng. Ind. Aerodyn.*, **186**, 32-48. <https://doi.org/10.1016/j.jweia.2018.12.013>
- [15] Yuan F., Yan, G., Honerkamp, R, Kakkattukuzhy, M.I, Zhao, M. and Mao, X. (2019), “Numerical simulation of laboratory tornado simulator that can produce translating tornado-like wind flow”, *J. Wind Eng. Ind. Aerodyn.*, **190**, 200-217. <https://doi.org/10.1016/j.jweia.2019.05.001>
- [16] Tang, Z., Zuo, D., James, D., Eguchi, Y. and Hattori, Y. (2018b), “Effects of aspect ratio on laboratory simulation of tornado-like vortices”, *Wind and Struct.*, **27**(2), 111-121. <http://dx.doi.org/10.12989/was.2018.27.2.111>
- [17] Cengel, Y. A. and Cimbala J.M. (2014), *Fluid Mechanics: Fundamentals and Applications*, (3rd Edition), McGraw Hill, New York, NY, USA.

Source Code Listing:

C/C++ code snippet for implementing the inlet velocity boundary condition in CFD model:

```
inlet
{
    type    fixedValue;
    value   #codeStream
    {
        codeIncludes
        #{
            #include "fvCFD.H"
        };
        codeOptions
        #{
            -I$(LIB_SRC)/finiteVolume/lnInclude \
            -I$(LIB_SRC)/meshTools/lnInclude
        };

        //libs needed to visualize BC in paraview
        codeLibs
        #{
            -lmeshTools \
            -lfiniteVolume
        };
        code
        #{
            const IOdictionary& d = static_cast<const IOdictionary&>
            (
                dict.parent().parent()
            );
        };
    };
}
```

```

const fvMesh& mesh = refCast<const fvMesh>(d.db());

const label id = mesh.boundary().findPatchID("inlet");
const fvPatch& patch = mesh.boundary()[id];

vectorField U(patch.size(), vector(0, 0, 0));

const scalar pi = constant::mathematical::pi;

const scalar S = 0.83;
const scalar a = 0.5;

const scalar z_0 = 0.00004;
const scalar C_1 = 0.106004476;

const scalar Vin = 1;

for (int i=0; i<patch.size(); i++)
{
    const scalar x = patch.Cf()[i][0];
    const scalar y = patch.Cf()[i][1];
    const scalar z = patch.Cf()[i][2];

// Implementing logarithmic variation of radial velocity component from the ground surface
    const scalar U_r = Vin*C_1*(log(1+(z/z_0)));
    const scalar U_t = 2*S*a*U_r;

// Assigning velocity vector at inlet after transformation from Cylindrical to Cartesian system and
// then assigning to respective Quadrants
// using if-else ladder

    if (x>=0 && y>=0)    // 1st Quadrant
    {
        const scalar alpha = pi + atan(y/x);
        U[i]=vector(((U_r)*cos(alpha)+(U_t)*cos(alpha-
pi/2)),((U_r)*sin(alpha)+(U_t)*sin(alpha-pi/2)),0.0);
    }
    else if (x<=0 && y>=0)    // 2nd Quadrant
    {
        const scalar alpha = atan(y/x);
        U[i]=vector(((U_r)*cos(alpha)+(U_t)*cos(alpha-
pi/2)),((U_r)*sin(alpha)+(U_t)*sin(alpha-pi/2)),0.0);
    }
    else if (x<=0 && y<=0)    // 3rd Quadrant
    {

```

```

        const scalar alpha = 2*pi + atan(y/x);
        U[i]=vector
        (((U_r)*cos(alpha)+(U_t)*cos(3*pi/2+alpha)),((U_r)*sin(alpha)+(U_t)*sin(3*pi/2+alpha)),
        0.0);
    }
    else    // 4th Quadrant
    {
        const scalar alpha = pi + atan(y/x);
        U[i]=vector(((U_r)*cos(alpha)+(U_t)*cos(alpha-
        pi/2)),((U_r)*sin(alpha)+(U_t)*sin(alpha-pi/2)),0.0);
    }
}
writeEntry(os, "", U);
#};
};
}

```

Appendix C: Mapping of Experimental Data onto a Contour Plot

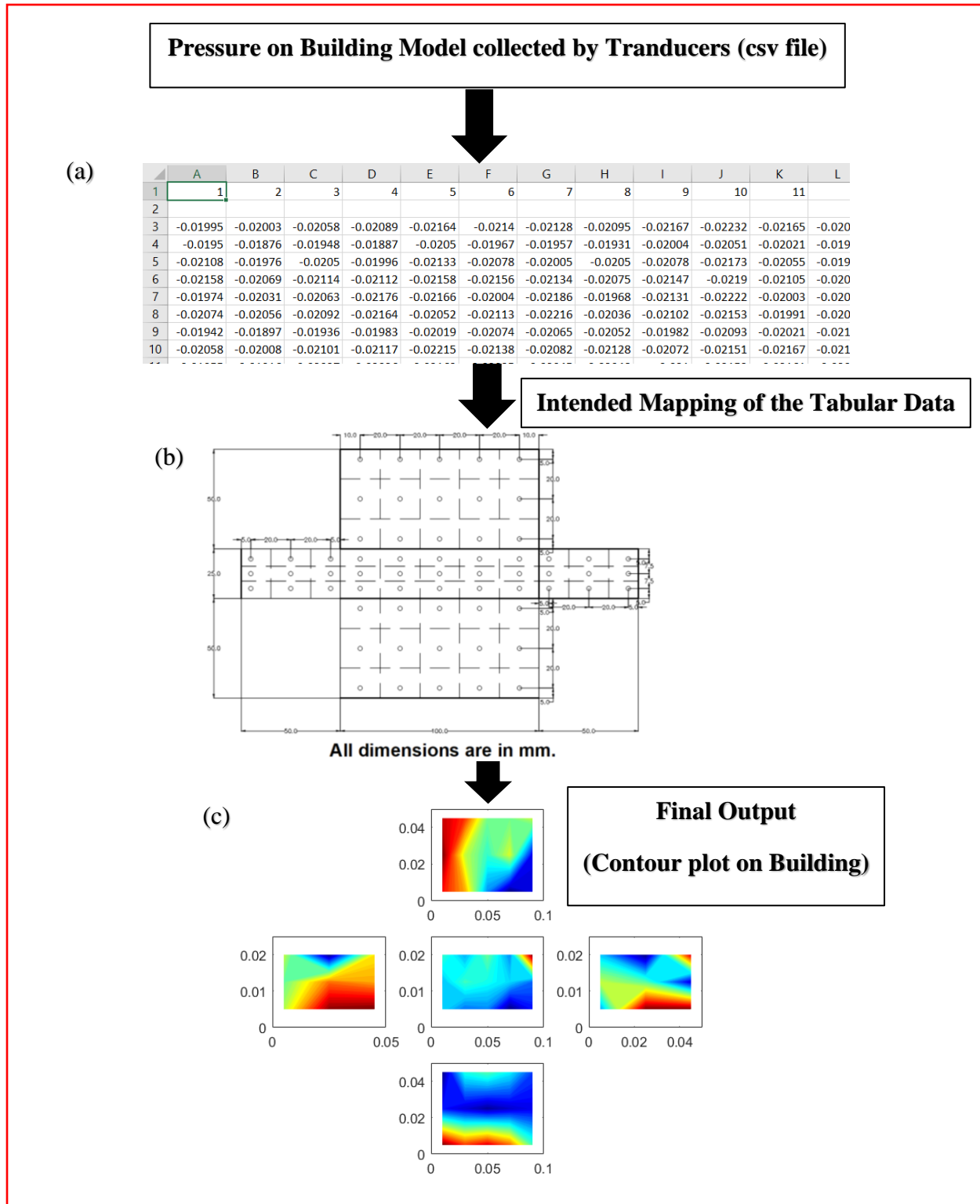


Fig. C-1. Demo for mapping the pressures recorded on building from csv file to a contour plot

In this section, the Matlab script used to map the pressure data (recorded by pressure transducers) from a csv file to a pressure contour plot is presented. As shown in Fig. C-1 (a), the recorded pressure values on the building are organized in a tabular format in csv file. The pressure values in the csv file corresponds to the probe locations as shown in Fig. C-1 (b). After mapping the data from csv file onto the faces of the building model, the final contour plot obtained is shown in Fig. C-1 (c). The Matlab script is listed below:

```
%% Matlab Script that reads csv file with Pressure Data collected by Pressure Transducers
% at Texas Tech University Tornado Simulator - VorTECH and
% outputs the pressure contour plots on the faces of Building Model
```

```
%% Distances in mm
x = [0,5,25,45,50,60,80,100,120,140,150,155,175,195,200];
y = [0,5,25,45,50,55,62.5,70,75,80,100,120,125];
building_height = 50;
building_length = 100;
building_width = 25;
```

```
%% Distances in m
x_m = x./1000;
y_m = y./1000;
building_height_m = building_height/1000;
building_length_m = building_length/1000;
building_width_m = building_width/1000;
```

```
%% Index Key for Mapping Experimental Pressure Data
P_int_face1_index_key = [1 2 3 4 5 6 7 8 9 10 11 12 13 14 15];
P_int_face2_index_key = [16 17 18 19 20 21 22 23 24];
P_int_face3_index_key = [25 26 27 28 29 30 31 32 33 34 35 36 37 38 39];
P_int_face4_index_key = [40 41 42 43 44 45 46 47 48];
P_int_face5_index_key = [49 50 51 52 53 54 55 56 57 58 59 60 61 62 63];
```

```
%% Building Face wise Contour Distribution
```

```
%% Face -1 Contouring
start_index_x = 5;
end_index_x = 11;
x_face1 = zeros(1,end_index_x-start_index_x + 1);

start_index_y = 1;
end_index_y = 5;
```

```

y_face1 = zeros(1,end_index_y-start_index_y + 1);

%% Local X-array for Face-1
k = 0;
for i = 1:(length(x_face1))
    x_face1(i) = x_m (start_index_x + k) - building_height_m;
    k = k + 1;
end

%% Local Y-array for Face-1
for i = 1:(length(y_face1))
    y_face1(i) = y_m(i);
end

P = zeros(length(x_face1),length(y_face1));

for i = 1:length(x_face1)
    for j = 1:length(y_face1)
        if(i == 1 || j == 1 || i == length(x_face1) || j == length(y_face1))
            P(i,j) = NaN;
        end
    end
end

%% Data Import
Exp_data =
importdata('A05_S082_LambdaT05_Beta00_r00_Run01_F67_RH33_2992inHg_20200209.csv')
;

% Row index to calculate no. of columns of 'P' matrix
i = 1;

Exp_face1_data = zeros(length(x_face1)-2,length(y_face1)-2);

P_int = zeros(length(Exp_face1_data),length(Exp_face1_data(i,:)));
P_int_1D = zeros(1,length(Exp_face1_data)*length(Exp_face1_data(i,:)));

n = 1;
k = P_int_face1_index_key(n);

for i = 1:length(Exp_face1_data(i,:))
    for j = 1:length(Exp_face1_data)
        P_int(i,j) = Exp_data(length(Exp_data),k);
        P_int_1D (k) = Exp_data(length(Exp_data),k);
        k = k+1;
    end
end

```



```

end

P_int = P_int';

for i = 1:length(x_face1)-1
    i1 = i-1;
    for j = 1:length(y_face1)-1
        j1 = j-1;
        if(i == 1 || j == 1 || i == length(x_face1) || j == length(y_face1))
            P(i,j) = NaN;
        else
            P(i,j) = P_int(i1,j1);
        end
    end
end
end

P = P';

P = P.*(6894.76);

density = 1.225;
max_Vt = 12;
Cp = P./(0.5*density*(max_Vt^2.0));

[X, Y] = meshgrid(x_face1,y_face1);
figure(1);
hold on;
subplot(3,3,8);
contourf(X,Y,Cp,101,'LineStyle','none');
colormap('jet');

%% Face-2 Contouring
start_index_x = 11;
end_index_x = 15;
x_face2 = zeros(1,end_index_x-start_index_x + 1);

start_index_y = 5;
end_index_y = 9;
y_face2 = zeros(1,end_index_y-start_index_y + 1);

%% Local X-array for Face-2
k = 0;
for i = 1:(length(x_face2))
    x_face2(i) = x_m (start_index_x + k) - building_height_m - building_length_m;
    k = k + 1;
end

```

```

%% Local Y-array for Face-2
k = 0;
for i = 1:(length(y_face2))
    y_face2(i) = y_m(start_index_y+k) - building_height_m;
    k = k+1;
end

P = zeros(length(x_face2),length(y_face2));

for i = 1:length(x_face2)
    for j = 1:length(y_face2)
        if(i == 1 || j == 1 || i == length(x_face2) || j == length(y_face2))
            P(i,j) = NaN;
        end
    end
end

%% Data Imports
Exp_data =
importdata('A05_S082_LambdaT05_Beta00_r00_Run01_F67_RH33_2992inHg_20200209_SV.
csv');

i = 1;
Exp_face2_data = zeros(length(x_face2)-2,length(y_face2)-2);

P_int = zeros(length(Exp_face2_data),length(Exp_face2_data(i,:)));
P_int_1D = zeros(1,length(Exp_face2_data)*length(Exp_face2_data(i,:)));

n = 1;
k = P_int_face2_index_key(n);

for i = 1:length(Exp_face2_data(i,:))
    for j = 1:length(Exp_face2_data)
        P_int(i,j) = Exp_data(length(Exp_data),k);
        P_int_1D(k) = Exp_data(length(Exp_data),k);
        k = k+1;
    end
end

P_int = P_int';

for i = 1:length(x_face2)-1
    i1 = i-1;
    for j = 1:length(y_face2)-1
        j1 = j-1;

```

```

        if(i == 1 || j == 1 || i == length(x_face2) || j == length(y_face2))
            P(i,j) = NaN;
        else
            P(i,j) = P_int(i1,j1);
        end
    end
end

P = P';
i1 = 1;
P_final = zeros(size(P));

% Reflecting matrix about X-axis
for i = length(P(:,1)):-1:1
    for j = 1:length(P)
        P_final(i,j)=P(i1,j);
    end
    i1 = i1+1;
end

P_final = P_final.*(6894.76);

density = 1.225;
max_Vt = 12;
Cp = P_final./(0.5*density*(max_Vt^2.0));

[X, Y] = meshgrid(x_face2,y_face2);

subplot(3,3,6);
contourf(X,Y,Cp,101,'LineStyle','none');
colormap('jet');

%% Face-3 Contouring
start_index_x = 5;
end_index_x = 11;
x_face3 = zeros(1,end_index_x-start_index_x + 1);

start_index_y = 9;
end_index_y = 13;
y_face3 = zeros(1,end_index_y-start_index_y + 1);

%% Local X-array for Face-3
k = 0;
for i = 1:(length(x_face3))
    x_face3(i) = x_m (start_index_x + k) - building_height_m;
    k = k + 1;
end

```

```

end

%% Local Y-array for Face-3
k = 0;
for i = 1:(length(y_face3))
    y_face3(i) = y_m(start_index_y+k) - building_height_m - building_width_m;
    k = k + 1;
end

P = zeros(length(x_face3),length(y_face3));

for i = 1:length(x_face3)
    for j = 1:length(y_face3)
        if(i == 1 || j == 1 || i == length(x_face3) || j == length(y_face3))
            P(i,j) = NaN;
        end
    end
end

%% Data Import
Exp_data =
importdata('A05_S082_LambdaT05_Beta00_r00_Run01_F67_RH33_2992inHg_20200209_SV.
csv');

% Row index to calculate no. of columns of 'P' matrix
i = 1;

Exp_face3_data = zeros(length(x_face3)-2,length(y_face3)-2);

P_int = zeros(length(Exp_face3_data),length(Exp_face3_data(i,:)));
P_int_1D = zeros(1,length(Exp_face3_data)*length(Exp_face3_data(i,:)));

n = 1;
k = P_int_face3_index_key(n);

for i = 1:length(Exp_face3_data(i,:))
    for j = 1:length(Exp_face3_data)
        P_int(i,j) = Exp_data(length(Exp_data),k);
        P_int_1D(k) = Exp_data(length(Exp_data),k);
        k = k+1;
    end
end

P_int = P_int';

for i = 1:length(x_face3)-1

```

```

i1 = i-1;
for j = 1:length(y_face3)-1
    j1 = j-1;
    if(i == 1 || j == 1 || i == length(x_face3) || j == length(y_face3))
        P(i,j) = NaN;
    else
        P(i,j) = P_int(i1,j1);
    end
end
end

P = P';
i1 = 1;
P_final = zeros(size(P));

% Reflecting matrix about X-axis
for i = length(P(:,1)):-1:1
    for j = 1:length(P)
        P_final(i,j)=P(i1,j);
    end
    i1 = i1+1;
end

P_final = P_final.*(6894.76);

density = 1.225;
max_Vt = 12;
Cp = P_final./(0.5*density*(max_Vt^2.0));

[X, Y] = meshgrid(x_face3,y_face3);
subplot(3,3,2);
contourf(X,Y,Cp,101,'LineStyle','none');
colormap('jet');

%% Face-4 Contouring
start_index_x = 1;
end_index_x = 5;
x_face4 = zeros(1,end_index_x-start_index_x + 1);

start_index_y = 5;
end_index_y = 9;
y_face4 = zeros(1,end_index_y-start_index_y + 1);

%% Local X-array for Face-4
k = 0;
for i = 1:(length(x_face4))

```

```

    x_face4(i) = x_m (start_index_x + k);
    k = k + 1;
end

%% Local Y-array for Face-4
k = 0;
for i = 1:(length(y_face4))
    y_face4(i) = y_m(start_index_y+k) - building_height_m;
    k = k+1;
end

P = zeros(length(x_face4),length(y_face4));

for i = 1:length(x_face4)
    for j = 1:length(y_face4)
        if(i == 1 || j == 1 || i == length(x_face4) || j == length(y_face4))
            P(i,j) = NaN;
        end
    end
end

%% Data Import
Exp_data =
importdata('A05_S082_LambdaT05_Beta00_r00_Run01_F67_RH33_2992inHg_20200209_SV.
csv');

% Row index to calculate no. of columns of 'P' matrix
i = 1;

Exp_face4_data = zeros(length(x_face4)-2,length(y_face4)-2);

P_int = zeros(length(Exp_face4_data),length(Exp_face4_data(i,:)));
P_int_1D = zeros(1,length(Exp_face4_data)*length(Exp_face4_data(i,:)));

n = 1;
k = P_int_face4_index_key(n);

for i = 1:length(Exp_face4_data(i,:))
    for j = 1:length(Exp_face4_data)
        P_int(i,j) = Exp_data(length(Exp_data),k);
        P_int_1D (k) = Exp_data(length(Exp_data),k);
        k = k+1;
    end
end

P_int = P_int';

```

```

for i = 1:length(x_face4)-1
    i1 = i-1;
    for j = 1:length(y_face4)-1
        j1 = j-1;
        if(i == 1 || j == 1 || i == length(x_face4) || j == length(y_face4))
            P(i,j) = NaN;
        else
            P(i,j) = P_int(i1,j1);
        end
    end
end
end

P = P';
i1 = 1;

P_final = zeros(size(P));

% Reflecting matrix about X-axis
for i = length(P(:,1)):-1:1
    for j = 1:length(P)
        P_final(i,j)=P(i1,j);
    end
    i1 = i1+1;
end

P_final = P_final.*(6894.76);

density = 1.225;
max_Vt = 12;
Cp = P_final./(0.5*density*(max_Vt^2.0));

[X, Y] = meshgrid(x_face4,y_face4);

subplot(3,3,4);
contourf(X,Y,Cp,101,'LineStyle','none');
colormap('jet');

%% Face-5 Contouring
start_index_x = 5;
end_index_x = 11;
x_face5 = zeros(1,end_index_x-start_index_x + 1);

start_index_y = 5;
end_index_y = 9;
y_face5 = zeros(1,end_index_y-start_index_y + 1);

```

```

%% Local X-array for Face-5
k = 0;
for i = 1:(length(x_face5))
    x_face5(i) = x_m (start_index_x + k) - building_height_m;
    k = k + 1;
end

%% Local Y-array for Face-5
k = 0;
for i = 1:(length(y_face5))
    y_face5(i) = y_m(start_index_y+k) - building_height_m;
    k = k + 1;
end

P = zeros(length(x_face5),length(y_face5));

for i = 1:length(x_face5)
    for j = 1:length(y_face5)
        if(i == 1 || j == 1 || i == length(x_face5) || j == length(y_face5))
            P(i,j) = NaN;
        end
    end
end

%% Data Import
Exp_data =
importdata('A05_S082_LambdaT05_Beta00_r00_Run01_F67_RH33_2992inHg_20200209_SV.
csv');

% Row index to calculate no. of columns of 'P' matrix
i = 1;

Exp_face5_data = zeros(length(x_face5)-2,length(y_face5)-2);

P_int = zeros(length(Exp_face5_data),length(Exp_face5_data(i,:)));
P_int_1D = zeros(1,length(Exp_face5_data)*length(Exp_face5_data(i,:)));

n = 1;
k = P_int_face5_index_key(n);

for i = 1:length(Exp_face5_data(i,:))
    for j = 1:length(Exp_face5_data)
        P_int(i,j) = Exp_data(length(Exp_data),k);
        P_int_1D (k) = Exp_data(length(Exp_data),k);
        k = k+1;
    end
end

```



```

    end
end

P_int = P_int';

for i = 1:length(x_face5)-1
    i1 = i-1;
    for j = 1:length(y_face5)-1
        j1 = j-1;
        if(i == 1 || j == 1 || i == length(x_face5) || j == length(y_face5))
            P(i,j) = NaN;
        else
            P(i,j) = P_int(i1,j1);
        end
    end
end

P = P';
i1 = 1;
P_final = zeros(size(P));

% Reflecting matrix about X-axis
for i = length(P(:,1)):-1:1
    for j = 1:length(P)
        P_final(i,j)=P(i1,j);
    end
    i1 = i1+1;
end

P_final = P_final.*(6894.76);

density = 1.225;
max_Vt = 12;
Cp = P_final./(0.5*density*(max_Vt^2.0));

[X, Y] = meshgrid(x_face5,y_face5);

subplot(3,3,5);
contourf(X,Y,Cp,101,'LineStyle','none');
colormap('jet');

%% End of Script

```

Appendix D: Computation of Tornado Pressures on Building Using OpenFOAM

The procedure to include a building model inside the CFD tornado simulator is described in this part. The main goal of this work is to establish a framework to study the interaction of tornado-like vortex with the building. In that regard, some key aspects of meshing and flow visualizations of contour plots are only discussed here. Further details about the model are provided at https://github.com/timusv5977/tornado_pressure_building. It is also pointed out that the flow field and/or the pressures on the building model are not validated in this section. Rather, the primary focus of this section is on setting up a framework to incorporate building models inside the computational domain for studying the interaction of tornado-like vortex with building models.

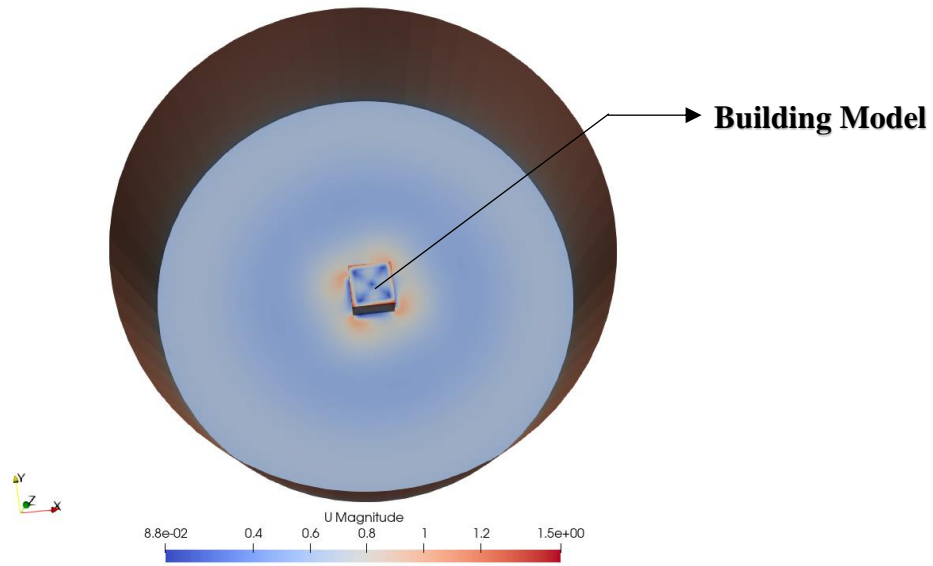


Fig. D-1. A cubical building model placed at the center of CFD tornado simulator

Meshing of Computational Domain

Firstly, a background mesh comprising of a cuboid (bounded by the extreme coordinates (-1.1 -1.1 -0.1) and (1.1 1.1 3.1)) was created as shown in Fig. D-2 (a). The “blockMesh” utility in OpenFOAM is used to create the background mesh. After this step, the 3D CAD model for CFD tornado simulator with the building model inside (as shown in Fig. D-2 (b)) is modeled. Once,

both the CAD model and the background mesh is ready as shown in Fig. D-2 (c), meshing of the computational domain is carried out using “snappyHexMesh” utility in OpenFOAM. The final mesh obtained after executing ‘snappyHexMesh’ command is shown in Fig. D-2 (d).

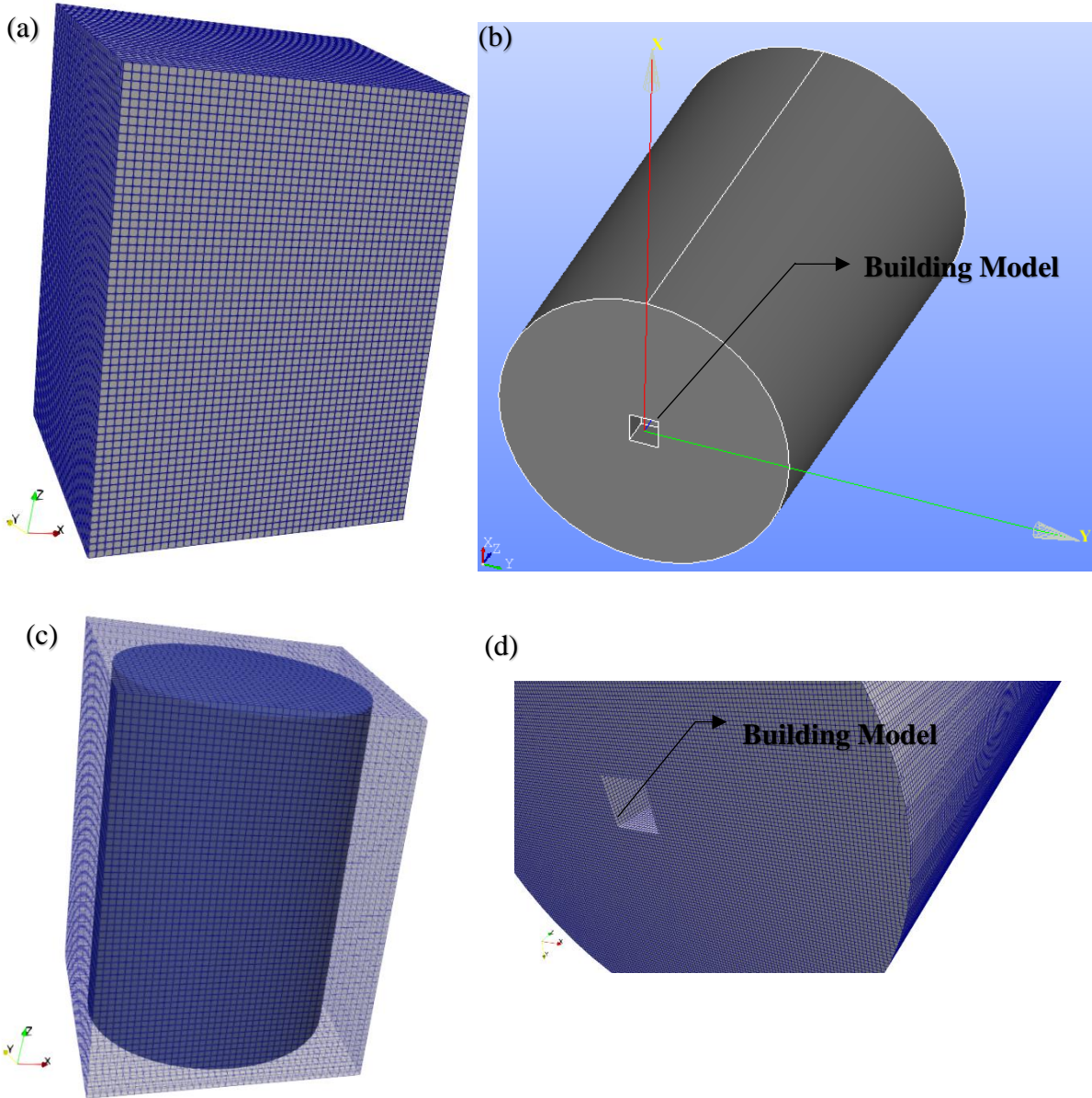


Fig. D-2. (a) Background mesh for the computational domain (b) 3D CAD model for CFD tornado simulator with building model inside (c) Background mesh and 3D CAD model (d) Final mesh obtained from “snappyHexMesh”

Flow Visualizations

The contour plot of pressure coefficients obtained by simulating the wind field of tornado-like vortex around a cubical building for a total non-dimensional time of $t^* = 10$ units is shown in Fig. D-3. As pointed out earlier, the results presented here are only a preliminary analysis to set up a framework to compute the pressure coefficients on a building subjected to tornado-like wind flow rather than proposing definitive values of pressure coefficients for analysis of wind load on the buildings. The pressure coefficients are computed using the following relation:

$$C_p = \frac{(P - P_\infty)/\rho}{0.5 U_{max}^2}$$

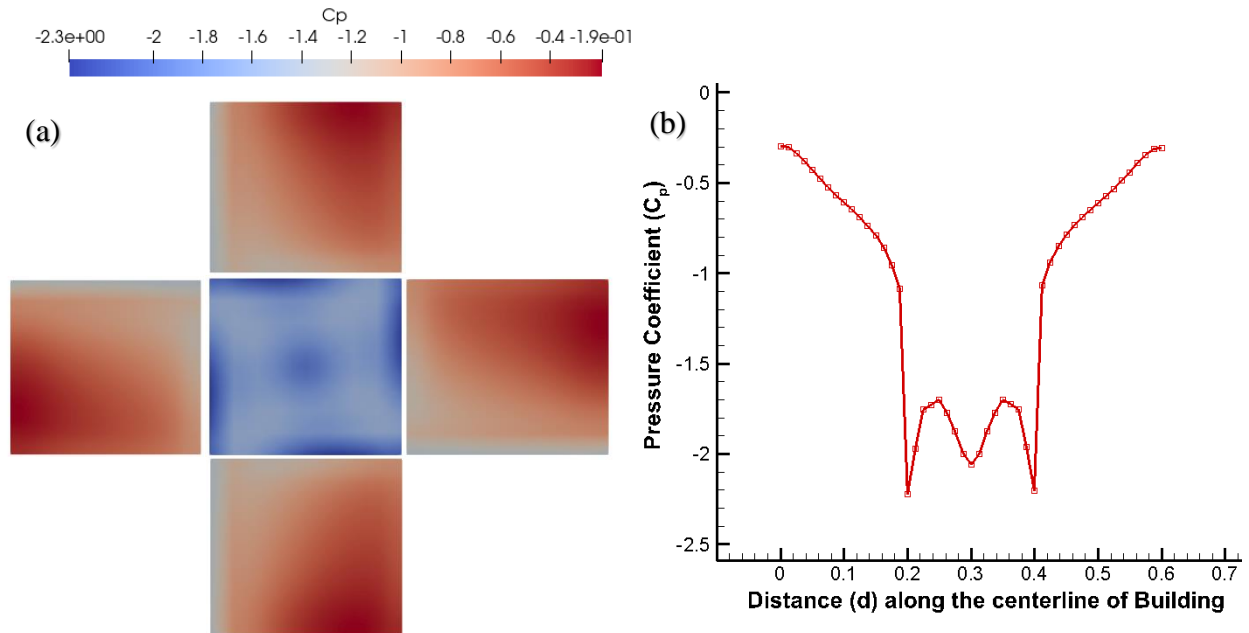


Fig. D-3. (a) Exploded view of pressure contour plot on the faces of building model (b) Pressure coefficient along the centerline of the building

For this work, the free-stream kinematic pressure (P_∞/ρ) is taken as $7.43168 \text{ m}^2/\text{s}^2$ and the maximum velocity (U_{max}) is taken as 1.5 m/s . Further details about the model are covered at https://github.com/timusv5977/tornado_pressure_building.

Appendix E: Parallel Simulation in OpenFOAM

Parallel simulation in OpenFOAM is based on the idea of domain decomposition in which the mesh and the associated fields are divided into different segments (sub-domains) and assigned to different processor cores to obtain the solution of individual sub-domains. Later, the solution of each sub-domain is re-constructed to obtain the solution of the whole domain. A detailed discussion of parallelism implemented in OpenFOAM can be obtained from:

<https://www.openfoam.com/documentation/user-guide/3-running-applications/3.2-running-applications-in-parallel>

E.1 Case Set Up in Parallel

In this section, the procedure for case set up for parallel simulation in OpenFOAM is described.

The necessary steps are discussed below in a sequential order:

1. At first, the mesh for the computational domain must be created (for instance, using “*blockMesh*”, the mesh for the computational domain is created).
2. Once, the mesh is created, it must be decomposed into different sub-domains (no. of sub-domains = no. of processor cores used in the parallel simulation). Before dividing the mesh into different sub-domains, the mesh decomposition method, and the number of cores to be used for the parallel simulation should be specified in “*decomposeParDict*” file inside the “*system*” directory. Finally, the following command is used for mesh partitioning into different sub-domains: *\$ decomposePar*
3. After completion of Step-2, the next step is to run the solver in parallel mode, which is accomplished by the following command:

\$ mpirun -np <no. of processor cores> solverName -parallel > logFileName &

4. Using the command above, the solver executes in parallel and the output in the screen is dumped into the file “*logFileName*”. The “&” used in the above command pushes the parallel simulation process to the background.
5. Once, the simulation is complete, the next step is to reconstruct the mesh and associated fields (such as velocity and pressure fields) from individual sub-domains. For this purpose, the following command should be used: *\$ reconstructPar*

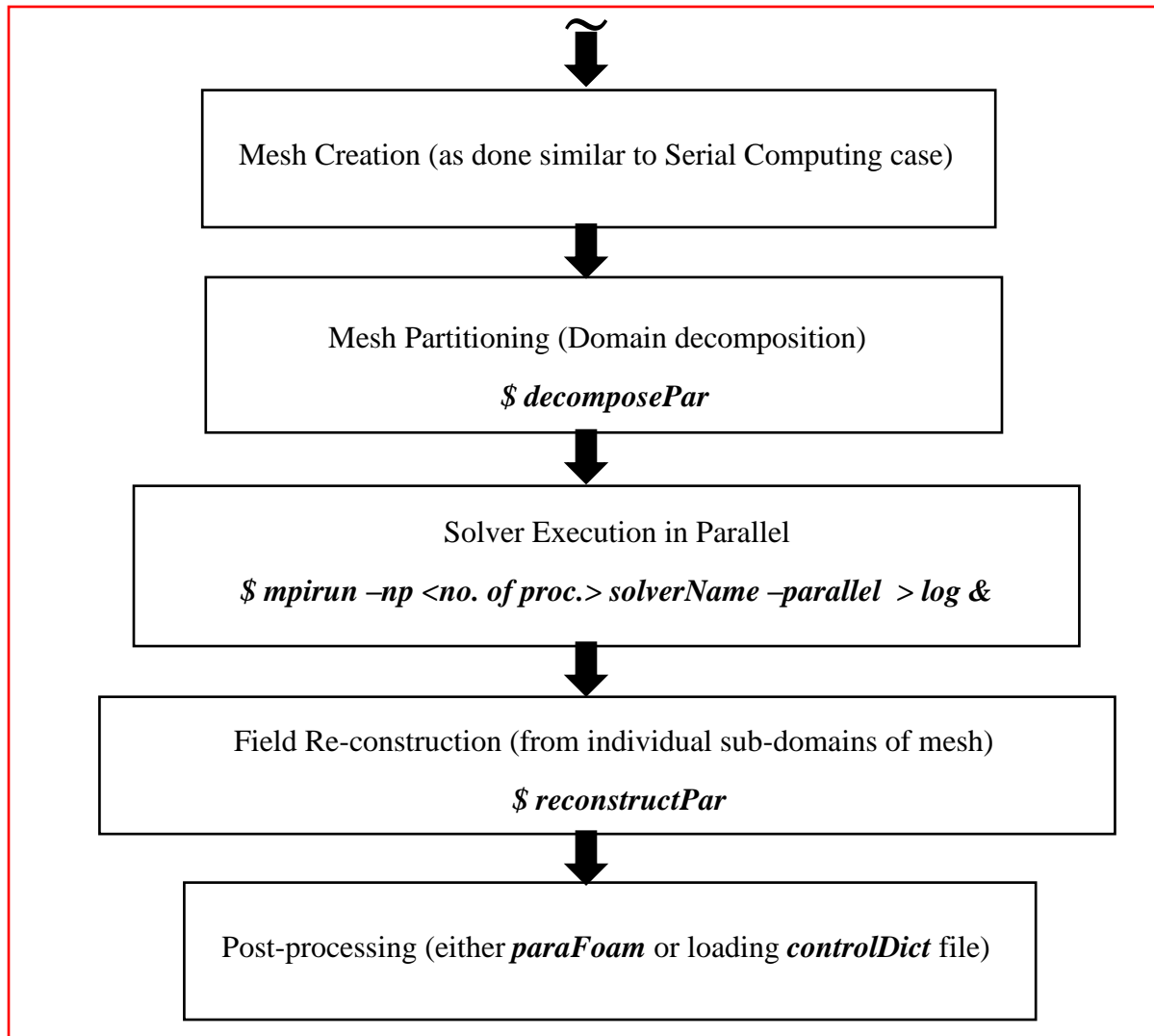


Fig. E-1. Flowchart demonstrating control flow for parallel simulation in OpenFOAM

A simple flowchart outlining the entire process from step - 1 until step - 4 is shown in Fig. E-1.

CURRICULUM VITAE

EDUCATION

Doctor of Philosophy, Civil Engineering (Wind/Structural)

May 2022

University of Arkansas, Fayetteville

Cumulative GPA: 4.00/4.00

Dissertation Title: Comparison and Validation of Tornado Wind Field and Tornado-induced Forces from CFD with TTU Experimental Measurements

Committee Members: R. Panneer Selvam, Micah Hale, Ernie Heymsfield, and Mark E. Arnold

Bachelor of Engineering, Civil Engineering

Oct. 2015

Tribhuvan University, Nepal

Aggregate Percentage: 74.24 %

RESEARCH EXPERIENCE

• **Graduate Research Assistant**

August 2018 – May 2022

Worked on a project “*Assessment of Tornado Loading on Low-Rise Buildings Using Computational Modeling and Tornado Simulator testing*” funded by National Science Foundation (NSF) awarded under Grant No. CMII-1762999.

- Compared and validated the wind field obtained from CFD model with experimental TTU tornado simulator measurements.
- Designed mesh and performed calculation of flow parameters to be used as input for CFD simulation of tornadoes using in-house FORTRAN codes.
- Comparison of tornado-induced pressures and wind loads on building obtained from CFD model with experimental TTU pressure measurements.
- Performed detailed data analysis of CFD simulations, prepared reports & manuscripts for journal publication as well as presented at various national and international venues.
- Developed a simple CFD model of tornado simulator to quantify wind loads on buildings produced by tornadoes using open-source software ‘OpenFOAM’
- Coded inlet velocity boundary condition using programming languages C/C++ while developing CFD tornado simulator model in ‘OpenFOAM’.

LICENSURE AND CERTIFICATION

Engineer in Training (Arkansas)

Mar. 2022

QUALIFICATIONS

- A multi-disciplinary engineer who pursues leadership roles.
- Delivers work on time in high-pressure settings in individual and team environments.
- An experienced writer and presenter of technical documents and reports.
- An experienced programmer in C/C++ languages with experience in Matlab and Python.
- An experienced user of Microsoft Office software: Word, Excel, and PowerPoint.

HONORS AND AWARDS

- Travel grant worth of \$750 to attend THWARTS-2019 Symposium at University of Illinois-Urbana Champaign, Urbana-Champaign.
- Graduate research assistantship at the University of Arkansas, Fayetteville (2018- 2022).
- Doctoral Academy Fellowship (2018-2022)
- Recipient of Full Scholarship and stipend to pursue Bachelor's degree in Civil Engineering from Institute of Engineering (IOE), Pulchowk Campus, Tribhuvan University.
- IOE 6th topper overall and 1st for Department of Civil Engineering in the entrance examination held for admission in IOE Pulchowk Campus for Bachelor's degree in 2011 with an aggregate score of 90.285%.

PUBLICATIONS

Journal Papers

Kashefzadeh, M.H., Verma, S., & Selvam, R.P., (2019), Computer modelling of close-to-ground tornado wind-fields for different tornado widths, *Journal of Wind Engineering and Industrial Aerodynamics*, 191, 32-40.

Verma, S., & Selvam, R.P., (2020), CFD to VorTECH Pressure-Field Comparison and Roughness Effect on Flow, *Journal of Structural Engineering*, 146, 9, 04020187.

Verma, S., & Selvam, R.P., 2021. Validation of Computational Fluid Dynamics Wind Field with Experimental Tornado Wind Field and Comparison of Touchdown Swirl Ratio in Different Tornado Chambers, *Wind and Structures*, 33, 367-381.

Conference Proceeding Papers

Verma, S., & Selvam, R.P., (2021), Effect of Height of the Tornado Chamber on Vortex Touchdown, In: Rushi Kumar B., Sivaraj R., Prakash J. (eds) *Advances in Fluid Dynamics. Lecture Notes in Mechanical Engineering*, Springer, Singapore, 495-507.

Verma, S., & Selvam, R.P. (2021), Differences in flow structures of tornado vortex and efficiency of different tornado chambers, 6th AAWE workshop, Clemson University, available from: <https://tigerprints.clemson.edu/cgi/viewcontent.cgi?article=1075&context=aawe>

Verma, S., Mansouri, Z., Selvam, R.P. (2021). Incorporating Two Weeks Open Source Software Lab Module in CFD and Fluids Courses, Paper presented at 2021 ASEE Midwest Section Conference, Virtual. DOI: [10.18260/1-2-1125.1128.1153-38325](https://doi.org/10.18260/1-2-1125.1128.1153-38325)

Mansouri, Z., Verma, S., Selvam, R.P. (2021). Teaching Modeling Turbulent Flow Around Building Using LES Turbulence Method and Open-source Software OpenFOAM, Paper presented at 2021 ASEE Midwest Section Conference, Virtual. DOI: [10.18260/1-2-1125.1128.1153-38326](https://doi.org/10.18260/1-2-1125.1128.1153-38326)

Conference Presentations

Selvam, R.P. & Verma, S. (2018). Effect of height of the tornado chamber on vortex touchdown, Presented at *International Conference on Application of Fluid Dynamics (ICAFD-2018)*, December 13-15, VIT, Vellore, India.

Selvam R.P. & Verma, S. (2019). Comparison of CFD model touchdown flow field with TTU experiment, Presented at *15th International Conference on Wind Engineering (ICWE15)*, September 1-6, 2019, Beijing, China.

- Verma, S., & Selvam, R. P. (2019). Flow dependency upon the convection region height of a CFD tornado simulator, Presented at *103rd Annual Meeting of the Arkansas Academy of Science*, March 29-30, Conway, Arkansas, USA.
- Verma, S., & Selvam, R. P. (2019). Comparison of CFD Flow Field with Experiment & Effect of Chamber Geometry on Touchdown, Presented at: *Tornado Hazard Wind Assessment and Reduction Symposium (THWARTS-2019)*, University of Illinois Urbana Champaign, October 14-15, Illinois, USA.
- Verma, S., & Selvam, R. P. (2021). Differences in flow structures of tornado vortex and efficiency of different tornado chambers. Presented at: *6th American Association of Wind Engineering (AAWE) workshop*, Clemson University, May 12-14, South Carolina, USA.
- Verma, S., Mansouri, Z. & Selvam, R.P. (2021). Incorporating Two Weeks Open Source Software Lab Module in CFD and Fluids Courses. Presented at: *2021 ASEE Midwest Section Virtual Conference*, University of Arkansas, Fayetteville, September 12-14, Arkansas, USA.
- Mansouri, Z., Verma, S. & Selvam, R.P. (2021). Teaching Modeling Turbulent Flow Around Building Using LES Turbulence Method and Open-source Software OpenFOAM. Presented at: *2021 ASEE Midwest Section Virtual Conference*, University of Arkansas, Fayetteville, September 12-14, Arkansas, USA.

Technical Report

Verma, S. & Selvam, R. P. (2021). An extended report on ‘Incorporating Two Weeks Open Source Software Lab Module in CFD and Fluids Courses. Available online: <https://github.com/rpsuark/ASEE21-OpenFOAM-Introduction/blob/main/ASEE-introduction.pdf>

MEMBERSHIPS AND PROFESSIONAL AFFILIATION

- American Association of Wind Engineering
- American Society of Civil Engineers
- Society of Industrial and Applied Mathematics (SIAM)
- Arkansas Academy of Science
- Registered Engineer (Registration No.: 13279 Civil “A” category), Nepal Engineering Council
- Nepal Engineers’ Association